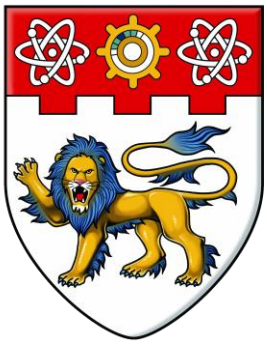

NANYANG TECHNOLOGICAL UNIVERSITY

# MAGNET-POLYMER COMPOSITE TRANSDUCERS

**NGUYEN QUANG VINH**

**SCHOOL OF MATERIALS SCIENCE AND ENGINEERING**

**2011**

# MAGNET-POLYMER COMPOSITE TRANSDUCERS

**NGUYEN QUANG VINH**

**School of Materials Science and Engineering**

A thesis submitted to the Nanyang Technological University

in fulfilment of the requirements for the degree of

Doctor of Philosophy

**2011**

# ACKNOWLEDGEMENT

I would like to express my most sincere gratitude to Prof. Raju V. Ramanujan, my advisor, for his constant guidance and mentoring. Thank you for sharing your wide spectrum of knowledge and experience that have made my work much more realizable. Your prompt advices have eased many obstacles during the project. Without you, this project would not have been possible. Over the years, you have been both my academic advisor and life mentor who always listens and teaches me valuable life lessons.

I am very grateful to Prof. Subbu Venkatraman, Prof. Rajdeep Rawat, Prof. Sridhar Idapalapati, Prof. Mahinda Vilathgamuwa and Prof. Su Haibin for invaluable technical guidance and facility support for some of the experiments.

I am thankful to the technicians from the school laboratories, especially Mr. Patrick Lai from the Organic Materials Lab and Ms. Yeow Swee Kuan from the Inorganic Materials Lab. You have been so helpful and approachable. I am appreciative of your great help during the experiments carried out throughout the project.

I thank my dear group mates, Akhilesh, Boon Hwee, Derrick, Jia Yan, Rebecca, Sibnath and Sreekanth. There has been so much fun in our group. I will remember our talks about technical matters and everything else under the sun.

I would also like to express my thanks to the Kauffman Foundation and the Nanyang Technopreneurship Center for giving me the chance to learn about entrepreneurship at some of the top innovative sites in the world. Throughout the Kauffman Global Scholars program, I gained a better understanding of how technologies can be best used to make the world a better place.

I am also hugely indebted for the unconditional love and support from my family. Thank you for making my life revolving about magnetism and actuation so fruitful.

# ABSTRACT

Current actuation technologies do not provide a satisfactory solution to the requirement of having a muscle like motion, such motion will be very useful in robotics, MEMS and biomedical applications, etc. Hence a magnetically actuated material was studied as an "artificial muscle". The material is a composite of a soft polymer with magnetic material as the filler (Magpol). Magpol composites are a new class of bio-inspired smart soft transducers for morphing, damping, and artificial muscle applications. Magpol exhibits large changes in shape and physical properties in response to an external magnetic field. This shape changing behavior of Magpol in an external magnetic field was studied and actuation performance investigated. The large change in electrical resistivity driven by the shape change was also examined for sensing applications. This versatile combination of actuation and sensing behavior results in attractive transducers.

Various actuation modes, including contraction, elongation and deflection were studied. These actuation modes can be combined to produce complex motions. A novel coiling mode was observed. Simply by changing boundary conditions, Magpol can exhibit a change in actuation mode from axial contraction to a novel coiling mechanism. The magnetic buckling which results in coiling was studied by computer simulation and analytical modeling. The analytically predicted magnetic fields for buckling agreed well with experimental values. The relationship between strain and magnetic field suggested that post buckling behavior is a stable symmetric bifurcation, which is useful for continuous actuation.

The actuation metrics of Magpol were studied, maximum strains were 40% for contraction, 60% for coiling and 80% for elongation. Maximum stress of up to 164 kPa, 184 kPa and 216 kPa were measured in contraction, coiling and elongation modes, respectively. These metrics are equal or better than those in natural muscles and most competing artificial muscle technologies. This thesis also presents the first report of work-loop measurement for this class of smart material. The maximum measured work values were 141 $kJ/m^3$ for contraction and 164 $kJ/m^3$ for coiling. The maximum work density of Magpol was higher than the maximum work density of mammalian

skeletal muscles. A proof-of-concept artificial muscle made from Magpol was demonstrated. Experiments on the dynamic properties showed that Magpol can achieve a strain rate of more than 1500 $\%.s^{-1}$ and respond to a driving frequency of up to 80 Hz. A strain-time model showed that the dynamic properties could be related to its unique "on-off" actuation behavior.

Percolation principles can be used to make this type of actuator an intrinsic self-sensor. The electrical resistivity of a polymer matrix containing fillers of iron particles and graphite flakes at percolation concentration is a strong function of mechanical strain and thus can be used for automatic sensing. Large changes in resistivity of three to four orders of magnitude and sensitivity (i.e., the change in resistivity caused by 1% change in strain) in the range of 1,000-10,000 were observed. Both actuation and sensing properties were successfully combined to demonstrate that Magpol possesses attractive attributes as a transducer, its soft, muscle like characteristics point to novel possibilities for biologically inspired applications.

# TABLE OF CONTENT

# LIST OF FIGURES

# LIST OF TABLES

# CHAPTER 1 - INTRODUCTION

## 1.1 Motivation

### *1.1.1 Smart Materials for Shape Changing Structures.*

Shape changing structures have attracted intense interest due to their attractive ability to morph and adapt to environmental conditions [1-3]. Such structures can be used in novel application areas of high current interest, including biomedicine, structural health monitoring, defense, aerospace, adaptive optics, robotics, etc. [4-8]. For example, aircrafts with morphing wings have been developed to optimize flight conditions [9]. Shape changing structures can also bring fresh ideas to existing products, including morphing dresses [10]. Artificial muscles are important examples of novel, bio-inspired morphing structures [11-13].

Shape changing structures [2, 14-18] are developed from smart materials which can change shape in response to external electrical, magnetic, chemical or thermal stimuli [12, 19]. However, a common drawback of current smart materials such as piezoceramics, magnetostrictive materials, shape memory alloys (SMAs), etc. is that strain or response time is typically too low [2]. For example, magnetostrictive or piezostrictive materials exhibit a typical actuation strain of only ~ $10^{-3}$ % [20]. SMAs have high actuation stress and strain but their typical working frequency is below 1 Hz due to the time dependent thermal diffusion process [21]. Therefore, there is an urgent need for further development of smart materials for shape changing structures. In addition, the ability to sense deformation is very desirable because it can provide accurate control of actuation without the addition of an external sensing mechanism, thus minimizing overall weight.

### *1.1.2 Artificial Muscles*

In recent years, great attention has been paid to artificial muscle systems which mimic human or animal movement [13]. In the field of artificial muscles, there is a strong need for a new platform of actuators that can perform the motion of natural muscles. The current actuation technologies, e.g., combustion engines and high performance motors require complex transition mechanisms and are unsuitable for non-repeating motions. Electric motors have lower force to mass ratio than natural

muscles [22]. Piezoelectric actuators can produce precise displacements but are limited by their low strains. The constraints of current actuation technologies make it a challenging talk to mimic the motion of humans. For example, the advanced humanoid Asimo robot from Honda can only walk at speeds of up to 1.6 km/h due to the limitations of the actuators used [23]. Therefore, a muscle-like actuation technology will greatly benefit human assisting devices, human implants and many other fields [24].

Recognizing the importance of such technology, the scientific community has increased its interest in soft actuators. Soft polymer based actuators are very useful as artificial muscles because their mechanical properties can be similar to natural muscles and they can be readily fabricated [25]. Since the pioneering work by Bar-Cohen [26], there have been a large number of publications on this topic, especially the class of electrically driven polymeric actuators known as electroactive polymers (EAPs). Until now, EAPs are the most commonly studied class of polymeric actuators for artificial muscles [27]. There was even a challenge to scientists and engineers to create an arm using EAP that can beat a human in an arm wrestling contest (the contest logo is shown in Figure 1-1). There are two main types of EAPs, the first is ionic EAPs, such as ion-polymer metal composites, conductive polymers and ionic gels. Ionic EAPs require low operating voltages (~ 1-2 V). However ionic EAPs exhibit slow response (typically 0.1-1 s), low actuation stress and there is a need for constant hydrolysis [28]. The second type of EAP is field activated EAPs, e.g., ferroelectric polymers, dielectric elastomers and electrostrictive graft elastomers [28]. Field activated EAPs are fast, the response frequency can be higher than 1 kHz and the response time is typically less than 10 ms, they can generate high force and operate at room temperature for extended times. However, they require high operating fields, as much as 200 V/μm [28]. This leads to safety and reliability concerns due to premature material breakdown. An EAP which combines the best performance metrics of the two types has not been found, hence there is a need for a different actuator system, such as magnet - polymer composites (Magpol).

Figure 1-1: Logo of the arm wrestling contest using EAP arms [29].

## 1.2 Magnet - Polymer (Magpol) Composites for Transducer Applications.

The idea of combining the flexibility of polymer matrix - magnetic filler composites with the excellent driving capability of external magnetic fields for novel transducer applications has been studied in this work. Generally, Magpol refers to composites of a flexible polymer matrix and filler of magnetic particles, such composites can be used as soft actuators [30-33]. Magpol is also termed ferrogel [31, 33-39], magnetic gels [40, 41], magnetic field sensitive gel [32, 42-46], magnetorheological elastomer [47, 48], or magnetoactive polymer [49]. The polymer can be either hydrogels [50-55], silicones [56-58], polyurethanes [59, 60] or rubber [61]; the magnetic particles can be either magnetically soft [49, 62] or hard [63, 64] magnetic materials. From the artificial muscle stand point, electric or magnetic fields are most effective for signal control [65]. The coupling of such fields with the elastic response of Magpol can result in powerful actuators. Zrinyi studied actuating ferrogels, which are hydrogels network hydrated by a ferrofluid [31, 32, 34, 35, 42, 44, 66] which is a magnetizable solution due to the presence of nanosized magnetic particles [67].

When Magpol samples are exposed to an external magnetic field, the magnetic field exerts a force on the magnetic particles. Due to the small size of the filler particles and strong interaction with molecules of dispersing liquids or the surrounding polymer chains, changes in molecular

conformation accumulate and lead to an overall shape change of the composite [35, 44], as depicted in Figure 1-2.

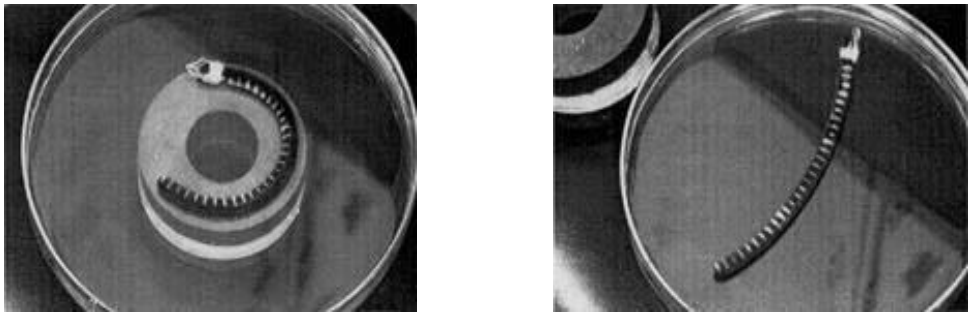

(a) (b)

Figure 1-2: Shape distortion of a ferrogel when exposed to a non-uniform magnetic field produced by a permanent magnet: (a) Gel located 15cm from magnet, (b) Magnet placed directly below ferrogel, exhibiting obvious shape change [68].

Magpol can provide significant advantages for novel remote, contactless applications including artificial heart and transducers for structural health monitoring. Actuation modes of Magpol includes elongation [44, 54, 69-72], contraction [65], deflection [30, 49, 63, 73-75], zigzag [76], shear [77], torsion [61, 78] and rotation [78, 79]. The response time to obtain the new shape was found to be less than 0.1 second and independent of the composite sample size [66]. Actuation strain of 60% [70], actuation stress of 6.8 kPa [54] and actuation work of 320 $J.m^{-3}$ were reported in elongation mode for poly(vinyl alcohol) hydrogel and $Fe_3O_4$ nanoparticle composites [70]. Actuation stress of up to 10 kPa and work density of up to 70 $J.m^{-3}$ were achieved in composites of silicone matrix and $Sm_2Co_7$ hard magnetic filler particles [63]. In contraction, composites of PVA hydrogel and $Fe_3O_4$ nanoparticles produced strain of up to 40% [65] and work density up to 400 $J.m^{-3}$ [65, 70]. During the deformation process, the volume of Magpol does not change, when the magnetic field is removed, the original shape is re-established. Figure 1-3 demonstrates the axial elongation and contraction of a ferrogel.

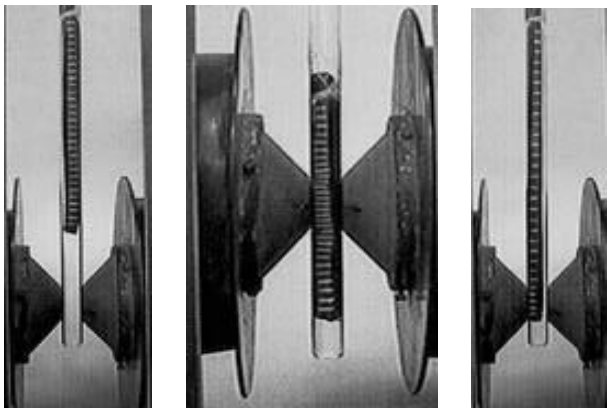

(a) (b) (c)

Figure 1-3: Shape change of a ferrogel in a non-uniform magnetic field: (a) Original length of ferrogel, (b) Contraction of ferrogel, (c) Elongation of ferrogel [68].

This versatility and good performance make Magpol a promising material for many applications, including fluid pumps [79], artificial muscles [80] and soft actuators [65, 81]. Magpol has also been used, especially in membrane form, in microchannels or peristaltic pumps for nanofluidic systems [82, 83]. Its shape changing characteristics can be combined with the principle of tuning the mechanical properties (e.g., elastic modulus) by an external magnetic field to develop novel dampers and seals [84].

Inorganic filler particles can be incorporated in polymers to form electrically conductive composites with novel properties [85, 86], applications for such electrically conductive polymers include chemical synthesis, biosensors, corrosion protection and microelectronic devices [87]. If percolation concepts are employed, this type of conductive composite can also be useful as mechanical sensors. The electrical resistivity of polymeric composites with conductive fillers at the percolation concentration is very sensitive to mechanical strain [88]. This phenomenon is usually termed piezo-resistivity or elasto-resistivity.

By adding electrically conductive fillers at appropriate concentrations to the polymer matrix in addition to the magnetic fillers, both actuating and sensing can be achieved in Magpol. The dual ability of actuation and self-sensing is very desirable because it can provide control of actuation without addition of an external sensing mechanism. The combination of actuator and sensor has

been studied previously but not explored fully, probably due to the inadequate actuator properties found in previous studies [63, 89]. An increase in actuator performance will make transducers based on Magpol more attractive for practical applications.

### 1.3 Novelty and Significance of Study.

Magpol belong to a group of "Intelligent materials" which are capable of reacting to various environmental stimuli such as electric or magnetic field, pH, temperature, sound, etc [19]. Magpol also represents a new class of magnetic field controlled elastic materials [32]. The elastic matrix, together with the magnetic properties of the fillers, allows tuning the shape changing behavior of Magpol by external magnetic fields, biocompatibility of Magpol can be obtained by choosing suitable polymers and magnetic materials [40].

Existing platforms for soft actuators exhibit a common drawback: They do not have both fast response to stimuli as well as the ability to deform in various directions. For example, thermally activated shape memory alloys can deliver high strain rates but only in deflection mode. Magnet - polymer composites can address such limitations with their unique mechanical properties. However, many aspects of this class of soft actuating material have not yet been explored. Therefore, actuating properties of Magpol were studied, and their performance was evaluated in this work.

The composite was found to exhibit several deformation modes such as contraction, elongation and deflection. A novel actuation mode of Magpol was also observed, the composite coils rather than contracts to reduce its length (Figure 1-4) [90]. This coiling was found to be the result of buckling of Magpol in an external magnetic field in a suitably constrained region. The strain, stress and work producing capability in elongation, contraction and coiling modes were also studied. Significant actuation of Magpol was feasible for magnetic fields produced by readily available hard magnets. This work also reports the first results of the evaluation of Magpol by the work-loop principle [91] used for characterizing artificial muscles [92]; the performance is significantly better than earlier reports [54, 93]. It is shown for the first time that Magpol outperforms natural muscles in terms of actuation stress, strain and work. This work also showed that Magpol actuators can respond to frequencies up to 80 Hz, and that strain rate higher than 1500 $\%.s^{-1}$ can be achieved.

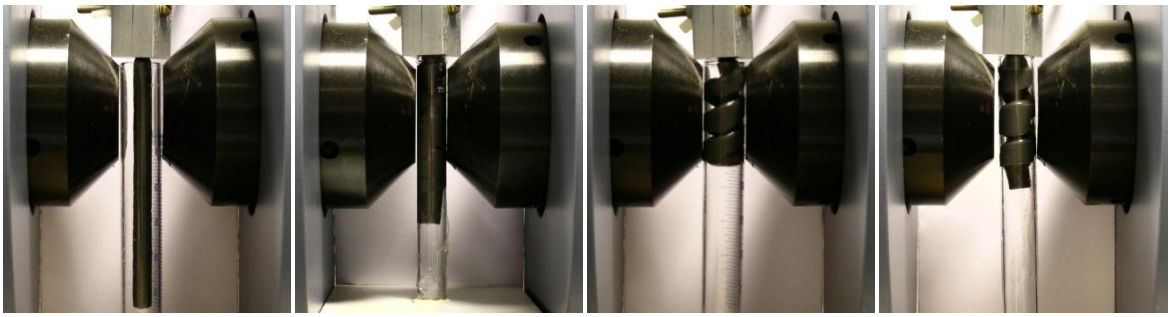

(a)Relaxed (b)Contracted (c) Coiled (d) Hybrid

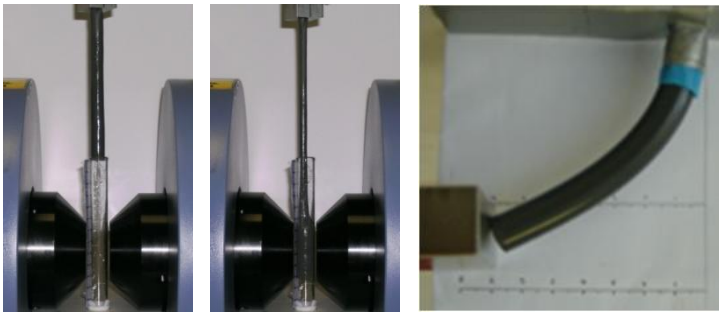

(d)Relaxed (e)Elongated (f) Deflected

Figure 1-4: Actuation modes of Magpol.

Interestingly, the actuation of the composites can be "sensed" by their piezo-resistive property. Piezo-resistivity is a phenomenon whereby the resistivity of a composite of a non-conductive matrix (usually a polymer) and conductive filler changes when the composite is deformed. Conductive Magpol composites were successfully fabricated and sensing properties investigated, the electrical resistivity of Magpol was found to exhibit high sensitivity to mechanical strain. This combination of actuation and sensing enabled a novel type of self-monitoring soft transducer. The transduction properties were determined for elongation, contraction and coiling modes. Proof-of-concept artificial muscles based on Magpol transducers were successfully demonstrated.

## 1.4 Scope of Study.

The goal of this work is to perform experimental and theoretical studies of Magpol transducers. Both actuating and sensing properties of such composites were studied. The experimental work includes synthesis, characterization of morphology, magnetic and mechanical properties, and evaluation of actuating, sensing and transduction performance. The theoretical studies include

mathematical modeling and computer simulation to understand the behavior of Magpol. In particular, an energy based mathematical model was employed to investigate actuation characteristics, modeling was also used to examine the dynamic properties of Magpol. Both mathematical and computer simulations were utilized to study the buckling of Magpol in a magnetic field which leads to coiling.

### 1.5 Description of Thesis.

Chapter 2 provides the background related to this work. It includes the actuation properties of Magpol and other competing platforms for artificial muscles and magnetic actuators. This chapter also discusses the desired properties of the polymer matrix and the magnetic fillers. The last part of Chapter 2 discusses the self-sensing ability of Magpol.

Chapter 3 details the experimental procedures, including the selection, preparation and characterization of the magnetic filers, the polymer matrix and the composite. The performance evaluation of actuation strain, stress and work and the dynamic properties of the composites are described in this chapter. This chapter also outlines experimental procedures for determining the sensing and transduction properties of Magpol.

Chapter 4 presents the description and discussion of the results obtained in this work, including the experimental results of the characterization and property evaluation of the magnetic materials and the polymers, as well as the actuation, sensing and transduction properties of Magpol. The results obtained from mathematical and computer simulations are also provided.

The major conclusions from this work are presented in Chapter 5.

# CHAPTER 2 - LITERATURE REVIEW

## 2.1 Actuator Technology

### *2.1.1 Definition*

Actuators, such as artificial muscles, are defined as controllable work-producing devices [94]. Actuators play a significant role in our daily lives and provide a wide range of applications (Figure 2-1).

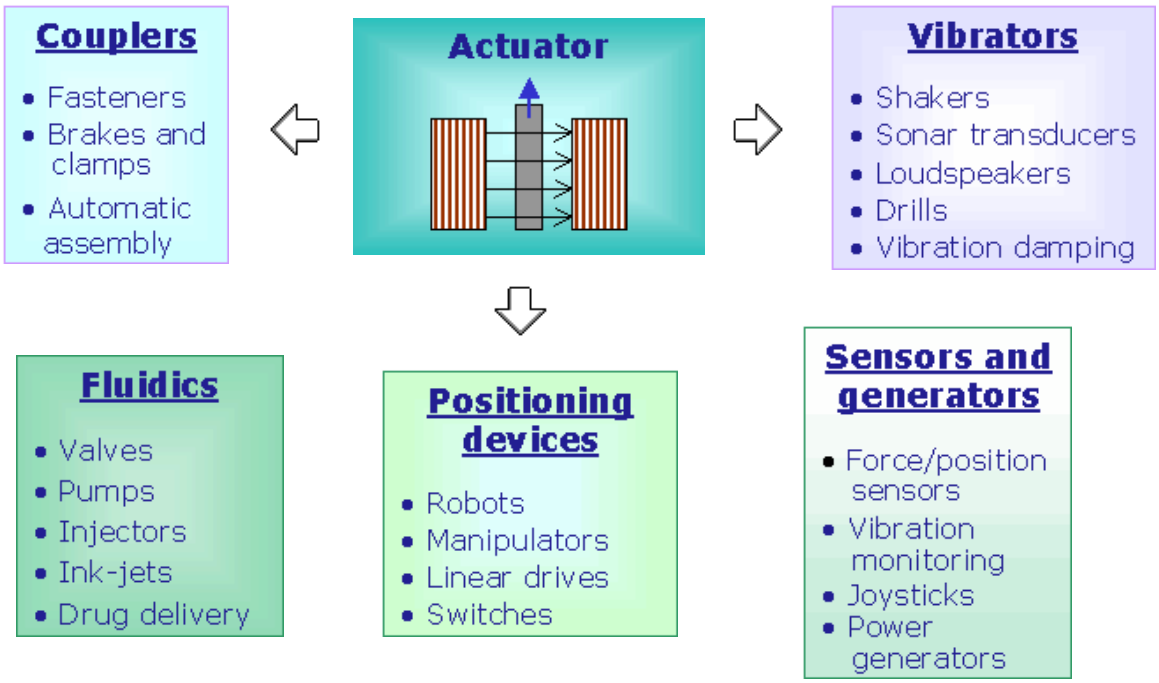


Figure 2-1: Typical applications of actuators [95].

### *2.1.2 Performance Indices of Actuators*

Actuators operate in vastly different mechanisms and offer a wide array of performance capabilities. To select a suitable material for an actuator, the corresponding performance characteristics of actuators have to be carefully considered. Fortunately, selection of the materials for actuators is well-established [96-101]. A number of important performance characteristics of actuators are listed in Table 2-1.

Table 2-1: Some performance indices of actuators [96]

| Performance Characteristics | Definition |
|---|---|
| Actuation stress $\sigma$ | The force per unit cross-sectional area generated by an actuator. |
| Maximum actuation stress ($\sigma_{max}$) | The maximum value of stress generated by an actuator in a single stroke. |
| Actuation strain ($\varepsilon$) | The nominal strain produced by an actuator. |
| Maximum actuation strain ($\varepsilon_{max}$) | The maximum value of actuation strain produced by an actuator in a single stroke. |
| Work | The amount of work of an actuator performs in cyclic operation. |
| Frequency | The number of cycles an actuator can perform in a second. |

In designing an actuator, one needs to consider multiple sets of characteristics. Property charts facilitate a systematic approach to selection of materials in terms of performance metrics [101]. When the performance of different classes of actuators are plotted on property charts, certain relationships become clear. For example, an important chart for actuator properties is actuation stress versus actuation strain diagram (Figure 2-2), which allows quantitative comparison among actuators. The outline of constant stroke in this figure reveals the potential competition between different actuation systems. The nearer a system lies near to the upper right corner of the diagram, the more energy capacity it can provide. For example, solenoids with a work capacity of 1-5 $kJ/m^{-3}$ are potential competitors of thermal expansion actuators with temperature change ranging from 10-100 K since both types of actuators lie near the same energy capacity diagonal of the diagram.

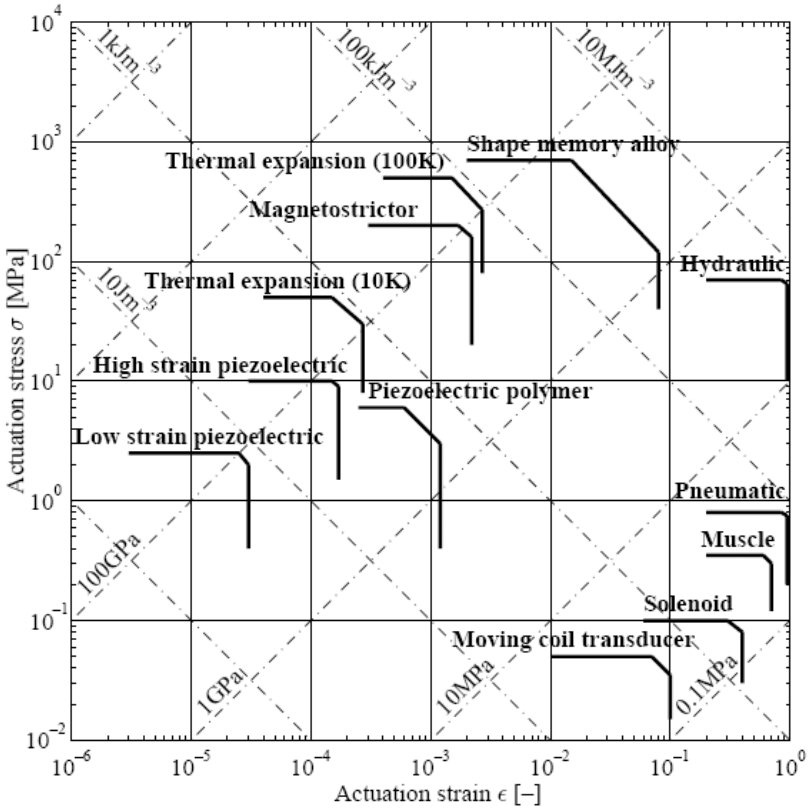


Figure 2-2: Actuation stress v/s actuation strain of common actuators. Heavy lines indicate the upper limits of performance [102].

However, performance characteristics are unique to an individual product; two actuators of the same class can have very different performance values [96]. Thus it is useful to use a set of normalized attributes that are, at least approximately, characteristic of an entire class of actuators. Figure 2-3 presents the normalized maximum force and displacement characteristics of available actuators. In practice, levers, gear, screws, etc. can be used to adjust certain performance metrics of actuators. The use of these mechanisms greatly expand the applicability of many actuators. For example, the displacement of a pneumatic and a solenoid actuator can be increased using a truss structure (Figure 2-4).

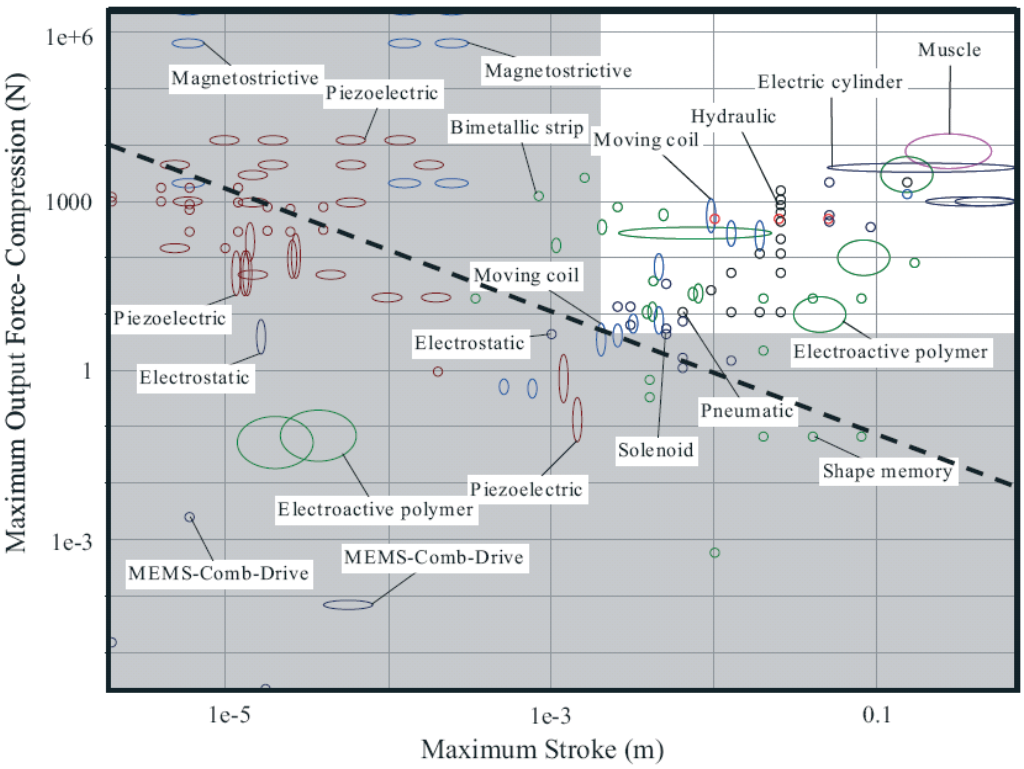


Figure 2-3: Normalized maximum actuator output force versus normalized maximum stroke for commonly used actuators [96].

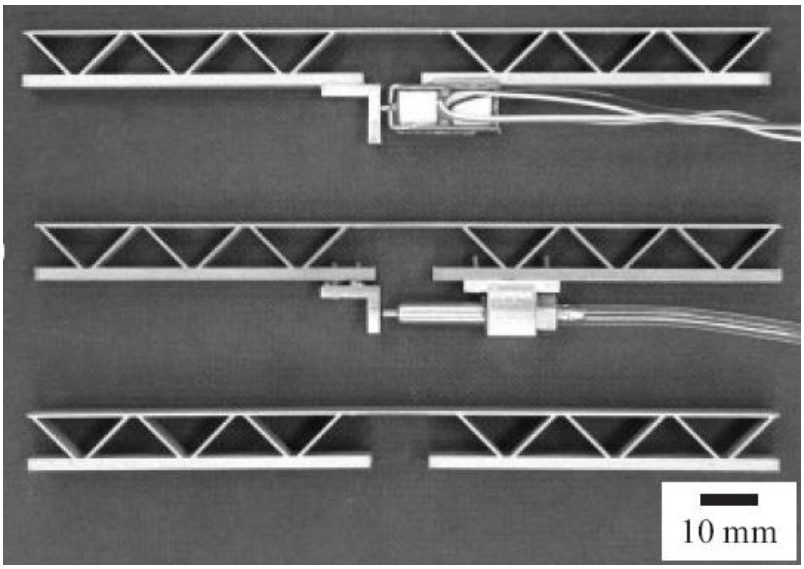


Figure 2-4: Integration a pneumatic and solenoid actuators to a truss structure [96].

The performance attributes of actuators are size-dependent. The absolute values change with size, and the performance characteristics of an actuator class change drastically for different length scales. For example, MEMS actuators promise favorable stress and work due to the enhancement of

strengths at small scales [97]. Many MEMS actuator classes do not have an equivalent actuator class on the macro scale, and the reverse is also true for several types of macro actuators. Some macro actuator classes cannot be fabricated in the microscale due to manufacturing difficulties.

Figure 2-3 can be modified (Figure 2-5) with the consideration of both macro and micro scales, the force capacity of electromagnetic and magnetostrictive actuators can be seen to be relatively low compared to other actuator types. It has been proven that magnetic force decreases quickly in the micron size range [103]. In typical magnetic MEMS devices, the maximum achievable displacement is between $10^{-5}$ m and $10^{-3}$ m and the maximum force is between $10^{-7}$ N and $10^{-4}$ N [97]. To achieve higher force and work, systems of higher magnetic energy density are desired. Unfortunately, the currently available choices of micromagnets are limited and not optimal for microsystems.

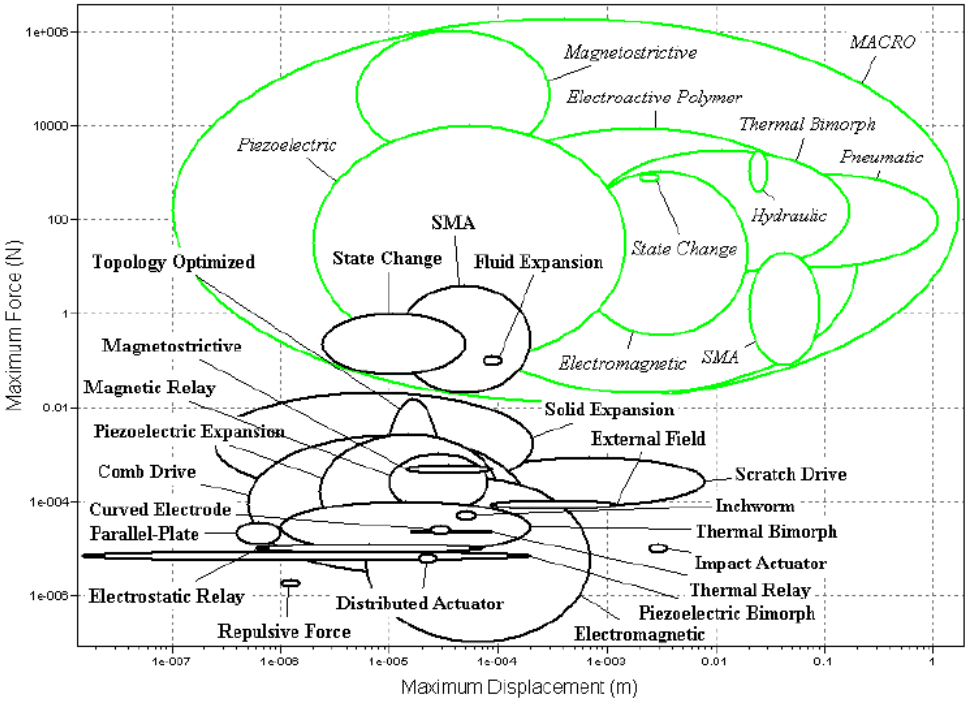


Figure 2-5: Actuation force v/s displacement chart of common MEMS and macro actuators [97].

Performance charts for other important characteristics such as specific stress, operating frequency, strain resolution, etc. are also available [96, 97, 102].

## 2.2 Actuators for Artificial Muscle Applications

### *2.2.1 Background*

Artificial muscles have been constructed from conducting polymers, dielectric elastomers, ferromagnetic SMAs, relaxor ferroelectric polymers, field driven liquid crystal elastomers, molecular actuators, ion polymer metal composites (IPMC), thermal activated SMAs and carbon nanotubes [104]. Electroactive polymers (EAPs) are especially popular due to similarities between the mechanical properties of natural muscles and polymers.[105]

### *2.2.2 Performance Indices of Artificial Muscles*

For artificial muscles, more specific indices than those introduced in section 2.1.2 are used to define their performance. Some important performance indices relevant to artificial muscles are included in Table 2-2.

Table 2-2: Performance indices for artificial muscles [24].

| Performance Characteristics | Definition |
|---|---|
| Stress | Typical force per cross-sectional area under which the actuator materials are tested. |
| Strain | Displacement normalized by the original material length in the direction of actuation. |
| Strain rate | Average change in strain per unit time during and actuator stroke. |
| Bandwidth | Frequency at which strain drops to half of its low frequency amplitude |
| Work density | Amount of work generated in one actuator cycle normalized by actuator volume. This does not include the volume occupied by electrolytes, counter electrodes, power supplies, or packaging. |
| Specific power | Power output per unit mass of actuator material. Typically only the mass of the material itself is considered. |
| Efficiency | Ratio of work generated to input energy. |
| Electromechanical coupling | Proportion of input energy that is transformed into work, including external work done by the actuator and stored internal mechanical energy generated in the actuator itself. |
| Cycle life | Number of useful strokes that the material can undergo. |
| Elastic modulus | Material stiffness multiplied by sample length and divided by cross-sectional area (before creep is induced) |
| Voltage | Operating voltage for electric field driven actuators |

More detailed descriptions of the performances indices for artificial muscles are presented in Appendix A.

## 2.3 Performance of Biological Muscle

The performance data of biological muscles is well-established (Table 2-3). These performance metrics are commonly used as benchmarks for artificial muscle studies.

Table 2-3: Performance of biological muscles [106].

| Metrics | Performance |
|---|---|
| Maximum Strain (%) | 40 |
| Maximum Isometric Stress (MPa) | 0.1 |
| Maximum Work Output (J/kg) | 0.18 - 40.57 |
| Maximum Power Output (W/kg) | 9 - 284 |
| Maximum Frequency (Hz)<br>Birds (Hummingbird)<br>Mammals (Mouse, Rabbit) | <br>50<br>6 - 18 |

#### 2.3.1.1 Force Characteristics of Biological Muscles

Muscles produce work by creating tension while contracting. Generally, force produced by muscles is proportional to the muscle length (length - tension property) and the muscle contraction velocity (force - velocity property). These two relationships are characteristic of muscle performance.

#### 2.3.1.2 Length - Tension Relationship

The length - tension relationship of muscles is represented by the isometric contraction, i.e., the muscle length is kept constant in the entire range of contraction [107]. In the isometric force generation process, the tension produced by muscles are counterbalanced by the reaction force of the measurement device. The length - tension relationship is characterized by the isometric length -

tension curve, which indicates the maximum force a muscle is able to produce while being held different discrete lengths. A typical isometric length - tension curve is shown in Figure 2-6.

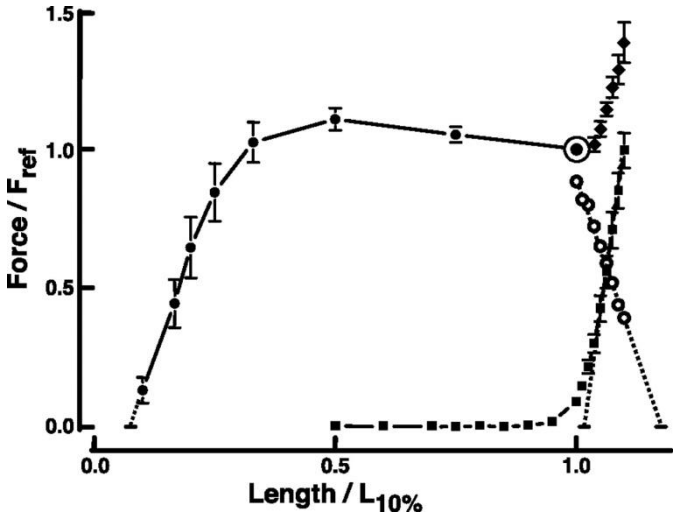


Figure 2-6: Length - tension relationship of porcine airway smooth muscle [108].

### 2.3.1.3 Force - Velocity Relationship

The force - velocity relationship of muscles is represented by the isokinetic contraction, i.e., muscles contract at a constant speed. Experimentally, a muscle is stimulated to contract against a constant load. The velocity during contraction is measured and then plotted as a function of the resistive force. The resulting curve is called the force - velocity relationship curve (Figure 2-7). Generally, normalized values of isometric force and muscle velocity are represented on force - velocity graphs.

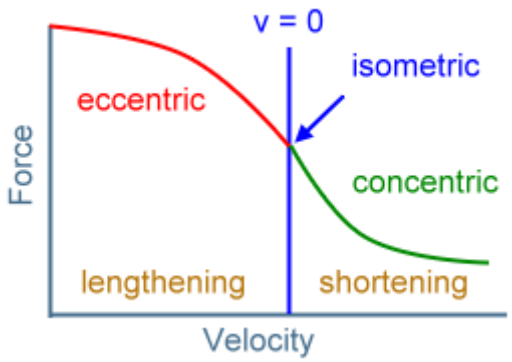


Figure 2-7: A typical force - velocity relationship curve of muscles [109].

#### 2.3.1.4 Muscle Work Measurement by the Work-loop Technique

The most important function of a muscle is its ability to perform work by contracting against a load [110, 111]. A static actuation property such as isometric force does not reflect the actual capacity of a muscle. When used to measure the force and power output of natural muscle, the work-loop method incorporates factors such as activation time and relaxation time of the muscle as well as time required for contraction, deactivation and force enhancement. Therefore, the work-loop technique can better reflect muscle functions *in vivo* [112].

The work-loop technique involves subjecting actuators to cyclic length changes. Soft actuators are attached to a movable lever, subjected to cyclic length changes as well as to stimuli at a distinct phase of their motion, while the force is constantly measured. The measured force is plotted against length on a graph, resulting in a loop whose area represents the net work done by the actuators in each cycle of activity [112]. Net work done by the actuators is equal to the work done during shortening less the work done during lengthening. A counterclockwise loop represents positive energy generated by the muscle while a clockwise loop suggests that the muscle is absorbing energy. Power output can be obtained by multiplying the net work per loop with the cycle frequency. The work-loop technique is based on the assumption that the length of actuators changes in a sinusoidal manner because most muscles involve repetitive contraction - relaxation cycles [113]. Figure 2-8 shows a typical work-loop of natural muscles, and calculation of the net work done by the muscle.

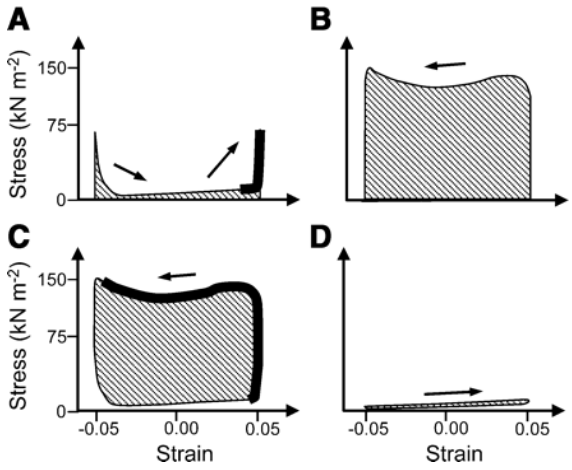


Figure 2-8: A typical work-loop graph. (a) Negative work done by muscles during lengthening, (b) Positive work done by muscles during shortening, (c) Net work done by muscles (B - A), (d) Net work done by muscles during a work-loop cycle. The thick line indicates the stimulation duration, and the arrows indicates the direction of the work-loop [114].

It has been suggested that work and power output of artificial muscles such as EAPs should be obtained using the work-loop technique [113, 115]. Figure 2-9 shows the work-loop of a dielectric polymer actuator, depicting work done during elongation and contraction due to electrical stimulation [116]. However, this technique has not been used in previous studies of Magpol.

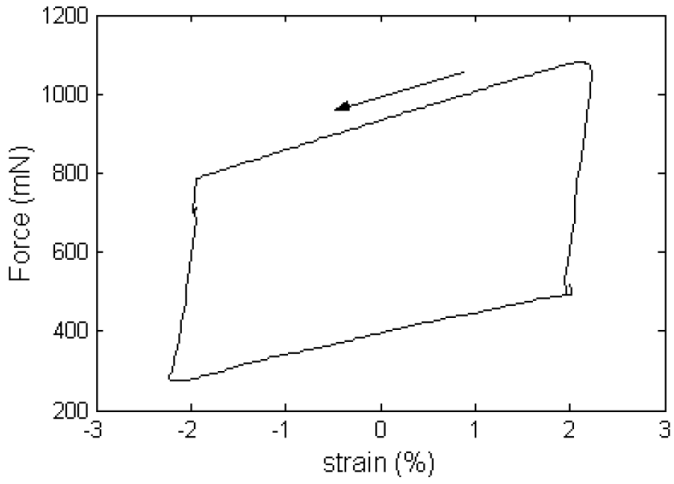


Figure 2-9: Work-loop of a dielectric polymer actuator [116].

## 2.4 Magnet - Polymer Composites for Artificial Muscle Applications

### *2.4.1 Deformation Characteristics of Magpol*

The use of Magpol as actuators was studied by Zrinyi *et al* [35]. In general, the deformation of ferrogels can be induced by either uniform or nonuniform magnetic fields. In a uniform magnetic field, the net force exerting on ferrogel samples is zero, the magnetostatic interactions between the magnetic dipoles dominate and may cause the filler particles to form a chain-like network[117]. However, shape deformation of ferrogel samples can occur in a uniform magnetic field due to demagnetization fields [118]. This was shown experimentally by Gollwitzer, who noticed that a ferrogel sphere elongated in a uniform magnetic field [80] (Figure 2-10). However, only a small deformation, of less than 1%, was observed in a homogeneous field due to the small and localized distribution of demagnetization field. It was later shown that the shape change of a ellipsoidal ferrogel sample in a uniform magnetic field depends on its geometry. A prolate spheroidal sample of aspect ratio K=a/b compresses in a uniform field if K exceeds a characteristic value of ~ 1.35, elongates when K < 1.35 and exhibits no shape change when K = 1.35 [119].

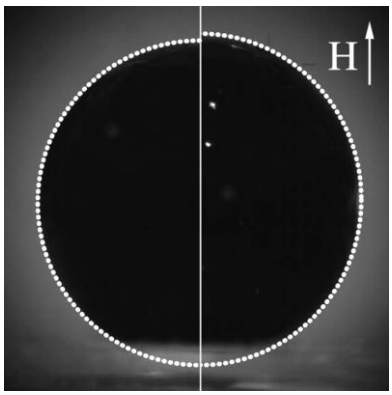


Figure 2-10: Distorted ferrogel ball in a uniform magnetic field [80].

In a nonuniform magnetic field, forces act on the magnetic particles due to the magnetic gradient. Due to the magnetic interaction between the magnetic particles and the strong adsorption between the particles and the polymer chains, changes in molecular conformation accumulate and eventually lead to shape changes. The final shape is established by the balance between magnetic forces acting on the particles and the elastic resistance of the polymer matrix. Shape change can be bending,

elongation, contraction, or a combination of these modes (Figure 2-11). Figure 2-11 shows that the sample was marked evenly along its length; in a nonuniform magnetic field, the marks were unevenly spaced, indicating inhomogeneous shape change (Figure 2-11).

Shape change due to the rotation of particles with shape anisotropy was also reported, but low strains, typically less than 1%, were achieved [69, 72].

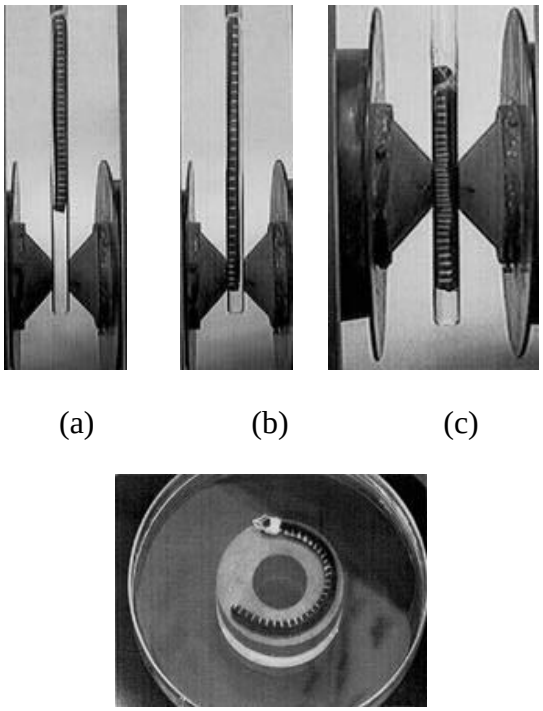

(a) (b) (c)

(d)

Figure 2-11: Shape change of ferrogel samples caused by an non-uniform magnetic field: (a) No external magnetic field is applied, (b) A magnetic field is generated below the lower end of the sample, (c) a magnetic field is generated at the middle of the ferrogel sample (d) Bending of a ferrogel sample induced by a permanent magnet [68].

The magnetic force density, $f_m$, acting on a ferrogel sample can be expressed as [35]

$$\mathbf{f}_m = \mu_0 \mathbf{M} \nabla \mathbf{H} \qquad \text{(Equation 2-1)}$$

$\mu_0$ is the magnetic permeability of vacuum, M is the sample magnetization, $\nabla H$ is the magnetic field gradient along the direction of deformation of the ferrogel. Since the driving force $(M\nabla)H$ varies in space, the deformation induced by a magnetic field is inhomogeneous. For uniaxial elongation or contraction, the deformation condition is [35]:

$$\lambda^3 - \beta(H^2_{top} - H^2_{bottom})\lambda - 1 = 0 \qquad \text{(Equation 2-2)}$$

where deformation $\lambda$ is the ratio of the elongated length and the original length. The parameter $\beta$ is defined as

$$\beta = \frac{\mu_0 \chi}{2G} \qquad \text{(Equation 2-3)}$$

where $\chi$ represents the initial susceptibility of the ferrogel, G is the composite's shear modulus and $H_{top}$ and $H_{bottom}$ represent the maximum and minimum magnetic field strength at the bottom and the top of a cylindrical ferrogel sample, respectively. When $H_{top} > H_{bottom}$, elongation occurs and when $H_{top} < H_{bottom}$, the ferrogel experiences unidirectional compression.

The stress and strain induced by a nonuniform magnetic field can be measured using the experimental setup shown in Figure 2-12.

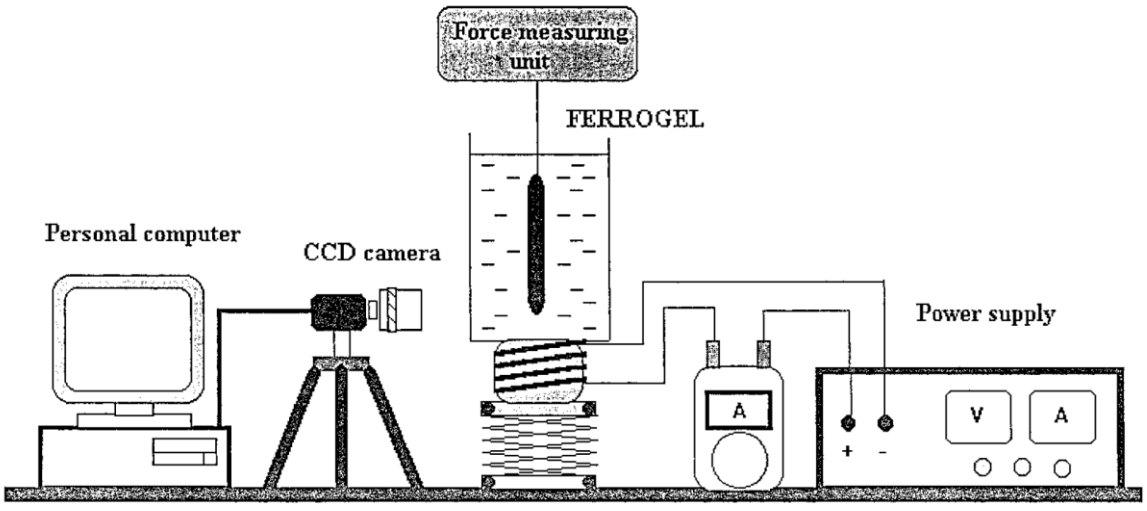


Figure 2-12: Schematic diagram of experimental setup to study actuation properties of ferrogels [42].

Figure 2-13 shows the relative displacement and force induced by a magnetic field as a function of current for a PVA ferrogel sample containing 4.95 wt% $Fe_3O_4$. It can be seen that the displacement of the ferrogel induced by the magnetic force is large. A giant 40% magnetostriction strain with 0.1 N induced force was obtained. A significant hysteresis was also observed during the elongation - contraction process of in both displacement and induced force. At small current values, a small displacement occurred and increased in a continuous manner with increasing current in the electromagnet. It was reported earlier that, in this regime, elongation strain is proportional to the square of current [32]. However, beyond a certain current value, an abrupt and large elongation occurred [35]. This abrupt change in the length of ferrogels took place within a very small range of current. Further increase of the current intensity led to a small increase in elongation.

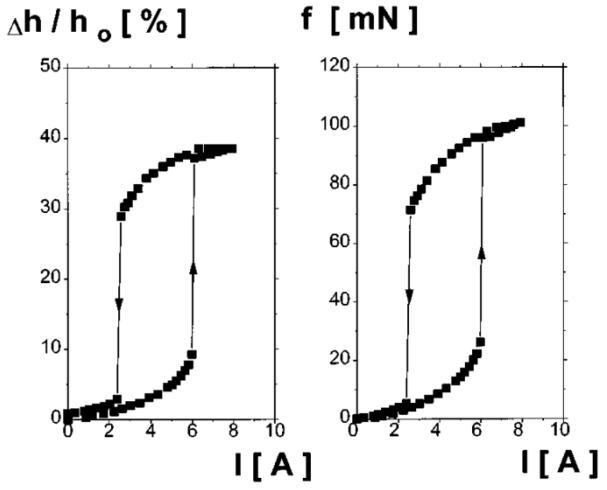


a) b)

Figure 2-13: Discontinuous elongation of a hydrogel with 5 wt% $Fe_3O_4$ [35].

The initial length of the gel, $h_0$ is 163 mm, $z_0$ = 54.2 mm a) Relative displacement as a function of current. b) Force as a function of current

The discontinuous deformation behavior of ferrogels is strongly dependent on the initial position of the ferrogel [35]. Figure 2-14 shows the dependence of relative displacement of the same sample as a function of current for four different values of sample - magnet distance. The initial position $z_0$ of the bottom of the gel relative to the electromagnet was varied, decreasing $z_0$ leads to a decrease in

both the degree of discontinuous displacement and the hysteresis in deformation. At a certain initial position, the displacement was continuous and there was no hysteresis.

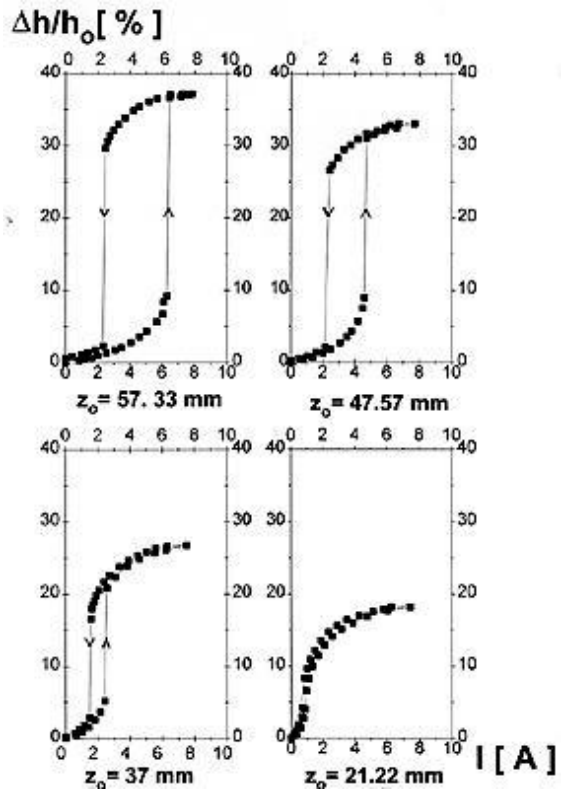


Figure 2-14: The effect of the initial position, $z_0$, on the discontinuous shape transition of ferrogel of 5.72 wt% PVA - 2.75 wt% $Fe_3O_4$: a) $z_0$ = 57.33 mm b) $z_0$ = 47.57 mm c) $z_0$ = 37.00 mm d) $z_0$ = 21.22 mm [35].

In conclusion, magnet - polymer composites showed great potential for actuation with their unique magneto-elastic properties and excellent strain of up to 40%. However, the nonlinear stress - strain relationship and especially the discontinuous shape transition and its strong dependence on initial position can be a challenge in controlling this novel actuator.

### *2.4.2 Performance Metrics of Magnet - Polymer Composites as Actuators*

#### 2.4.2.1 Magnet - Polymer Composites Compared to Other Magnetic Actuators

It is important to know the performance of Magpol actuators compared to other types of actuators. Figure 2-15 shows actuation force versus action strain for different types of magnetic actuators. It

can be seen that Magpol possesses the highest actuation strain among magnetic actuators. However, it produces the lowest actuation force. This suggests that improvement of force would be an important part of a study on magnet - polymer actuators.

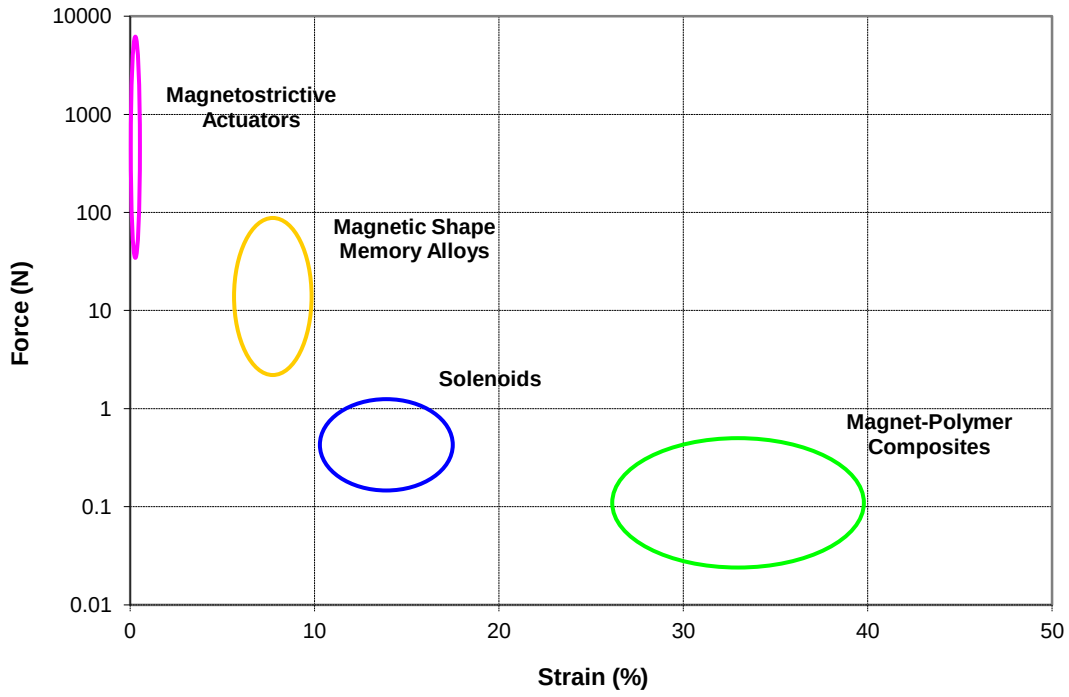


Figure 2-15: Performance chart of actuation force versus actuation strain for magnetic actuators [96, 120, 121].

### 2.4.2.2 Magnet - Polymer Composite Compared to Other Artificial Muscles

From the artificial muscle point of view, a similar comparison of available technologies, including Magpol, was performed. Figure 2-16 presents the performance chart of actuation stress versus actuation strain of these materials. Magpol has actuation strain very similar to that of natural muscle. Again, it is evident that actuation stress needs to be improved in order for Magpol to be a practical replacement of natural muscle.

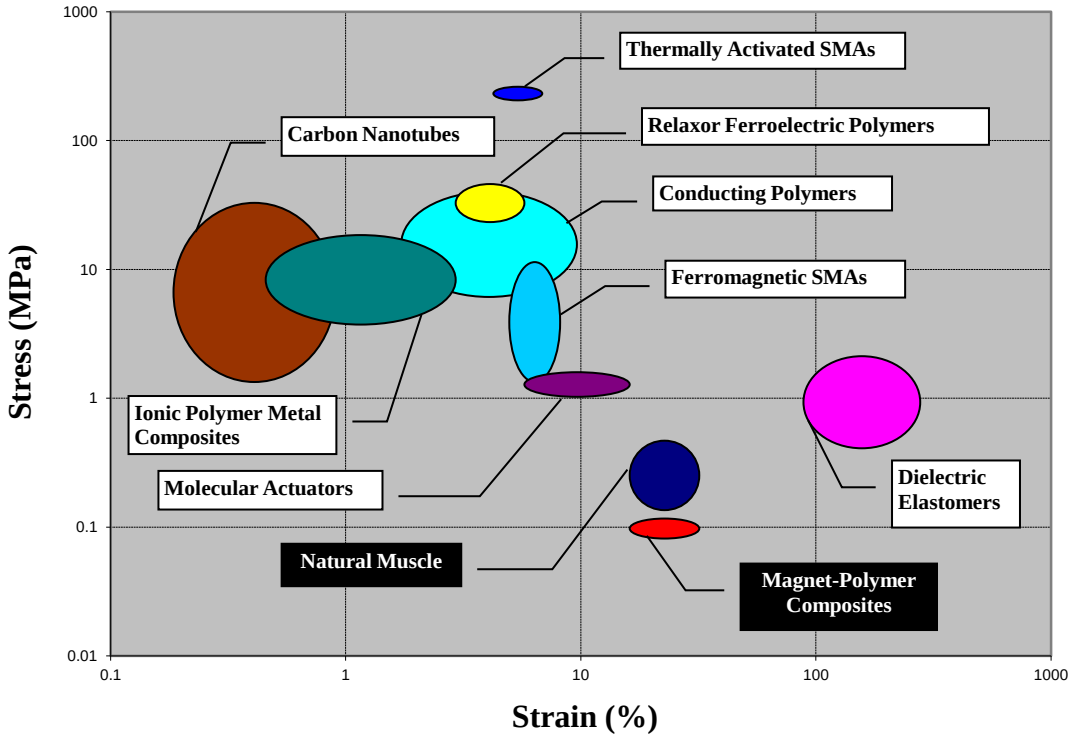


Figure 2-16: Performance chart of actuation stress versus actuation strain for artificial muscle materials[12].

### *2.4.3 Modeling the Shape Change Behavior of Magpol*

For the setup shown in Figure 2-12, Zrinyi developed a mathematical model between elongation strain and current density as follows [35]:

$$\frac{\lambda^3-1}{\lambda}\frac{1}{e^{-2\alpha|z|}-e^{-2\alpha|z_0+h_0|}}=\beta k_I I^2 \qquad \text{(Equation 2-4)}$$

where:

$\lambda$ is the deformation ratio, $\lambda = h/h_0$

z is the coordinate of the lower end of the ferrogel sample, $z_0$ is the initial position of the lower end of the sample.

$\alpha$ is the characteristic constant of the field distribution

$k_I$ is the characteristic constant of the electromagnet used.

$\beta = \frac{\mu_0 \chi}{2G}$, G is the composite's shear modulus

The model is based on the assumption that the stable configuration of Magpol samples is established when the tensile stress σ is balanced with the magnetic force $f_M$ along the sample axis. Equation 2-4 was derived from Equation 2-2 with the assumption that the magnetic field distribution along the sample axis can be expressed as:

$$H(z) = H_{\max}.e^{-\alpha|z|} \qquad \text{(Equation 2-5)}$$

where $H_{max}$ is the magnetic field strength at the electromagnet pole center.

This model can be used to explain the discontinuous elongation of Magpol, as Equation 2-4 can have multiple solutions for λ, which represent meta-stable states of Magpol during elongation (Figure 2-17). From Equation 2-4, it could be seen that sample length ($h_0$), initial sample position ($z_0$), and the distribution of magnetic field (α) play very crucial roles in the deformation behavior of Magpol.

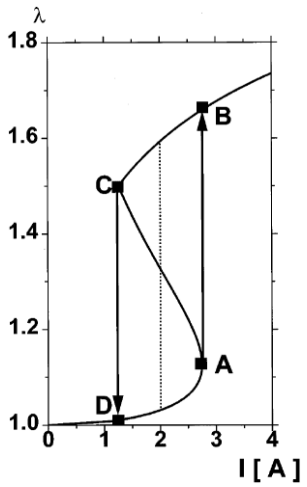


Figure 2-17: The elongation strain v/s current as predicted by Equation 2-4 [35].

Diguet utilized a demagnetization approach to explain the influence of sample aspect ratio on elongation [122]. The model is based on the assumption that the shape change is mainly driven by the reduction of demagnetizing energy. As a short sample stores higher energy than a long one, a magnetized sample elongates to reduce its demagnetizing energy. Modeling the shape change is based on the change of total energy of sample, which can be described by:

$$E_{tot} = \Delta E_d + E_{elas} \quad \text{(Equation 2-6)}$$

where $\Delta E_d$ is the reduction of demagnetizing energy of the composite as the result of strain and $E_{elas}$ is the elastic energy of the composite, which can be calculated as follows:

$$\Delta E_d = \frac{1}{2}\mu_0 M_{composite}^2 \Delta n_{sample} V_{composite} \quad \text{(Equation 2-7)}$$

$$E_{elas} = \frac{1}{2} E_{composite} \varepsilon^2 V_{composite} \quad \text{(Equation 2-8)}$$

$M_{composite}$, $V_{composite}$ and $\Delta n_{sample}$ are the magnetization, volume and demagnetization factor of the Magpol sample, respectively. $E_{composite}$ is the Young's modulus of the sample and $\varepsilon$ is the strain.

Figure 2-18 shows the change of total energy with strain for different aspect ratios. The minimum of each curve determines the stable strain for each aspect ratio. A larger aspect ratio leads to higher strains. However, this model failed to explain the discontinuous behavior of Magpol's actuation.

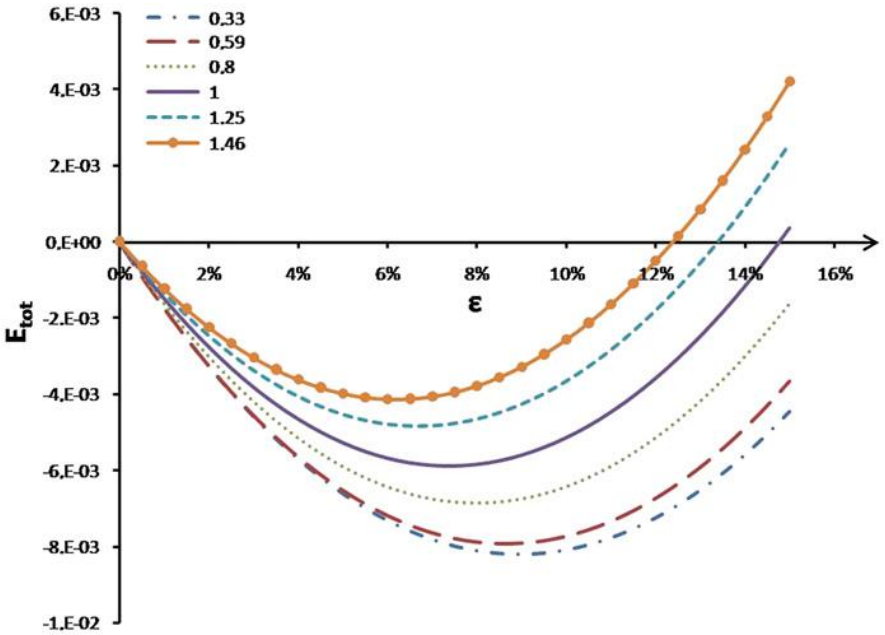


Figure 2-18: Total energy as a function of strain for samples of different aspect ratios [122].

Szabo proposed that the deformation behavior of Magpol can be modeled by studying its change in Helmholtz free energy (denoted *A*) [42]. *A* can be expressed as the sum of the magnetic energy component (denoted $A_M$) which favors deformation and the elastic energy component (denoted $A_E$)

which resists deformation. The stable deformation of Magpol is the balance of these two energy terms, i.e., when *A* is at its minimum value.

$$A = A_M + A_E \quad \text{(Equation 2-9)}$$

$$A_M = \frac{1}{2}\int_{A_M} M.H.dV = -\frac{\chi a_o}{2\mu_o \lambda_z}\int_{z_o - L_0}^{z_o} B^2(z)\,dz \quad \text{(Equation 2-10)}$$

$$A_E = \frac{1}{2}GV(\lambda_z^2 + \frac{2}{\lambda_z} - 3) \quad \text{(Equation 2-11)}$$

where $\chi$ is the magnetic susceptibility, $a_o$ is the initial cross-sectional area of the samples, $\mu_o$ is the permeability of free space, $z_o$ is the distance from the center of the pole pieces to the upper sample end, and $L_o$ is the initial specimen length. Poisson's ratio of rubber-like materials is approximately 0.5 [123]; therefore, constant volume condition was assumed. *G* is the shear modulus of the polymer matrix, *V* is the specimen volume, and $\lambda_z$ is the strain ratio along the z direction, which can be expressed as:

$$\lambda_z = \frac{L}{L_0} = \frac{\varepsilon}{100} + 1 \quad \text{(Equation 2-12)}$$

The magnetic field along z direction, B(z), can be expressed as [42]:

$$B(z) = B_{\max} f(z) \quad \text{(Equation 2-13)}$$

with $f(z) = 1 - kz^2$ if $|z| < \delta$, or $f(z) = (1 - k\delta^2)\exp\left[-\gamma(|z| - \delta)\right]$ if $|z| \geq \delta$

where $B_{max}$ is the magnetic field at the center of the electromagnet poles, $\delta$ is the electromagnet pole radius, $k = \gamma / (2\delta + \gamma\delta^2)$ is the decay constant of the electromagnetic field, and $\gamma$ is a characteristic constant of each electromagnet.

The schematic of the two energy terms and the total Helmholtz energy is presented in Figure 2-19 below.

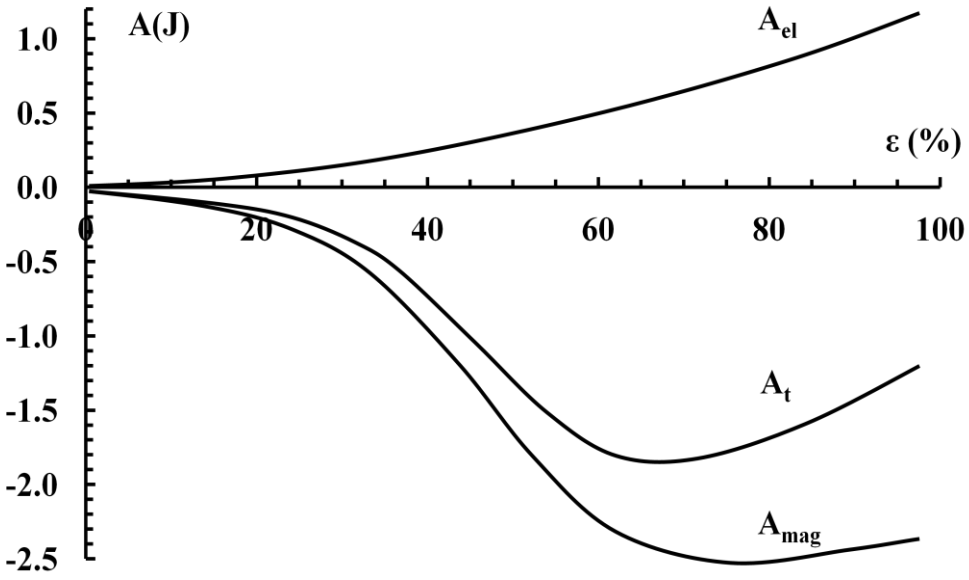


Figure 2-19: Energy v/s strain of Magpol [42]

Snyder *et al* further examined the energetics of Magpol during deformation to understand its deformation behavior with the following assumed parameter values: shear modulus $G$ of 60 kPa, dipole radius $\delta$ of 1.5cm, constant $\gamma$ of 40 $cm^{-1}$, volumetric concentration $\Phi_m$ of iron filler particles of 2%, and magnetic susceptibility $\chi$ of 21.2 $\Phi_m$ [42].

Magpol's strain at a given magnetic field is established when $A$ is at minimum. Therefore, the strain - field relationship can be established using the above model by increasing the magnetic field value $B_{max}$, followed by studying the strain - energy relationship for each value of $B_{max}$. The strain value at which $A$ is at minimum was paired with the corresponding $B_{max}$ value to yield the strain - field profile (Figure 2-20). The strain - field profile is similar to the experimental observation described in Figure 2-13 and also consists of 5 stages: a small and continuous increase in strain followed by an abrupt, discontinuous transition and a small continuous strain as the field is increased, and an abrupt, hysteretic relaxation as the field is decreased back to zero.

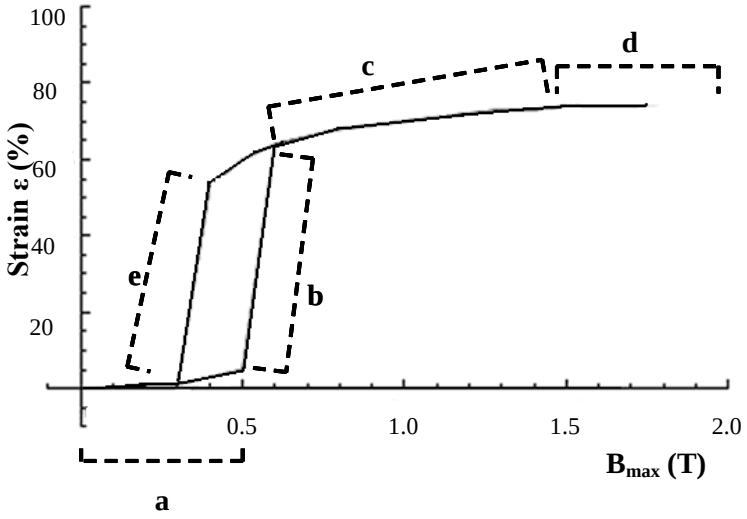


Figure 2-20: Modeled elongation strain as a function of magnetic field which consists of a) small and continuous strain, b) discontinuous transition, c) post-threshold strain, d) saturation and e) discontinuous relaxation ($L_0$ = 10cm, $z_0$ = 1.5 $L_0$ and aspect ratio = 3) [124].

Figure 2-21 shows the Helmholtz free energy as a function of strain at different magnetic field values for the samples with strain - field profile described in Figure 2-20. In the small magnetic field region, there is only one energy minimum. In the range from 0.36 T to 0.57 T, there exist two separate energy minima which represent the stable condition (global minimum) and metastable condition (local minimum) (further illustrated in Figure 2-22).

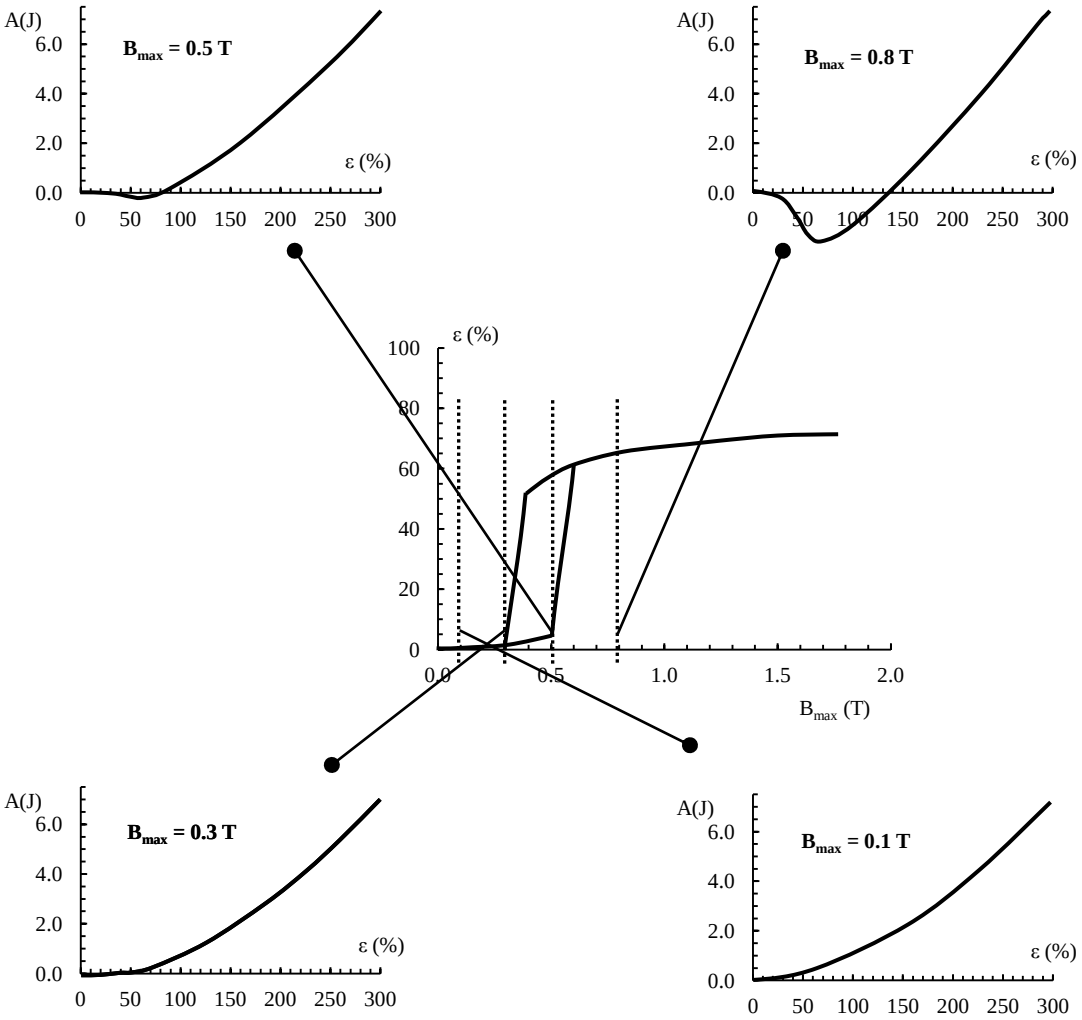


Figure 2-21: Strain - field profile and the corresponding energy profiles for Magpol samples of $L_0$ = 10 cm, aspect ratio = 3 and $z_0$ = 1.5 $L_0$ at different values of $B_{max}$: 0.1T, 0.3T, 0.5T and 0.8T [124].

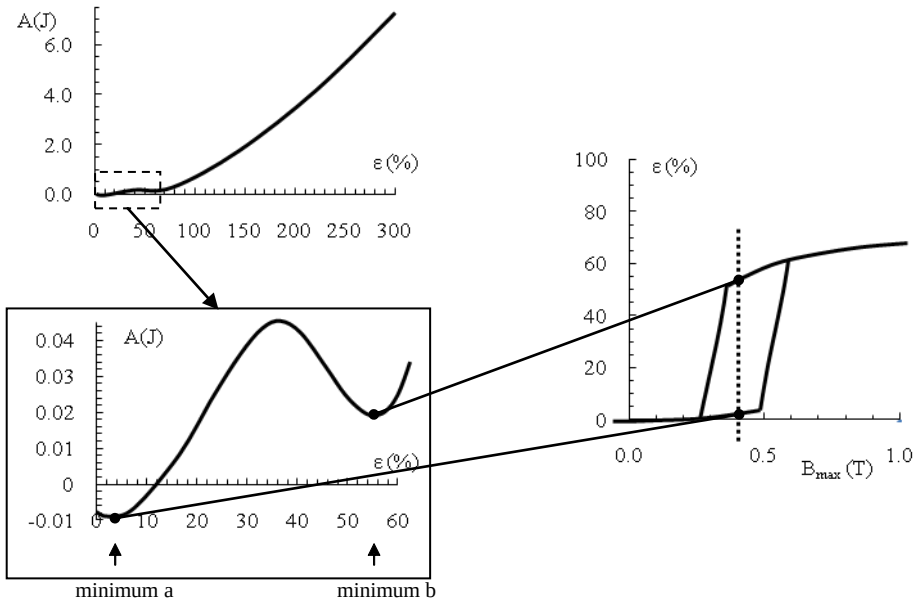


Figure 2-22: Illustration of the existence of two energy minima for Magpol samples of $L_0$ = 10 cm, aspect ratio = 3 and $z_0 = 1.5\ L_0$ when $B_{max}$ = 0.4 T [124].

The discontinuous behavior can be understood by examining the first and second derivatives of *A*. Figure 2-23 shows *A'* as a function of strain for different magnetic field values, the energy minima correspond to the strain values at which *A'* = 0. However, discontinuous deformation occurs when both A' and A" are simultaneously equal to zero. This is in agreement with catastrophe theory which predicts that buckling of structures due to magnetic forces occurs when both A' = 0 and A" = 0 [125]. When this condition is satisfied, the energy barrier between the two minima disappear, permitting the whole system to shift freely from one energy minima to the other. For the samples described by Figure 2-20, the threshold magnetic field values at which discontinuous deformation take place are 0.36 T and 0.57 T, respectively. Between these two values, the system has two minima, but only continuous deformation was observed due to the energy barrier between these energy minima.

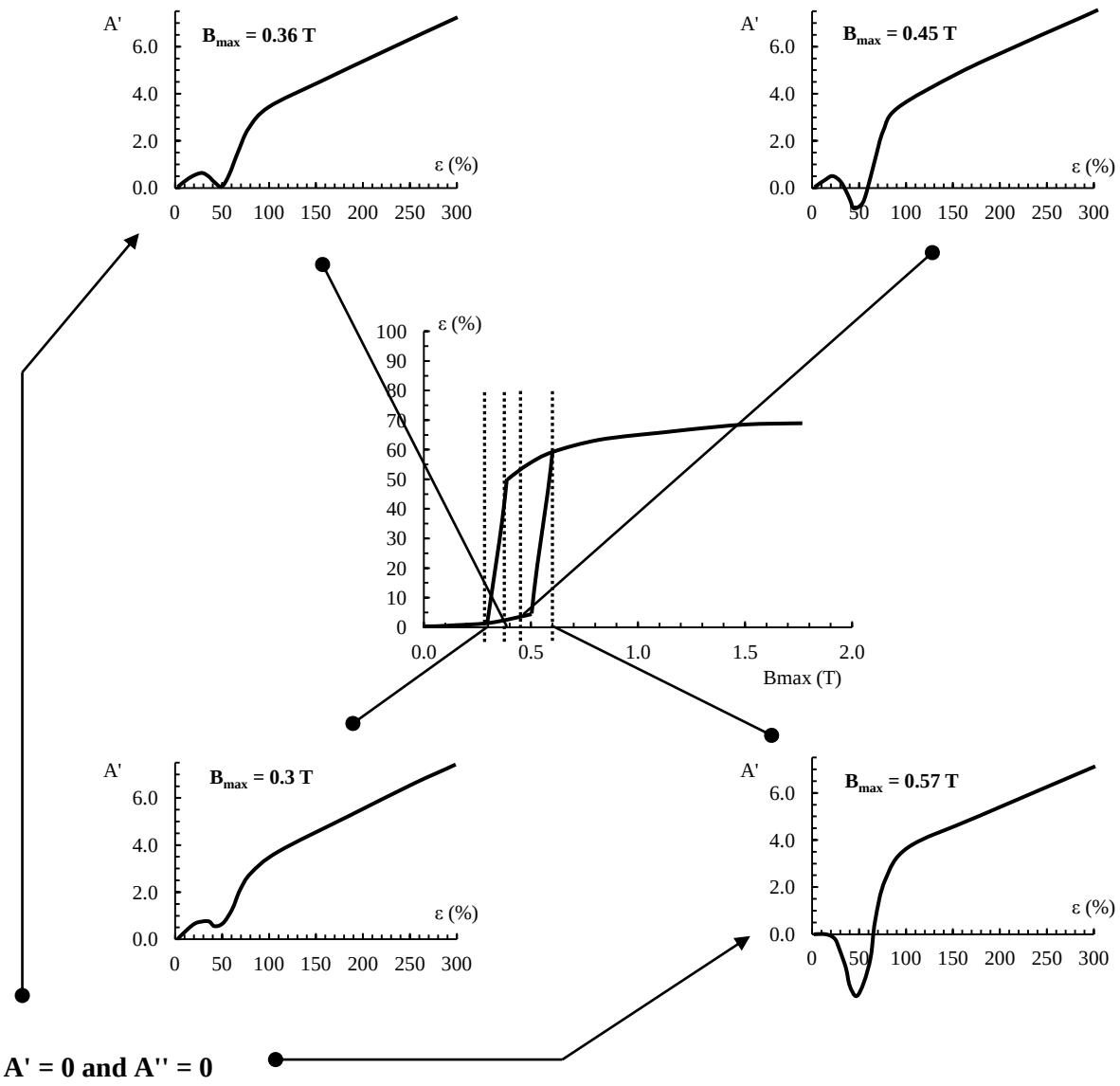


Figure 2-23: Strain - field profile and the corresponding first derivative of energy for Magpol samples of $L_0$ = 10 cm, aspect ratio = 3 and $z_0$ = 1.5 $L_o$ at different values of $B_{max}$: 0.3 T, 0.36 T, 0.45 T and 0.57T [124].

Figure 2-24 further illustrates the link between the elimination of energy barrier between the minima and discontinuous deformation. At low magnetic fields (represented by curve (a)), there is a single minimum which corresponds to a small value of strain. As the magnetic field increases, the free energy has two minima, leading to a bifurcation process (curve (b)). The elongation ratio corresponding to the second minimum is significantly higher than the equilibrium elongation ratio before bifurcation. As the magnetic field increases further, e.g., to (c), the second minimum has a lower energy. However, the system does not shift to this lower energy state due to the energy barrier, the second energy minima is a local one and the system is in a metastable state. As the magnetic field continues to increase, the energy barrier decreases in height, the energy difference between the two minima gets larger. At a certain threshold value ($B_{max}$ = 0.57 T in this example) the energy barrier vanishes, the system shifts to the new, lower energy state; the second minimum becomes the global minimum and the system is in the higher strain state. Hence, an abrupt change in strain occurs, the corresponding magnetic field is the ON threshold field. When the magnetic field is decreased, a reverse process occurs, the first minimum at lower strain becomes the global minimum again and thus the system has an abrupt relaxation. The magnetic field at this point is the OFF threshold field. The ON and OFF threshold fields are not equal due to the energy difference between the two minima. This also explains the hysteresis observed in the strain - field profile of Magpol in elongation mode.

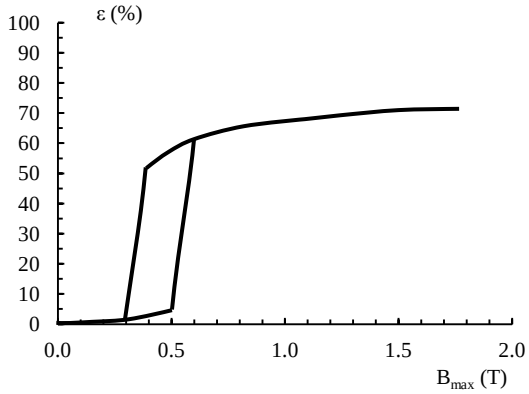


a) Strain - field profile

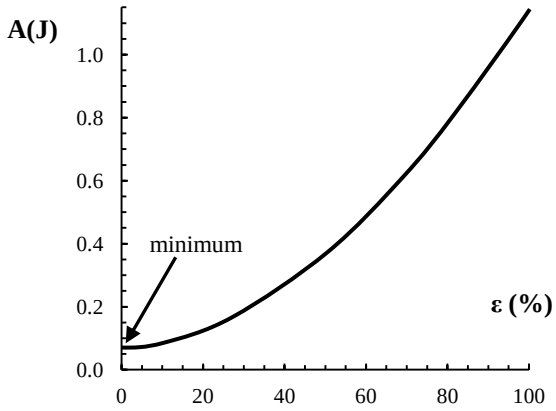


b) $B_{max}$ = 0.1 T

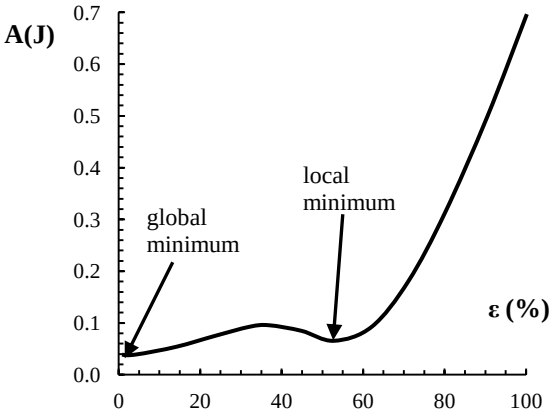


c) $B_{max}$ = 0.4 T

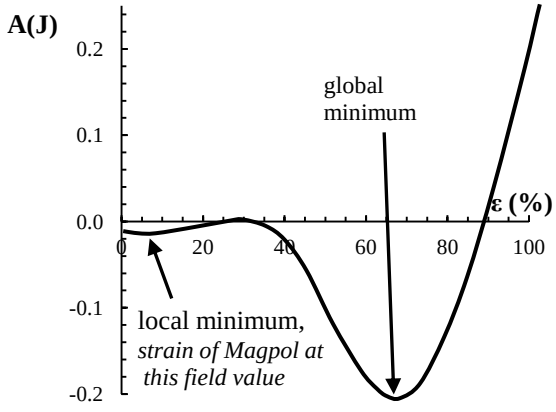


d) $B_{max}$ = 0.5 T

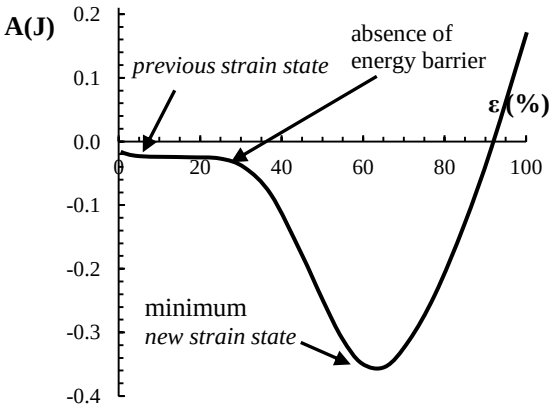


e) $B_{max}$ = 0.57 T

Figure 2-24: a) Strain - field profile, b - e) energy profiles at particular magnetic field strength of interest ($L_o$ = 10 cm, $z_o = 1.5L_o$, aspect ratio = 3) [124].

Continuous elongation can also be observed for certain geometrical configurations [68]. Continuous elongation occurs when the value of the magnetic energy component relative to the deformation energy is decreased (Figure 2-19), leading to the absence of bifurcation of the total energy, i.e., only a single energy minimum exists. This case can be achieved by decreasing the magnetic energy (e.g., by increasing sample length $L_0$ or decreasing sample distance $z_0$) or by increasing deformation energy (i.e., by decreasing sample aspect ratio). Figure 2-25 shows an example of continuous elongation of samples with $L_0$ = 1cm, aspect ratio = 1 and $z_o$ = 1.5 $L_0$.

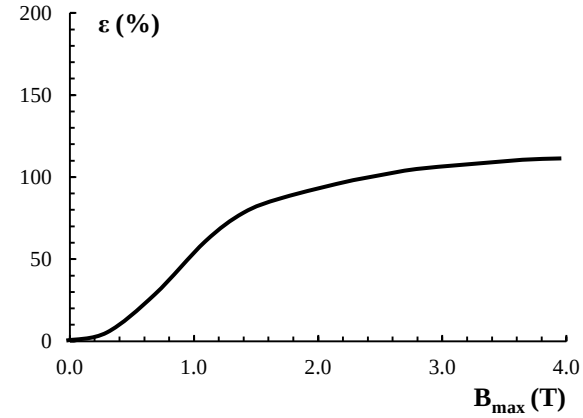


a)

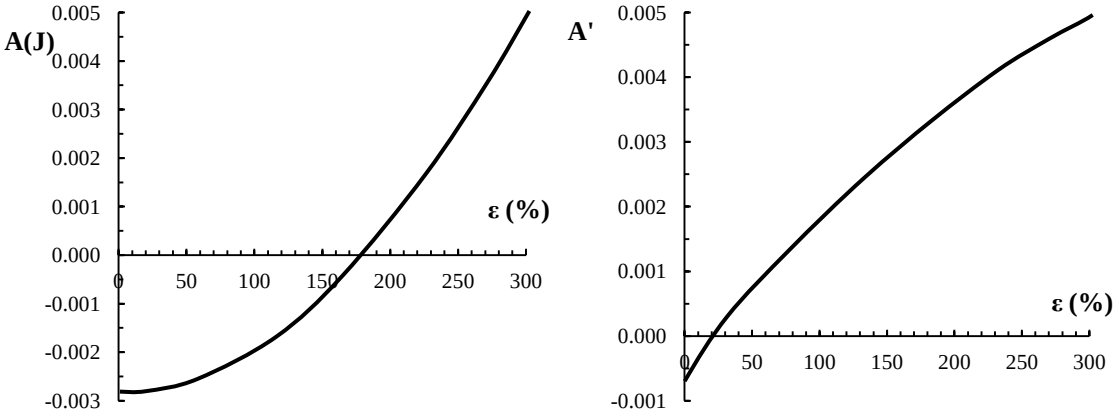


b) $B_{max}$ = 0.5 T

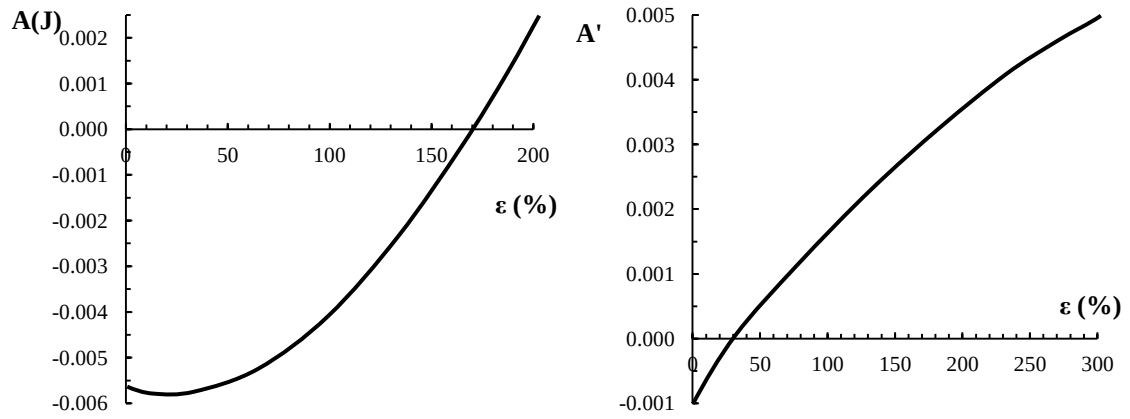


c) $B_{max}$ = 0.7 T

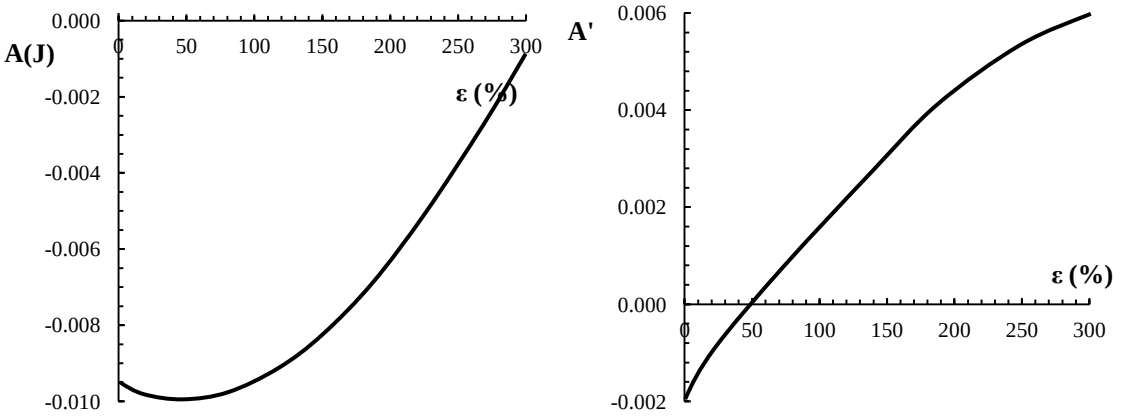


d) $B_{max}$ = 0.9 T

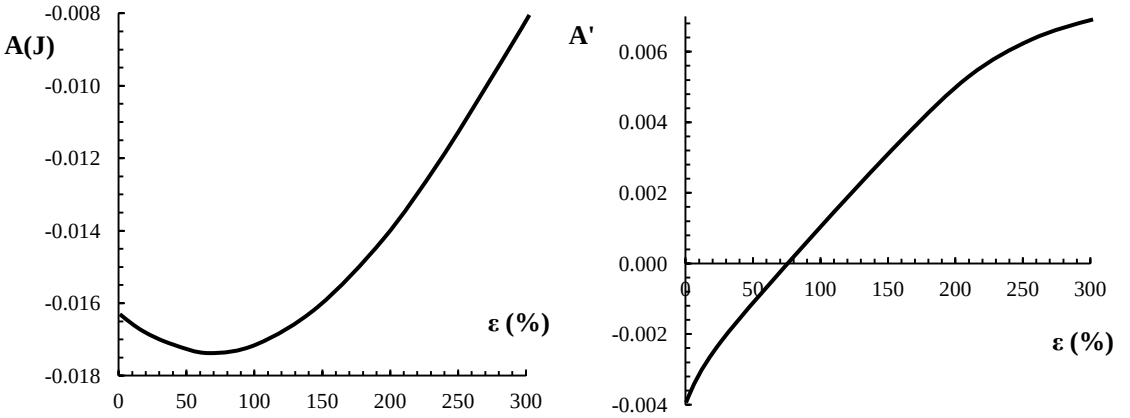


e) $B_{max}$ = 1.2 T

Figure 2-25: Illustration of the gradual, continuous strain mechanism of Magpol: a) Strain profile, b)-e) energy, and first derivative of energy for various magnetic field strengths ($L_0$=1cm, aspect ratio=1, $z_o$=1.5$L_0$) [124].

The contraction behavior of Magpol can also be studied using the energetic model described above with the center of the magnet poles is in between the sample ends. The same strain - energy approach was used to determine the strain - field profile. The results (Figure 2-26) suggest that Magpol exhibits only continuous contraction due to the lack of bifurcation, in agreement with experimental observations (section 4.2.3).

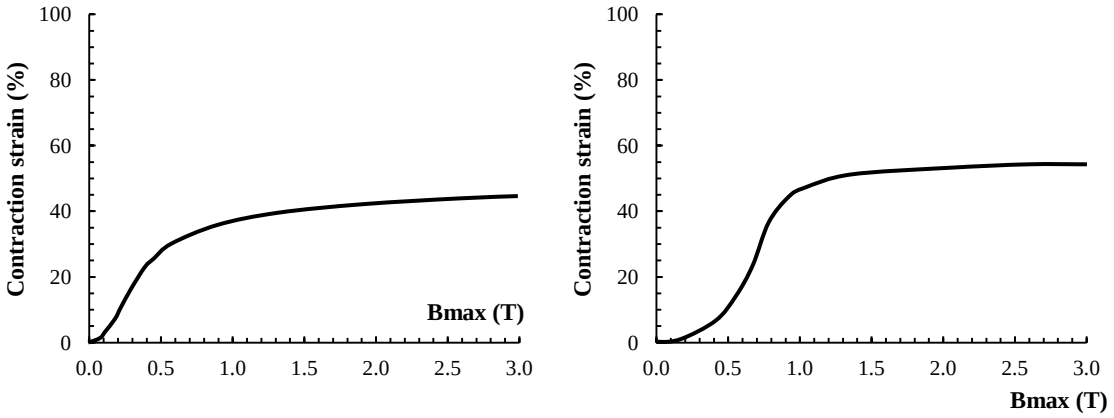


a) $L_0$ = 5 cm b) $L_0$ = 25 cm

Figure 2-26: Simulated contraction strain - field profiles of Magpol samples (aspect ratio = 7) [124].

### *2.4.4 Effects of Material and Geometric Parameters on Magpol's Actuation.*

Szabo reported that increasing the polymer's shear modulus decreases the maximum strain and increases the threshold magnetic field [42]. Increasing the filler concentration leads to a decrease in the hysteresis and threshold field and a slight increase in the maximum strain [68]. A study of the effect of sample shape on Magpol's actuation also revealed that higher aspect ratio leads to a lower strain. From the previous discussion, when subjected to an external magnetic field, the stable configuration of Magpol is established by the balance between the magnetic energy $A_M$ which favors deformation and the elastic energy $A_E$ which hinders deformation. Increasing $A_M$ leads to lower magnetic field threshold and higher strain values. $A_M$ can be increased by improving the magnetic properties or increasing the cross-sectional area of Magpol samples, or by decreasing the distance between the samples and magnetic field source. On the other hand, increasing $A_E$ leads to higher magnetic field threshold and lower strain. $A_E$ can be increased by increasing the shear modulus or increase the sample volume. This explains the finding reported in the previous studies.

An increase in aspect ratio causes a reduction in strain because it reduces the value of magnetic energy relative to elastic energy. For example, assuming that the sample volume and thus the elastic energy remain unchanged, a higher aspect ratio leads to a smaller cross-sectional area and, therefore, to a smaller magnetic energy.

The key differences in the dependence of $A_M$ and $A_E$ on geometric parameters can be exploited to tune the deformation behavior of Magpol, and actuators can be designed using this energy based approach [126]. Table 2-4 presents the influence of the key geometric parameters, i.e., sample length, aspect ratio and distance to the magnetic field source, on various actuator characteristics of Magpol.

Table 2-4: Characteristics of Magpol as a function of various geometrical parameters [126].

| **Effect on Actuator Characteristics** | **Increasing Magnitude of** | | |
|---|---|---|---|
| | **Aspect Ratio** | **Length** | **Distance from Source** |
| Pre-threshold strain | peak | -- | 0 |
| Post-threshold strain | 0 | 0 | ++ |
| Maximum (saturated) strain $\varepsilon_{max}$ | + | pk | ++ |
| ON threshold field | -- | ++ | ++ |
| Magnetic field at saturated strain | -- | ++ | ++ |
| Strain rate at threshold | ++ | pk | ++ |
| Hysteresis | pk | ++ | ++ |

| **Symbol** | **Meaning** |
|---|---|
| 0 | No influence |
| + | Negligible increase |
| ++ | Significant increase |
| -- | Significant decrease |
| pk | Peak-like response (initial increase followed by decrease) |

### *2.4.5 Dynamic Actuation Properties of Magnet - Polymer Composites*

As mentioned earlier in section 2.3.1.4, biological muscles rarely operate under static conditions, but typically in cyclic operations. Therefore, static actuation properties are insufficient to reflect the actual performance of Magpol.

Several technical applications of Magpol depend on how quickly it can respond to a modulated magnetic field [127], therefore it is useful to investigate the maximum frequency at which Magpol can operate. In addition, a study has shown that maximum muscle power is generated at a unique frequency [128].

Zrinyi investigated the dynamic behavior of ferrogels driven by a modulated magnetic field in the frequency range between 0.01 and 100 Hz. Figure 2-27 shows the frequency dependence of response of ferrogels to the modulated magnetic field. It can be seen from the top plot that the amplitude of the response increased with increasing frequency up to a certain value. However, further increase in driving frequency led to a drastic decrease of oscillation amplitude. Furthermore, there was also a significant phase shift in ferrogels' response. Based on these observations, it was concluded that the ferrogel was able to operate at a maximum operating frequency of 40 Hz, depending on the structure and size of the magnet - polymer composite [127].

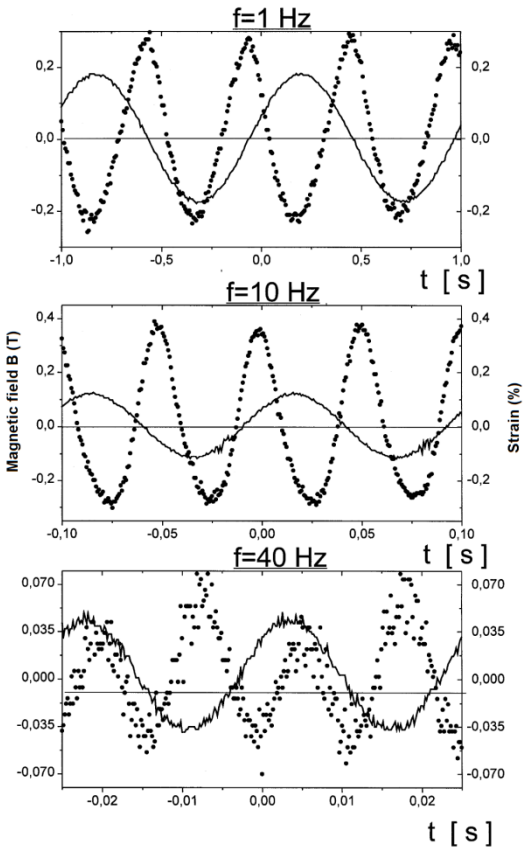


Figure 2-27: Response of ferrogels to a modulated magnetic field. The solid line represents sinewave of the stimulus, the dotted line represents the response of the ferrogel [127].

A recent study reported that ferrogels responded to a driving sinusoidal magnetic field of up to 40 Hz and the limit is due to the visco-elastic nature of the composite[129]. However, the strain showed a significant shift with time, the strain values achieved were significantly lower than those reported by Zrinyi, probably due to the higher plasticity of the polymer gel used .

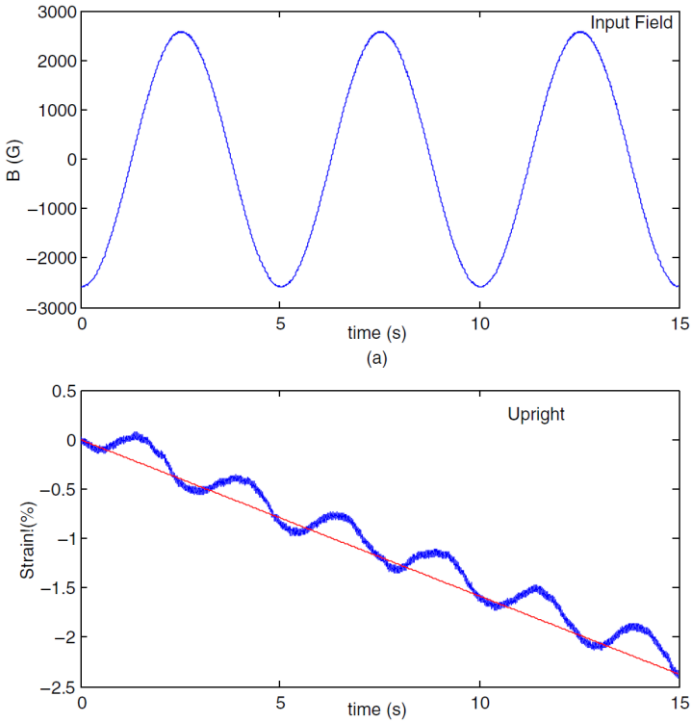


Figure 2-28: Shift in dynamic strain profile with time due to the visco-elastic characteristics of ferrogels [129].

## 2.5 Magnetic Force

### *2.5.1 Magnetic Field Energy*

The magnetic energy density for a constant permeability material is expressed as [120]:

$$w_{mag} = \frac{B^2}{2\mu} = \frac{1}{2}BH \qquad \text{(Equation 2-14)}$$

For materials with a nonlinear B - H curve, the energy density can be expressed as:

$$w_{mag} = \int H \cdot dB \qquad \text{(Equation 2-15)}$$

This energy density is the area to the left of the B - H curve of Figure 2-29. The area under the B-H curve is called the co-energy density $w_{co}$. The sum of co-energy density and energy density is constant and equals to HB [120]:

$$w_{mag} + w_{co} = HB \qquad \text{(Equation 2-16)}$$

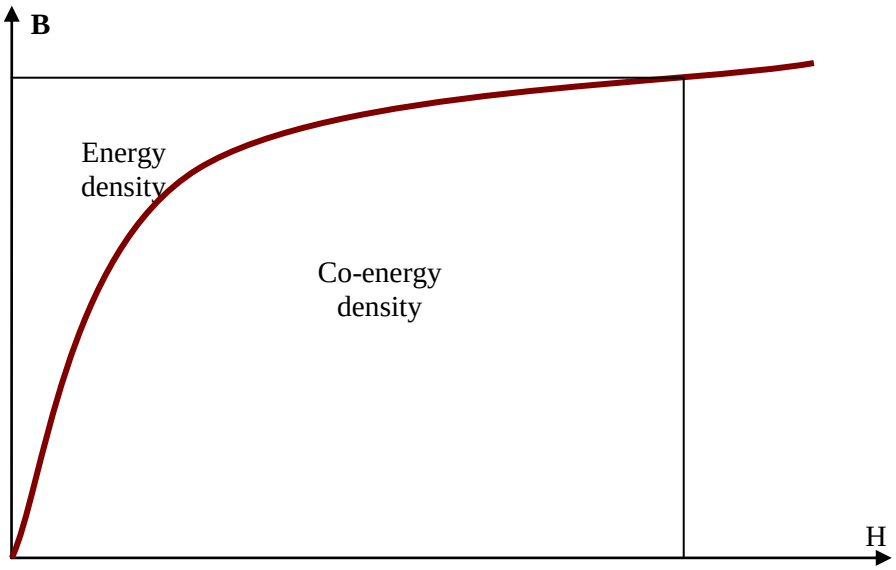


Figure 2-29: Energy density and co-energy density for a material with nonlinear B - H curve [120].

For constant permeability materials, energy density and co-energy density are equal and have the value of $\frac{1}{2}BH$ .

Since the energy density $w_{mag}$ is the magnetic energy per unit volume in a magnetic field, the total energy stored is the integral of $w_{mag}$ over a volume [120]:

$$W_{mag} = \int w_{mag} dV \qquad \text{(Equation 2-17)}$$

For constant permeability materials, the stored magnetic energy is given as:

$$W_{mag} = \int \frac{B^2}{2\mu} dV \qquad \text{(Equation 2-18)}$$

### *2.5.2 Magnetic Force*

The magnetic force is related to the magnetic field H, the force between two magnetic poles is proportional to the product of their pole strength, p and inversely proportional to the square of the distance between them, i.e.,

$$F_{magnetic} \sim \frac{p_1 \cdot p_2}{r^2} \qquad \text{(Equation 2-19)}$$

To understand what causes the force, we can think of the first pole generating a magnetic field H, which in turn exerts a force on the second pole. Therefore:

$$F_{magnetic} = \left(\frac{p_1}{r^2}\right) p^2 \qquad \text{(Equation 2-20)}$$

One of the methods for determining magnetic force is the virtual work method which states that the force in a specific direction equals the derivative of stored energy with respect to that direction:

$$F_s = \frac{\partial W}{\partial s} \qquad \text{(Equation 2-21)}$$

To calculate the magnetic force acting on a constant permeability material, consider the simple magnetic system shown in Figure 2-30.

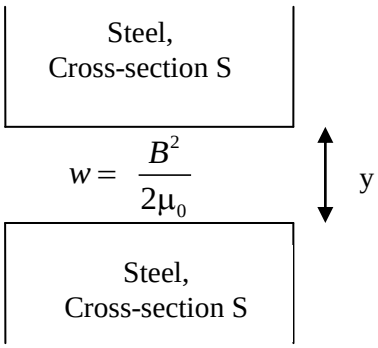


Figure 2-30: A magnetic system with steel poles and energy stored in the air gap [120].

The stored magnetic energy in the air gap of volume V, as discussed in the previous section is

$$W_{mag} = \int \frac{B^2}{2\mu_0} dv = \frac{B^2}{2\mu_0}.V \qquad \text{(Equation 2-22)}$$

And thus the magnetic force acting along the vertical axis is [120]:

$$F_{magnetic} = F_y = \frac{\partial W_{mag}}{\partial y} = \frac{\partial\left(\frac{B^2}{2\mu_0}.V\right)}{\partial y} = \frac{B^2}{2\mu_0}\frac{\partial V}{\partial y} = \frac{B^2}{2\mu_0}.S \qquad \text{(Equation 2-23)}$$

If the steel poles have finite permeability $\mu_s$, there is an additional force term due to the volume change of the steel poles. The force expression above becomes:

$$F_{magnetic} = S.B^2 \left( \frac{1}{\mu_0} - \frac{1}{\mu_s} \right) \qquad \text{(Equation 2-24)}$$

If the materials in the system of interest have a nonlinear B - H relationship, the magnetic virtual work can be derived from the B - H curves at different spatial positions. For example, if the magnetic properties of the steel component in the above actuator configuration is non-linear, the virtual work done by the system equals the area between curve 1 and 2 in the B - H diagram of the steel (Figure 2-31). Curve 1 corresponds to the high-reluctance position with a large air gap while curve 2 represents the low-reluctance position with a shorter air gap. If the input is a constant current, the area equals to the difference in co-energies. Therefore the magnetic force for nonlinear B - H materials is [120]:

$$F_{magnetic} = \left. \frac{\partial W_{co}}{\partial s} \right|_{I=const} \qquad \text{(Equation 2-25)}$$

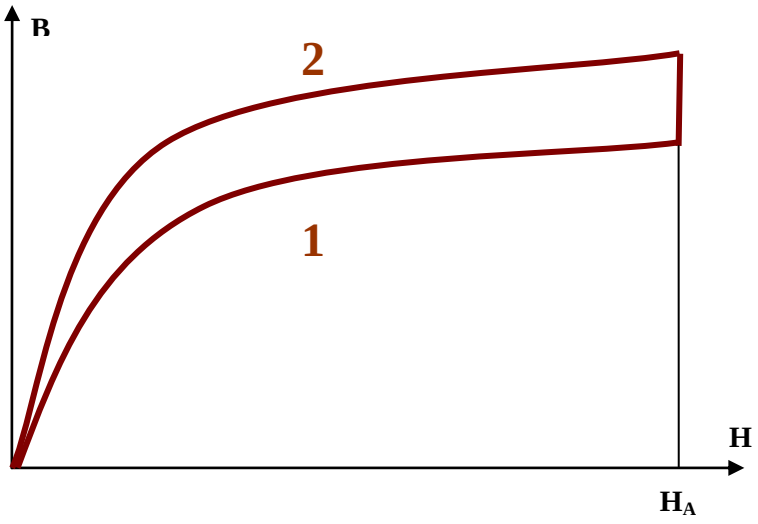


Figure 2-31: B - H curves of a typical steel pole at large air gap (1) and reduced air gap (2) [120].

### *2.5.3 Magnetic Force Acting on Particles*

For a small magnetic particle with a magnetic moment M, the force acting on it due to a magnetic field gradient $\nabla B$ is [130]:

$$F_m = V_{particle}.M(\nabla B) \quad \text{(Equation 2-26)}$$

When a small magnetic particle with volume $V_P$ is embedded in a matrix, its magnetic energy density in a linear isotropic medium is expressed as $\frac{1}{2}BH$. The magnetic energy of the fluid enclosed in this volume is

$$\frac{1}{2}HB_mV_m = \frac{1}{2}\mu_m V_m H^2 \quad \text{(Equation 2-27)}$$

where $B_m = \mu_m H$ and $\mu_m = \mu_0(1+\chi_m)$ is the permeability of the matrix. If the matrix material enclosed in this volume $V_P$ is replaced by the particle, the energy associated with the particle is now $\frac{1}{2}HB_pV_p = \frac{1}{2}\mu_f V_P H^2$ where $B_p = \mu_p H$ and $\mu_p = \mu_0(1+\chi_p)$ is the permeability of the particle. The energy gain of the system U is the difference between these two energies and for a constant permeability material, this is a good approximation. Thus $U = \frac{1}{2}(\mu_p - \mu_m)V_p H^2$. Hence, the magnetic force can be written as:

$$\overrightarrow{F_m} = \frac{1}{2}\mu_0 \chi V_p \nabla(H^2) \quad \text{(Equation 2-28)}$$

, where $\chi = \chi_p - \chi_m$ is the difference between susceptibilities of the particle and the matrix [131]. Therefore, effective ways of enhancing the magnetic force on particles include (i) increasing the susceptibility of the particle, (ii) increasing the magnetic field gradient and (iii) using a strong magnetic field. Particle size also plays an important role since the force is proportional to the particle volume [132, 133]

If the material is ferromagnetic, i.e., permeability is a function of field strength, the above formulae do not apply. Instead, the force can be written as follows:

$$F_{mag} = \frac{\partial W_{mag}}{\partial x} = \frac{\partial W_{mag}}{\partial H}\frac{\partial H}{\partial x} \quad \text{(Equation 2-29)}$$

For a specific configuration, $\frac{\partial H}{\partial x}$ does not depend on the type of material which the particle is made of. Thus the force acting on a ferromagnetic particle is proportional to $\frac{\partial W_{mag}}{\partial H}$, which equals to $\frac{dA}{dH}$ (Figure 2-32). Rewriting this ratio yields:

$$\frac{dA}{dH} = \frac{HdB}{dH} = H\mu_H \qquad \text{(Equation 2-30)}$$

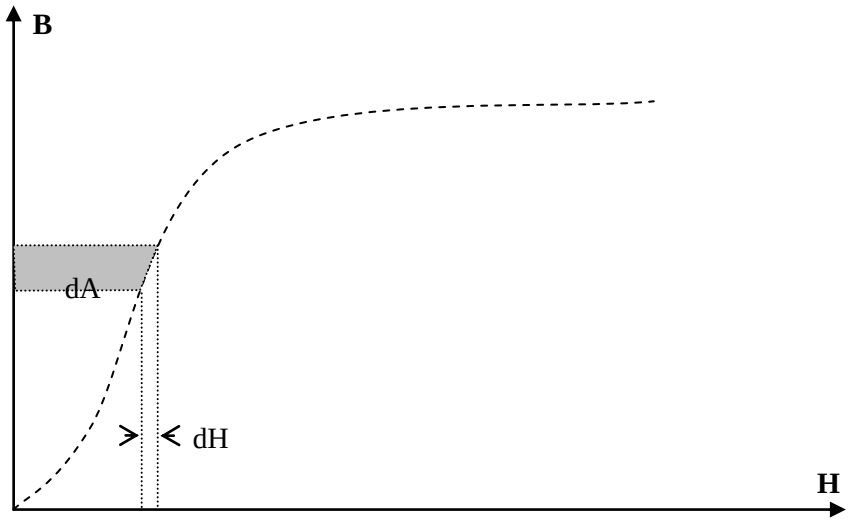


Figure 2-32: Differential magnetic energy of a nonlinear permeability particle.

It is again seen that a particle with high permeability is required for improving the magnetic response. When the filler is ferromagnetic, the magnetization M can saturate at a relatively low magnetic field strength. In this case, the magnetic force acting on a ferromagnetic particle is:

$$F_m = V.M_S(\nabla B) \qquad \text{(Equation 2-31)}$$

This indicates that high $M_S$ values are required for particles subjected to strong magnetic fields [132].

In conclusion, high values of permeability and saturation magnetization are required to achieve a high magnetic force acting on the particles.

## 2.6 High Permeability Magnetic Materials.

As discussed in the previous section, increasing the magnetic force acting on the particles requires high values of permeability and magnetization saturation. Clearly, soft magnetic materials are appropriate choices. Magnetically soft materials that can be produced in mass quantity include iron, silicon steels, low carbon irons, iron - cobalt alloys, iron - nickel alloys, ferritic iron - chromium alloys, and ferrites.

Most soft magnetic alloys consists of at least one of the following ferromagnetic elements: iron, nickel, or cobalt. Several alloying elements can also be added to control crystallographic parameters in order to achieve high permeability, low coercive force, and low hysteresis loss. Iron alloys are the most common soft magnetic materials. The effect of various alloying elements on the saturation induction of iron is shown in Figure 2-33. Additions of most alloying elements to iron lower its saturation induction ($B_s$), except for cobalt increases the saturation induction up to 2.4 T at approximately 35% Co. Copper, chromium, or molybdenum can be added to 80% Ni - 20% Fe alloys to optimize crystal structure and achieve high magnetic permeabilities [134].

Another class of magnetic materials with high permeability is amorphous alloys, or metallic glasses. Amorphous alloys are materials that are rapidly quenched from the melt, so the long range order of crystalline structure is absent and they exhibit very low intrinsic magnetic anisotropy [135]. One of the most important families of amorphous alloys is based on the composition of $T_{80}M_{20}$ where T is one or more of the transition metals (i.e., Co, Cr, Fe, Mn, Mo, Ni, Pd, etc.) and M is one or more of the metalloid elements (i.e., B, C, P or Si). However, the saturation magnetization of an amorphous transition - metalloid (T - M) alloy is generally smaller than that of a crystalline alloy of the transition metal. The low anisotropy leads to a very low intrinsic coercive force ($H_c$) and very high permeability. This set of magnetic properties has made metallic glasses useful for applications requiring soft magnetic materials.

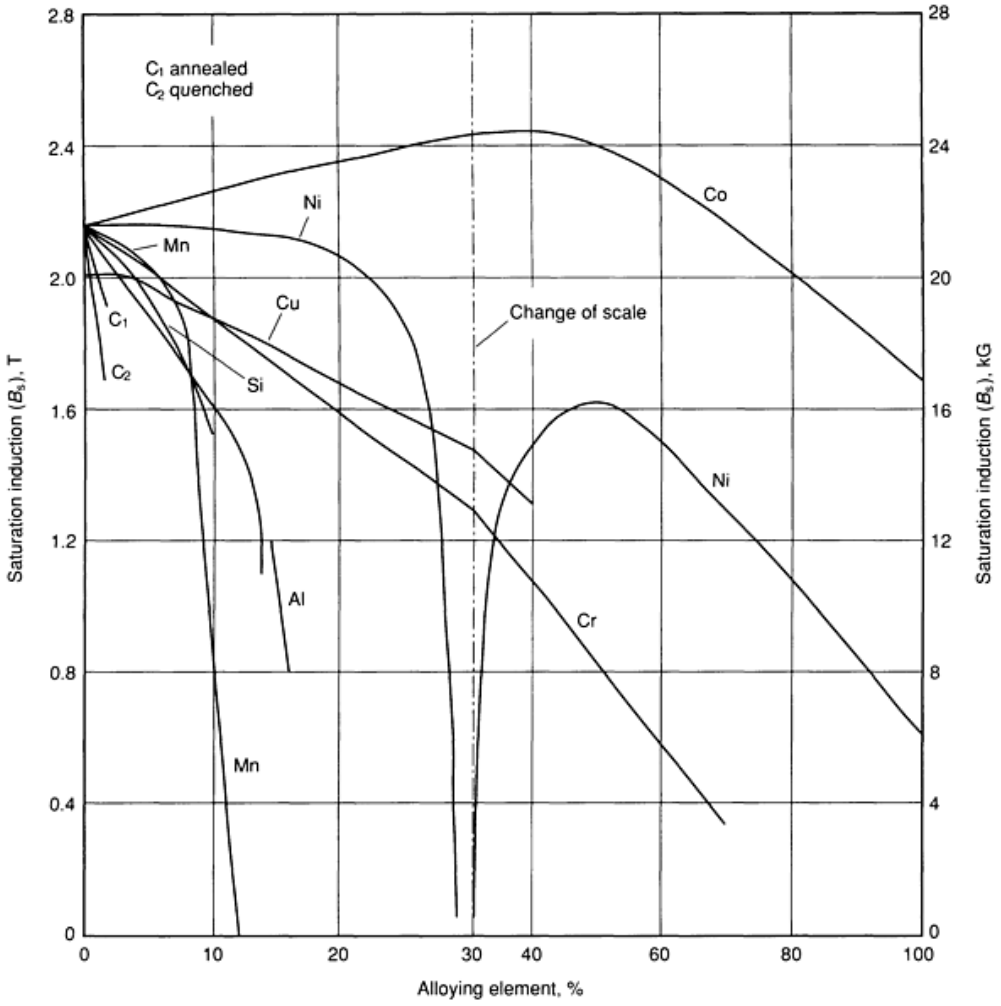


Figure 2-33: Effect of alloying elements on room-temperature saturation induction of iron [136].

Table 2-5 below summarizes the important and commercially available high permeability soft magnetic materials:

Table 2-5: Magnetic properties of high permeability metals and alloys [134, 137-140].

| **MATERIAL** | **COMPOSITION (wt%)** | **INITIAL $\mu_0$** | **MAX. $\mu_{max}$** | **$H_C$ ($Am^{-1}$)** | **$B_S$ (T)** | **REF.** |
|---|---|---|---|---|---|---|
| **Pure elements** | | | | | | |
| Cobalt | Pure Cobalt | 70 | 250 | - | 1.76 | [134, 137, 138] |
| Iron | Commercial 99 Fe | 200 | 6000 | 70 | 2.16 | [134, 137] |
| Iron | Pure 99.9 Fe | 25 000 | 350 000 | 0.8 | 2.16 | [134, 137] |
| Nickel | Pure Nickel | 110 | 600 | - | 0.62 | [134, 138, 139] |
| **Low carbon steel** | | | | | | |
| Mild steel | Fe - 0.1 % C - 0.1 % Si | 800 | 1 100 | 200 | - | [134, 137] |

| | | | | | | |
|---|---|---|---|---|---|---|
| | - 0.4 % Mn | | | | | |
| **Silicon steels** | | | | | | |
| Silicon - iron | 96 Fe - 4 Si | 500 | 7 000 | 40 | 1.95 | [134, 137] |
| Silicon - iron (110)[001] | 97 Fe - 3 Si | 9 000 | 40 000 | 12 | 2.01 | [134, 137] |
| Silicon - iron {100} <100> | 97 Fe -3 Si | - | 100 000 | 6 | 2.01 | [134, 137] |
| **Iron - Aluminum alloys** | | | | | | |
| Alperm or Alfenol | 84 Fe - 17 al | 3 000 | 55 000 | 3.2 | 0.80 | [134, 137] |
| Alfer | 87 Fe - 13 Al | 700 | 3 700 | 53 | 1.20 | [134, 137] |
| Aluminum - iron | 96.5 Fe - 3.5 Al | 500 | 19 000 | 24 | 1.90 | [134, 137] |
| Sendust | 85 Fe - 10 Al - 5 Al | 36 000 | 120 000 | 1.6 | 0.89 | [134, 137] |
| **Nikel - Iron alloys** | | | | | | |
| Hypernik | 50 Fe - 50 Ni | 4 000 | 70 000 | 4 | 1.60 | [134, 137] |
| Deltamax {100} <100> | 50 Fe - 50 Ni | 4 000 | 70 000 | 4 | 1.60 | [134, 137] |
| Isoperm {100} <100> | 50 Fe - 50 Ni | 90 | 100 | 480 | 1.60 | [134, 137] |
| 78 Permalloy | 78 Ni - 22 Fe | 4 000 | 100 000 | 4 | 1.05 | [134, 137] |
| Supermalloy | 79 Ni - 16 Fe - 5 Mo | 100 000 | 1000 000 | 0.15 | 0.79 | [134, 137] |
| Mumetal | 77 Ni - 16 Fe - 5 Cu - 2 Cr | 20 000 | 100 000 | 4 | 0.75 | [134, 137] |
| **Cobalt - Iron alloys** | | | | | | |
| Hyperco | 64 Fe - 35 Co - 0.3 Cr | 650 | 10 000 | 80 | 2.42 | [134, 137] |
| Permendur | 50 Fe - 50 Co | 500 | 6 000 | 160 | 2.46 | [134, 137] |
| 2V - Permendur | 49 Fe - 49 Co - 2 V | 800 | 4 000 | 160 | 2.45 | [134, 137] |
| Supermendur | 49 Fe - 49 Co - 2 V | - | 60 000 | 16 | 2.40 | [134, 137] |
| **Nickel - Iron - Cobalt alloys** | | | | | | |
| 25 Perminvar | 45 Ni -30 Fe -25 Co | 400 | 2 000 | 100 | 1.55 | [134, 137] |
| 7 Perminvar | 70 Ni - 23 Fe - 7 Co | 850 | 4 000 | 50 | 1.25 | [134, 137] |
| Perminvar (magnetically annealed) | 43 Ni - 34 Fe - 23 Co | - | 400 000 | 2.4 | 1.50 | [134, 137] |
| **Ferrite** | | | | | | |
| Iron Oxide | $Fe_3O_4$ | 1-7 | 10 | - | 0.6 | [134, 139, 140] |
| **Amorphous alloys** | | | | | | |
| $Fe_{80}B_{20}$ [b] | | - | 80 000* | 8 | 1.6 | [134, 137] |
| $Fe_{80}B_{20}$ [b] | | - | 300 000 | 3 | 1.6 | [134, 137] |
| $Fe_{40}Ni_{40}P_{14}B_6$ [c] | | - | 58 000* | - | 0.78 | [134, 137] |
| $Fe_{40}Ni_{40}P_{14}B_6$ [c] | | - | 275 000 | 5 | 0.78 | [134, 137] |
| $Fe_{78}B_{13}Si_9$ [d] | | - | 600 000 | - | 1.56 | [134, 137] |
| $Fe_{81}B_{13.5}Si_{3.5}C_2$ [e] | | - | 300 00 | 6 | 1.61 | [134, 137] |
| $Fe_{66}Co_{18}B_{15}Si_1$ [f] | | - | 400 000 | - | 1.8 | [134, 137] |
| $Fe_{40}Ni_{38}B_{18}Mo_4$ [g] | | - | 12 000* | 8 | 0.88 | [134, 137] |
| $Fe_{40}Ni_{38}B_{18}Mo_4$ [g] | | - | 800 000 | 0.6 | 0.88 | [134, 137] |
| $(Co,Fe)_{70}(MoSiB)_{30}$ [h] | | - | 600 000 | 0.4 | 0.55 | [134, 137] |
| $(Co,Mo,Fe,Mn)_{77}(Si,B)_{23}$ [i] | | - | 300 000 | 1.0 | 0.8 | [134, 137] |
| $Co_{58}Ni_{10}Fe_5(B,Si)_{27}$ | | - | 600 000 | 0.24 | 0.55 | [134, 137] |

[b] Metglas 2605; [c] Metglas 2826; [d] Metglas 2605S-2; [e] Metglas 2605SC; [f] Metglas 2605CO; [g] Metglas 2826MB; [h] Vitrovac 6025; [i] Vitrovac 6030.

## 2.7 Finite Element Method (FEM) for Computing of Magnetic Force

### *2.7.1 Finite Element Method for Electromagnetic Computation*

As discussed in section 2.5.2, magnetic force is directly related to magnetic energy, which is in turn related to magnetic flux density B. For simple magnetic systems, the reluctance method can be used to find flux density B and thus the magnetic force. However, calculation of reluctance can be very complex and does not provide high accuracy for more complicated systems. Thus it is useful to use the finite element method for the analysis of magnetic force in magnetic devices [120].

Mathematically, the finite element method is used for finding approximate solutions of partial differential and integral equations for engineering problems, such as heat transport phenomenon [141]. The principle of this method involves replacing differentials such as $\partial x$ with finite differences $\Delta x$. This can be done by dividing the device and the surrounding space into a grid which contains numerous finite elements. This process is called discretization. In a finite element model, regions with intricate geometry require fine discretization and those without intricate regions do not require detailed discretization.

The procedure of finite element modeling consists of four main steps:

1) Subdivision of geometry into finite elements: All 2D or 3D geometries must be clearly designated and subdivided into finite elements.
2) Materials: The magnetic properties of the materials used in the model must be provided. For nonlinear materials, the B - H curves are required.
3) Excitations: The excitation input(s) is/are required for modeling. The excitation(s) can be current, current density or voltage.
4) Boundary conditions: Information on symmetry and/or external magnetic flux is/are required for accurate generation of gridwork.

The above steps are called preprocessing. With the above information, the problem can be solved and users can extract the desired output. For example, Figure 2-34 shows a simple clapper solenoid actuator and its flux lines, magnetic flux density distribution and energy density generated by Ansoft Inc.'s Maxwell SV software [142]

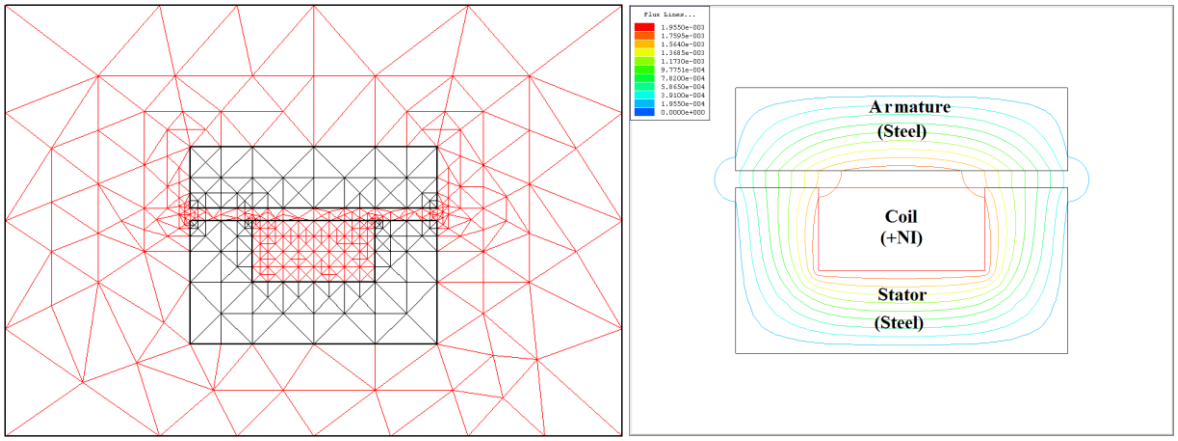


(a) (b)

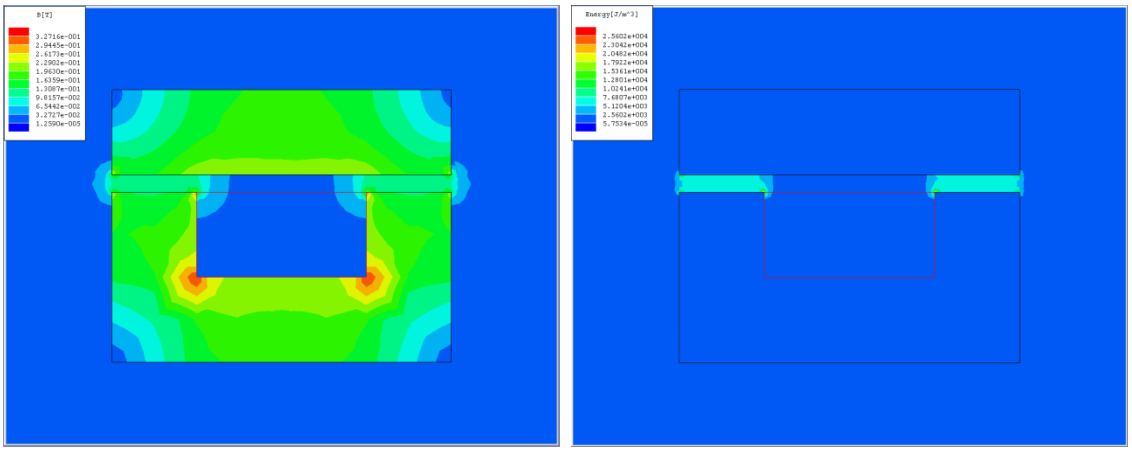

(c) (d)

Figure 2-34: Finite element modeling of a simple clapper solenoid actuator using Maxwell SV software: (a) Mesh graph, (b) Flux line plot, (c) magnetic flux density distribution plot and (d) energy density plot [120].

Most FEM software packages utilize the virtual work method in an algorithm designed to obtain the total magnetic force on any geometric part [120]. For example, consider a thin iron sheet of dimension 10 x 50 x 2 mm placed near a Nd - Fe - B permanent magnet of dimensions 10 x 10 x 20 mm (Figure 2-35 (a)). The simulation results and the computed magnetic acting on the strip are displayed in Figure 2-35 (b) - (f).

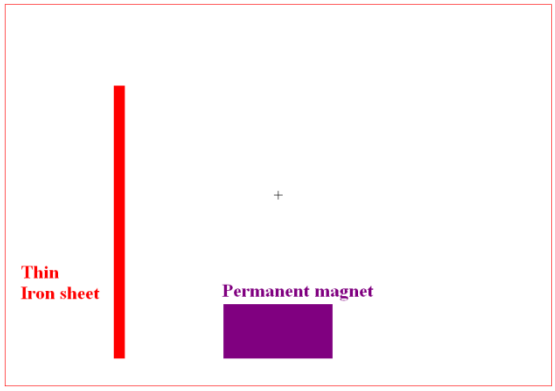


(a) Schematic model

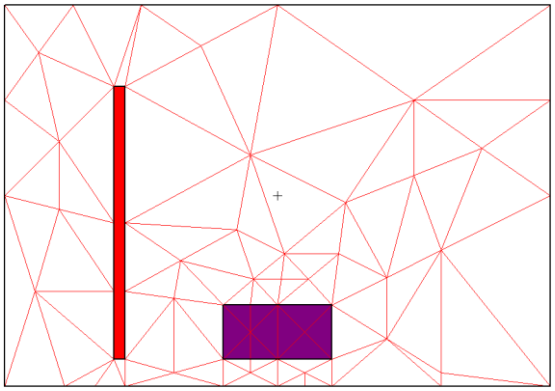

(b) Mesh diagram

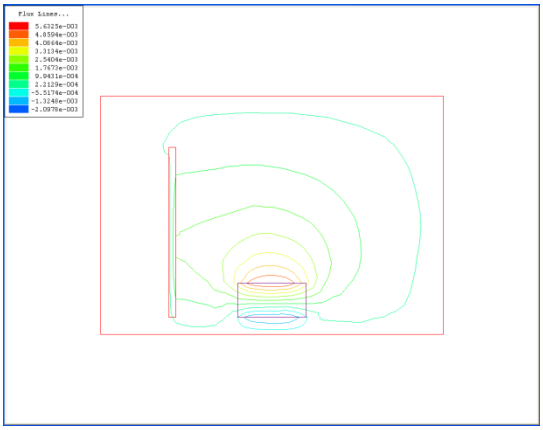

(c) Flux line plot

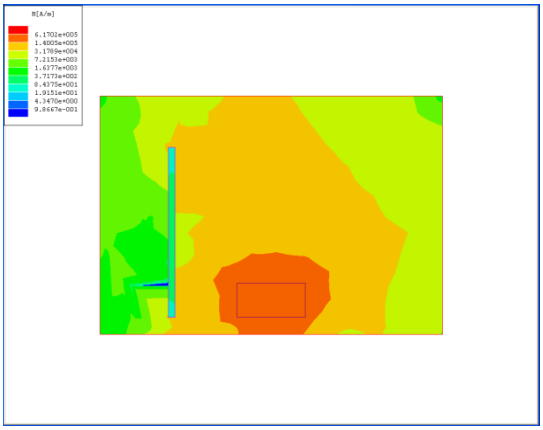

(d) H distribution plot

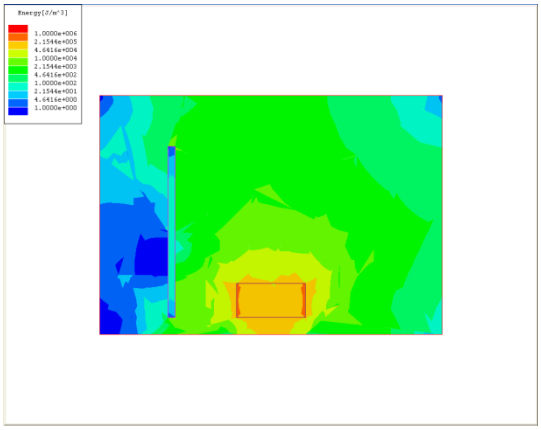

(e) Energy density distribution plot

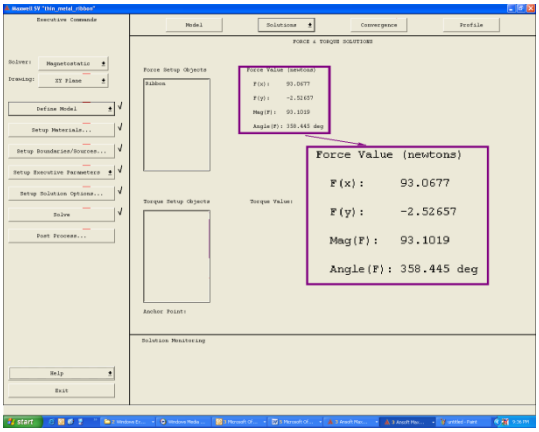


(f) Computed magnetic force

Figure 2-35: FE analysis of magnetic force acting on a thin iron strip by a permanent magnet [120].

### *2.7.2 Coupled FEM Simulation for Multiphysics Problems.*

A scientific problem is often related to multiple fields of physics. For example, it is common to study the heat generated by current, and/or then study the geometry deformation due to the heat generated in the structure. This type of problem is also referred to as coupled field problems.

The use of FEM simulations for electromechanical or magnetomechanical systems has been mostly used in MEMS designs [143-146], e.g., magnetic MEMS beams.

Uncoupling or decoupling methods have been widely used to solve coupled field problems. Uncoupling/decoupling modeling is a method in which the system of interest is studied in separated physics; the result of single modeling is then applied for subsequent studies of other physics. Tang *et al* used this method to examine polysilicon combdrive transducers [147]. Tang's model has been widely used, especially for the design of combdrive actuators and resonators.

Subsequently, an improved simulation method using sequential coupling was developed which yielded more accurate coupled - field solutions. This method is widely used in several commercial FE analysis packages, including ANSYS® [148]. Interactions between two different fields, e.g., mechanical and magnetic fields, is incorporated in the simulation process. An iterative process is required to obtain a reasonable solution. Therefore, the main issue in this method is convergence. To achieve higher accuracy, coupling can be accompanied by remeshing or extra morphing ,i.e., by the process of updating the vectors of nodal displacement during the solution. Of course, the tradeoff for higher accuracy is more computing time.

Recently, new modeling formulations have been introduced by modifying the model element. Avdeev *et al* introduced a tetrahedral transducer finite element algorithm based on the Newton - Raphson method with internal morphing capability [149]. The new formulation allowed accurate modeling of electromechanical systems [150]. Unfortunately, there is no similar element available for magneto - mechanical systems, which is of interest of this study.

The simulations conducted in this work are based on the direct and sequential coupling methods available in ANSYS software. Qualitative and quantitative comparisons of the available modeling

methods mentioned above were performed [151, 152], the results demonstrated that direct and sequential coupling methods are accurate and suitable for large deflection simulations.

## 2.8 Visco-Elastic Behavior of Polymeric Materials.

In general, a perfect elastic (Hookean) material exhibits tensile stress proportional to the tensile strain, i.e.:

$$\sigma = \text{constant}.\varepsilon \qquad \text{(Equation 2-32)}$$

where the constant is the modulus of elasticity.

On the other hand, a perfect viscous (Newtonian) fluid exhibits shear stress proportional to the rate of shear strain, i.e.,:

$$\tau = \text{constant}.\dot{\gamma} \qquad \text{(Equation 2-33)}$$

where the constant is the viscosity of the fluid.

Polymeric materials exhibit mechanical behavior in between these two ideal scenarios, and are thus termed visco-elastic materials. The stress is a function of both time and strain, i.e.,:

$$\sigma = f(\varepsilon, t) \qquad \text{(Equation 2-34)}$$

In simple form, the behavior of polymeric materials can be assumed to be only time-dependent, i.e,

$$\sigma = f(t).\gamma \qquad \text{(Equation 2-35)}$$

The time-dependent characteristics of polymeric materials are shown typically by creep when a constant stress is applied, or by stress relaxation when a constant strain is applied. The time-dependent behavior of polymeric materials is the result of three types of deformation [153]:

1. Ordinary elastic deformation due to stretching of polymer chains. This type of deformation is instantaneous and independent of temperature.
2. High elastic deformation due to uncoiling of polymer chains. This type of deformation is not instantaneous, its rate is temperature-dependent.

3. Viscous deformation due to sliding of polymer chains. This type of deformation is irreversible and is often assumed to have a constant rate with a constant applied stress.

Based on these three types of deformation, the mechanical behavior of polymeric materials can be modeled by combinations of ideal springs representing Hookean characteristics, and dashpots (i.e., mechanical damping devices utilizing viscous friction) representing Newtonian characteristics. Simple models for polymeric materials include the Maxwell model, which is a series combination of a spring and a dashpot, and the Voigt model, a parallel combination of a spring and a dashpot [154]. Fundamentally, the modulus (i.e., in stress relaxation) is best predicted by the Maxwell model, whereas the compliance (i.e., creep or strain recovery) is better approximated by Voigt model [155].

In general, the behavior of polymeric materials is so complicated that it cannot be described by the simple models mentioned above, but instead by multi-element models. A multi-element model which is particularly suitable for modulus modeling is the Maxwell - Weichert (or generalized Maxwell) model, which consists of multiple Maxwell elements coupled in parallel. Other approaches for multi-element modeling include the Voigt - Kelvin model which is a serial combination of multiple Voigt elements [155] and the four-element model which incorporates a Maxwell element and a Voigt element in series [156].

## 2.9 Conductive Metal Filled Polymer Composite

### *2.9.1 Electrical Properties of Conductive Polymer Composites*

It is well known that the electrical conductivity of polymeric materials can be modified by the addition of conducting fillers [157] [158]. The conducting fillers can be graphite, carbon black (CB), metallic particles, conducting polymers such as Polyaniline (PAN) or a combination of these materials [158]. The behavior of such composites, especially the dependence of electrical conductivity on filler type, content, size and shape, has been studied; the conduction mechanism of such materials is generally believed to be governed by the percolation phenomenon [159]. This term refers to a situation in which the filler fraction is above a critical value called percolation threshold, the fillers are then statistically in direct contact with one another, forming conducting paths throughout the sample. Figure 2-36 shows a typical variation of conductivity as a function of filler

concentration. Attention should be drawn to the logarithmic scale of conductivity to appreciate the drastic increase of the conductivity at the percolation threshold.

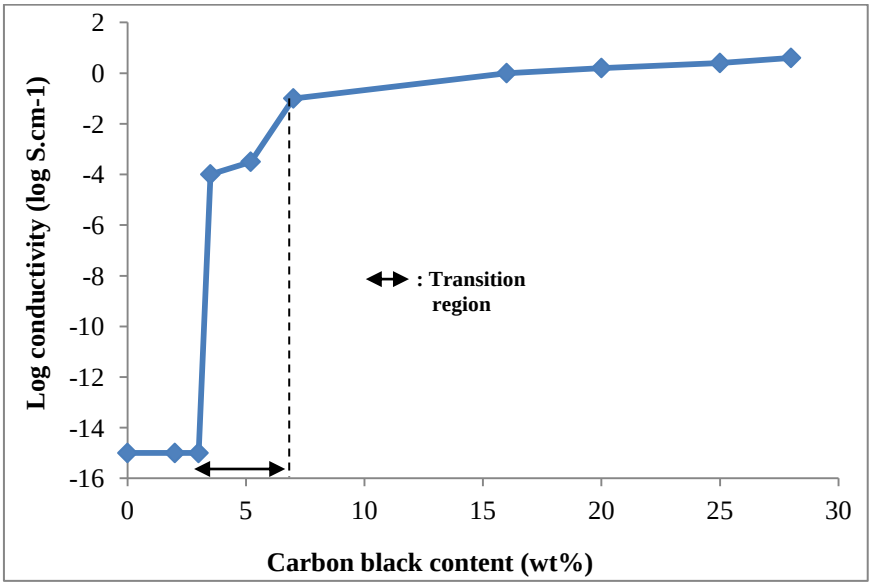


Figure 2-36: Conductivity of carbon black (CB) filled Polyethylene (PE) (adapted from [160])

The main parameter that determines the conducting behavior of filled polymers is filler volume fraction. There have been various models proposed to predict the effect of this parameter [161-170]. Other physical properties of both the filler and the polymer matrix also strongly affect the conduction behavior [171]. Firstly, different forms of the same filler (e.g. carbon black, carbon fibers, graphite…) can have different effects [172]. A typical threshold value for carbon black filler is about 5 - 10 vol%, while it can be much higher for graphite and metal fillers (about 20 - 30 vol%) [173, 174]. Past studies also suggested that for spherical fillers, a smaller particle size will lower the percolation threshold whereas eccentric fillers with larger values and range of aspect ratios will lower the percolation threshold [175-178]. The processing technique was also found to be important since it affects the distribution and degradation of particles [179].

Another significant factor that influences the conductivity of the composite is the surface characteristics of both the filler and the polymer matrix. Generally, a smaller difference between the surface energies of the fillers and polymer leads to better wetting of the filler by the polymer. As a result, both the percolation threshold and the overall resistivity of the composite reduce. Therefore a larger difference between the surface energies of the constituent components is desirable [180].

There are four major classes of models for the conductivity of the conduction - insulation composite: statistical, thermodynamic, geometrical and structure-oriented models. These models are described and reviewed in detail elsewhere [160, 179]. Experiments were performed to assess the accuracy of these methods, the results suggested that the thermodynamic model proposed by Mamunya [180] and structure-oriented models are more useful in describing the dependence of conductivity on filler content. However, the statistical approach is preferred in most cases due to its simplicity and reasonable accuracy. Ultimately, what is lacking is a universal model which can explain all the experimental results.

Also, in practice, it is difficult to obtain accurate conductivity values. Factors which introduce significant errors include the error in calculation of true volume fraction, uncertainties in conductivity measurement, estimation of absolute size and aspect ratio of the conductive fillers [160].

### *2.9.2 Conductive Polymer Composites as Deformation Sensors.*

The electrical properties of a conduction - insulation composite are strongly dependent on the distribution of the conducting fillers. Since strain induces a change in filler distribution, the conductivity of such a composite is expected to be a strong function of shape deformation, especially when the polymer matrix is highly elastic and the concentration is in the percolation transition region. This phenomenon is usually termed piezo-resistance or elasto-resistance. Therefore, conduction - insulation composites are very promising *in situ* sensors for detecting deformation [181-184] or as pressure gauges [184, 185]. Such strain sensors are particularly useful in applications incorporating flexible structures. For example, Figure 2-37 shows a schematic and the feedback response of a flexible sensor based on CB filled styrene butadiene rubber (SBR) to be used in performance testing of parachutes [186]. Previous studies have shown that the piezoresistive properties of polymer composites strongly depend on various factors. The significant factors include the characteristics of the constituents [187], their adhesion and cohesion, the processing technique [188] and also the prehistory of the composite [189]. In addition, the conductivity also depends on testing conditions: deformation rate, measurement duration, temperature, etc. , the effects of these parameters are discussed elsewhere [190, 191].

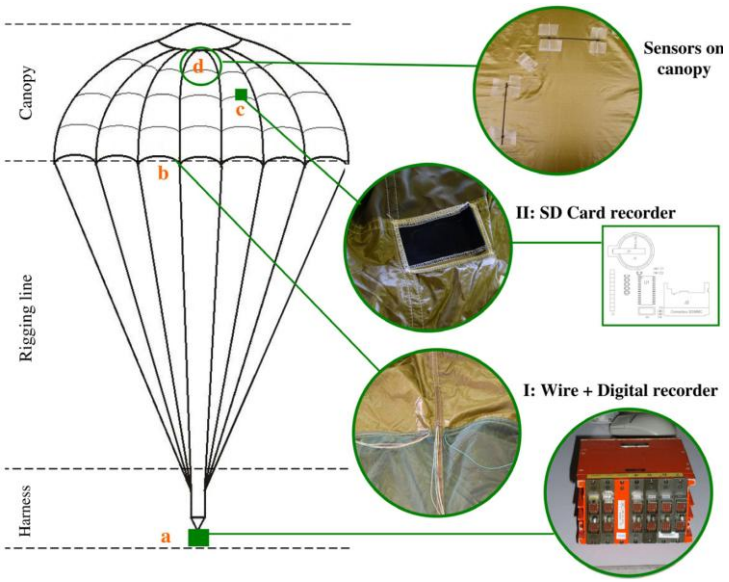


(a) Configuration of the sensor system

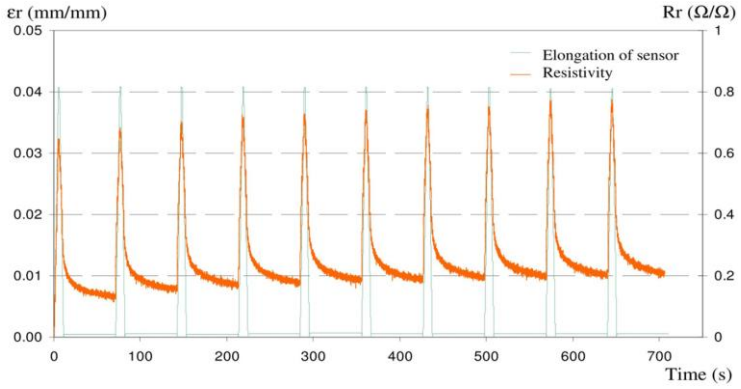


(b) Electrical response of the sensor during 10 elongation cycles

Figure 2-37: Flexible sensor system for parachute tests based on CB filled SBR [186].

For the case of magnet - polymer composites, if the magnetic particles are electrically conductive (e.g., Co, Fe, Ni or their alloys), the composites are expected to exhibit piezo-resistive effects. The volume fraction of the magnetic particles should be within the transition region, i.e., slightly above the percolation concentration. However, Zrinyi [68] suggested that the concentration of the particles should be below the percolation threshold of the polymer to maintain the highest possible elasticity of the composite. Therefore, it is important to study the effect of particle concentration for an optimal balance between actuation and sensing properties of the composite.

2.9.2.1 Resistivity/Conductivity Change of Conductive Polymer Composites in Compression

Ausanio *et al* [88, 192] studied the change of resistivity of silicone - nickel composites induced by compression. The results (Figure 2-38) showed a very sharp change of resistivity, ~ $10^9$ Ω.cm, induced by a compression strain as small as 2.5%. The reduction of resistivity was due to the formation of new conducting paths of the particles as the sample volume was decreased.

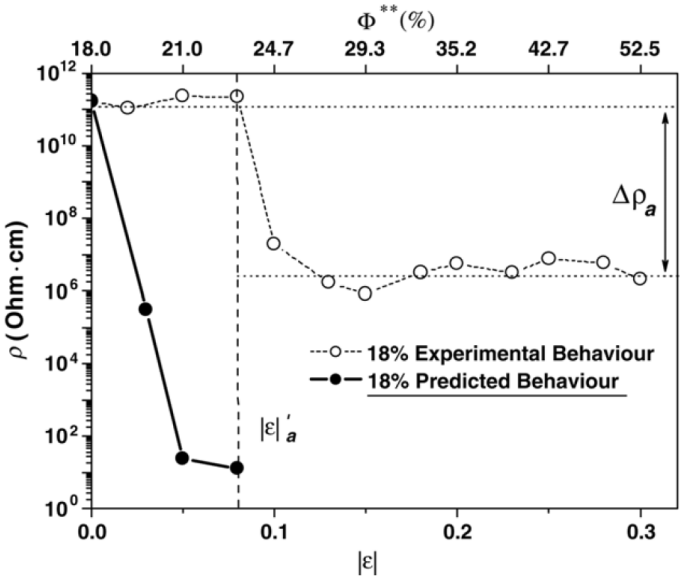


Figure 2-38: Resistivity of Ni - filled silicone as a function of strain. The upper x-axis represents the corresponding volume fraction of the Ni particles [88].

However, another study on high density polyethylene (HDPE) loaded with foliated graphite (FG) [175] showed that the change of resistivity/conductivity depends significantly on the magnitude of compressive pressure. For example, the resistivity of the samples decreased with increasing compressive pressure up to a critical value, beyond which the resistivity increased with increasing pressure (Figure 2-39). The behavior of the composite at low filler concentration can be explained by the degradation of the conducting chains. The change of resistivity/conductivity with strain is a result of two simultaneous and competing processes: the degradation of existing conducting channels and the formation of new ones [191, 193-195]. These two mechanisms are controlled by two factors: change in inter-particle distance between the particles due to shape deformation and rotation/translation of the particles in the polymer matrix as a result of reorientation of polymer chains. The contribution of these two factors to the formation/degradation of conduction paths varies

for different polymer and filler configurations[196]. For the results presented in Figure 2-39, deformation in the low pressure range decreased the distance between the graphite sheets and thus reduced the composite resistivity. In the higher pressure range, deformation effectively disrupted the existing conductive networks, thereby increasing the overall resistivity.

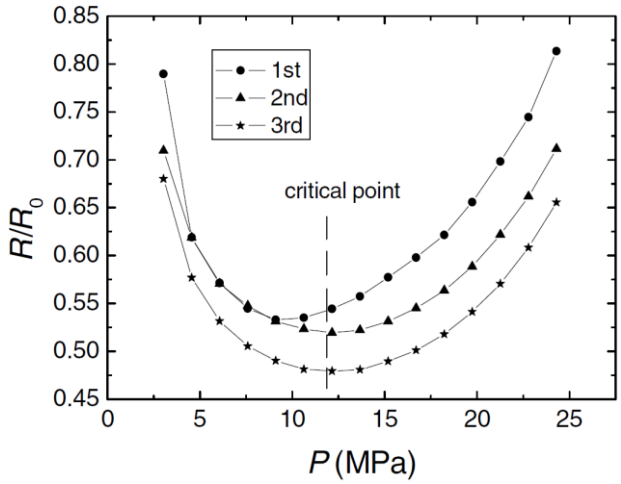


Figure 2-39: The change of resistivity of HDPE - FG nanocomposite with cyclic compressive pressure [175].

#### 2.9.2.2 Resistivity/Conductivity Change of Conductive Polymer Composites in Tension

The variation of conductivity of conduction - insulation composites as a result of tensile strain has been studied [190, 191, 193-195]. During elongation, as the modulus of the fillers is usually much higher than that of the polymer, the fillers do not break but there is a gap between the filler and the matrix, leading to a decrease in conductivity.

Aneli *et al* [190] showed that the resistivity as a function of axial strain for silicone - CB composites varies with increasing filler content. At low filler concentrations, resistivity decreased with increasing axial elongation strain, and reversed smoothly back to the orginial state upon the release of stress. A similar observation was reported for epoxy - multi walled carbon nanotubes (MWCNT) composites [187] and silicone - CB composites [197]. The reduction of resistivity can be explained by the formation of new conducting chains caused by transverse contraction, especially for polymers with high Poisson's ratio. At high filler concentrations, resistivity increased steadily with increasing axial elongation strain. Interestingly, a plateau of resistivity - strain curves was observed, which

showed a balance between the degradation and formation of conducting chains in the structure [190]. The change of resistivity with strain also depends significantly on the strain rate, due to the time-dependent relaxation processes of the polymer chains.

Zhang *et al* reported that improvements in piezo-resistive properties of conductive polymer composites can be achieved in thin forms [198]. Large changes of resistance (~ 2 orders of magnitude for 80% tensile strain), good linearity and low percolation threshold(~ 0.4 wt%) was observed for 250 μm thick films of Spandex - MWCNT composites (Figure 2-40).

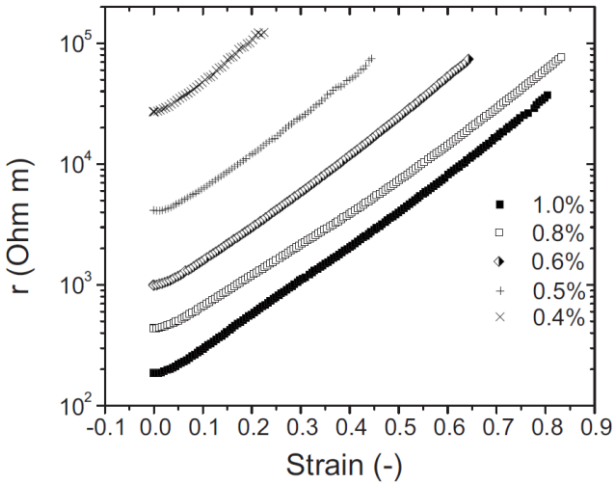


Figure 2-40: Resistance of Spandex - MWCNT composites as a function of strain for various filler concentration [198].

### 2.9.2.3 Sensing Properties of Conductive Polymer Composites in Cyclic Strains

Ausanio's study of the change of resistivity of silicone - nickel composites upon removal of decompression stresses suggested a hysteresis behavior, as shown in Figure 2-41. Removal of the compression stress introduces large change in resistivity, which is useful for detecting cyclic strains.

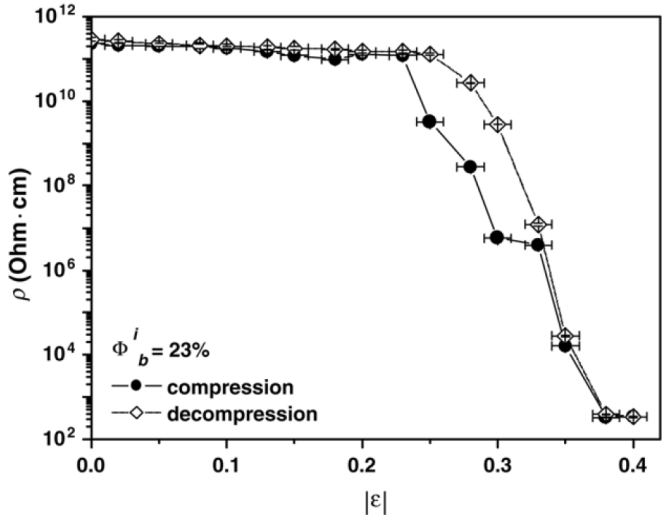


Figure 2-41: Hysteresis behavior of resistivity of silicone - 18 vol% nickel composite, percolation threshold =23% [88].

A study of the cyclic piezoresistivity of silicone - CB composites suggested that pre-stress can improve repeatability and reduce hysteresis when the load is less than the pre-stress value [199].

The longitudinal and transverse resistivities of natural rubber - CB composites as a function of strain during loading - unloading cycles has been studied [190], the hysteresis behavior was the result of two overlapping effects: the orientation of high resistivity primary structures and the decomposition of the bonds between the fillers and the polymer chains. Hence, the hysteresis behavior of the piezo-resistive effect in conductive polymer composites matches with hysteresis of mechanical tension.

2.9.2.4 Time-dependent Properties of Resistivity of Conductive Polymer Composites.

The resistivity relaxation of CB filled styrene butadiene rubber with time under shear strain can be expressed by the following equation [200]:

$$R_t = R_0 t^{-m} \qquad \text{(Equation 2-36)}$$

where $R_t$ is the resistance at time $t$, $R_0$ is the initial resistance and constant $m$ is the characteristic resistance relaxation rate of the composite.

Kost *et al* [201] studied the evolution of resistivity of silicone - CB composites immediately after application of tensile stress. The results suggested that the change of resistivity with time coincides

with the kinetics of mechanical tension. The decrease of resistivity with time during relaxation of tensile stress is due to the movement of polymer chains. The change of resistivity with time can be described by a general Maxwell model (section 2.8). Another study on silicone - CB composites confirmed that this relationship between resistivity change and stress relaxation also holds true for compressive loads [202, 203]. Similar relationships were also observed immediately after mechanical stress is released, the resistivity of conductive polymer composites exhibited a time-dependence that can be described by a general Maxwell function [204]. For constant load conditions, the change in resistivity can be understood by the Voigt - Kelvin model [205].

# CHAPTER 3 - EXPERIMENTAL PROCEDURES

## 3.1 Material Selection

### *3.1.1 Selection of Magnetic Filler Particles*

From the property data of the commonly available soft magnetic materials presented in Table 2-5, a number of candidates were identified: pure iron, oriented silicon - iron, Sendust, Permalloy, Supermalloy, Mumetal, Supermendur, Perminvar and amorphous alloys.

The selection process using Cambridge Engineering Selector Software [206] showed consistent results with the above selection. Figure 3-1 shows the property chart of various soft magnetic materials with $B_S$ higher than 0.75 T and $\mu_{max}$ higher than 10 000.

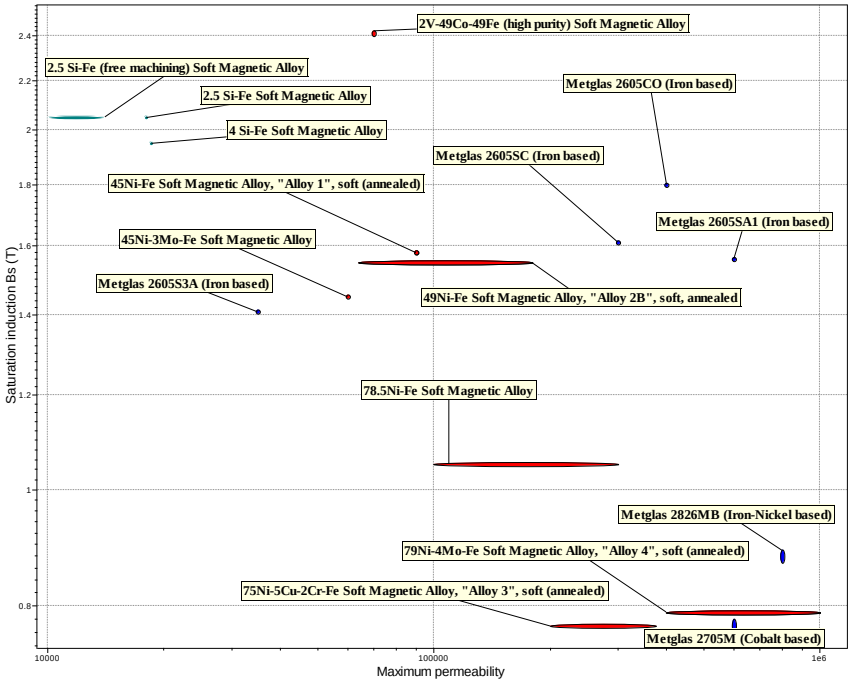


Figure 3-1: Materials selection of the magnetic fillers using Cambridge Engineering Selector. Property chart showing the candidate materials with $\mu_{max} \geq 10\,000$ and $B_S \geq 0.75$ T.

### *3.1.2 Selection of Polymer*

A high degree of flexibility is required for the polymer matrix. Candidate polymers include elastomers and polymer gels, the mechanical properties of PVA hydrogels and common elastomers were collected from various sources [207-222] for the selection of the polymer matrix for Magpol.

Figure 3-2 shows the property chart of 100% modulus (modulus value at 100% tensile strain) versus tensile strength. It is evident that PVA hydrogels and silicones were the most flexible among the candidate polymers and were chosen in this study.

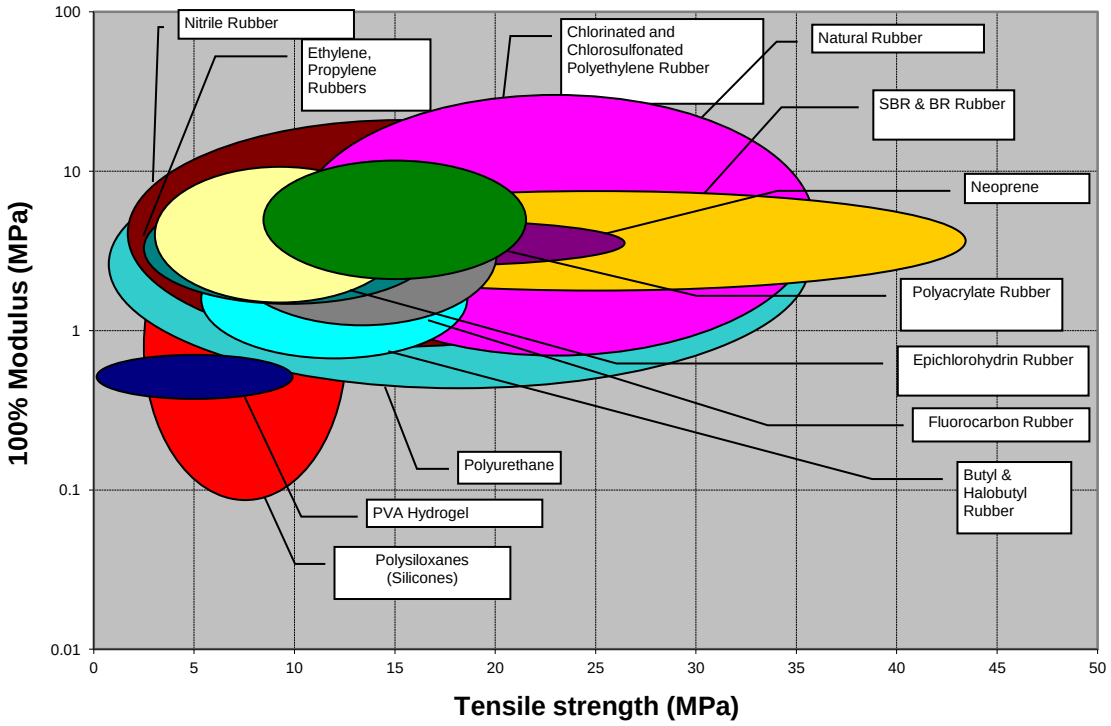


Figure 3-2: Property chart of soft polymers [207-222].

## 3.2 Material Preparation

### *3.2.1 Preparation of Polymers*

#### 3.2.1.1 Preparation of Poly(Vinyl Alcohol) (PVA) Hydrogels

In a typical experiment, 23 wt% PVA hydrogel was prepared by mixing 23 g of PVA hydrogel dry powder, MW 80,000 - 120,000 to 77 grams of distilled water to form a milky solution. The mixture was then heated to 80 - 90°C by a hot plate and stirred by a magnetic stirrer. The solution viscosity increased drastically after ~ 10 min., stirring and heating was continued for 3 min. to homogenize the mixture. Upon cooling, the product is a transparent, semi-viscous substance. To achieve desirable mechanical properties, the samples were subjected to several freezing - thawing cycles. The freezing of samples was done in a chemical grade refrigerator set at 20˚C for 1 day. Frozen

samples were then thawed at room temperature for half a day before undergoing the next freezing process.

3.2.1.2 Preparation of Silicone Elastomers.

The silicone used in this project is ECOFLEX00-10, a platinum catalyzed addition curing product (Smooth-on Inc.) [223]. The raw materials consist of 2 parts, part A and part B. The silicone is produced by mixing these two parts in a 1:1 volume ratio. For sample preparation, a predetermined amount of part B was poured into a container and mixed for 1 min. The same volume of part A was then poured into the container. The mixture was stirred carefully to achieve homogeneity and poured into a mold to achieve the final sample shape, curing is completed after 1 day at room temperature.

### *3.2.2 Preparation of Magnetic Particles*

The magnetic materials used in this study include:

1. Iron oxide powders of size <5 μm (Aldrich) and nanosized iron powder with average size of ~ 10 nm.
2. Iron powder: including iron powders ( size <10 μm, Alfa Aesar) and nickel - coated iron powders prepared by the electroless coating method.

3.2.2.1 Synthesis of Nanosize $Fe_3O_4$ Iron Oxide (Magnetite) Particles.

The nanosize iron oxide particles were synthesized via the co-precipitation method described by Caruntu et at [224]. Iron chloride salts, $FeCl_3$ and $FeCl_2$, were each dissolved separately at 2:1 molar ratio in deionized water. The two salt solutions were then combined and ammonium hydroxide was added to the aqueous solution until the reaction mixture reached pH 9. The final mixture was then washed and centrifuged thoroughly to remove byproducts and excess reactants. The magnetic particles were then collected using magnetic separation and stored in a vacuum chamber for complete drying.

3.2.2.2 Coating of Micron Sized Iron Particles Using Electroless Nickel (EN) Method

Micron sized iron powders were coated with nickel using the electroless coating method. The coating chemicals (MacDermid Planar Electroless Nickel [225]) consisted of two parts (A+B). An

EN bath was prepared by mixing the two parts with deionized water in a volume ratio of A:B:Water = 6.6:15:78.4, the mixture was heated to 80˚C by a hot plate. A dummy nickel piece was immersed in the EN bath, bubbles on the surface of the metal piece were observed after ~ 30 s, the bath was balanced and ready for the EN process. The iron particles were put in the bath and strong agitation maintained with a magnetic stirrer. The reaction process was run for 10, 20 and 30 min, after which the particles were removed, washed several times and dried in a vacuum chamber.

### *3.2.3 Preparation of Magpol*

Magpol samples were prepared by incorporating magnetic fillers into the polymer matrix before crosslinking was complete. For the PVA hydrogel matrix, the particles were mixed with the solution before the heating process. For the silicone samples, in a typical experiment, 10 ml of the precursor and 10 ml of Pt-based curing agent were mixed and stirred for 5 min using an overhead stirrer. Iron powder with mass ranging from 2.3 g to 102 g was then slowly mixed with the polymer in increments of 1 g. For the silicone - graphite - iron composites, in a typical experiment, iron and graphite particles were mixed together in pre-calculated amounts according to the intended filler fraction before adding to the pre-cure silicone compound. The mixing process took 30 min., the mixture was then subjected to vacuum to remove bubbles and then transferred into a cylindrical mold diameter 1.1 cm and length 15 cm. The samples reached their final shape and mechanical properties after curing for one day at room temperature. Samples of length $L$ were prepared by cutting the as-cured samples to a length $L_{max}$ of 13 cm. Segmented samples (Figure 3.3) were prepared by injecting desired amounts of uncured silicone - iron mixture to the mold, followed by addition of uncured silicone. These samples composed of two different regions: one containing magnetic particles and the other is pure silicone.

(a) (b) (c) (d)

Figure 3-3: Segmented magnet - polymer composites with different doped/undoped proportions: (a) 3cm/10cm, (b) 7cm/6cm, (c) 10cm/3cm and (d) 0cm/13cm

## 3.3 Characterization Techniques:

### *3.3.1 Characterization of Filler Particles.*

The properties of filler particles were studied using various experimental techniques. Their morphology was studied by JEOL 5310, 6360 and 6340F Scanning Electron Microscopes (SEM). The synthesized nanoparticles were examined by a JEOL 2010 Transmission Electron Microscope (TEM). Particle size was analyzed using ImageJ software [226]. The composition was studied using the Energy Dispersive X-ray Analysis (EDX) attachment of the SEM. The magnetic properties used were measured using a Lakeshore 7404 Vibrating Sample Magnetometer (VSM), the room temperature magnetization curves were fitted to mathematical functions using TableCurve2D software.

### *3.3.2 Characterization of Polymer Matrix*

The mechanical properties were studied using an Instron 5567 tensile tester according to ASTM D 638-03 standard. The mechanical properties of the polymer were also studied using the Physica MCR501 rheometer. The morphology of the polymers was studied using the SEM. For PVA hydrogel samples, drying of samples was carried out before SEM investigations.

### *3.3.3 Characterization of Magpol*

The properties of Magpol were studied with various tools. The mechanical properties were studied using the same equipments and methods used for characterizing the pure polymers. Strain relaxation behavior was studied by releasing the sample from 80% tensile strain to the unstrained state. For the magnetic properties measurements, the composite samples were cut into thin films and mounted on a thin film holder for VSM measurements. Sample cross-sections were prepared for morphological studies by cutting the samples with a sharp knife. The morphology of the composites was inspected using a JEOL 6340F Scanning Electron Microscope operating at 15 kV.

### *3.3.4 Experimental Setup*

The experimental setup for testing the actuation properties of Magpol is shown in Figure 3-4. The magnetic field was generated by a Lakeshore CM-4 dipolar electromagnet, the magnetic field strength can be controlled by varying the current through the electromagnet coils. One end of the sample was fixed to an aluminum holder while the other end was free. The sample was placed within a cylindrical glass tube, the sample surfaces and the glass tube were lubricated by a low viscosity machine oil ($\nu$ = 9.6 $m^2/s$) to minimize friction. Different actuation modes were obtained by setting appropriate sample positions; the sample elongated when the free end was above the middle of the pole pieces and contracted or coils when the free end was below the middle of the electromagnet. The sample displacement was measured using an Acuity AR600 triangulation laser displacement sensor (resolution of 61 μm) and the generated force was recorded using a Vernier dual range force sensor (resolution of 0.01 N). The force sensor was attached to the fixed end of the sample in elongation mode and to the free end in contraction and coiling modes. The work performed in contraction and coiling modes was measured using the work-loop method [91]. The

experimental setup for the work loop method was similar to the setup described above. The samples were subjected to repeated cycles of lengthening and shortening and the force was measured. The actuation strain was set at 70% of the maximum strain for each mode, i.e., 30% strain in contraction mode and 40% strain in coiling mode, respectively. A magnetic field of 1.5 Tesla was applied (removed) at the end of the lengthening (shortening) phases. Sample work loops were measured at a frequency of 0.5 Hz, net work per cycle usually decreases with increasing cycle frequency or strain rate [227].

For testing of dynamic actuation of Magpol, a similar experimental setup was used. However, the magnetic field was generated by a air-cooled Phywe 06480.01 dipolar electromagnet driven by a Dynatronix DPR40-30-100 pulse power supply, the magnetic field strength and frequency were varied by changing the voltage pulses generated by the power supply. The current was measured by a Fluke 43B power analyzer, the magnetic field strength was determined by a calibrated field - current curve.

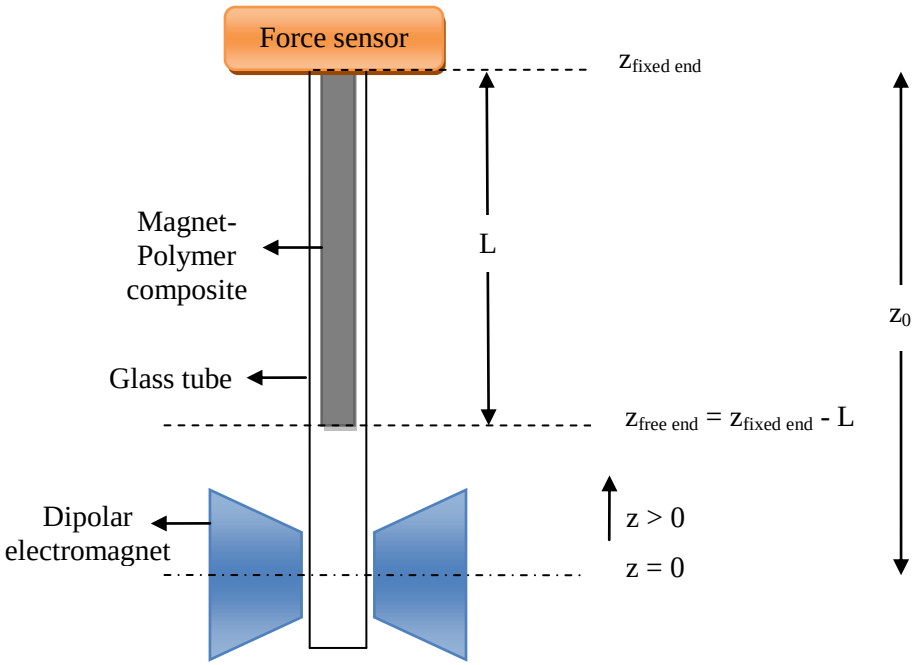


Figure 3-4: Experimental setup to study actuation properties of Magpol.

### 3.4 Finite - Element Simulation

Magneto - structural analysis was conducted using ANSYS Multiphysics© to understand the initial stages of coiling behavior of Magpol. The samples, the surrounding air and the electromagnet were modeled using coupled-field SOLID98 elements. Coupled-field elements allowed magnetic and structural components to be solved simultaneously rather than sequentially and thus provide faster and more accurate results (section 2.7.2). The actual dimensions of samples and the pole pieces were used, the electromagnet's coils were modeled by two racetrack coils of the same dimensions. These elements were contained in a spherical air region with a diameter 60 times the air-gap size to ensure far-field conditions. Mesh size refinement was performed for elements within the air-gap region and at sharp edges. Experimental values of magnetic properties and Young's modulus were input in the model. The effect of gravity was included using the experimental sample density.

### 3.5 Characterization of Sensing Properties of Magpol

The electrical properties of Magpol samples were measured using the four point methods [228]. The sensing properties of silicone - graphite or silicone - graphite - iron composites were studied by monitoring the electrical resistivity of samples subjected to externally applied tensile strain. The samples were clamped to an Instron 5567 tensile tester with both ends insulated by sand papers. Tensile strain was applied and released for 5 cycles by the tensile tester while the electrical resistance was recorded. The time dependence of sample resistance was studied by initially elongating the samples to 60% strain at $5\%.s^{-1}$ and holding for 5 min. while the electrical resistance was recorded.

### 3.6 Testing of Transduction (Actuation and Self-sensing) Properties

The transduction properties of Magpol were studied by evaluating the relationship between the actuation strain and the electrical resistivity of the composite. The samples were studied in experimental setups similar to the actuation tests described in section 3.3.4 and the electrical resistance was recorded as a function of time. The actuation modes studied in this work include elongation, contraction and coiling. Three different setups were employed for each actuation mode:

samples without load, samples subjected to a small load (6.4 kPa), samples subjected to a high load (21.2 kPa).

# CHAPTER 4 - RESULTS AND DISCUSSION

The results of the synthesis, characterization, tests and modeling of Magpol smart composites are described in this chapter. Magpol samples of silicone, iron and graphite, were prepared, and their actuating characteristics for deflection, elongation, contraction and coiling modes were studied. Other aspects related to actuation, including work and dynamic properties, were also examined. Studies of the sensing and transduction properties of silicone - graphite - iron Magpol were also conducted. Lastly, a discussion of the performance of Magpol compared to other state-of-the-art actuators and transducers is presented.

## 4.1 Physical Properties

### *4.1.1 Physical Properties of Magnetic Particles*

#### 4.1.1.1 Nanosized Magnetite ($Fe_3O_4$) Particles

Nanosized $Fe_3O_4$ particles were successfully synthesized by the method described in section 3.2.2.1. Figure 4-1 shows the TEM micrograph of these particles, the average particle size was ~ 11 nm.

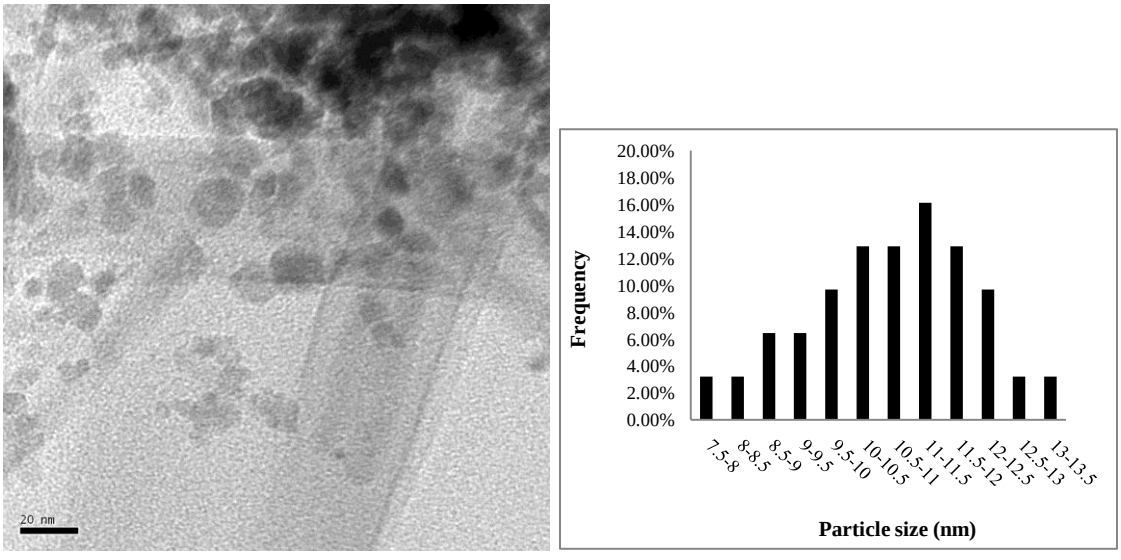


(a) Micrograph (b) Paticle size distribution

Figure 4-1: TEM micrograph and particle size distribution of the synthesized $Fe_3O_4$ nanoparticles.

#### 4.1.1.2 Commercial Iron Particles

Figure 4-2 shows the scanning electron micrographs of the iron particles (size specification < 10 µm), the particle size was distributed in a range of 0.1 µm - 5 µm. The EDX analysis results (Figure 4-3) indicated that the surface of the particles was oxidized.

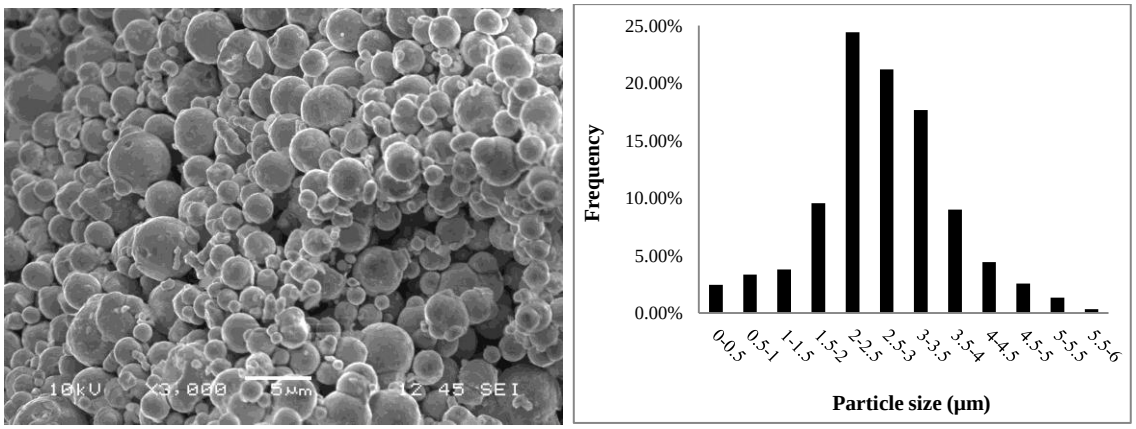


(a) Micrograph (b) Particle size distribution (average size = 2.7 µm)

Figure 4-2: Scanning electron micrographs of iron particles, size specification < 10 µm.

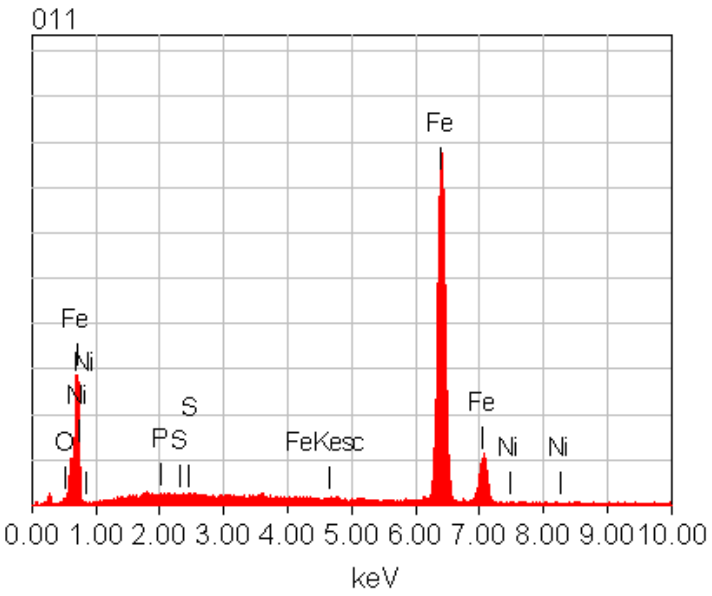


| Element | mass% | Compound | mass% |
|---|---|---|---|
| O | 22.30 | | |
| P K | | | |
| S K | 0.04 | SO3 | 0.1 |
| Fe K | 77.66 | FeO | 99.9 |
| Ni K | | | |
| Total | 100 | | 100 |

Figure 4-3: EDX analysis of iron particles, size specification < 10 µm.

4.1.1.3 Nickel Coated Iron Particles.

The oxide layer of the iron particles was undesirable because it prevents the particles from conducting electricity. To improve electrical conductivity, nickel was coated onto the surface of the iron particles using the EN method. Nickel was chosen because it is superior to iron in oxidation resistance and is also a ferromagnetic element. Figure 4-4 shows the scanning electron micrographs of the nickel coated iron particles for 10, 20 and 30 min coating duration. The size of the particles increased with coating time, especially after 20 min. Coalescence also started to occur after 20 min.

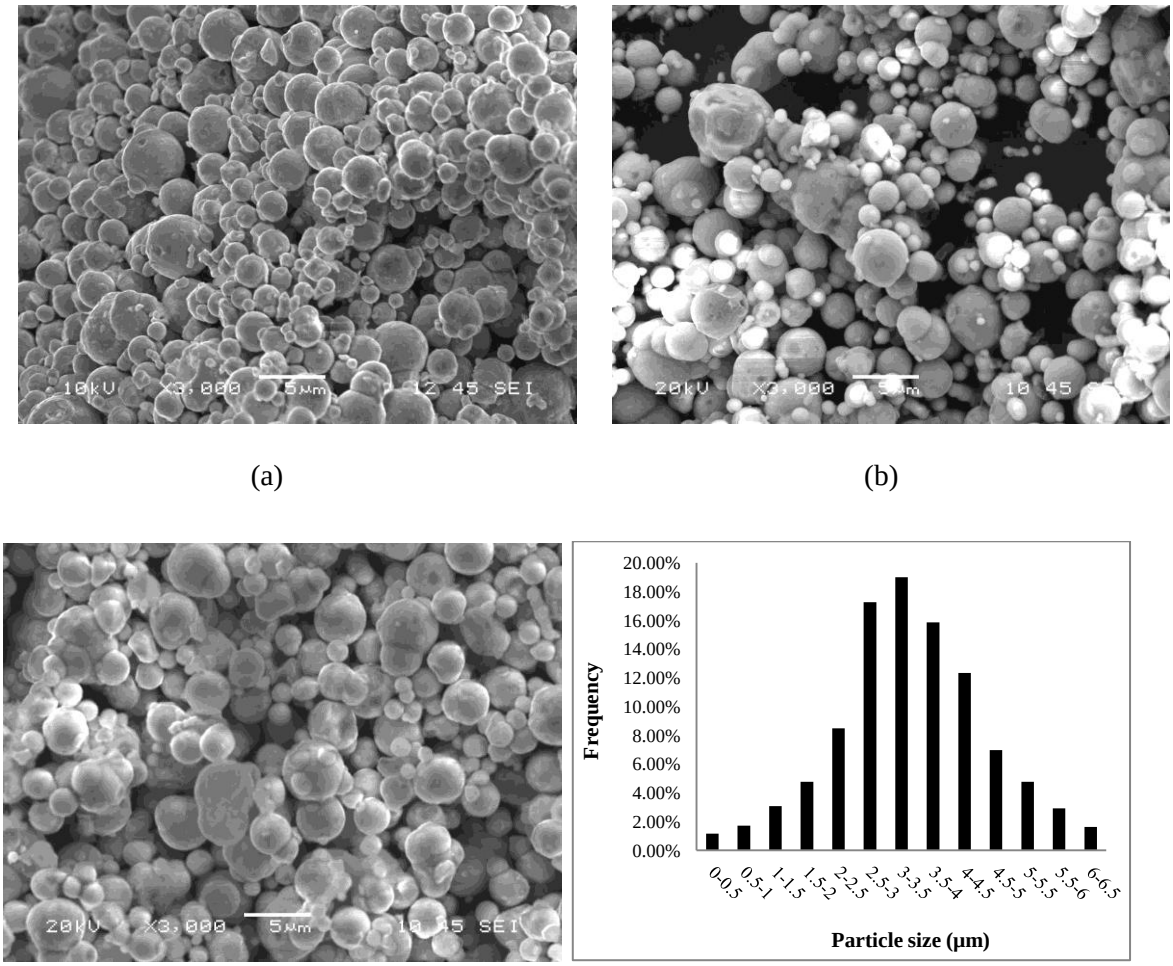


(a) (b)

(c) (d)

Figure 4-4: Scanning electron micrographs of iron particles with electroless nickel coatings: (a) Pure iron particles, (b) 10 min. coating, (c) 20 min. coating, (d) Particle size distribution after 20 min. coating (average size = 3.4 µm)

Beyond 20 min. of coating time, a foreign columnar structure formed (Figure 4-5). The result of EDX analysis on the surface of an isolated particle after being coated for 20 min. (Figure 4-6) suggested that nickel is successfully coated on the iron particles. Unfortunately, the Ni surface was also oxidized, as suggested by the EDX result. Subsequent electrical test of composite samples of silicone and Ni-coated Fe particles confirmed that the conductivity of such composite is not detectable and is thus not suitable for studies of sensing properties.

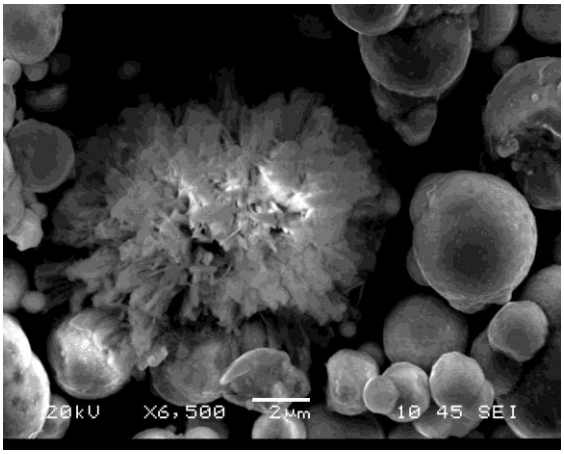


Figure 4-5: Columnar structure formed during EN coating of iron particles for 30 min.

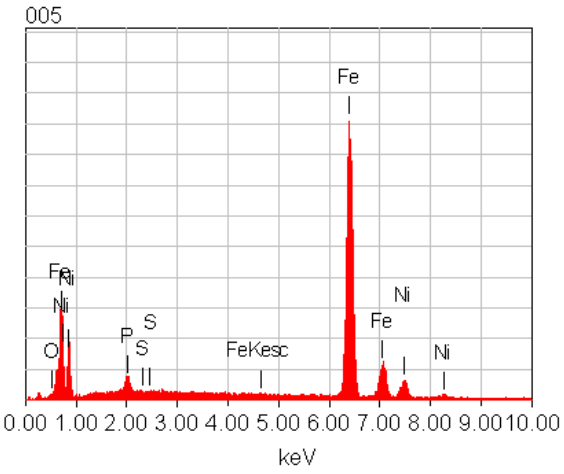


| Element | mass% | Compound | mass% |
|---|---|---|---|
| O | 23.26 | | |
| P K | 1.33 | P2O5 | 3.05 |
| S K | 0.03 | SO3 | 0.07 |
| Fe K | 68.48 | FeO | 88.1 |
| Ni K | 6.9 | NiO | 8.78 |
| Total | 100 | | 100 |

Figure 4-6: Result of EDX analysis performed on iron particles after 20 min. of EN coating.

#### 4.1.1.4 Magnetic Properties of Filler Particles

Figure 4-7 shows the room temperature magnetization curves of the micron sized iron powders, the micron sized iron oxide powders and the synthesized iron oxide nanoparticles. Both the iron and

iron oxide particles exhibited typical soft magnetic properties, i.e., a non-linear magnetization curve with small hysteresis. The measured value of susceptibility of the iron particles was 18, consistent with previously reported values [229, 230]. A summary of their magnetic properties are listed in Table 4-1.

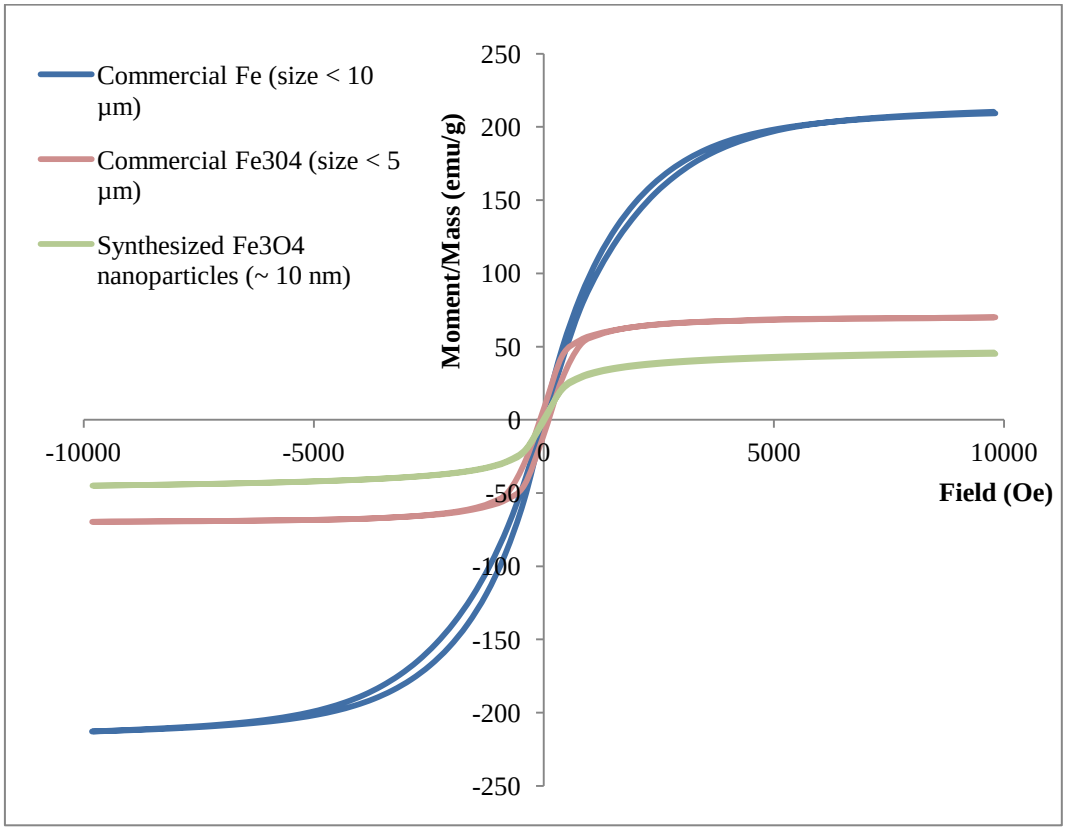


Figure 4-7: Magnetization curves of the filler particles

Table 4-1: Magnetic properties of the filler particles.

| Type of magnetic particle | Magnetization saturation $M_s$ (emu/g) | Coercivity $H_{ci}$ (G) | Retentivity Mr (emu/g) | Susceptibility χ |
|---|---|---|---|---|
| Iron, < 10 µm | 211 | 29 | 1 | 18 |
| $Fe_3O_4$, < 5µm | 70 | 95 | 9 | 7 |
| Synthesized nanosize $Fe_3O_4$, ~ 12nm | 45 | 15 | 1 | 5 |

The actuation of Magpol is directly related to the magnetic force acting on the particles in the composite. As discussed in section 2.5.3, the requirements for high magnetic force include high susceptibility $\chi$, high saturation magnetization $M_S$, large particle size $V_P$ and high magnetic field gradient $\nabla B$ [130, 133, 231]. The first three requirements are directly related to the intrinsic magnetic properties of the particles while the last requirement is related to the strength and distribution of the external field. As can be seen in Table 4-1, the choice of magnetic powder has a large impact on the magnetic response of filler particles in the presence of an external magnetic field. Iron particles with good susceptibility, saturation magnetization and ready availability in powder form were chosen as the magnetic filler. The average size of the particles also has a significant effect on the magnetic properties of the particles. The size of the iron particles was selected to be in the micron range due to the good balance between magnetic properties and interfacial adhesion with the polymer matrix. Particle size in the nanometer range allows better adhesion due to greater surface area but magnetic properties usually deteriorate due to spin disorder and oxidation [135, 232]. Generally, smaller size reduces $M_S$ value [135] and also introduces new characteristics such as single domains and superparamagnetism [233, 234]. On the other hand, as the particle size increases, it is more difficult to achieve a homogeneous distribution of particles.

### *4.1.2 Physical Properties of Polymers*

Since the early work done by Zrinyi and coworkers [34], PVA hydrogel matrix with magnetic fillers was considered to be promising. Work performed on the mechanical properties of PVA hydrogels by other researchers also suggested that this material has suitable properties for biological applications [235-239]. PVA Hydrogels can be prepared via various methods [240-248], including the freezing-thawing technique. Figure 4-8 shows the enhancement of mechanical properties with the number of freezing - thawing cycles for both the PVA hydrogel and the composite of PVA Hydrogel and $Fe_3O_4$ micron sized particles. As can be seen from the graph, both types of materials yielded better mechanical properties with increasing number of freezing - thawing cycles. However, the storage modulus of the composite was consistently lower than that of the PVA hydrogel samples due to the presence of air bubbles in the composite. The formation of these bubbles was easier due to $Fe_3O_4$ particles acting as nucleation sites for bubbles during sample preparation.

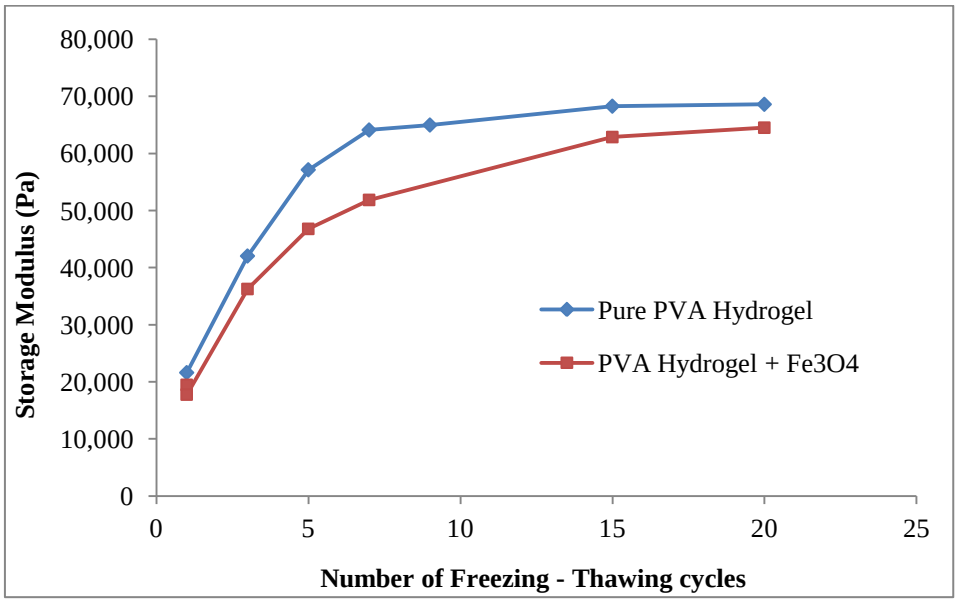


Figure 4-8: Storage modulus of pure PVA Hydrogel and (PVA Hydrogel + $Fe_3O_4$) composite as a function of freezing - thawing treatment cycles.

The drawback of using hydrogels as an artificial muscle is the requirement of constant hydration. Another limitation of PVA hydrogels is that they cannot be stored for a long time because their physical and mechanical properties are strongly affected by aging. Aging in PVA hydrogels causes negative and unpredictable effects on their mechanical properties [248]. The effect of freezing - thawing and aging on both PVA and its composite with $Fe_3O_4$ particles was confirmed (Figure 4-9), both pure PVA gel and PVA - $Fe_3O_4$ composite exhibited an increase in storage modulus, ranging from 6.6% to 21.8% in 30 - 45 days.

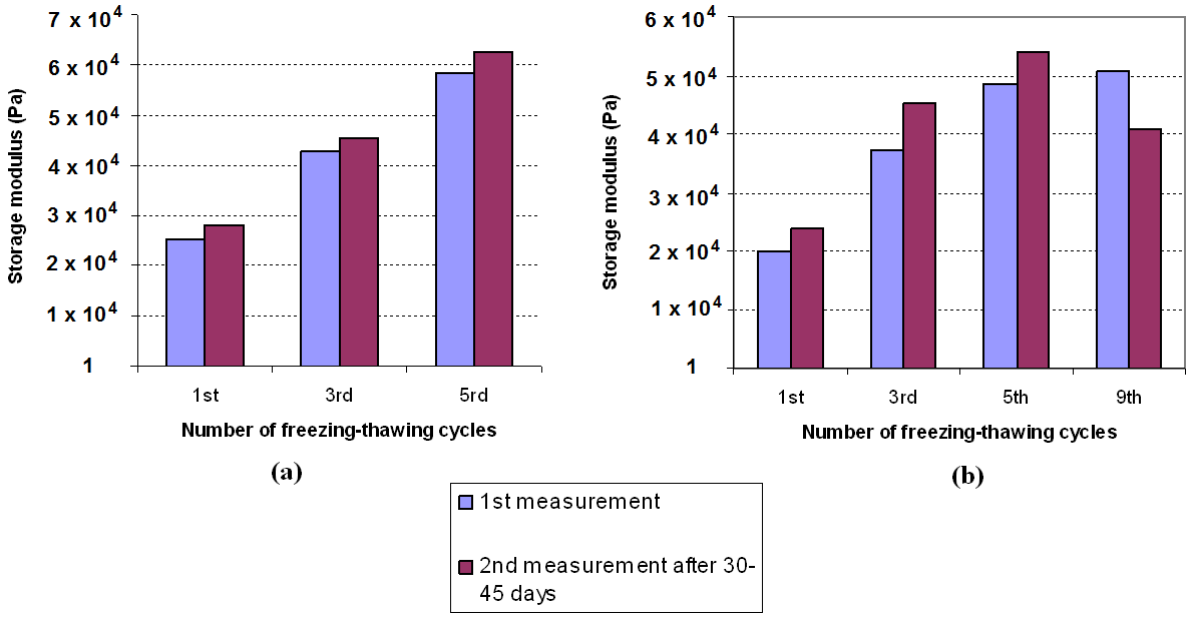


Figure 4-9: Effect of aging on storage moduli of (a) PVA hydrogel and (b) PVA hydrogel - $Fe_3O_4$ composite

Other polymers which possess favorable properties and biocompatibility include polysiloxanes (i.e., silicone) or polyurethane. Figure 4-10 shows the tensile properties of ECOFLEX00-10 silicone and PVA hydrogel, suggesting that silicone has higher flexibility and maintains its elastic properties over a larger strain range than PVA hydrogels.

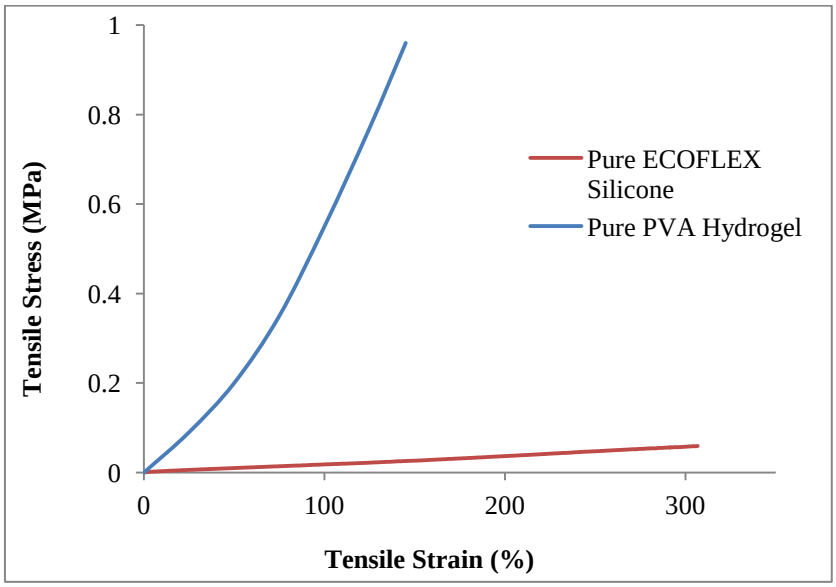


Figure 4-10: Tensile properties of pure ECOFLEX0010 Silicone and PVA Hydrogel.

### *4.1.3 Physical Properties of Magpol*

The physical properties relevant to actuation performance of Magpol include mechanical and magnetic properties. High flexibility, strain and load carrying capacity are desirable mechanical properties; high magnetic susceptibility ($\chi$) and $M_S$ are the magnetic properties of interest. These properties can be achieved by the appropriate selection of the polymer matrix and the type as well as the concentration of the filler particles. Silicone elastomers and iron particles were chosen as the matrix and filler, respectively, based on these requirements.

Scanning electron micrographs of silicone - iron composite samples in both secondary electron and backscattered electron modes are shown in Figure 4-11. Aggregates with size ranging from 0.1 µm to 5 µm were observed. The SEM micrographs of silicone - graphite composites are shown in Figure 4-12. The graphite flakes (average size of 15 µm, Figure 4-12(a)) can be mixed with silicone at percolation concentration to form electrically conductive silicone - graphite composites (Figure 4-12(b)). The SEM micrographs of silicone - graphite - iron composites are shown in Figure 4-12(c). Due to the significantly smaller size of the iron filler particles compared to the graphite flakes, the iron particles could be interspersed between the graphite flakes without disrupting the percolation network.

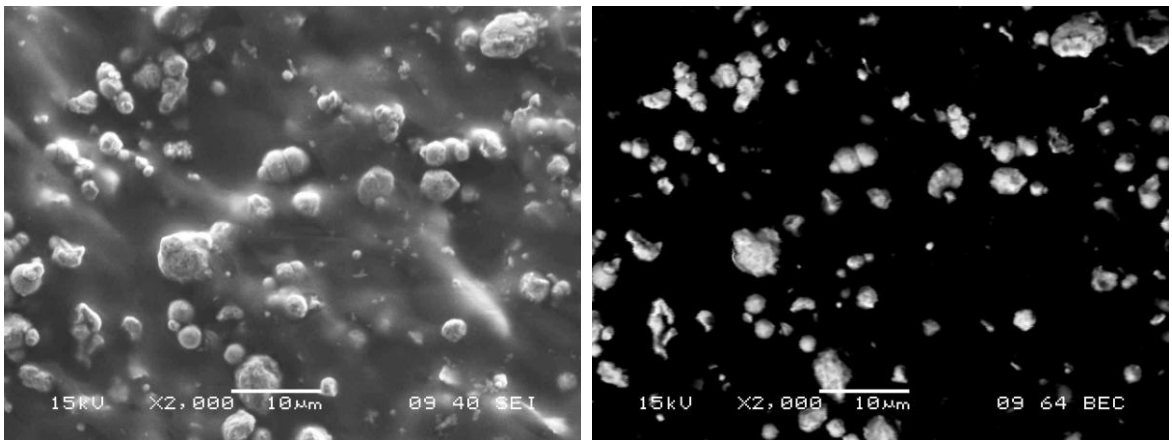


(a) Secondary electron micrograph (b) Backscattered electron micrograph

Figure 4-11: Scanning electron micrographs of silicone - 20 wt% Fe samples.

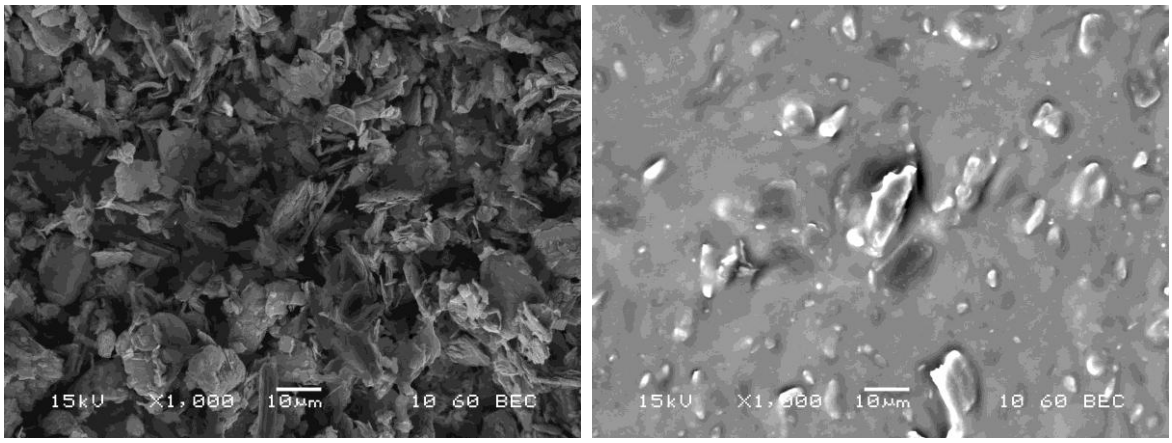


(a) (b)

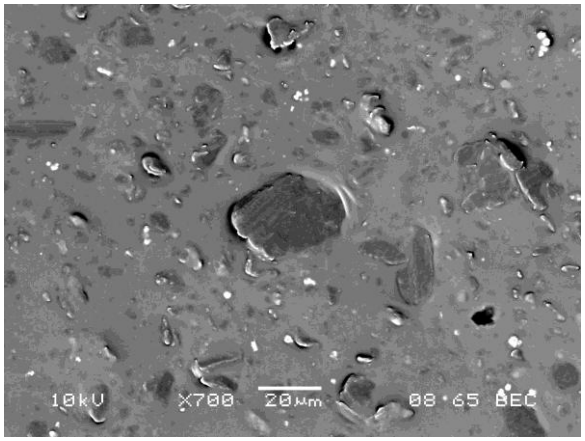


(c)

Figure 4-12: Scanning electron micrographs of (a) graphite particles (b) Silicone - 25 vol% graphite composite; (c) Silicone - 25 vol% graphite - 40 wt% Fe graphite composite.

Room temperature magnetization curves of (a) the iron filler particles and (b) silicone - 50 wt% Fe samples are shown in Figure 4-13. The silicone - 50 wt% Fe samples exhibited qualitatively similar magnetic properties to those of the iron particles. The linear increase of saturation magnetization value of the composite with increasing concentration of the magnetic particles (inset in Figure 4-13(b)) suggested that the magnetic properties of the composites were not significantly affected by particle aggregation.

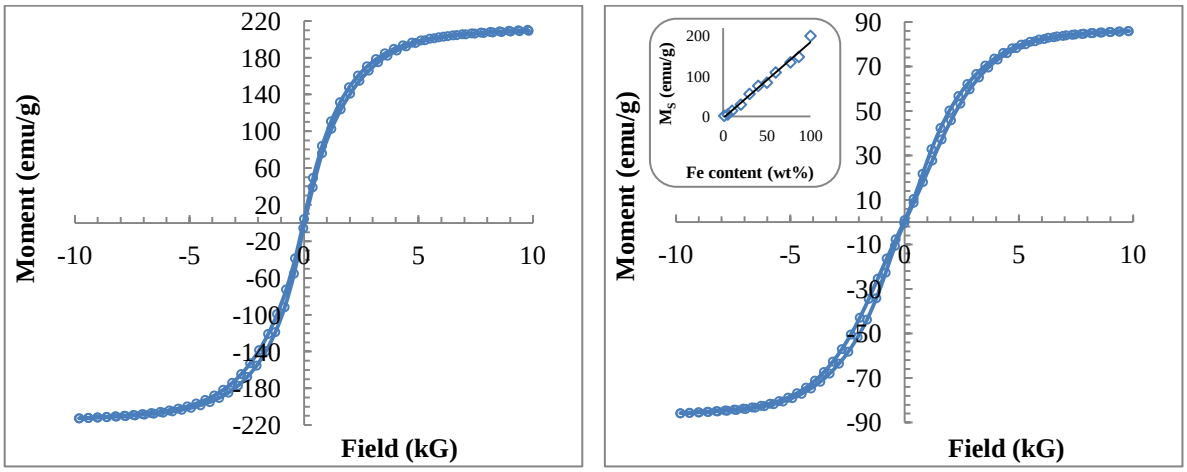


(a) Fe particles

(b) Silicone - 50 wt% Fe composite

Figure 4-13: Magnetization curves of (a) the Fe particles used and (b) Silicone - 50 wt% Fe composite, the inset shows the magnetization saturation of the composites at different Fe concentrations

The tensile properties of Magpol samples for various filler concentrations are shown in Figure 4-14. The modulus and strength of the composite increased with increasing filler concentration, while the elastic range decreased with increasing filler concentration. However, composites at all filler concentrations studied in this work remained elastic up to a tensile strain of 100%. Previous studies suggested that the mechanical properties of Magpol can be improved further by pre-alignment of the magnetic particles by an external magnetic field during the curing stage of the polymer matrix, 80% increase in tensile strength, 200% increase in tensile modulus and 300% increase in compressive modulus have been reported [49, 249]. Real-time dynamic control of mechanical properties can also be achieved by an external magnetic field, which is useful for damping devices used in automobile industry [250, 251].

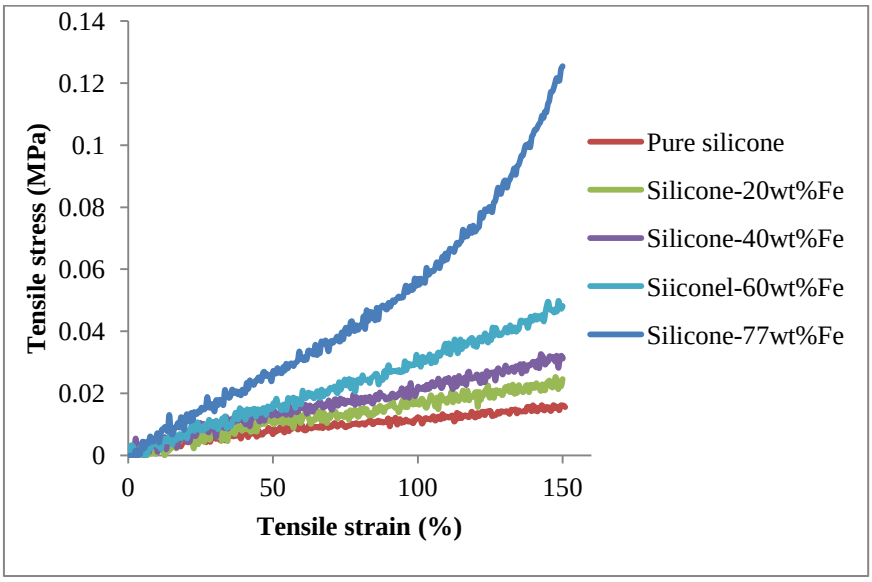


Figure 4-14: Tensile properties of Magpol at various filler concentrations

Magpol composites exhibited fast relaxation from the elongated state, the average relaxation time of silicone - 60 wt% Fe samples was 34 ms (Figure 4-15). Due to inertia, slight contraction and a "bounce" were observed, full recovery to the rest state occurred in less than 0.5 s.

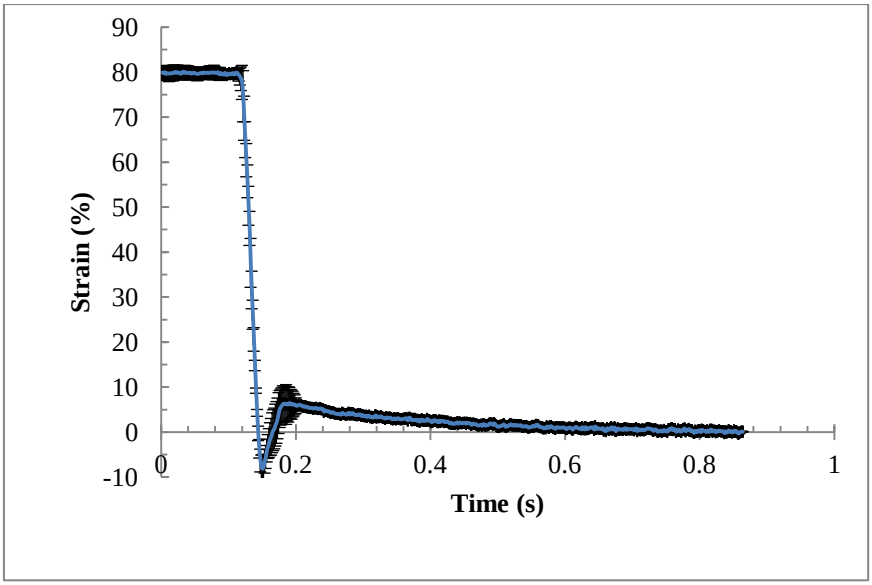


Figure 4-15: Relaxation of strained silicone - 60 wt% Fe samples.

## 4.2 Actuation Properties

The composite is capable of a variety of actuation modes: elongation, contraction, deflection and coiling (Figure 1-4). Different actuation modes can be readily achieved by changing boundary conditions. Studies carried out for each actuation mode are described in this section.

### *4.2.1 Deflection*

Figure 4-16 shows the deflection test results of cylindrical samples of size 12mm (D) x 70mm (L) made of PVA hydrogel and various concentrations of iron powders, it can be seen that the maximum deflection increased with increasing filler concentration. For each filler concentration, the deflection also increased with increasing magnetic field strength. Interestingly, there existed a certain value of the magnetic field strength beyond which the deflection of the composite increased drastically.

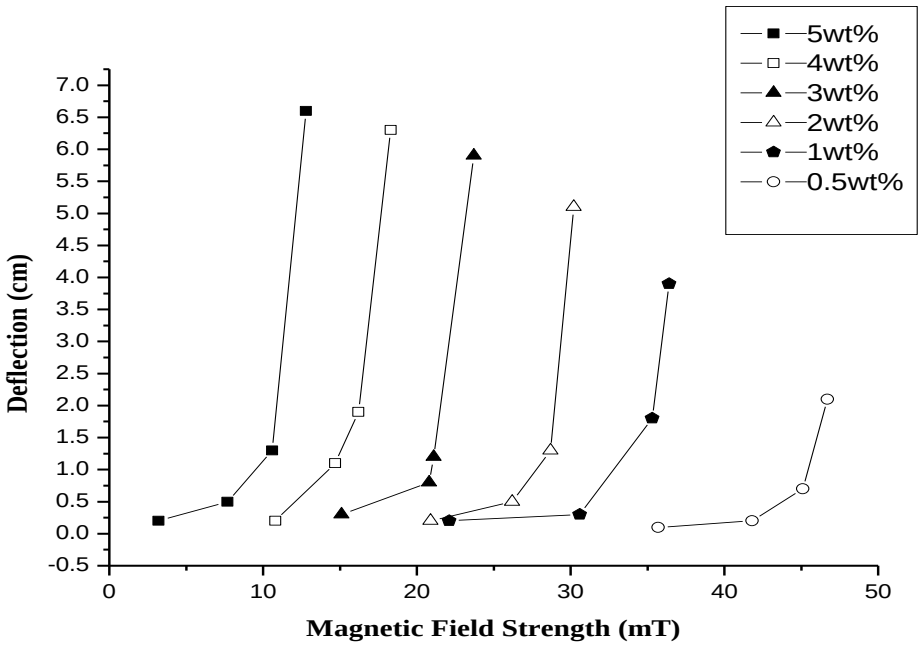


Figure 4-16: Deflection as a function of magnetic field strength of PVA hydrogel - Fe samples

To explain the deflection of Magpol, magnetic finite element simulation using ANSYS software was performed [148]. Figure 4-17 shows the distribution of magnetic field of a N35 block permanent magnet of size 50 x 100 x 20 mm used for the deflection experiment, the magnetic field strength, H, decays sharply with distance from the magnet. Figure 4-18 shows the measured magnetic field

strength as a function of distance at various locations and directions. A is the central point of the small face along the y-axis, B is the middle point on the edge of the small face along the y-axis, C is the middle point on the edge of the long face along the x-axis, D is the middle point at ¼ the length of the long face along the x-axis and E is the central point of the long face along the x-axis.

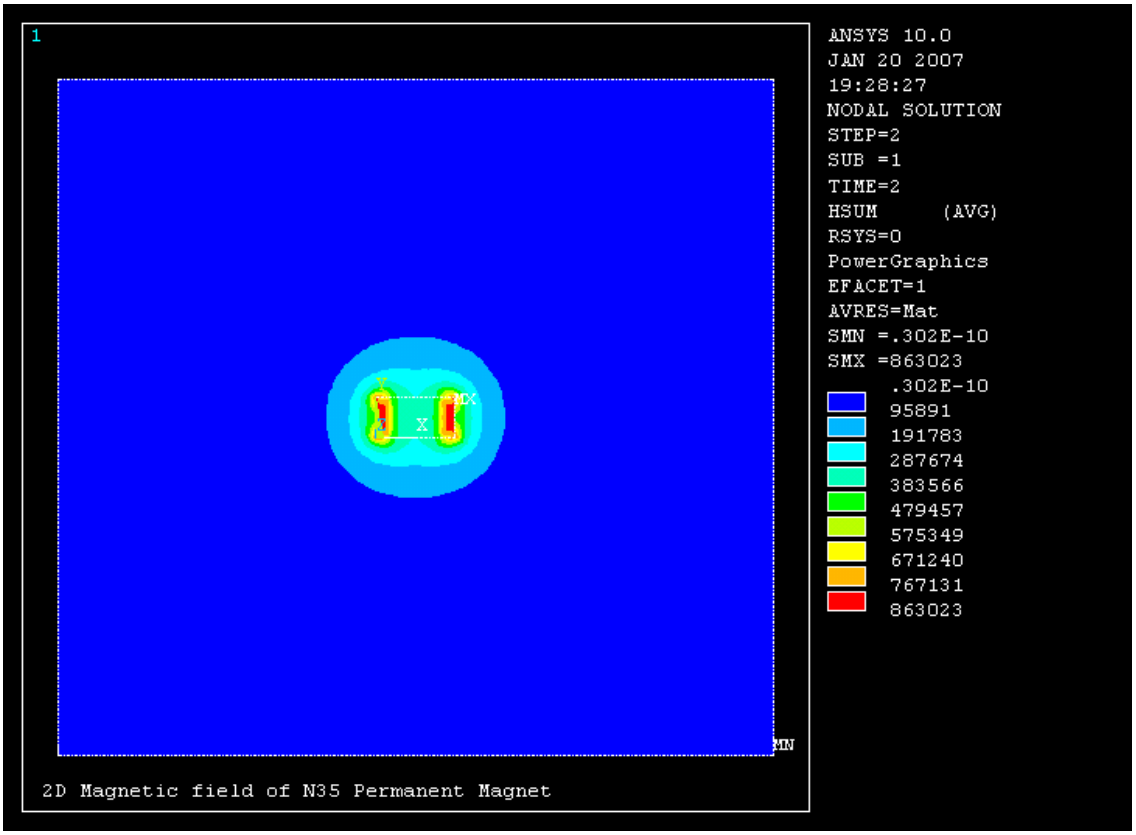


Figure 4-17: ANSYS simulation of magnetic field surrounding an N35 permanent magnet.

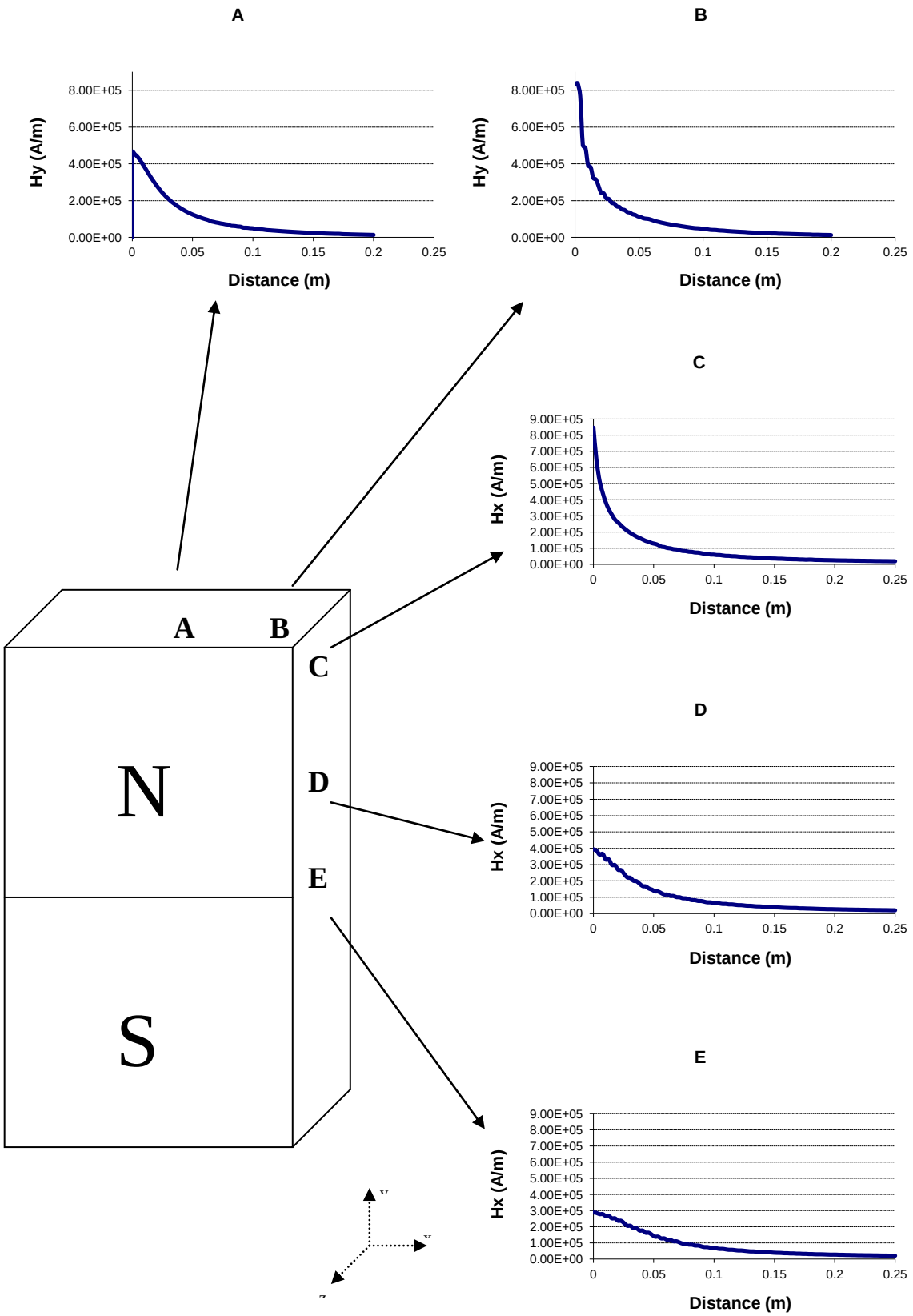


Figure 4-18: Distribution of magnetic field strength of a N35 permanent magnet at various locations.

Since magnetic force is mainly influenced by the field gradient (section 2.5.2), it is important to examine the magnetic field gradient around the magnet. The distribution of magnetic field strength H as a function of distance (Figure 4-18) can be satisfactorily modeled by a second order exponential decay function:

$$y = A_1.\exp(-x/t_1) + A_2.\exp(-x/t_2) + y_0 \qquad \text{(Equation 4-1)}$$

For example, the magnetic field strength at point C in Figure 4-18 can be modeled with the following parameters:

$y_0 = 6.7 \times 10^3$

$A_1 = 442.4 \times 10^3$

$t_1 = 6.6 \times 10^{-3}$

$A_2 = 356.2 \times 10^3$

$t_2 = 38.7 \times 10^{-3}$

The original data and the fitted function curve described the above parameters are shown in Figure 4-19, the magnetic field gradient was derived and is also shown in the figure. Beyond a distance of about the size of the permanent magnet (i.e. a few centimeters around the magnet), both the magnetic field and the gradient are negligible. These two quantities increase as the distance from the point of measurement to the magnet decreases. The gradient changes at a much faster rate than the magnetic field strength, especially ~ 2 cm away from the magnet. This drastic change in gradient accounts for the threshold behavior of the deflection of the magnet - polymer composite.

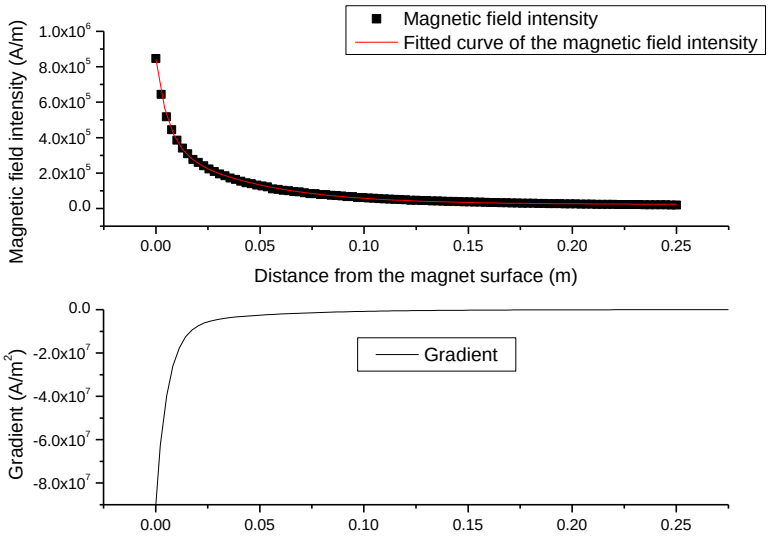


Figure 4-19: Magnetic field intensity and gradient distribution at point C.

A series of magneto - structural simulations using ANSYS multiphysics software was carried out. Figure 4-20 shows the visual results of the simulation, Figure 4-21 shows a comparison of the deflection as a function of magnetic field intensity obtained from the simulation and the experimental data. As can be seen from the two figures, the simulation results agreed well with the experimental observations and data, suggesting that computer modeling can be very useful in designing Magpol actuators.

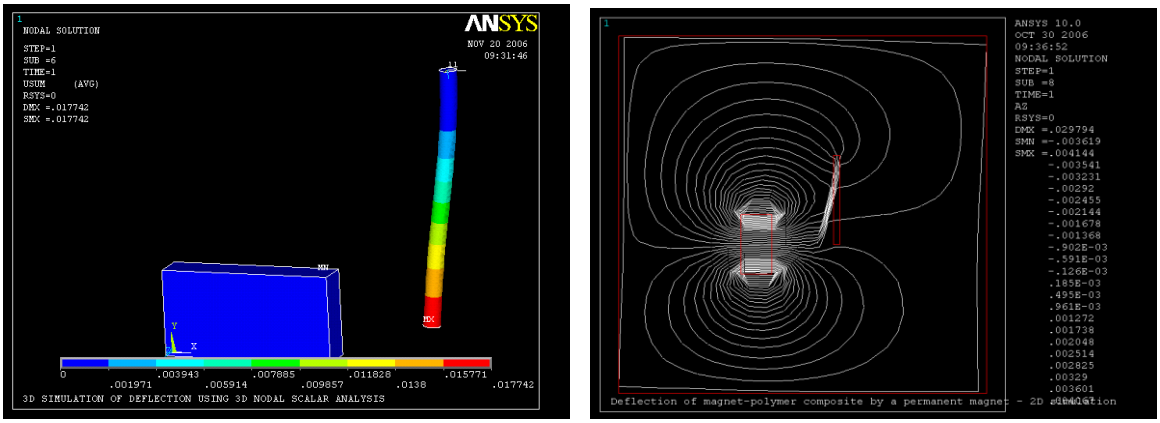


(a) Deformation plot (b) 2D flux plot

Figure 4-20: Deflection simulation of Magpol using ANSYS Multiphysics.

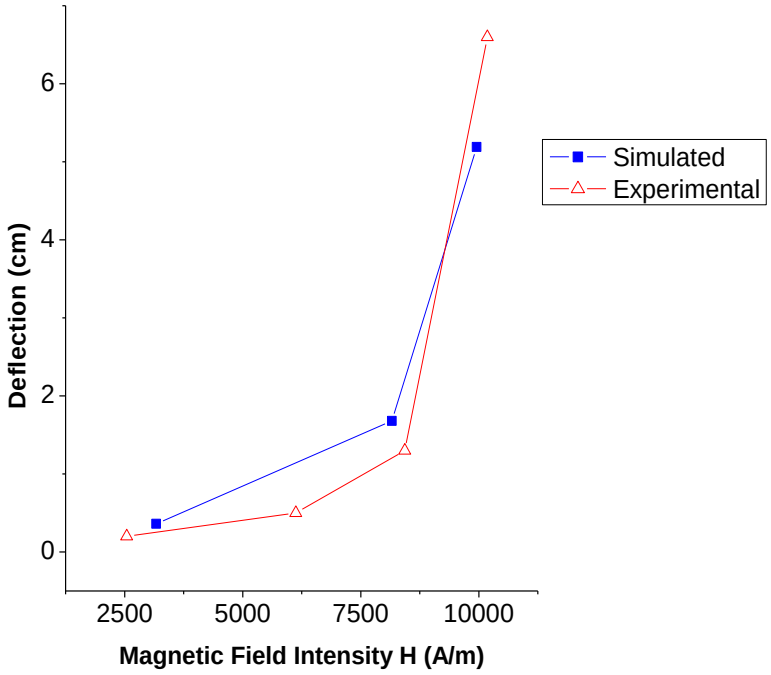


Figure 4-21: Deflection values obtained from simulation and experiment of PVA hydrogel - 5 wt% $Fe_3O_4$ samples.

While the sharp change in the magnetic field gradient is commonly observed in existing magnetic field sources, the large deflection of Magpol produced by a permanent magnet is worth noting. It is well known that magnetic materials can change their shape due to magnetic forces acting on their body, the study of this phenomenon is called magneto-solid mechanics [252-254]. However, the unique properties of the large deflection and the sharp threshold in deflection can only be found in Magpol because of its unique combination of magnetic properties and high flexibility. A similar deflection experiment with a steel rod would yield very low deformation due to the high stiffness of the material. Clearly, the "soft" mechanical properties play a crucial role in the giant magneto - elasticity observed in Magpol.

Liu *et al* exploited the high magnitude deflection of Magpol to improve the performance of EAPs [255]. By adding $Fe_3O_4$ nanoparticles to a polypyrrole matrix, actuation can be controlled by either an electric field or a magnetic field. The additional contribution from the magnetic capability allow the hybrid composite to achieve performance significantly higher than that of conventional polypyrrolle actuators. The deflection angle of the composite in the presence of an electric field was

limited to 44.2° and increased by more than 50% to 67° when a small magnetic field of 24.8 mT was applied. When a magnetic field of 116.2 mT was applied, the composite was able to bend an angle of 111° .

The different threshold values at different particle concentrations can lead to interesting applications. Ramanujan proposed an artificial finger system constructed from Magpol with graded magnetic concentration [30]. The samples were made up of different segments of particle concentrations; each segment had a different magnetic field threshold value for deflection. Therefore, when the samples were exposed to a magnetic field with uniform distribution of gradient, the parts with high concentrations (i.e. the tip of the "finger") deflected the most whereas the parts with lower concentration deflected at much less extents, giving rise to a motion similar to human fingers.

### *4.2.2 Elongation*

Figure 4-22(a) shows the axial elongation strain of cylindrical silicone - 40 wt% Fe Magpol samples. The path traced by points along 0 - I - II - III is the sample elongation as the magnetic field (measured at the free end) was increased, the path traced by points along III - IV - V is the relaxation as the magnetic field was decreased back to zero. The samples exhibited significant mechanical hysteresis during relaxation, this hysteresis is not related to the magnetic hysteresis of the composite [35]. Interestingly, the dependence of elongation actuation upon magnetic field did not follow a linear relationship. Instead, a clear threshold behavior was observed. The elongation increased slowly with magnetic field from point 0 to point I until a threshold magnetic field was reached. When this threshold field was crossed, a large and abrupt elongation occurred (from point I to point II). This behavior was observed in Magpol over a large range of filler concentrations. The threshold field as a function of filler concentration is shown in the inset of Figure 4-22(a), the threshold field values ranged from 0.5 T to 1.4 T, these field values can be achieved by permanent magnets. Figure 4-22(b) shows the elongation strain of silicone - iron Magpol as a function of filler concentration, samples with filler concentration above 5 wt% exhibited abrupt shape change. Beyond the threshold field, the post-threshold strain was also the maximum strain for filler

concentration in the range of 10 to 60 wt% of Fe. Above 60 wt% Fe, the post-threshold strain is less than the maximum strain, the sample continued to elongate after the abrupt shape change. Interestingly, the actuation strain of Magpol exceeded the maximum strain of natural skeletal muscle by 100% [12, 256].

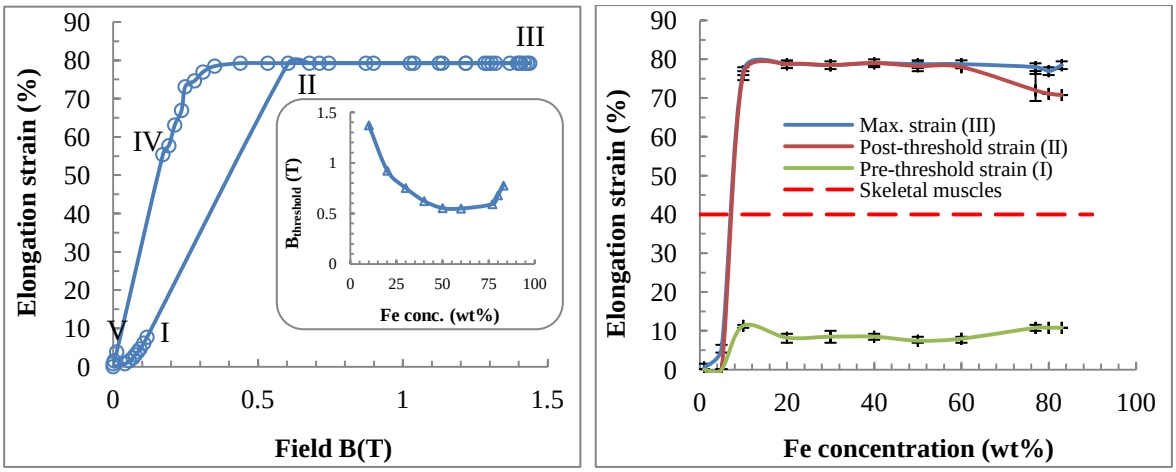


(a) (b)

Figure 4-22: (a) Elongation strain as a function of magnetic field strength of a silicone - 40 wt% Fe during elongation (I - III) and relaxation (III - V) - the inset shows the threshold field (measured at II) as a function of filler concentration; (b) Elongation strain of Magpol at the different stages described in (a) as a function of filler concentration.

As discussed in section 4.2.1, the magnetic field is mainly concentrated near the magnetic source, therefore only the part of the composite within the high field region contributes significantly to the shape deformation. Segmented samples were prepared to determine the portion of the composite which plays the most significant role in actuation. The samples had two different parts, the free end was a silicone matrix dispersed with 10 wt% iron particles while the fixed end was pure silicone. The proportion containing filler ($L_{filled}/L_{total}$) was varied in the range of 0.2 to 0.8 with a total sample length $L_{total}$ of 13 cm. The elongation v/s field curves of such samples are shown in Figure 4-23. Samples with the shortest magnetic loaded segment ($L_{filled}/L_{total}$ = 0.2) exhibited the lowest axial strain. However, the threshold field was similar to that of full samples, implying that the drastic shape change was caused only by the portion of the sample near the magnetic source. The axial

strain profile of samples with $L_{filled}/L_{total}$ = 0.8 was close to those of homogeneous samples, suggesting it is possible to reduce filler amount without significantly decreasing actuation strain. Interestingly, samples with $L_{filled}/L_{total}$ = 0.5 had a lower threshold field than those of homogeneous samples, due to the lower stiffness of the unfilled silicone region (Figure 4-14). In summary, an optimal ratio of magnetic and non-magnetic segments can be used to obtain high strain at lower magnetic fields.

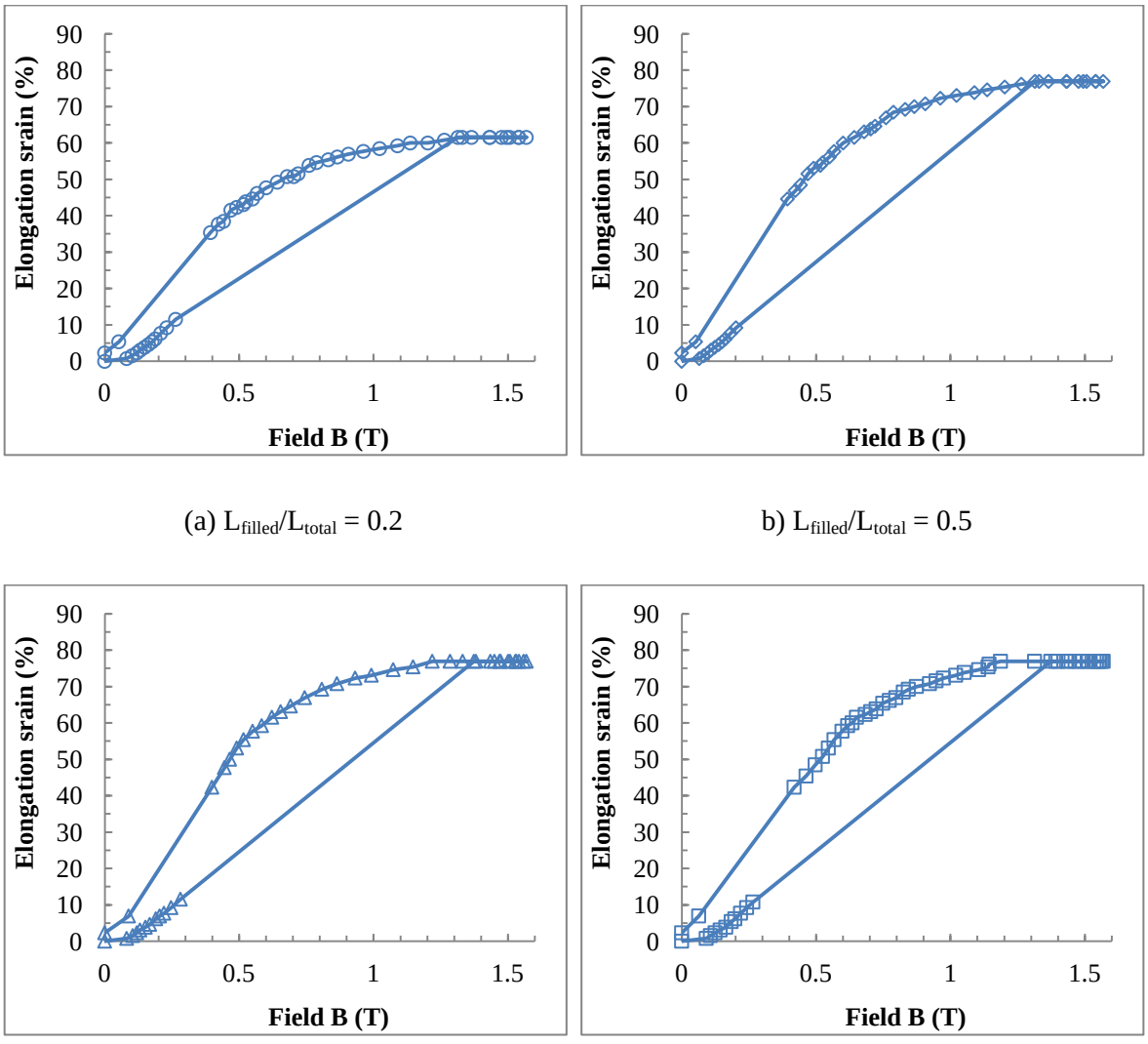


(a) $L_{filled}/L_{total}$ = 0.2

b) $L_{filled}/L_{total}$ = 0.5

c) $L_{filled}/L_{total}$ = 0.8

d) $L_{filled}/L_{total}$ = 1

Figure 4-23: Axial actuation of silicone - 10 wt% Fe composites: ((a) - (c)) segmented samples of different Fe loaded proportions; (d) homogeneous samples.

Figure 4-24(a) shows the elongation stress of silicone - 60 wt% Fe samples as a function of magnetic field strength. The elongation stress also exhibited threshold behavior, the threshold magnetic field coincided with the threshold magnetic field of elongation strain. However, unlike elongation strain, the stress continued to increase when the field increased beyond the threshold field. The elongation stress was strongly dependent on filler concentration (Figure 4-24 (b)). As filler concentration increased, the maximum, post-threshold as well as pre-threshold stress values also increased. Importantly, samples with filler concentration higher than 60 wt% exhibited maximum stresses higher than the maximum sustainable stress of natural skeletal muscles [12, 256]. The threshold field for such samples is about 0.8 T, which can be obtained by common permanent magnets (Figure 4-24(a-inset)).

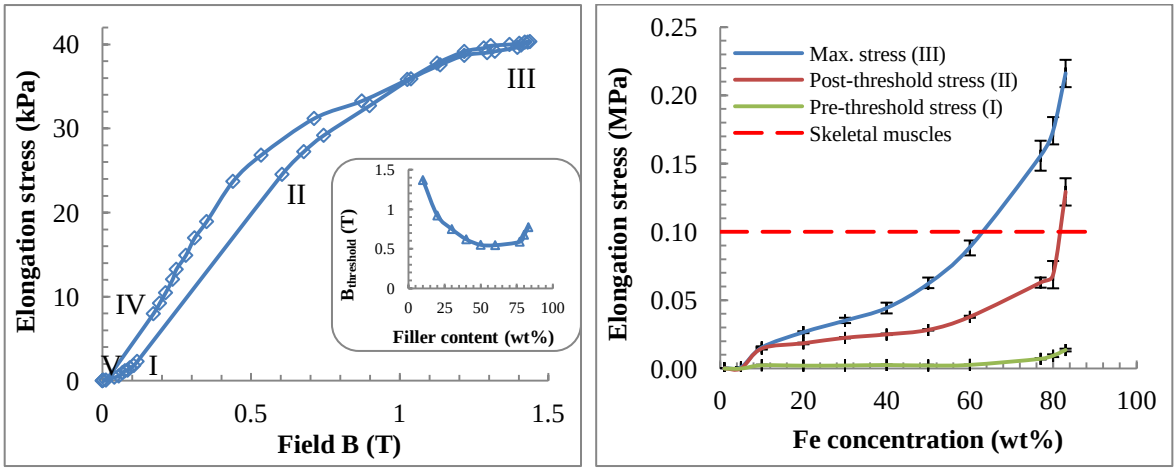


(a) (b)

Figure 4-24: Elongation stress of Magpol: (a) Actuation stress as a function of magnetic field of a silicone - 60 wt% Fe sample, the inset shows the threshold field (measured at II) as a function of filler concentration; (b) Maximum actuation stress as a function of the filler concentration.

Elongation in Magpol was found be discontinuous (Figure 4-22). Continuous elongation can also be achieved by decreasing the distance between the sample and the magnet [257]. The elongation characteristics are determined by the spatial distribution of the magnetic field. Figure 4-25 shows the experimental data of the magnetic field and its gradient generated by the electromagnet. Due to the tail cone shape of the pole pieces (plotted in same scale of the figure), the magnetic field decayed

rapidly in space and formed two regions (denoted as I and II) of high magnetic field gradient. Region I corresponded to the abrupt transition and region II to abrupt relaxation. When the free end of the sample was outside the region between I and II, i.e., $z_{free\ end} > z_{II}$, discontinuous elongation occurred. Continuous elongation was observed when the free end of the sample was within the region between I and II, i.e. $z_{II} > z_{free\ end} > z_{II}$.

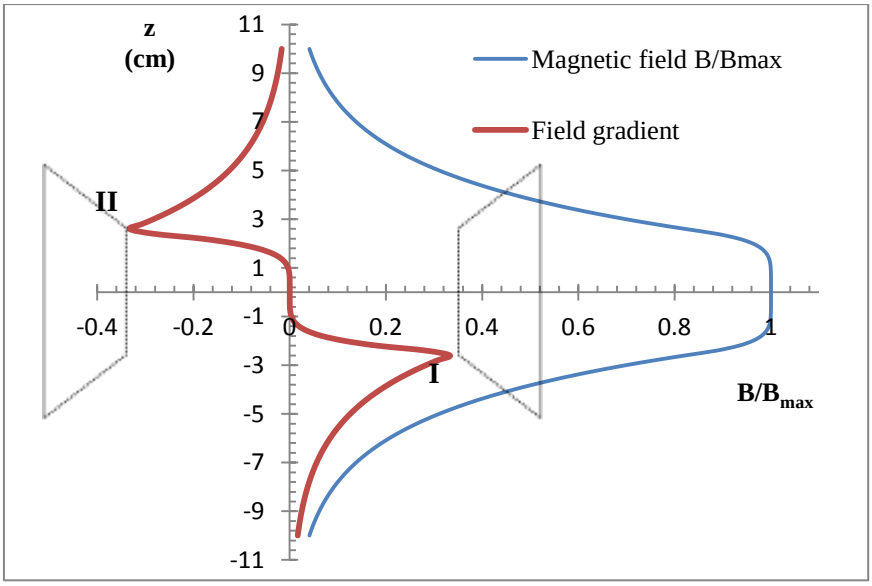


Figure 4-25: Normalized magnetic field and the field gradient of the electromagnet used. The dotted lines show the position of the magnet poles. I and II are regions of high magnetic field gradient.

Due to this spatial distribution of the magnetic field, only the parts of the sample within the high magnetic field region are subjected to significant magnetic force. This observation can be used to tune the threshold field value and thus optimize Magpol's actuation using segmented samples (Figure 4-23) [54].

The continuous increase of actuation stress with magnetic field is also the result of the magnetic field distribution. As the magnetic field was increased, the part of the sample above the electromagnet poles continued to be attracted to the high magnetic field gradient region (position II in Figure 4-25) while the free end is "locked" at the lower edges of the magnet poles (position I in Figure 4-25). The increasing slope of the actuation stress with magnetic field is due to the magnetoelastic effect, the elastic modulus of Magpol increases with increasing applied field. The

actuation forces produced in elongation, contraction and coiling are the result of the stresses in the composite, which is proportional to the elastic modulus of the composite.

### *4.2.3 Contraction*

Magpol samples can be placed in contraction mode by positioning the free end below the magnet pole pieces. Figure 4-26(a) shows the contraction strain as a function of field strength for silicone - 60 wt% Fe samples. Hysteresis was observed, similar to the case of elongation. However, gradual contraction was observed instead of an abrupt shape change. Figure 4-26(b) shows the dependence of maximum contraction strain on magnetic filler concentration. Contraction strain was small for samples with low magnetic filler concentration (below 5 wt% of Fe). Maximum strain increased when filler concentration increased from 5 wt% to 20 wt%, it reached a maximum when filler concentration was in the range of 40 wt% to 60 wt%. The maximum strain decreased when filler concentration was more than 60 wt% due to increased sample stiffness (Figure 4-14). In contraction mode, the maximum strain achieved was 40%, equivalent to that of skeletal muscles. A demonstration model of Magpol as a artificial bicep muscle is shown in Figure 4-27. This "bicep" can contract and relax repeatedly, creating a motion similar to that of a human arm.

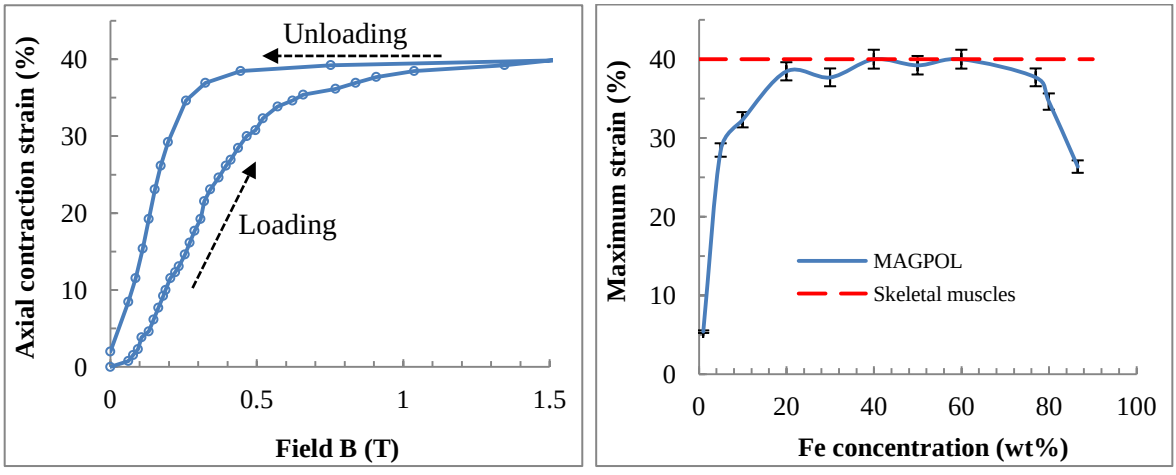


(a) (b)

Figure 4-26: (a) The contraction strain as a function of magnetic field for silicone - 60 wt% Fe samples, (b) Maximum contraction strain as a function of the filler concentration.

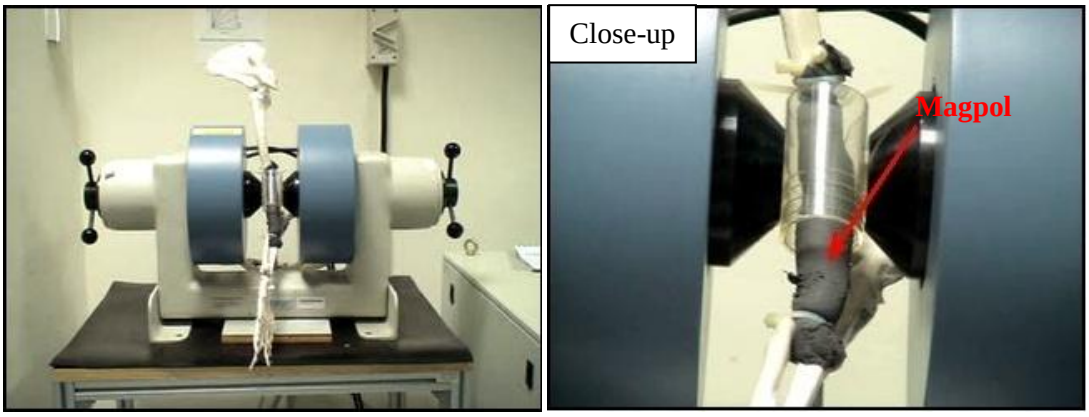


(a) When Magpol bicep relaxes

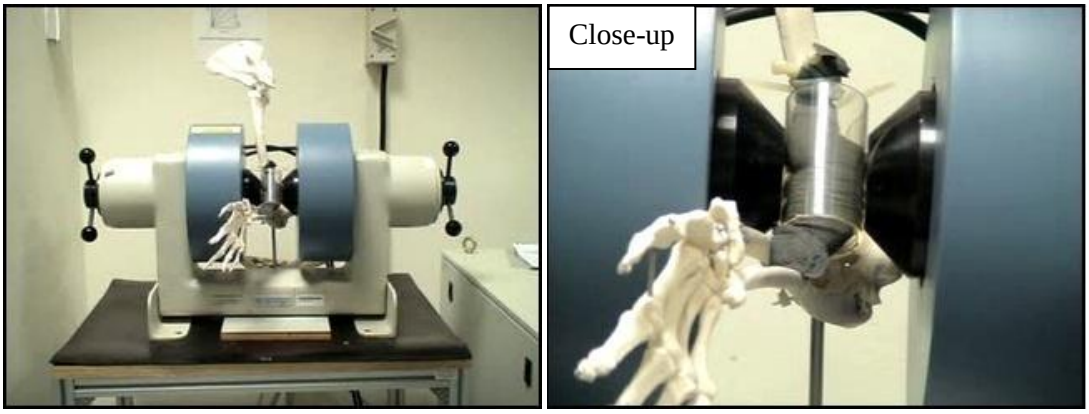


(b) When the Magpol bicep contracts

Figure 4-27: Model of an artificial bicep muscle based on Magpol (indicated by the arrow).

The contraction stress produced by Magpol with 60 wt% and 83 wt% filler concentration are represented by surface and contour graphs ( Figure 4-28). The relationship of contraction stress with the contraction length ($\Delta L$) and the sample length $L/L_{max}$ was studied; for a given sample length, contraction stress decreased as contraction length increased. This is similar to the length - tension behavior found in natural muscles (section 2.3.1.2) [258]. Furthermore, the maximum value of contraction stress (164 kPa) was obtained for a sample length $L/L_{max}$ of 0.7 (Figure 4-28(b)), suggesting that for a given magnetic field distribution and filler concentration, there is an optimal sample length which results in highest stress.

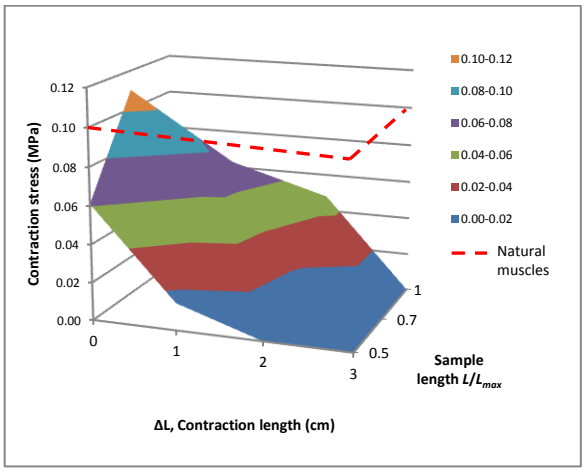


(a) Silicone - 60 wt% Fe - surface graph

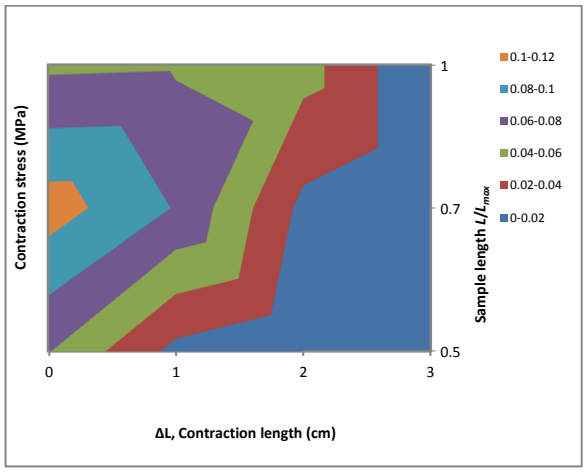


(b) Silicone - 60 wt% Fe - contour graph

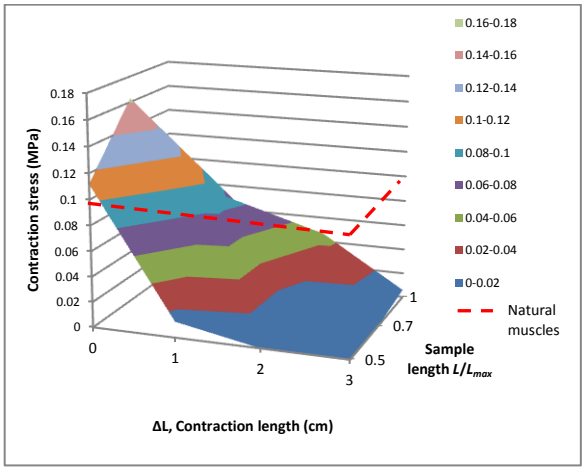


(c) Silicone - 83 wt% Fe - surface graph

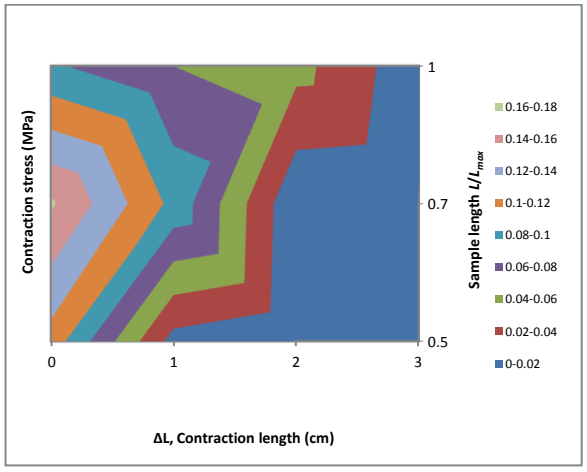


(d) Silicone - 83 wt% Fe - contour graph

Figure 4-28: Isometric contraction stress as a function of contraction length and sample length of (a) Silicone - 60 wt% Fe samples represented by a surface graph, in comparison with skeletal muscle stress, (b) Silicone - 60 wt% Fe samples represented by a contour graph, (c) Silicone - 83 wt% Fe samples represented by a surface graph, in comparison with skeletal muscle stress, (d) Silicone - 83 wt% Fe samples represented by a contour graph.

### *4.2.4 Coiling*

In the experimental setup, a cylindrical glass tube was used to constrain radial deformation and prevent samples from sticking to the magnet poles. Interestingly, different shape change modes were observed by using tubes of different diameters ($d_{tube}$). Magpol samples exhibited axial contraction when a tube of diameter to sample diameter ratio $k = d_{tube}/d_{sample}$ equal to 1.2, (Figure 1-4 (b)). When

a larger tube of $k$ = 1.6 was used, a novel coiling mode was observed (Figure 1-4 (c)). Under the influence of an external magnetic field, the entire sample coiled and conformed to the space within the glass tube. When $k$ = 1.4, a hybrid mode, i.e., a combination of both coiling and axial contraction, was observed (Figure 1-4 (d)),. Figure 4-29 shows the change of maximum contraction strain with tube diameter for various filler concentrations, contraction strains increased with increasing tube diameter.

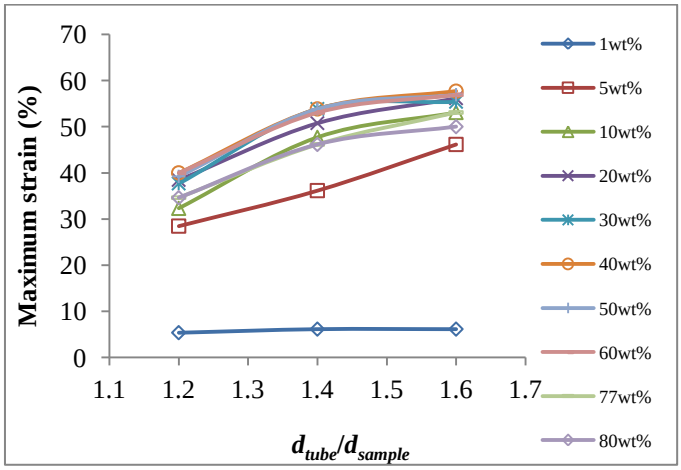


Figure 4-29: The maximum contraction strain as a function of the diameter of the cylindrical guide.

The different stages of the coiling mechanism are shown in Figure 4-30. The first stage involved a small sample contraction caused by a weak magnetic field (Figure 4-30(a)). When a critical magnetic field was crossed, the samples buckled (Figure 4-30(d)), a further increase of the magnetic field resulted in a helical shape in order to conform to the large diameter of the tube (Figure 4-30(g) - (h)).

The initiation of coiling was examined by magneto-structural modeling. The results (Figure 4-30(b),(c),(e),and (f)) revealed that coiling of Magpol was initiated by local buckling in the region between the electromagnet poles. Within this space, the magnetic field gradient was highest and therefore the magnetic force acting on Magpol samples was greatest. The large compressive force caused the flexible composite structure to buckle.

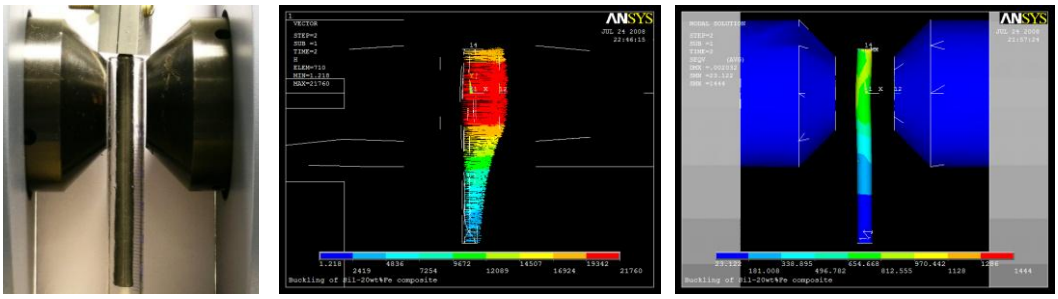

(a) B = 0.11 T (b) Magnetic field intensity (A/m) (c) Stress (Pa)

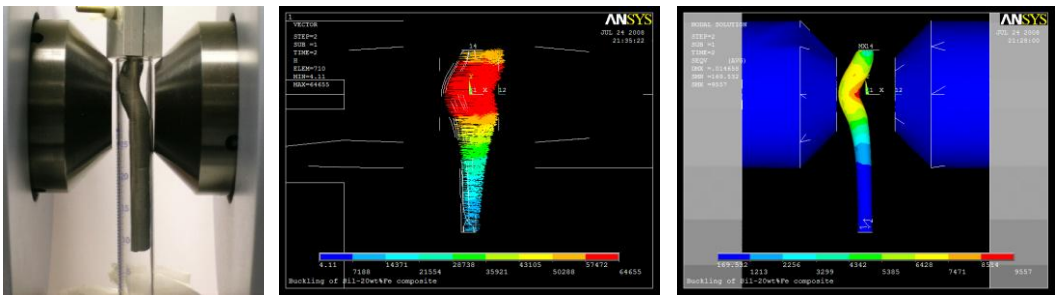

(d) B = 0.216 T (e) Magnetic field intensity (A/m) (f) Stress (Pa)

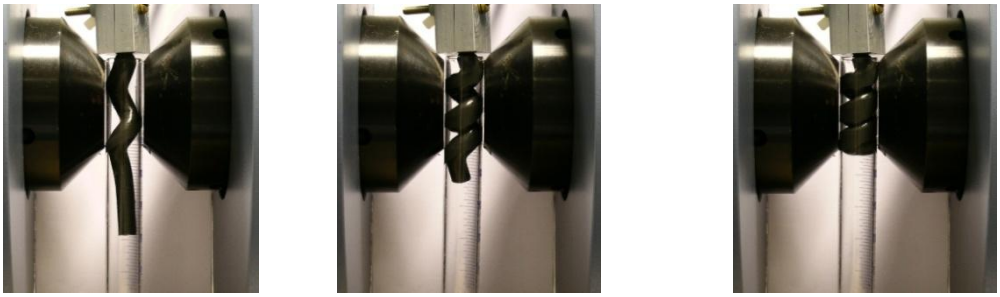

(g) B = 0.324 T (h) B = 0.433 T (i) B = 1 T

Figure 4-30: The coiling behavior of silicone - 20 wt% Fe samples at different stages as observed by experiment and simulation: (a) B = 0.11T, the sample remained straight, stress builds up in the sample; (b) and (c) Magnetic field density plot and stress distribution plot obtained from FEM simulation when B = 0.11 T; (d) B = 0.216T, the sample started to bulge ; (e) and (f) Magnetic field density plot and stress distribution plot obtained from FEM simulation when B = 0.216 T; (g) B = 0.324 T and (h) B=0.433 T, The sample coiled due to the cylindrical spatial constraint; (i) B = 1 T, The coiling configuration reached its limit.

The coiling strain v/s magnetic field for silicone - 60 wt% Fe samples is plotted in Figure 4-31(a). The graph is smooth and can characterized by three different stages. During the first stage, the sample length decreased slightly, the second stage represented sample coiling and was initiated by buckling, which led to coiling in the region between the electromagnet pole pieces. The initial coil then propagated towards the free end of the sample as the magnetic field was increased. The last stage involved reduction in coil height due to the attraction to the region of high magnetic field gradient (i.e., the region between the poles), this process is similar to the compression of a spring. This process continued until each ring of the coil physically touched each other. Among the three stages of coiling process of Magpol, the second stage is most important as it contributes more than 2/3 of the overall actuation strain. This stage can be achieved by a magnetic field strength of about 0.5 Tesla, which can be easily obtained from common permanent magnets.

As the magnetic field was decreased, the coil structure relaxed and eventually uncoiled to return to the original straight shape. The entire actuation cycle exhibited hysteresis, i.e., the shortening and relaxing strain values were not equal at the same field strength, similar to the case of contraction. The magnetic field required to attain a given strain value was lower for coiling compared to contraction. The maximum coiling strain for various filler concentrations is shown in Figure 4-31(b). For most filler concentrations, coiling strain was higher than contraction strain by ~ 50% and was also higher than the maximum strain of natural muscles.

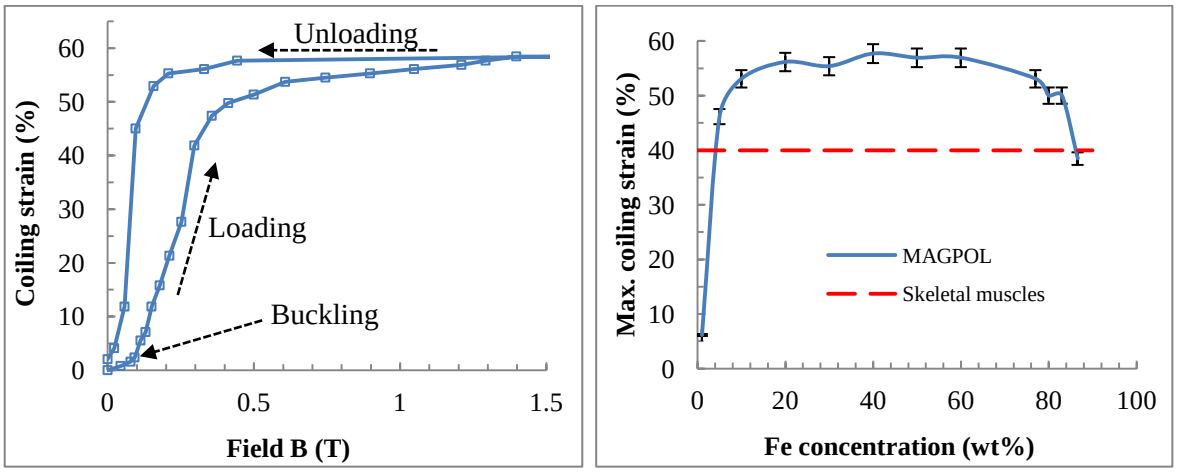


(a) (b)

Figure 4-31: The coiling mode of Magpol: (a) Coiling strain curve as a function of magnetic field; (b) Maximum coiling strain as a function of the filler concentration.

The relationship between coiling stress and the coiling length ($\Delta L$) and sample length $L/L_{max}$ was studied, the results (Figure 4-32) revealed that the relationship of coiling stress with coiling length and sample length exhibited similar trends to those of contraction stress. Coiling stress showed a similar peak-like relationship with initial sample length, similar to the behavior observed for contraction stress. However, coiling stress is 10 - 15% higher than the corresponding contraction stress for all cases. The highest maximum coiling stress (184 kPa) was also obtained for a sample length $L/L_{max}$ of 0.7. It is worth mentioning that the coiling stress is also higher than the maximum stress of skeletal muscles [12]. This considerable improvement in actuation performance facilitates a wider range of applications for Magpol actuators.

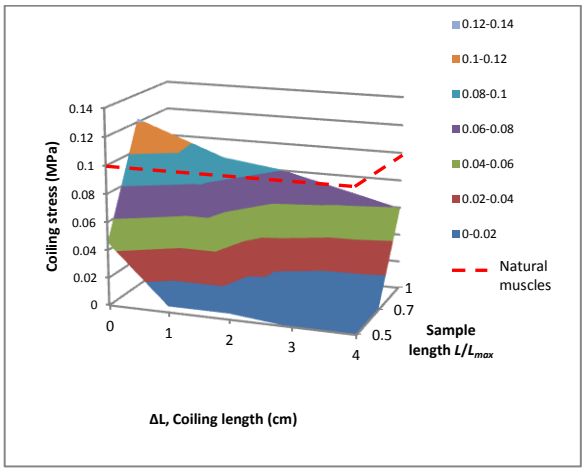


(a) Silicone - 60 wt% Fe, surface graph

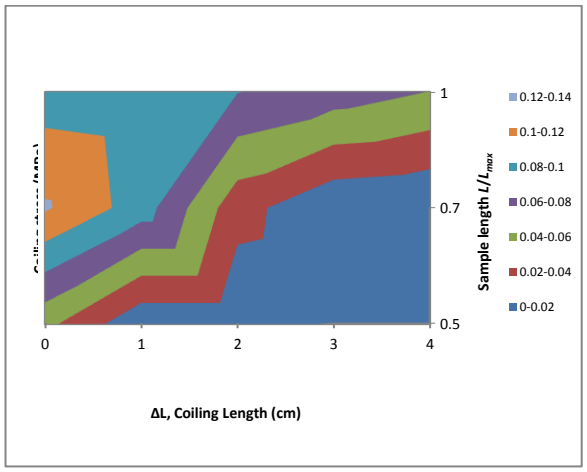


(b) Silicone - 60 wt% Fe, contour graph

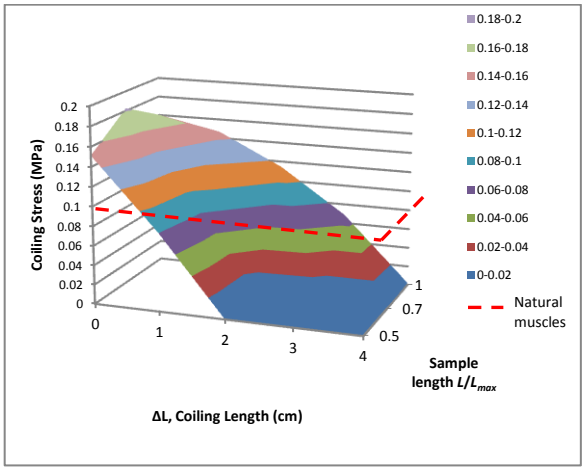


(c) Silicone - 83 wt% Fe, surface graph

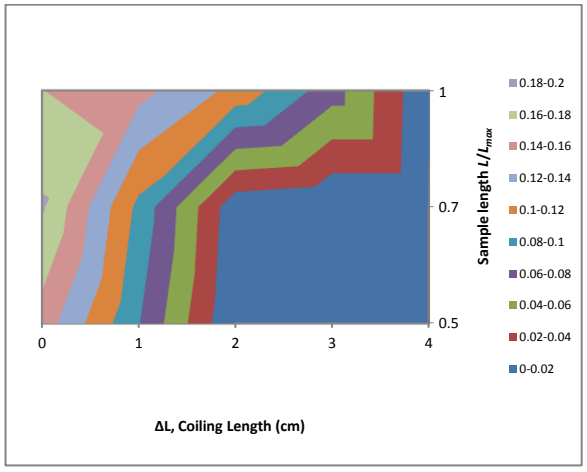


(d) Silicone - 83 wt% Fe, contour graph

Figure 4-32: Isometric coiling stress as a function of contraction length and sample length of (a) Silicone - 60 wt% Fe samples represented by a surface graph, in comparison with skeletal muscle stress, (b) Silicone - 60 wt% Fe samples represented by a contour graph (c) Silicone - 83 wt% Fe samples represented by a surface graph, in comparison with skeletal muscle stress, (d) Silicone - 83 wt% Fe samples represented by a contour graph.

#### 4.2.4.1 Analysis of Coiling Behavior of Magpol

As described in the previous section, increasing magnetic field led to sample contraction, buckling followed by coiling. It has been shown previously that increasing compressive force acting on a rod like object in a cylindrically constrained region after buckling results in a helical shape [259]. Due to Magpol's highly flexible structure and ability to produce strong magnetic force, coiling is the natural

contraction mechanism. However, if the diameter of the cylindrical constraint is small, only axial contraction was observed instead of coiling due to the lack of radial displacement. As a result, two criteria must be fulfilled for coiling to take place. The first is that buckling has to occur, the second is that the size of the cylindrical constraint must be in a suitable range.

The magnetic buckling of Magpol can be understood by first considering the total load acting on the samples, this load is related to the magnetic force and the sample weight (Figure 3-4):

$$\boldsymbol{P} = \boldsymbol{F}_{magnetic} - \boldsymbol{W}_{weight} \qquad \text{(Equation 4-2)}$$

where $F_{magnetic}$ is the magnetic force exerting on Magpol sample. According to section 2.5.2, and $F_{magnetic}$ can be calculated by the following equation [68]:

$$F_{magnetic} = \int_V M.\nabla B.dV = \int_{z_{bottom}}^{z_{top}} M.\frac{\delta B}{\delta z}.adz = \int_{B_{bottom}}^{B_{top}} a.M(B).dB \qquad \text{(Equation 4-3)}$$

where $a$ is the cross-sectional area. $W_{weight}$ is the sample weight and can be expressed as:

$$W_{weight} = \int g.dm = \int_V \rho.dV.g = \int_{z_{bottom}}^{z_{top}} \rho.g.adz \qquad \text{(Equation 4-4)}$$

As buckling takes place at small strain, the sample cross-sectional area can be assumed constant. Therefore, the total load can be computed as:

$$P = a.\int_{B_{bottom}}^{B_{top}} M(B).dB - a.\int_{z_{bottom}}^{z_{top}} \rho.g.dz \qquad \text{(Equation 4-5)}$$

The *M(B)* function can be acquired by fitting the experimental magnetization curves (section 4.1.3) with sixth order polynomial functions and thus the magnetic force can be calculated from Equation 4-3. The magnetic field $B_{bottom}$ (at $z_{bottom}$) and $B_{top}$ (at $z_{top}$) were experimentally measured and hence the load $P$ can be computed.

Euler's formula, which states that buckling of a long sample takes place when the load acting on it exceeds a critical value $P_{cr}$, which can be calculated by [260]:

$$P_{cr} = \frac{\pi^2 EI}{(KL)^2} \qquad \text{(Equation 4-6)}$$

where $E$ is the Young's modulus of the composite, $I$ is the area moment of inertia of the sample, $L$ is the unsupported length of the sample and $K$ is the effective length factor.

Since the samples had one end fixed and was loosely constrained in a cylindrical tube, there are two relevant cases for buckling analysis. The first case is fixed and free end model ($K$ = 2) and the second is fixed and pinned end model ($K \approx 0.7$)

From Equation 4-2 and Equation 4-6, it can be seen that buckling occurs when $F_{magnetic} > (W_{weight} + P_{cr})$. Based on this, $P_{cr}$ can be computed and $B_{cr}$ can be estimated. Figure 4-33 shows that $B_{cr}$ of silicone - 20 wt% Fe samples should lie in the 0.2 - 0.23 T range, in good agreement well with the experimental $B_{cr}$ value of 0.223 T.

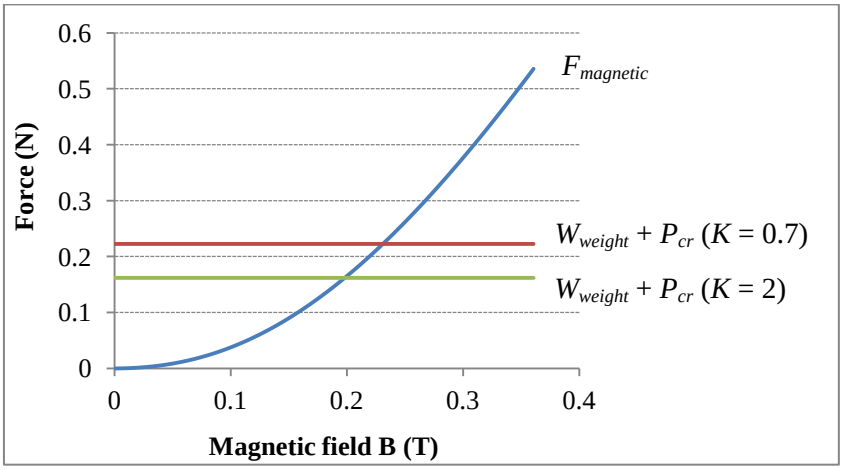


Figure 4-33: Use of the model to predict the buckling magnetic field for silicone - 20 wt% Fe samples, $B_{cr}$ = 0.223 T.

The experimental load $P$ acting on the samples can be calculated from Equation 4-5 using the experimental sample density and buckling magnetic field values. This load was compared to the theoretical critical load values for the following two scenarios of buckling: (a) full sample buckling (i.e., the effective buckling length is equal to the sample length) and (b) local buckling near the magnet pole region (i.e., the effective buckling length is equal to magnet pole diameter) (Figure 4-34). It can be seen that buckling should occur in the second case because the experimental load

values lie in the range limited by the predicted load curves. This was in agreement with experimental observations and supported by the magneto-structural simulation.

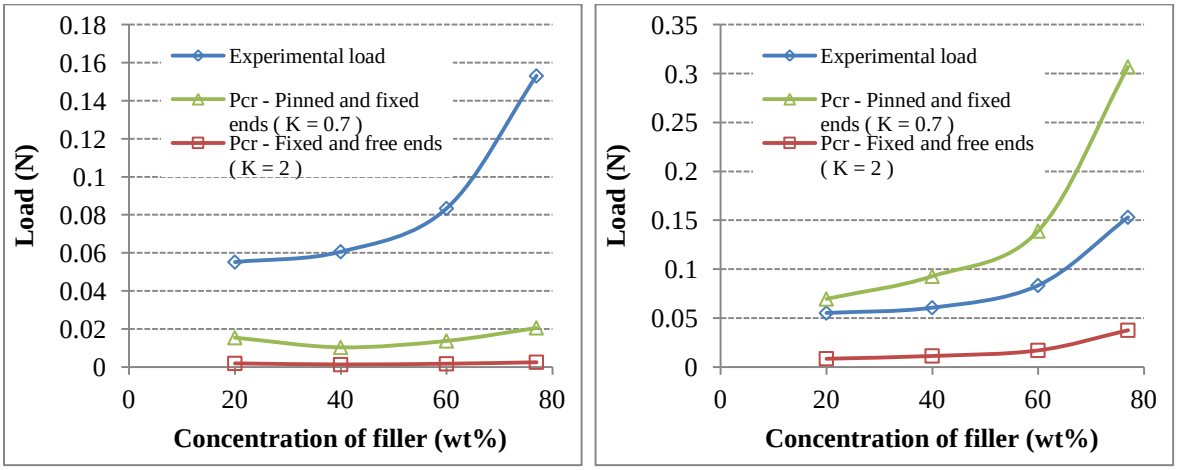


(a) (b)

Figure 4-34: Load as a function of filler concentration for different effective buckling lengths of Magpol samples: (a) Effective length = sample length (L = 13cm) (b) Effective length = magnet pole diameter (L = 5cm)

#### 4.2.4.2 Comparison of Buckling in Magpol with Other Magnetoelastic Buckling Phenomena

The post-buckling shape of Magpol (Figure 4-30(d)) is similar to kink instabilities observed in flexible current carrying conductors under self-generated magnetic fields [261] or the instability of a long current carrying wire in a longitudinal magnetic field [262, 263]. The overall coiling shape (Figure 4-30(h)) is also identical to the post-buckling shape of a ferromagnetic whisker under compressive force caused by a longitudinal magnetic field [263, 264].

The continuous coiling strain profile (Figure 4-31(a)) suggests that Magpol exhibits a stable post-buckling behavior, which can be characterized by a stable symmetric bifurcation [125]. This behavior is similar to the buckling of column structures. However, many other magneto-elastic buckling phenomena are unstable, i.e., can be characterized by a limit point beyond which an abrupt change in shape or a "snapping" action takes place [254, 265]. The continuous coiling process of Magpol is suitable for actuator applications. Another advantage of symmetric bifurcation is that the resulting actuation is relatively insensitive to misalignments or material inhomogeneities [254].

### 4.3 Work

The ability of Magpol to perform work was studied using the work loop method employed in artificial muscles studies [116, 266]. Figure 4-35 shows the typical work loop of Magpol in contraction and coiling actuation for silicone - 50 wt% Fe samples, the area of the loop yields the work produced. Table 4-2 presents the values of work and work density (work per unit mass) of silicone - 50 wt% Fe samples of various sample lengths. As in the cases of contraction and coiling stress, there is an optimal sample length at which the highest work density value was obtained. For contraction, the optimal sample length is $L/L_{max}$ = 0.7; the optimal sample length for coiling was 0.8 due to the larger sample length required to form the coil.

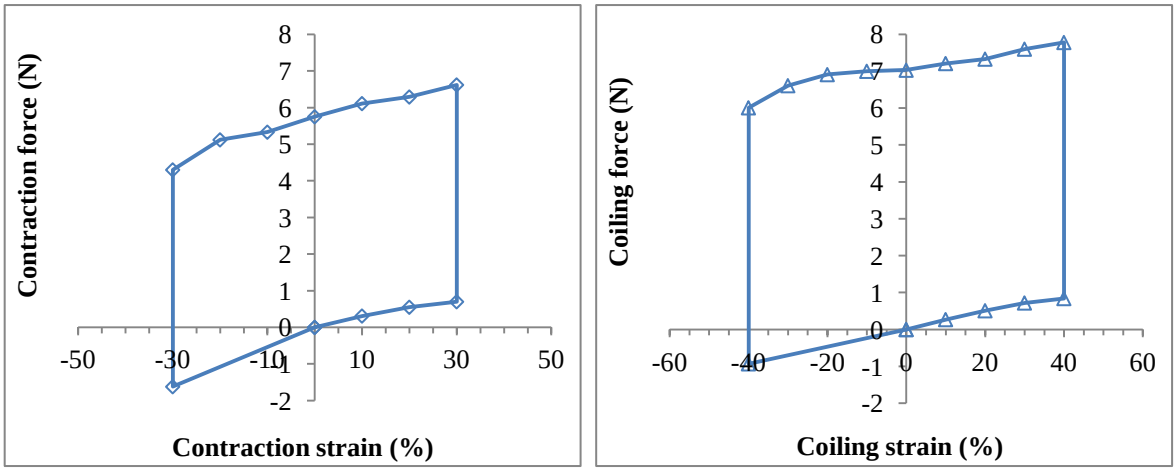


(a) Contraction (b) Coiling

Figure 4-35: Work loops of silicone - 50 wt% Fe samples with length $L/L_{max}$ = 0.8 in (a) contraction and (b) coiling modes

Table 4-2: Work and work density of silicone - 50 wt% Fe for various sample lengths.

| Sample length $L/L_{max}$ | Contraction | | Coiling | |
|---|---|---|---|---|
| | Work (J) | Work density (J/kg) | Work (J) | Work density (J/kg) |
| 1 | 0.27 | 11.60 | 0.52 | 22.60 |
| 0.8 | 0.35 | 19.70 | 0.56 | 31.42 |
| 0.7 | 0.36 | 23.65 | 0.41 | 27.12 |
| 0.5 | 0.24 | 19.44 | 0.29 | 23.45 |

Figure 4-36 shows work density values of silicone - iron Magpol for various filler concentrations in contraction and coiling modes, the work density values increased with filler concentration, Magpol can exceed the work density value of skeletal muscles for filler concentration greater than 70 wt% [267].

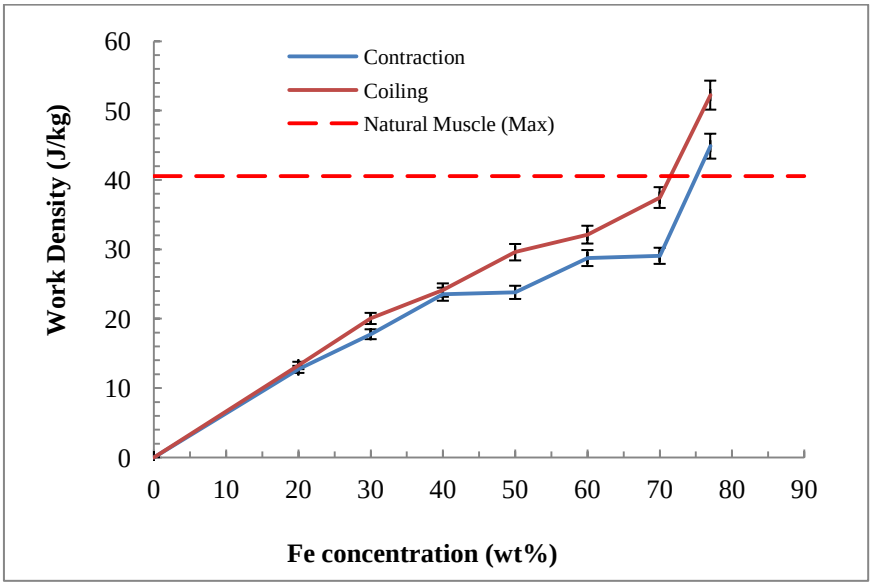


Figure 4-36: Work density of Magpol with various filler concentration produced in contraction and coiling mode.

## 4.4 Dynamic Properties

Figure 4-37(a) shows the axial elongation strain as a function of modulated magnetic field of silicone - 60 wt% Fe Magpol samples using the experimental setup described in section 3.3.4. Similar strain profiles to those described in section 4.2.2 was observed. The path traced by points along 0 - I - II - III represents the sample elongation as the magnetic field (measured at the midpoint between the pole centers) was increased. The path traced by points along III - IV - V indicates the relaxation as the magnetic field was decreased to zero. Clear threshold behavior was observed during elongation and relaxation of samples. Both ON and OFF threshold magnetic field values for Magpol with varying filler concentration are plotted in Figure 4-37(b).

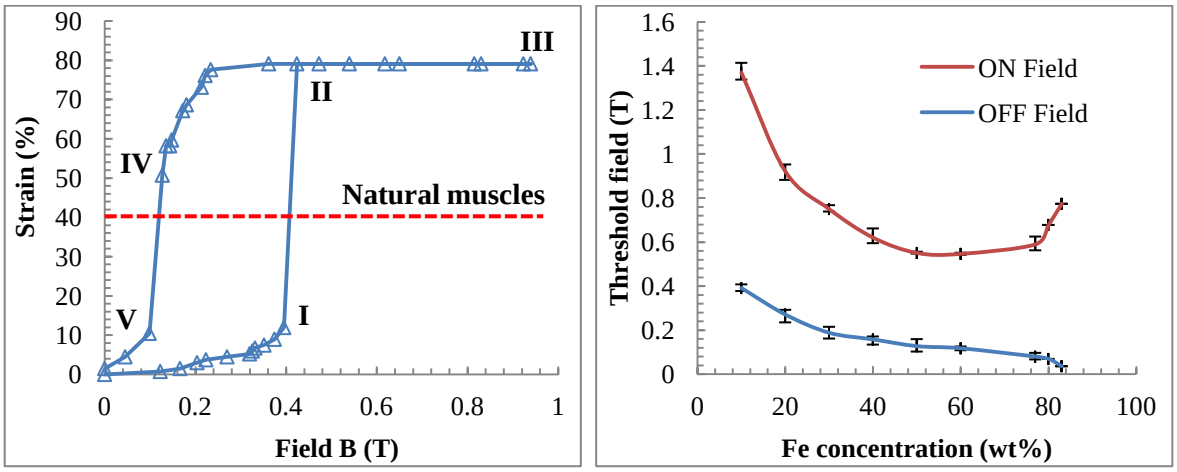


Figure 4-37: (a) Elongation strain as a function of magnetic field strength of a silicone - 60 wt% Fe during elongation (0 - III) and relaxation (III - V), (b) The threshold fields at different Fe concentrations.

Generally, the maximum strain values of actuators decrease with increasing actuation frequency [24]. The frequency dependence of actuation strain of silicone - 60 wt% Fe samples is shown in Figure 4-38. Below 1 Hz, 80% strain was achieved, similar to the maximum static strain described in Figure 4-37. Above 1 Hz, the strain decreased sharply to 1% at 80 Hz, the highest frequency for detectable shape change. The strain - time profile was consistent for all cases. The bandwidth for Magpol actuation, defined as the frequency at which the actuation strain value is reduced to half, was approximately 4 Hz.

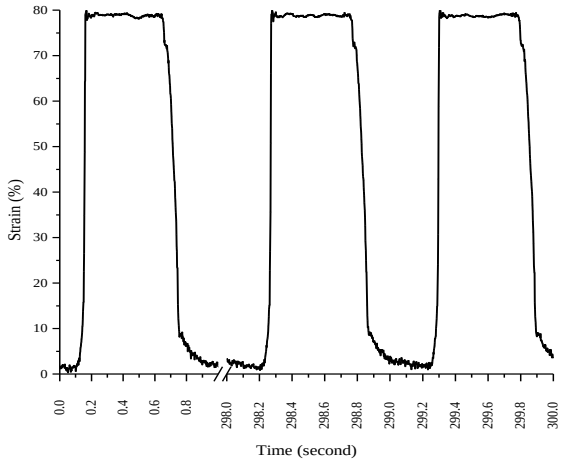


(a) 1 Hz

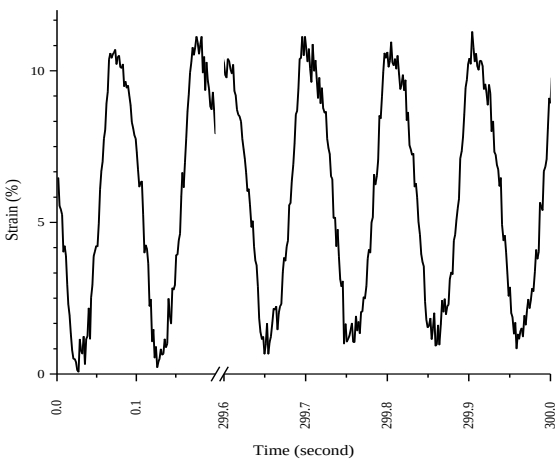


(d) 10 Hz

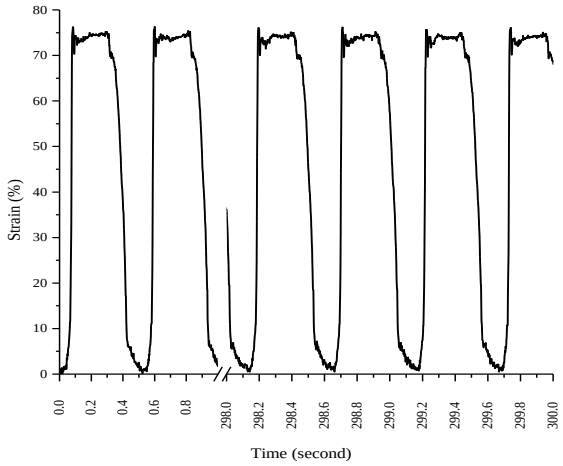


(b) 2 Hz

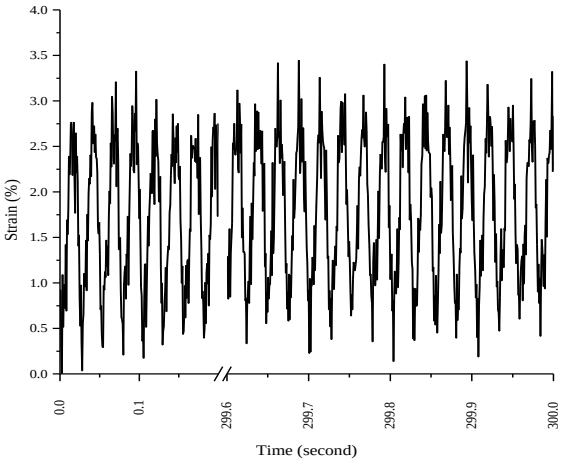


(e) 40 Hz

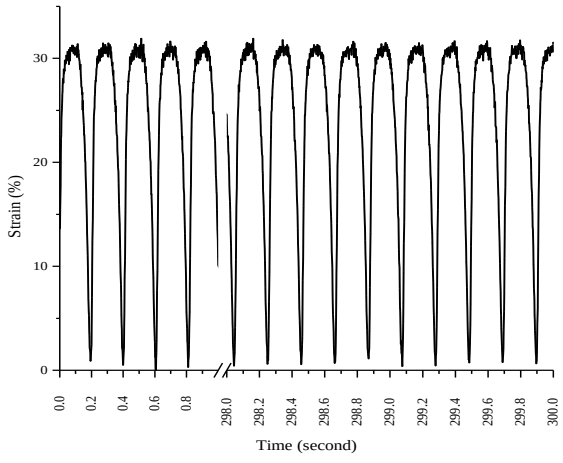


(c) 5 Hz

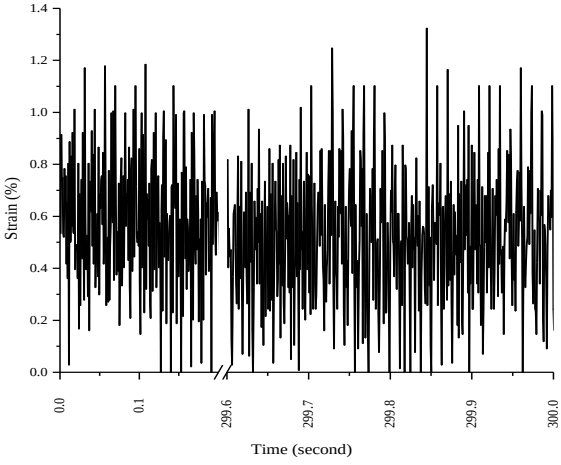


(f) 80 Hz

Figure 4-38: Elongation strain of silicone - 60 wt% Fe samples as function of time at different actuation frequencies.

The dynamic properties of Magpol varied with filler concentrations. For lower filler concentration, actuation strain decreased faster with increasing frequency. When the filler concentration is 10 wt% or less, the samples did not exhibit abrupt shape change and exhibited low strain values even at 1 Hz (Figure 4-39). Samples with filler concentration in the 40 wt% - 60 wt% range showed similar characteristics (Figure 4-38). For concentrations higher than 60 wt%, at frequencies greater than 5 Hz, samples elongated but did not relax as the magnetic field was reduced.

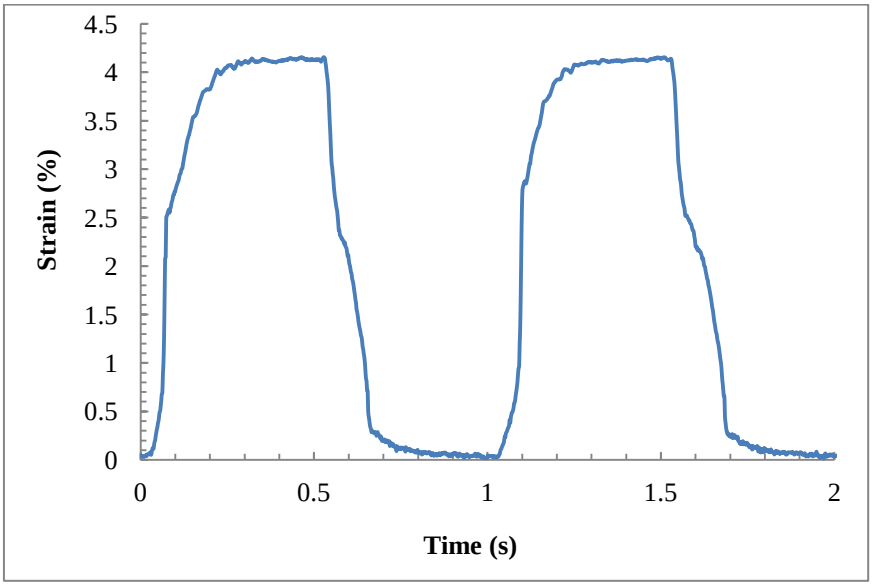


Figure 4-39: Continuous actuation of silicone - 10 wt% Fe samples at 1 Hz

For different frequencies, the plots of magnetic field v/s time are shown in Figure 4-40, the magnitude of the magnetic field decays with increasing frequency due to the strong inductive effect of the magnetic coils.

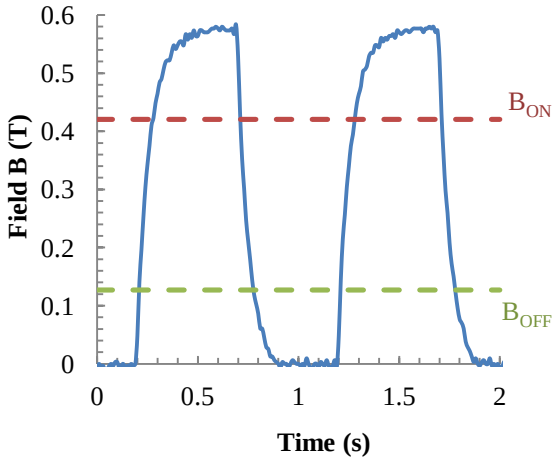


(a) 1 Hz

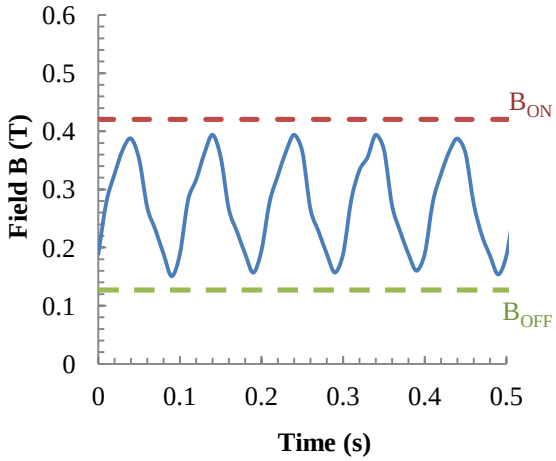


(d) 10 Hz

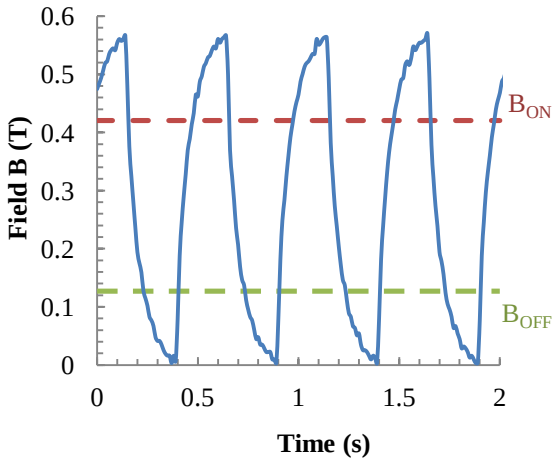


(b) 2 Hz

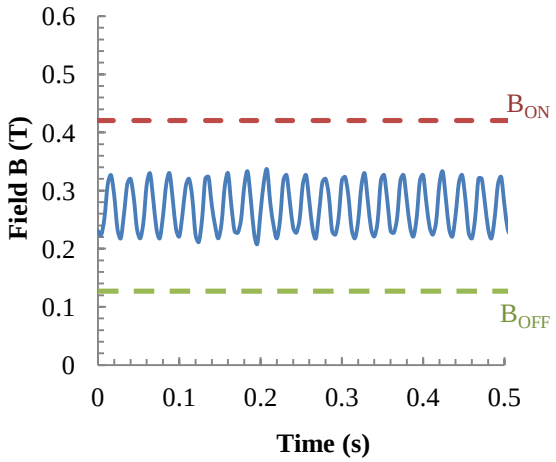


(e) 40 Hz

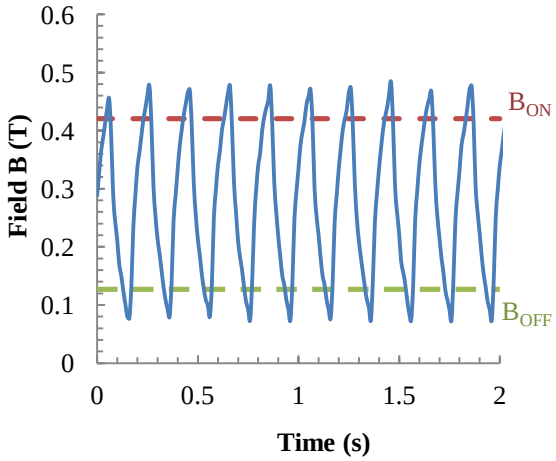


(c) 5 Hz

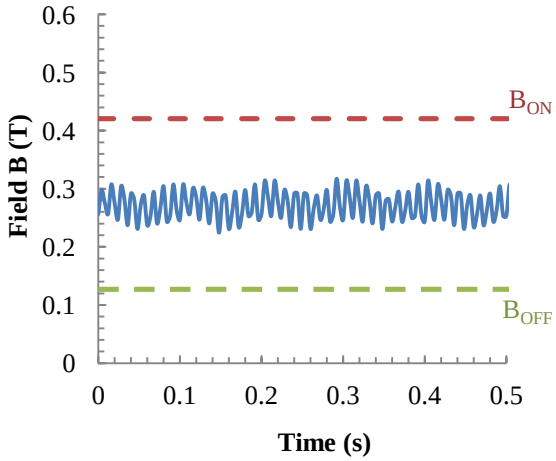


(f) 80 Hz

Figure 4-40: The variation of magnetic field with time for varying frequency, with reference to the ON and OFF threshold magnetic field values of silicone - 60 wt% Fe samples.

The decrease in maximum strain with increasing frequency is commonly found in actuator systems [24]. The frequency dependence of maximum strain of Magpol, especially at low frequencies, is mainly due to slow relaxation kinetics (Figure 4-38(a - c)). Below 5 Hz, relaxation took ~ 4 times longer than actuation due to inertia, the visco-elastic characteristics of the polymer and the slow rate of reduction of magnetic field generated by the electromagnet.

To study the relative contribution of these factors, the dynamic strain characteristics were modeled by relating the magnetic field (Figure 4-40) to the static strain - field profile (Figure 4-37). The modeled dynamic strain is shown in Figure 4-41. The model assumed time-independent elastic properties of composite since the static strain - field relationship was measured after each stable strain state was established. This model also incorporated the time dependence of the magnetic field due to the inductive effect. As discussed in section 4.2.2, large elongation is induced when the magnetic field strength is higher than the ON threshold field, and large relaxation takes place when the magnetic field strength is lower than the OFF threshold field. At frequencies below 5 Hz, the magnetic field crossed both the ON threshold and OFF threshold fields, resulting in large elongation and relaxation. The maximum strain in this case was independent of frequency. When the frequency is higher than 5 Hz, the magnitude of the magnetic field did not reach the threshold field values, hence the strains were in the continuous region (i.e., region 0 - I in Figure 4-37a)) and decreased with increasing frequency.

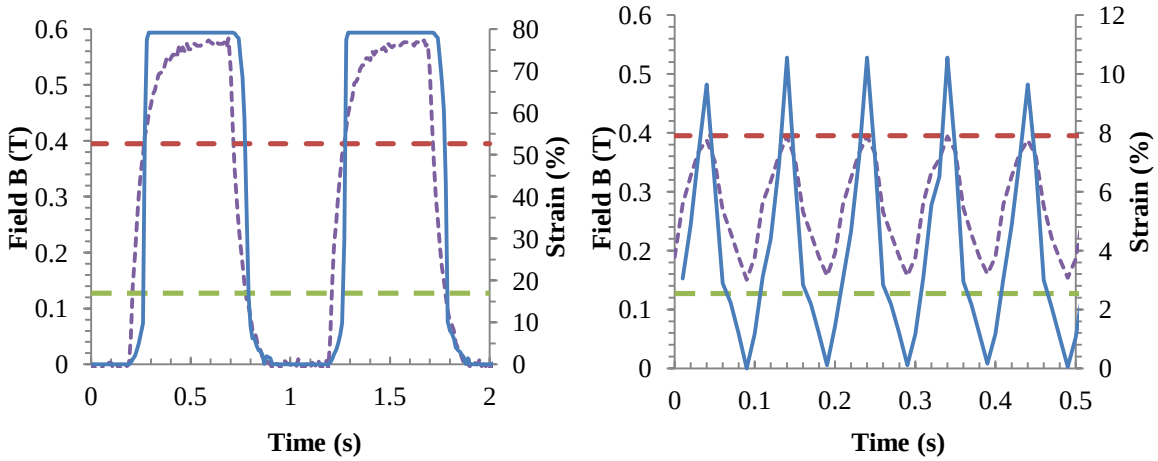


(a) 1 Hz




(d) 10 Hz

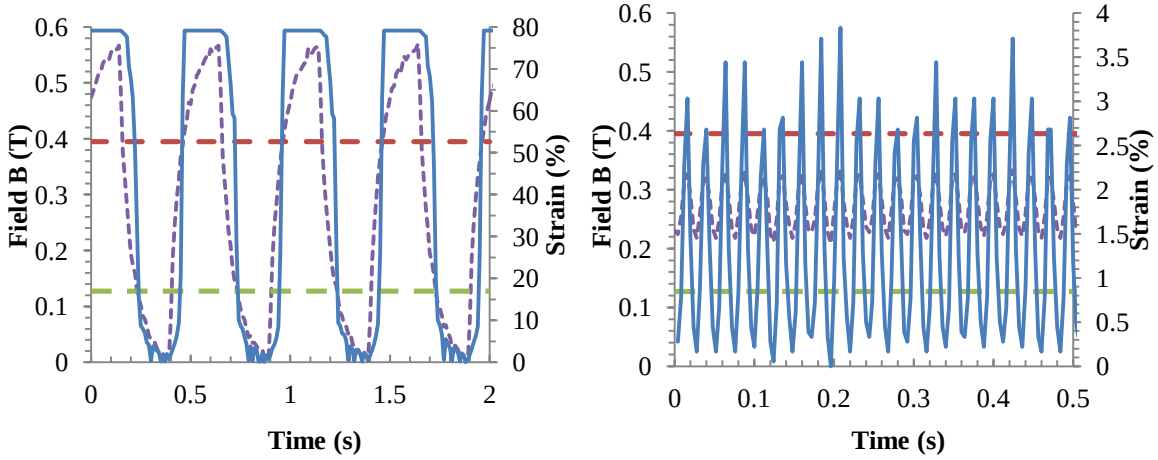


(b) 2 Hz




(e) 40 Hz

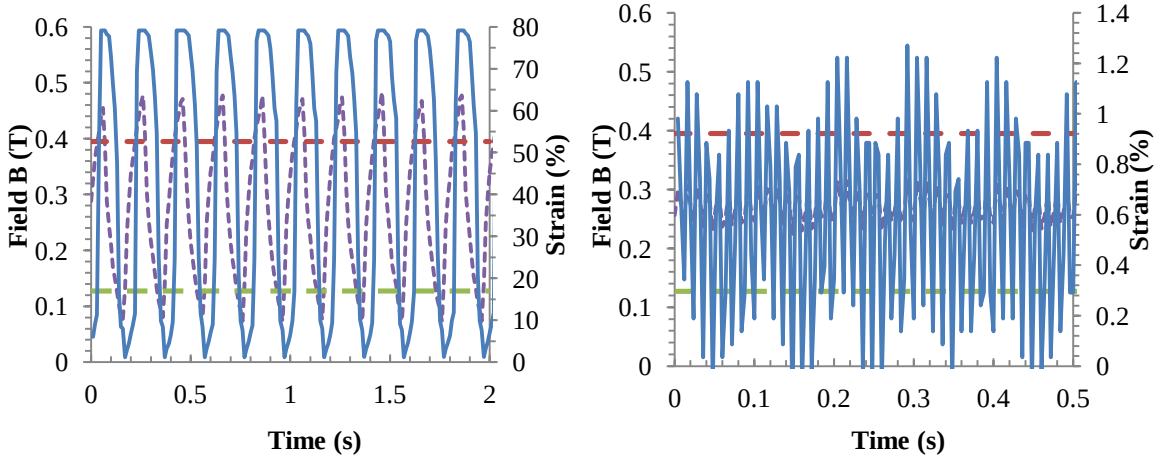


(c) 5 Hz




(f) 80 Hz

Figure 4-41: Modeled strain (solid curves) of silicone - 60 wt% Fe samples based on the magnetic field (dotted curves) and the static strain - field relationship. The dotted lines represent the ON and OFF thresholds.

Comparison of the experimental strain values (Figure 4-38) with the predicted strain values (Figure 4-41) shows that the samples exhibit time independent elastic properties for frequencies less than 1 Hz. The experimental strain values decreased with increasing frequency up to 5 Hz while the predicted strain values remained the same. In the range of 10 Hz to 80 Hz, i.e. when the samples actuated in the continuous regime, the experimental and predicted strains were again similar. Thus, continuous actuation is relatively insensitive to time dependent mechanical properties whereas discontinuous actuation is time dependent.

In the continuous regime, Magpol behaved like a Hookean material, hence the rate of change of the magnetic field was the limiting factor in dynamic actuation, this was valid for driving frequencies up to 80 Hz (the maximum frequency studied in this work). In the discontinuous regime, the actuation behavior shows the effect of visco - elastic behavior on dynamic actuation. The effect of magnetic field is more pronounced because of slow relaxation processes, relaxation time (106 ms) was about thrice that obtained from mechanical relaxation tests (34 ms) (section 4.1.3). For a square pulse magnetic field, the maximum frequency value for discontinuous actuation ( $f^*_{discontinuous}$ ), can be calculated as below:

$$f^*_{discontinuous} = \frac{1}{t'_{relaxation} + t_{elongation}} \qquad \text{(Equation 4-7)}$$

where $t'_{relaxation}$ is the mechanical relaxation time and $t_{elongation}$ is the time for elongation. This yields a $f^*_{discontinuous}$ value of ~ 13 Hz. The experimental value of the transition from discontinuous to continuous actuation is 5 Hz, the difference between the predicted and experimental values is because an exact square pulse magnetic field was not generated.

The model could also predict the behavior for samples of varying filler concentration. For filler concentrations less than 60%, the ON threshold field increases with decreasing concentration (Figure 4-37(b)), thus there is a greater tendency for continuous actuation. Even at 1 Hz, silicone - 10 wt% Fe samples actuated in the continuous regime because the maximum magnetic field did not cross the ON threshold field (at 1T) (Figure 4-42). For filler concentration higher than 60 wt%, the

OFF threshold value decreased with increasing filler concentration. Hence when the frequency increased beyond a certain value, e.g., 5 Hz for 77 wt% samples, the OFF threshold value fell below the minimum magnetic field required for sample relaxation.

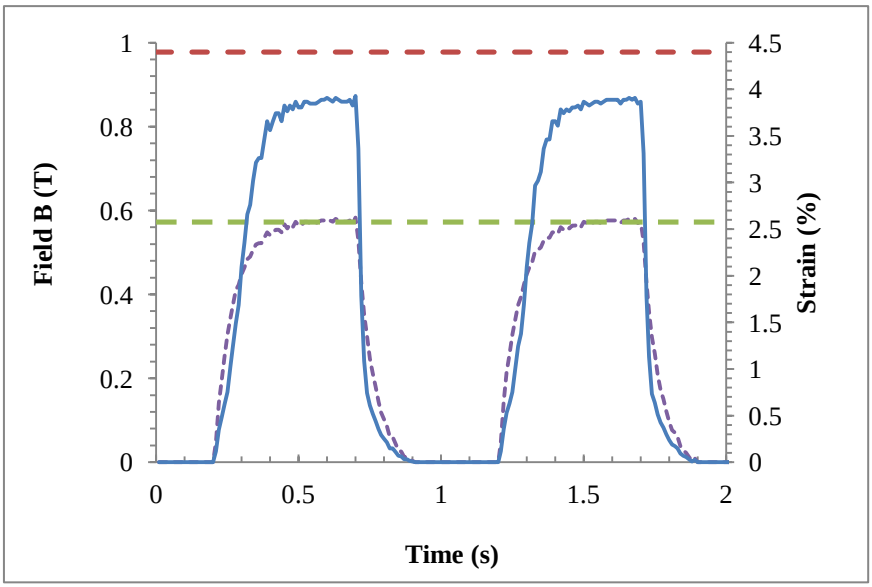


Figure 4-42: Modeled strain (solid curves) of silicone - 10 wt% Fe samples at 1 Hz. The dotted curves represent the magnetic field, the dotted lines represent the ON and OFF thresholds.

## 4.5 Sensor Properties

Polymeric composites with electrically conductive filler concentration above the percolation threshold can become conductive due to the physical contact of particles which forms a conductive path within the composite [160]. At such filler concentrations, the composite becomes sensitive to mechanical strain, e.g., electrical resistance changes of ~ 2 orders of magnitude were observed in samples of poly(ethylene - tetrafluoroethylene) containing conductive carbon black subjected to 10% strain [191]. Therefore, strain sensors can be fabricated from such composites.

Metallic particles with sizes smaller than 100 µm in a polymer matrix tend to oxidize and form a oxide surface layer [268], hence silicone composites with magnetic iron, nickel and cobalt filler particles at percolation concentration do not show appreciable conductivity. Mixing graphite flake fillers in addition to iron filler particles can result in good electrical conductivity and thus sensing behavior of Magpol.

The resistivity of the silicone - graphite composite as a function of filler concentration is presented in Figure 4-43 (a). Interestingly, the resistivity changes over several orders of magnitude as a function of graphite concentration, which is in qualitative agreement with theoretical predictions [160]. When the graphite concentration is low, the graphite particles are separated leading to high resistivity. At percolation concentrations, long-range conduction paths can form resulting in much lower resistivity, the percolation transition region spans from 20 vol% to 30 vol% of graphite. This is in agreement with previous studies utilizing similar constituents [269].

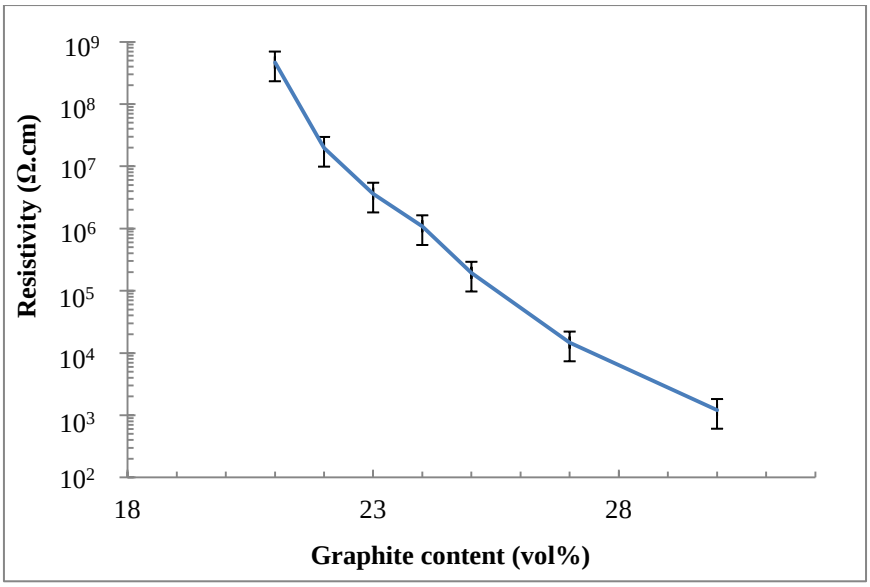


Figure 4-43: The resistivity of silicone - graphite composite as a function of graphite content.

Figure 4-44 shows the change of resistivity with externally applied tensile strain for samples loaded with various graphite concentrations. When a uniform tensile strain was applied, the graphite concentration has a significant effect on the piezo-resistive properties. Samples with concentrations of graphite below 15vol% did not exhibit significant sensing properties. Sensing properties were achieved in samples with concentration of graphite above 18 vol%, the resistivity decreased sharply as the applied strain increased. Systems with higher percolation threshold and high Poisson's ratios were reported to exhibit a sharp decrease in resistivity with strain [190]. Interestingly, a huge change in resistivity of more than 4 orders of magnitude was observed in silicone - 18% vol graphite samples subjected to a tensile strain of 100%. Such a large piezo-resistive behavior is very useful for sensing. This composite can be used to "sense" its own deformation by monitoring the electrical

resistivity and correlating it to the strain. Magpol's resistivity - strain profile exhibited hysteresis. The resistivity change showed small hysteresis for samples with up to 25 vol% graphite concentration. Above 25 vol% of graphite concentration, inconsistent resistivity - strain profiles was observed due to the increased plasticity of samples with high filler loading. Therefore, 18-25 vol% graphite concentrations can achieve both significant piezo-resistive behavior and reversibility.

In addition, a clearly-defined strain threshold in Magpol samples was also observed above which the resistivity decreased significantly. For silicone - graphite composites with 18 vol% filler concentration, the threshold strain was 40%. The value of the strain threshold decreased with increasing graphite concentration. Silicone - 20 vol% graphite samples exhibited a strain threshold of 10% and silicone - 25 vol% graphite samples did not show any strain threshold behavior. Knowing the strain threshold as a function of graphite concentration, different types of sensors can be tailored. Composites with graphite concentration above 20 vol% can be used to make sensors for detecting continuous deformation while composites with 18 vol% of graphite can be used to fabricate on-off detection sensors.

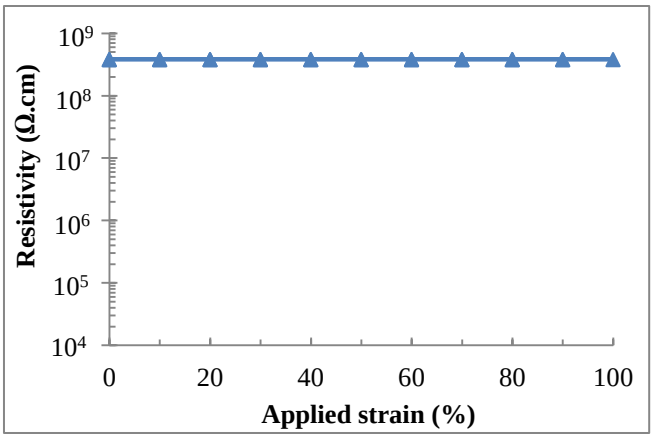


(a) Silicone - 15 vol% graphite samples

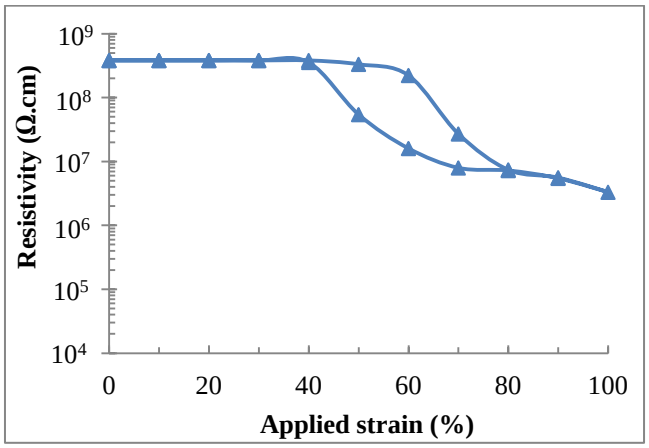


(b) Silicone - 18 vol% graphite samples

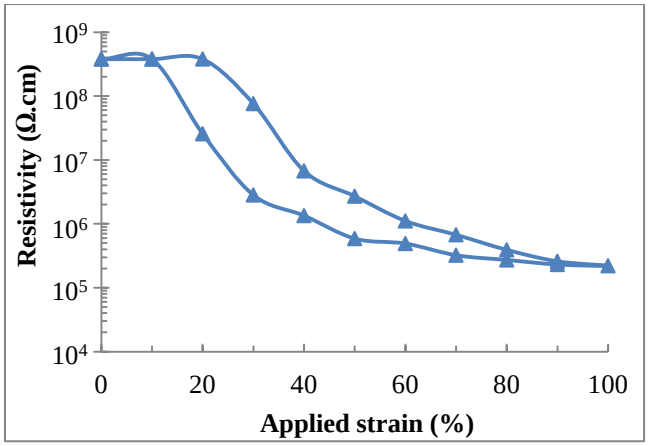


(c) Silicone - 20 vol% graphite samples

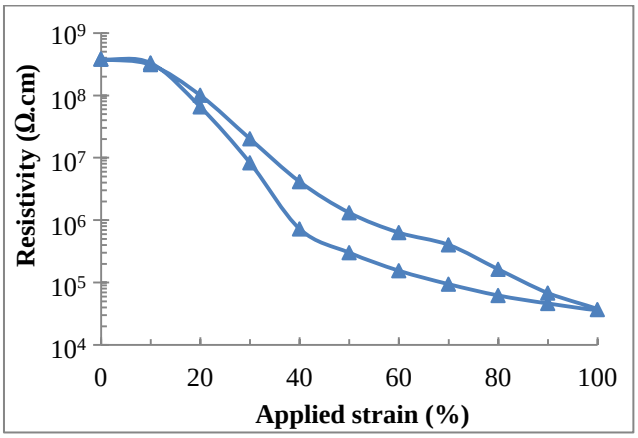


(d) Silicone - 25 vol% graphite samples

Figure 4-44: Resistivity as a function of strain of silicone - graphite composite with various graphite concentrations.

Figure 4-45 shows the resistivity of silicone - graphite - iron composites as a function of applied strain. For a given graphite concentration, the addition of iron particles reduced the effect of threshold strain, silicone - 18 vol% graphite - 40 wt% Fe samples had a threshold strain of 20%, lower than that of silicone - 18 vol% graphite samples The presence of iron particles did not affect the magnitude of resistance change of silicone - 20 vol% graphite and silicone - 22 vol% graphite samples.

The resistivity change with mechanical strain is due to the formation of the new conduction paths and the destruction of old ones. The change in resistivity of conductor - insulator composites with elongation has been variously reported to increase [270], decrease, or initially increase then decrease [271] with elongation strain. In this study, the resistivity of Magpol was found to consistently decrease with strain for all strain modes. The resistivity - strain profile exhibited good reversibility for concentration range of 18 - 25 vol% graphite due to the strong bonds between the conductive particles and the polymer matrix [272].

Nonconductive strain sensors can also be constructed from composites of polymer and magnetic particles. For example, the magnetization of a composite of silicone and hard magnetic ($Sm_2Co_7$) particles changes linearly with axial strain and can be detected by an induction coil [273]. Composites of magnetic particle chains in a polymer matrix can be employed as micromechanical sensors to probe bending rigidity at the molecular scale [274].

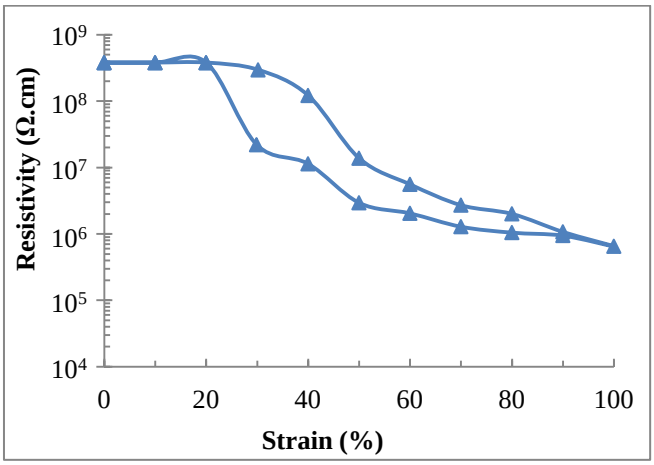


(a) Silicone - 18 vol% graphite - 40 wt% Fe samples

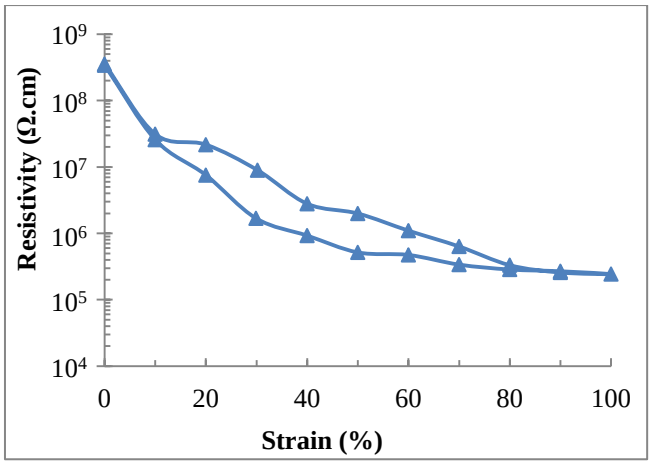


(b) Silicone - 20 vol% graphite - 40 wt%Fe samples

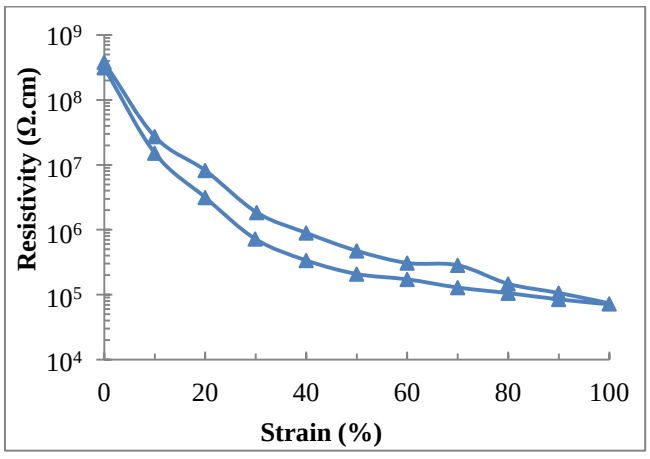


(c) Silicone - 22 vol% graphite - 40 wt% Fe samples

Figure 4-45: Resistivity v/s strain of silicone - graphite - iron samples with various graphite concentrations.

The change of resistivity of silicone - graphite and silicone - graphite - iron composites with time is presented in Figure 4-46. The resistivity decays with time and can be satisfactorily modeled by a generalized Maxwell model [155, 156] , the values of $A_0$, $A_1$, $A_2$, $\tau_1$ and $\tau_2$ are presented in Table 4-3

$$\rho = A_0 + A_1 \exp\left(\frac{-t}{\tau_1}\right) + A_2 \exp\left(\frac{-t}{\tau_2}\right) \qquad \text{(Equation 4-8)}$$

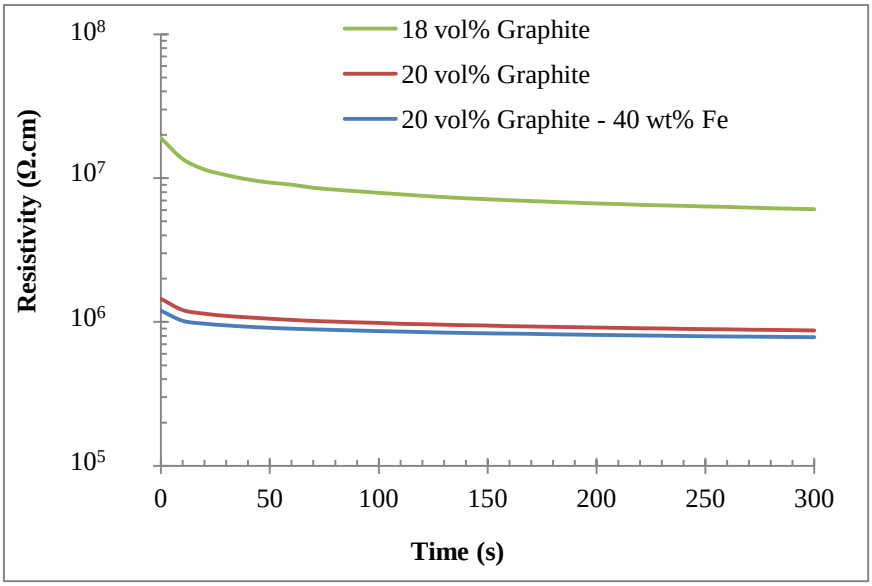


Figure 4-46: Time dependence of resistivity of Magpol samples at 60% elongation.

Table 4-3: Parameter values of Equation 4-8 for different Magpol samples (Figure 4-46).

| Samples | $A_0$ (Ω.cm) | $A_1$ (Ω.cm) | $A_2$ (Ω.cm) | $\tau_1$ (s) | $\tau_2$ (s) |
|---|---|---|---|---|---|
| 18 vol%Graphite | $5.9 \times 10^6$ | $7.4 \times 10^6$ | $5.7 \times 10^6$ | $1.0 \times 10^{-1}$ | $1.0 \times 10^{-2}$ |
| 20 vol% graphite | $8.5 \times 10^5$ | $2.9 \times 10^5$ | $3.0 \times 10^5$ | $1.3 \times 10^{-1}$ | $8.3 \times 10^{-3}$ |
| 20 vol% graphite - 40 wt% Fe | $7.6 \times 10^5$ | $2.1 \times 10^5$ | $2.1 \times 10^5$ | $1.3 \times 10^{-1}$ | $7.7 \times 10^{-3}$ |

The change of resistivity with time during sample deformation is commonly observed in conductive polymer composites. The time-dependence of resistivity is due to the sliding of polymer chains. In

contrast to previous findings reporting increases in resistivity [190], the observed decrease in resistivity is due to the large aspect ratio of the graphite flakes which creates more conduction paths as the polymer chains move. This "relaxation" is the cause of the hysteresis observed in the resistivity - strain curves, similar to the hysteretic stress - strain curves in polymeric materials due to stress relaxation.

## 4.6 Transducer Properties

Silicone - graphite - iron composites can be used as transducers due to the dual ability to actuate and sense deformation [63, 89]. Such samples exhibited shape change when a magnetic field was applied, the resulting change in resistivity was monitored. Figure 4-47 to Figure 4-49 show the actuation strain as a function of resistivity of silicone - 20 vol% - 40 wt% Fe graphite samples in contraction, coiling and elongation modes, respectively. This composition was chosen because it exhibited the best combination of sensing ability and reversibility. For contraction and coiling modes, 3 different loading conditions were examined: no load, a small load (6.4 kPa applied stress) and high load (21.2 kPa applied stress). In elongation mode, the high load caused excessive pre-elongation to the samples, hence only no load and small load conditions were tested. In all modes, resistivity decreased as the sample actuated and increased as the sample relaxed when the magnetic field was removed, the change in resistivity was two to three orders of magnitude.

Loading resulted in better retraceability for contraction and coiling modes, the residual strain was reduced when the sample was loaded. The external load also affected the strain - resistivity profile, greater hysteresis was observed in contraction mode but not in coiling mode. In elongation, stress induced by the external load resulted in greater sample elongation and residual strain.

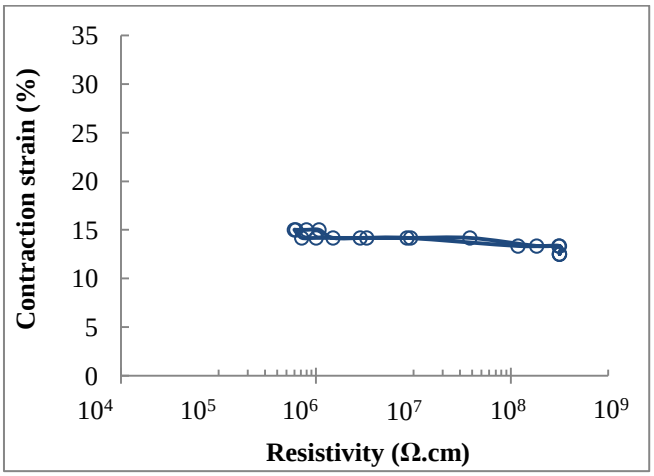


(a) no load

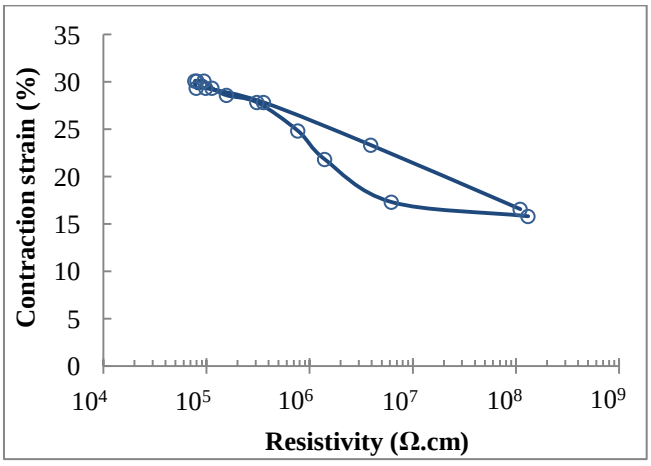


(b) small load (6.4 kPa)

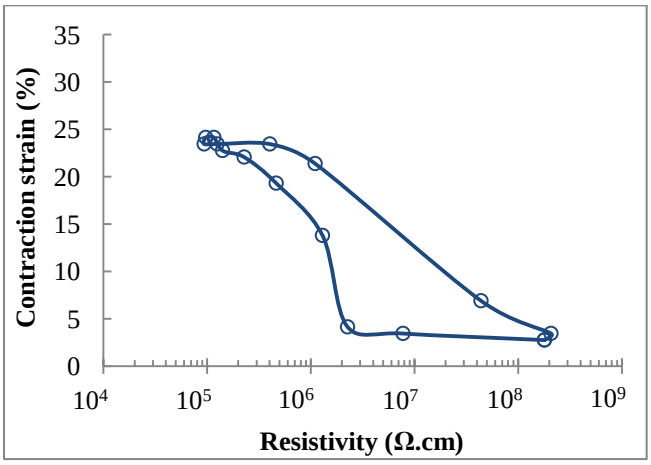


(c) high load (21.2 kPa)

Figure 4-47: Transduction property of silicone - 20 vol% graphite - 40 wt% Fe samples in contraction mode.

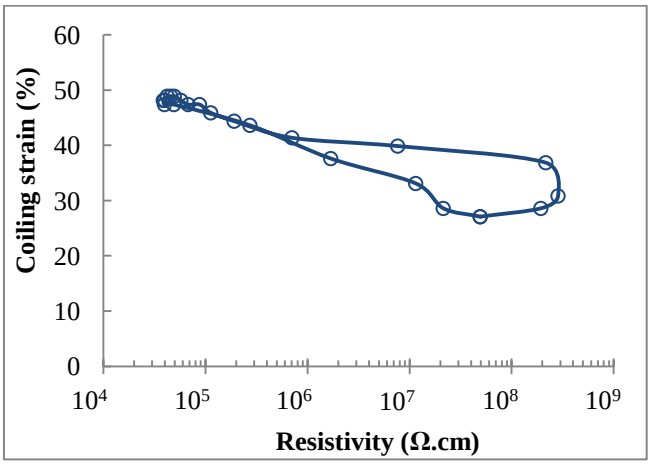


(a) no load

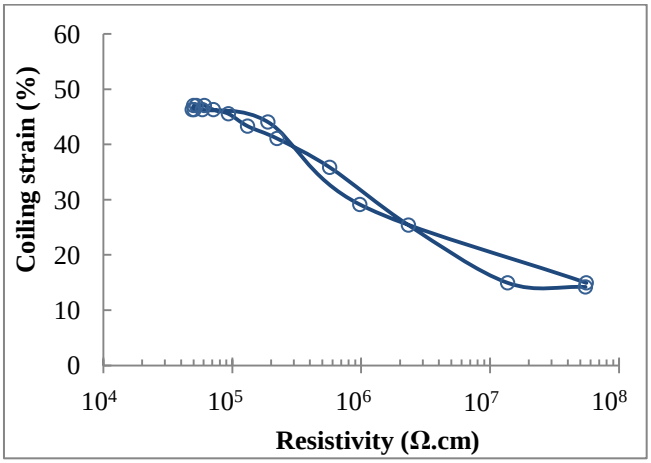


(b) small load (6.4 kPa)

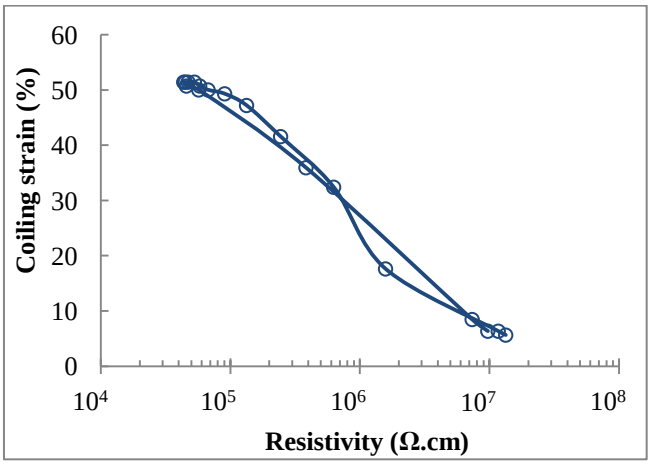


(c) high load (21.2 kPa)

Figure 4-48: Transduction property of silicone - 20 vol% graphite - 40 wt% Fe samples in coiling mode.

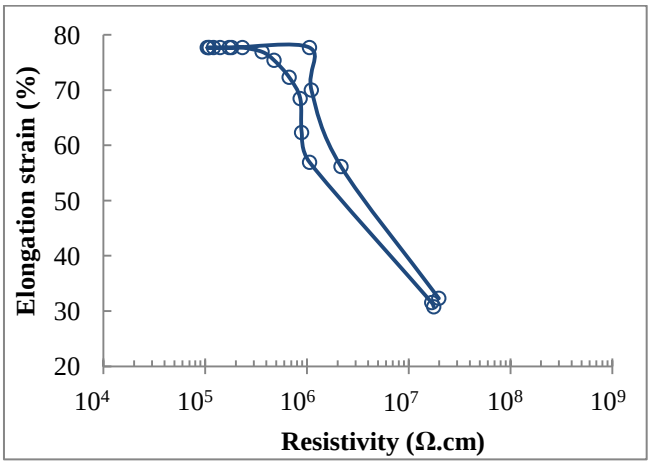


(a) no load

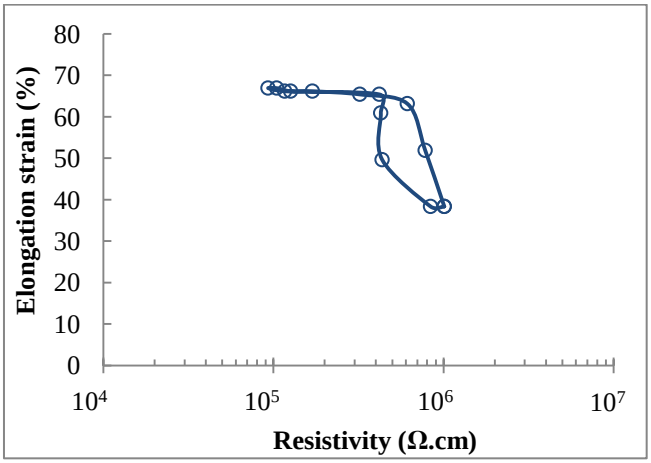


(b) small load (6.4 kPa)

Figure 4-49: Transduction property of silicone - 20 vol% graphite - 40 wt% Fe in elongation mode.

## 4.7 Applications of Magpol

### *4.7.1 Magpol as Actuators*

The deformation of Magpol can be induced by either homogeneous or inhomogeneous magnetic fields. In this study, the shape change of Magpol was due to the force on the magnetic particles along the direction of increasing gradient of an inhomogeneous magnetic field (section 2.5.3), this mechanism results in much higher actuation strain than that observed in homogenous magnetic fields. An advantage of Magpol actuators is that different modes of shape change can be readily achieved by controlling the sample position relative to the magnetic field source (Figure 1-4).

Placing Magpol off axis results in deflection, placing Magpol on the symmetry axis gives rise to either elongation or contraction. The contraction mechanism can be either axial contraction or coiling, depending on the ratio of the radial constraint and the sample diameter.

The previous sections have shown that the actuation of the composite is a result of several factors. Firstly, the actuation depends on the magnetic properties of the composite, which in turn depends on the characteristics of the magnetic fillers and their concentration, better magnetic properties yield superior actuation performance. Secondly, the actuation depends on the mechanical properties of the polymer matrix. The more flexible the polymer is, the better the actuation performance. Lastly, actuation depends on the characteristics of the driving magnetic field, especially its gradient. Obtaining higher magnetic gradient and magnetic field strength can be performed using different magnetic sources (i.e. different types, geometries), changing the magnetic field strength (e.g., using "harder" permanent magnets or increasing the electromagnet current) or varying the distance between the actuator and the magnetic source.

The results from this work demonstrated the feasibility of Magpol as a soft actuator. The actuation performance of Magpol showed considerable improvement compared to previously reported values. The elongation strain of Magpol (Figure 4-22) was 30% higher than previously reported values [42, 70]. The contraction strain was comparable to that of natural muscles (Figure 4-26). The strain obtained in the coiling mode was 50% higher than that of contraction (Figure 4-31). The actuation stress values of Magpol reported in this study surpass the maximum sustainable stress of mammalian skeletal muscles (Figure 4-24 - 16). Two important actuation metrics, force and strain, of Magpol and other common actuators were plotted on a property chart (Figure 4-50) [18, 96, 97, 99, 101, 102, 275-279]. It can be seen that the improvements in Magpol performance reported in this work has significantly increased the material's competitiveness, especially among magnetically driven actuators. The actuation strain of Magpol is highest among the members in this group. Magpol has higher actuation stress than solenoids and moving coil actuators and work capacity is 164 $kJ/m^3$, better than the work capacity of 156 $kJ/m^3$ achieved by twin boundary reorientation magnetic SMA [280]. A similar comparison of force and strain capabilities was performed for Magpol and other artificial muscles (Figure 4-51) [12, 24, 26, 65, 68, 256, 281], Magpol has

actuation properties closest to natural muscles. The performance improvement of Magpol reported here is related to the materials used in this study. This is due to the lower stiffness (Figure 4-13(c)) and superior magnetic properties (Figure 4-13) compared to previous studies which utilized stiffer polymers [59-61] or fillers with inferior magnetic properties [49, 62]. Iron particles have good magnetic properties in powder form and the selected silicone is a highly flexible polymer.

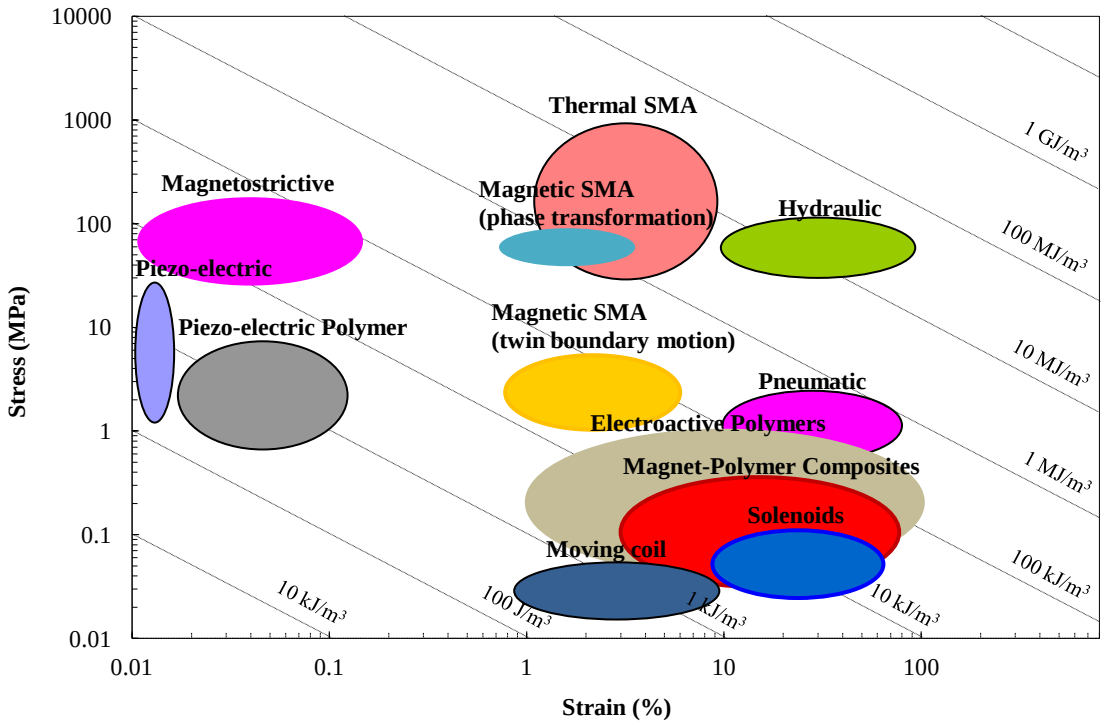


Figure 4-50: Typical force and strain characteristics of Magpol and other actuation technologies [18, 96, 97, 99, 101, 102, 275-279].

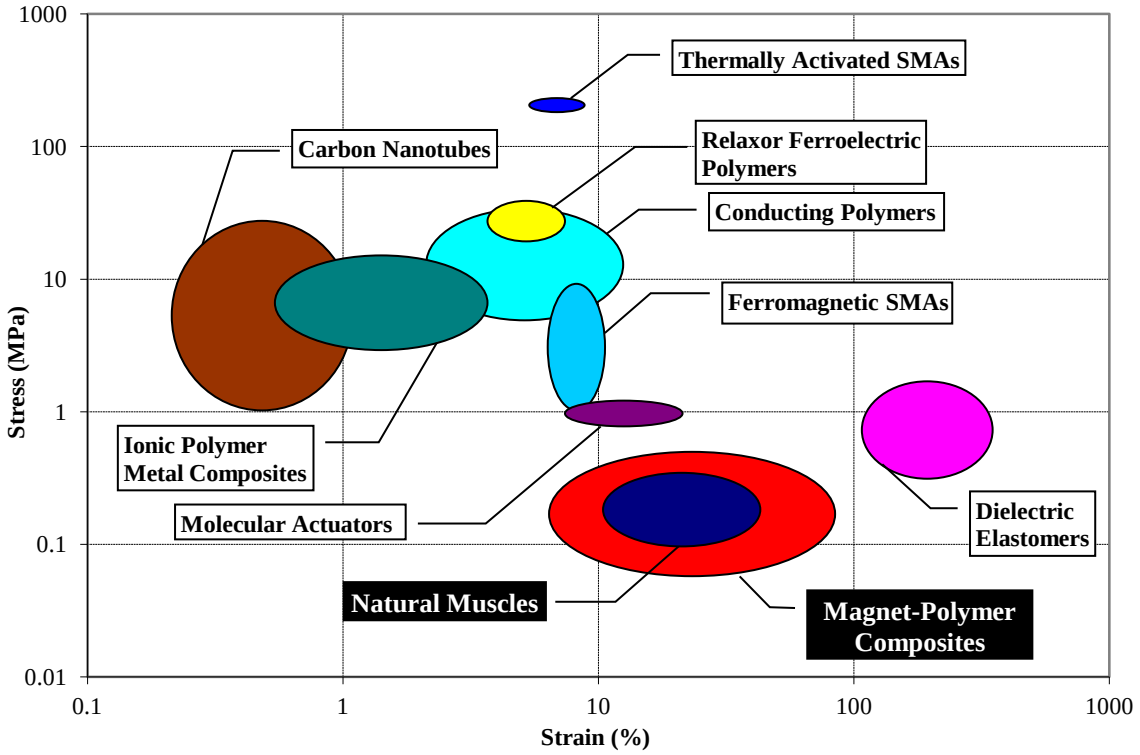


Figure 4-51: Stress and strain chart of Magpol and other muscle technologies [12, 24, 26, 65, 68, 256, 281].

The work capability of Magpol was also found, for the first time, to exceed that of natural muscles, making this class of actuator attractive for artificial muscles applications (Figure 4-35-36). A study of artificial muscles based on carbon nanotube aerogel sheets reported actuation strain of up to 220%, isometric force of up to 3.2 MPa and high frequency of up to 1100 Hz [25]. However, this material exhibited rather limited work capacity (less than 30 J/kg) and a single lateral mode of actuation. Magpol offers an attractive alternative for artificial muscle applications with its low cost, attractive actuation performance (strain, stress and work equal or higher than those of natural muscles) and multiple actuations modes.

Furthermore, Magpol actuators are highly tunable using geometric parameters such as sample size, shape, aspect ratio, distance to magnetic source and geometry of the magnet as well as material composition (e.g., type and concentration of magnetic fillers and the type of polymer matrix) [126]. The sharp threshold behavior observed in Magpol can be useful for switching applications. A suitable range of these parameters can be used to optimize the composite for a specific requirement

(i.e., maximum strain, maximum stress or maximum work). The performance of Magpol can be also enhanced if the design of magnetic source is considered. For example, an array of magnetic coils and the timing of current passing through these coils was controlled to generate a travelling magnetic field, resulting in a worm-like locomotion of magnet - polymer composites [282].

The maximum actuation frequency achieved in the study of dynamic properties of Magol is 80 Hz, higher than earlier reported values for a PVA hydrogel - $Fe_3O_4$ composites [66]. This frequency is comparable to that of the fastest wing beat of hummingbirds [283]. Magpol can actuate up to 24,000 cycles at 80 Hz without change in strain characteristics. This is in contrast to conducting polymer actuators which reported shifting of strain profile [284] and short life (<10,000 cycles for strains of 2%) [285]. The cycle number reported in this study was due to experimental limitations and not by material properties, and can be extended further. The strain rate and strain of Magpol and other competing artificial muscles are shown on a property chart (Figure 4-52). Magpol can sustain higher strain rate than natural muscles, and is close to that of field driven EAPs. The actuation strain of Magpol is also higher than natural muscles. Coupled with the "soft" biomimetic mechanical properties (Figure 4-13(c)), this performance makes Magpol a very promising candidate for artificial muscles.

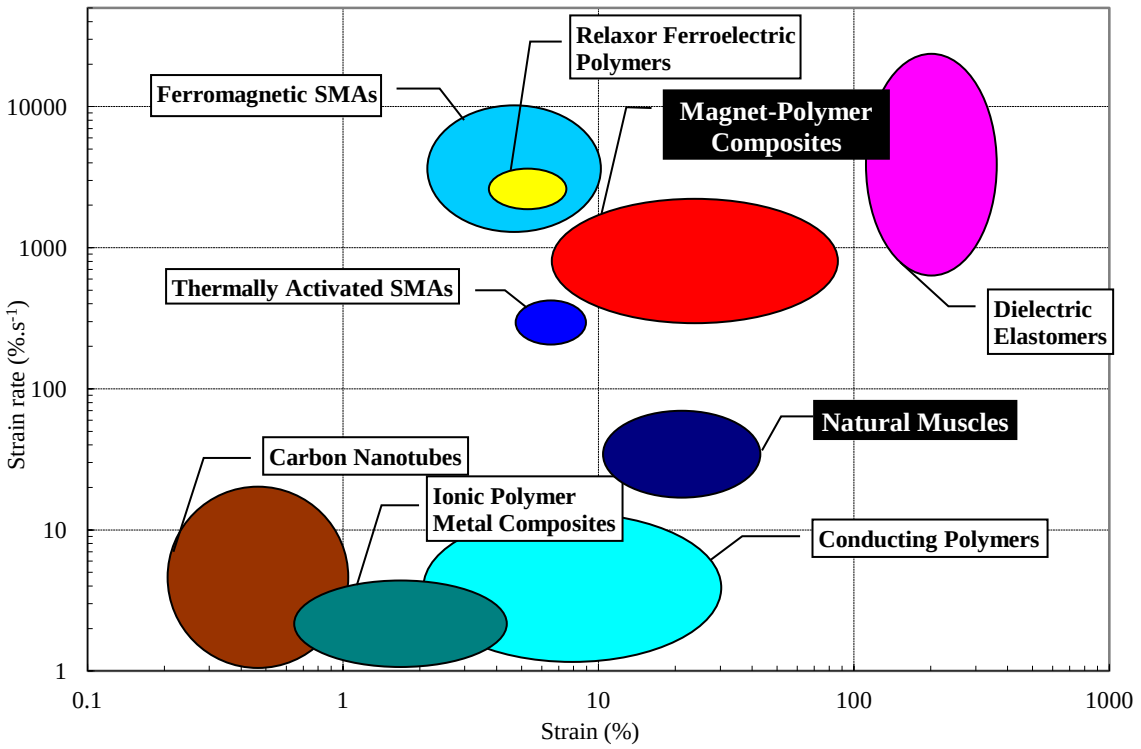


Figure 4-52: Strain rate versus strain for various artificial muscle technologies [12, 19, 24, 26, 65, 68, 256, 281].

Another advantage of this new class of actuator is the lack of a requirement for an integrated driving source. This may lead to many applications which require contactless, noninvasive control, such as human implants and aerospace devices. An example of potential applications for Magpol is a remotely operating heart pump. This may be the solution for the number one cause of death worldwide. In the United States alone, more than 100,000 people die each year from heart failure. From the pioneering work by Dr. William Devries in 1982 [286], it was shown that patients of heart failure can use artificial heart pumps to extend their lives before receiving a donated heart. Since then, there have been many attempts to develop artificial heart pumps with rotary motor and pneumatic pumps are the most common types. However, all of the current technologies require opening patients' chests to let either electrical wires or fluid pipes run through to function. This causes severe infection problems which limit the lifetime of artificial heart pump users to typically less than two years. Even the recently FDA approved AbioCor heart by Abiomed [287], an MIT based company, can only promise 6 months of extended waiting time for the patients. A solution for

this problem is a transdermal energy transport mechanism by AC electromagnetic field, but so far has only limited success has been achieved [288]. All these facts emphasize the importance of a remotely controlled heart pump. Magnet - polymer actuators can be an excellent candidate. Further study of the composite for the application of artificial heart pump can lead to impactful and interesting findings.

### *4.7.2 Magpol as Transducers*

In this study, Magpol exhibited large changes in resistivity when subjected to mechanical strains. This property makes Magpol suitable for highly sensitive sensors. The sensitivity S, defined as the change in the output signal (i.e., resistivity) for a given change in the input signal (i.e., strain), of Magpol is in the range of 1,000 - 10,000 for silicone - graphite and 1,000 - 5,000 for silicone - graphite - iron. As a comparison, the S value of piezo-resistive strain gauges ranges from -12.1 (Nickel) to 6.1 (Platinum) [289]. For clip gauges, the theoretical sensitivity ranges from 1.45 for twin cantilever to 7.53 for single cantilever design [290]. The sensitivity of Magpol can be improved further if smaller particles are used. It has been reported previously that 4 orders of resistivity change upon 40% tensile stress was achieved for isoprene - nanosized CB composites [291].

Another significant advantage of Magpol transducers is the low stiffness (less than 0.06 MPa for silicone - iron composites, less than 0.08 MPa for silicone - graphite - iron composites). Magpol's stiffness is one of the lowest among contact sensors. This is an attractive feature because the low stiffness minimizes interference with the loading of systems. Magpol sensors can be also used for biological systems for which traditional contact sensors are unsuitable [98]. The high flexibility of Magpol makes it useful for applications which require soft actuation, e.g., artificial muscles.

The work on transduction properties showed that Magpol is capable of producing significantly higher strain and resistivity change compared to previous studies. A maximum strain of 1.4% was reported for silicone - SmCo composites [63] and a maximum strain of less than 1% was observed for silicone - graphite - iron composites [89]. This work also reported the first results of sensing and transduction properties of Magpol in coiling mode. Among the studied transducer modes, coiling shows the best reversibility and smallest hysteresis. It was demonstrated that Magpol actuators

exhibit higher actuation strain and stress in coiling mode than the axial contraction mode, and that these values are also higher than those of biological muscles [90]. A demonstration of Magpol transducer in coiling mode is shown in Figure 4-53. The composite was capable of lifting a mass 2.5 times its own weight while simultaneously exhibiting a large change in resistance, which can be used for external control and feedback purposes.

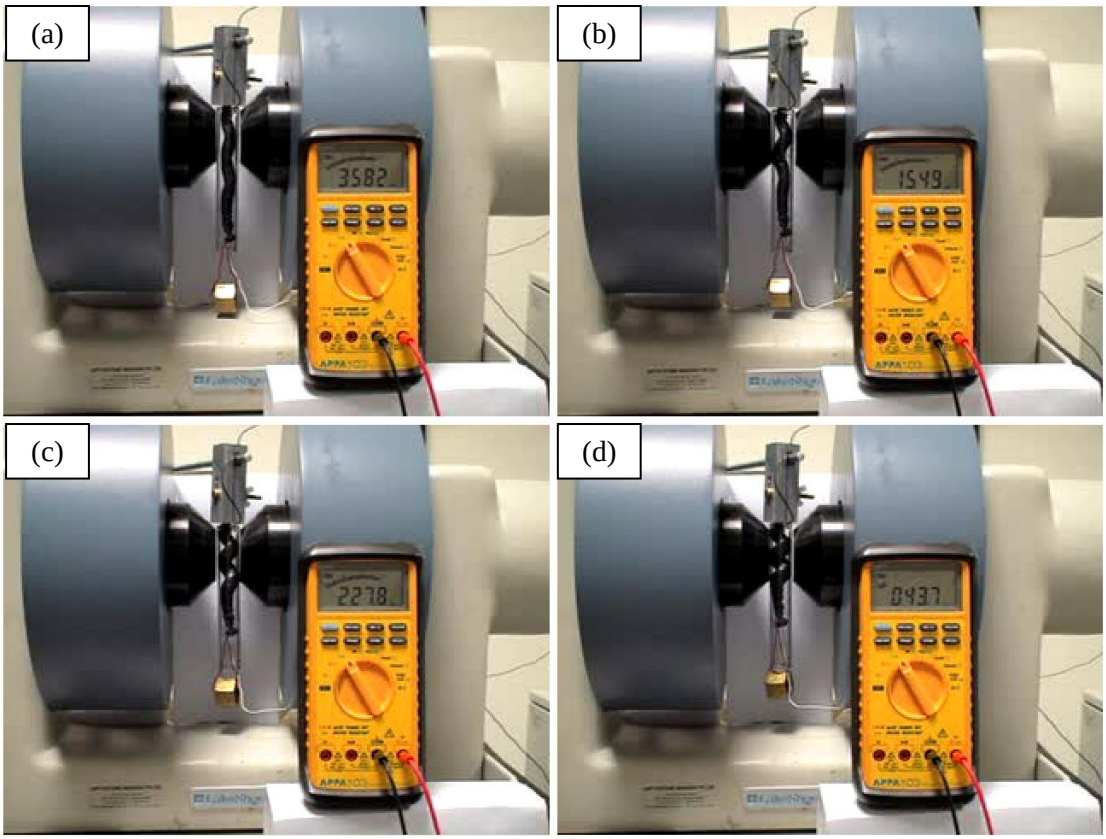


Figure 4-53: Demonstration of Magpol transducer in coiling mode. The ohmmeter shows the resistance change of the sample during coiling process. (a) R = 2582 kΩ, (b) R = 1549 kΩ, (c) R = 227.8 kΩ, (d) R = 43.7 kΩ

# CHAPTER 5 - CONCLUSIONS

Magnet - polymer composites (Magpol) possess fascinating transducer properties due to their combination of soft mechanical properties and the ability to produce significant actuation driven by magnetic fields. However, insufficient research has been done on this promising material, especially on the important actuation aspects and the improvement of the actuation force. In this work, the behavior of Magpol transducers was studied and the performance metrics of Magpol transducers were determined. Materials optimization was carried out, composites of highly flexible silicone elastomers and highly magnetic iron particles were synthesized, characterized and their shape change behavior in an external magnetic field was studied. Different actuation modes were achieved by setting appropriate boundary conditions. The actuation and transduction performance of Magpol in elongation, contraction and coiling modes were examined and the following conclusions were reached:

- For the first time, shape change of Magpol in the coiling mode was observed. With appropriate boundary conditions, the composite coiled rather than contracted under a compressive magnetic force.
- The maximum strain achieved was 40% for contraction, 60% for coiling, and 80% for elongation. These values did not depend strongly on the filler concentration. The actuation strain of Magpol was highest among magnetically driven actuators and was equal or higher than the maximum strain achieved by mammalian skeletal muscles.
- With suitable materials and sample geometry, the stress values of Magpol can reach up to 164 kPa for contraction, 184 kPa for coiling and 216 kPa for elongation. This is the first time such high values were reported. In fact, the maximum actuation stress of Magpol was higher than the maximum sustainable stress of mammalian skeletal muscles.
- This work reported the first results on work measurement of Magpol based on the work-loop method. The maximum measured work values were 141 $kJ/m^3$ for contraction and 164 $kJ/m^3$ for coiling. Magpol's work capacity was comparable to that of magnetic SMAs, and

higher that of mammalian skeletal muscles. Magpol in a geometry similar to bicep muscle was demonstrated.

- The composite was capable of actuating without lag or strain shift in response to modulated magnetic fields of up to 80 Hz. Below 2 Hz, the composite exhibited a strain profile similar to the static case. The visco-elastic characteristics of the composite did not affect actuation behavior at low frequencies. At low actuation frequencies, the fast and abrupt elongation allowed strain rate of up to 1500 $\%.s^{-1}$ to be achieved, competitive with field - driven EAPs.

- At higher frequencies, both time dependent mechanical properties and the inductive effect of the magnetic source reduced actuation strain. Continuous deformation was less time dependent than discontinuous actuation. In practice, for high actuation strain, design of Magpol actuators should include discontinuous actuation. When high actuation frequency is of higher priority, the design should incorporate continuous actuation.

- Magpol exhibited highly tunable actuator characteristics. Continuous or sharp threshold behavior can be produced for linear actuator and switching applications, respectively. Simple changes in sample geometry, type and concentration of magnetic filler as well as external magnetic field can be exploited to tune threshold behavior, actuation and relaxation response, actuation strain, actuation stress and work capacity. This versatility is a very useful feature for the design of Magpol based systems.

- When the filler volume fraction is in the percolation range (i.e., from 20 vol% to 30 vol%), the electrical resistivity of silicone - graphite composites was very sensitive to mechanical strain. The sensitivity of Magpol sensors was found to be in the range of $1 \times 10^3$ - $1 \times 10^4$, which can be useful for highly sensitive sensing devices. The resistivity - strain relationship also exhibited threshold behavior, which can be useful for on-off switches or detectors.

- Both sensing and actuation capabilities can be combined in Magpol. Sensing is governed by percolation of graphite particles while actuating can be the results of magnetic force acting on the iron particles. Transduction properties of silicone - graphite - iron samples were studied in coiling, contraction and elongation modes. Significant strain values and resistivity

change were observed. The coiling mode showed the best reversibility and smallest hysteresis. A prototype of Magpol transducer in coiling mode was presented to demonstrate the potential of Magpol transducers.

- The low Young's modulus values of Magpol are also promising for soft transducers and biological applications. Further research should focus on reducing magnetic field requirements. Since magnetic forces are dependent on the magnetic field gradient, designs of magnetic sources with greater field gradient can also be studied to further improve the performance of Magpol.

# REFERENCES


1. Spillman Jr, W.B., Sirkis, J.S., and Gardiner, P.T., *Smart materials and structures: What are they?* Smart Materials and Structures, 1996. **5**: p. 247-254.
2. Barsoum, R.G.S., *Active materials and adaptive structures.* Smart Materials and Structures, 1997. **6**(1): p. 117-122.
3. Wada, B.K., *Adaptive structures: an overview*. Journal of Spacecraft and Rockets, 1990. **27**(3): p. 330-337.
4. Aizawa, S., Kakizawa, T., and Higasino, M., *Case studies of smart materials for civil structures.* Smart Mater Struct, 1998. **7**(5): p. 617-626.
5. Bandyopadhyay, K. *Smart materials and aerospace structures.* in *Indo-Russian Workshop on Micromechanical Systems*. 1999. Delhi: SPIE.
6. Kim, M.H., *Simultaneous structural health monitoring and vibration control of adaptive structures using smart materials.* Shock and Vibration, 2002. **9**(6): p. 329-339.
7. Pettit, G.W., Robertshaw, H.H., and Inman, D.J., *Morphing wings for unmanned aircraft.* Smart Materials Bulletin, 2001. **2001**(11): p. 7-12.
8. Wagg, D., Bond, I., Weaver, P., and Friswell, M., *Adaptive structures: engineering applications*. 2007, Chichester: John Wiley and Sons. 291.
9. Abdulrahim, M., Garcia, H., and Lind, R., *Flight Characteristics of Shaping the Membrane Wing of a Micro Air Vehicle.* Journal of Aircraft, 2005. **42**(1): p. 131-137.
10. Ross, R. *Transforming Clothes*. Technology Review 2006 [cited 2009 11/17]; Available from: http://www.technologyreview.com/computing/17639/.
11. Willner, I., Basnar, B., and Willner, B., *From Molecular Machines to Microscale Motility of Objects: Application as" Smart Materials", Sensors, and Nanodevices.* Advanced Functional Materials, 2007. **17**(5): p. 702 - 717.
12. Bar-Cohen, Y., *Electroactive Polymer (EAP) Actuators as Artificial Muscles–Reality, Potential and Challenges*. 2nd ed. 2004, Bellingham, WA, USA: SPIE Press. 765.
13. Bar-Cohen, Y. and Breazeal, C., *Biologically inspired intelligent robotics*. 2003, Bellingham, WA, USA: SPIE Press. 406.
14. Cao, W., Cudney, H.H., and Waser, R., *Smart materials and structures.* 1999. **96**(15): p. 8330-8331.
15. Dapino, M.J., *On magnetostrictive materials and their use in adaptive structures.* Structural Engineering and Mechanics, 2004. **17**(3-4): p. 303-330.
16. Matsuzaki, Y., *Recent Research on Adaptive Structures and Materials: Shape Memory Alloys and Aeroelastic Stability Prediction.* Journal of Intelligent Material Systems and Structures, 2005. **16**(11): p. 907-918.
17. Pai, D.M., Sundaresan, N.R., and Cadenhead, N. *The use of piezoelectric materials in smart structures*. in *National Educators' Workshop*. 2003. San Jose: NASA.
18. Leo, D.J., *Engineering analysis of smart material systems*. 2007, Hoboken: John Wiley and Sons. 556.
19. Shahinpoor, M. and Schneider, H.J., *Intelligent materials*. 2008, Cambridge: Royal Society of Chemistry. 532.

20. Pan, M.J., Rehrig, P.W., Kucera, J.P., Park, S.E.E., and Hackenberger, W.S. *Comparison of actuator properties for piezoelectric and electrostrictive materials*. in *Smart Struct. Mater.: Act. Mater. : Behav. Mech.* 2000. Newport Beach: SPIE.

21. Duerig, T.W., Melton, K.N., Stockel, D., and Wayman, C.M., *Engineering aspects of shape memory alloys*. 1990, Rushden: Butterworth-Heinemann.

22. Hollerbach, J.M., Hunter, I.W., and Ballantyne, J., *A comparative analysis of actuator technologies for robotics.* The robotics review 2 table of contents, 1992: p. 299-342.

23. *Honda Worldwide | P3 | Specifications*. [cited 10/10/2005]; Available from: http://world.honda.com/ASIMO/P3/spec/.

24. Madden, J.D.W., Vandesteeg, N.A., Anquetil, P.A., Madden, P.G.A., Takshi, A., Pytel, R.Z., Lafontaine, S.R., Wieringa, P.A., and Hunter, I.W., *Artificial muscle technology: physical principles and naval prospects.* IEEE Journal of Oceanic Engineering, 2004. **29**(3): p. 706-728.

25. Aliev, A.E., Oh, J., Kozlov, M.E., Kuznetsov, A.A., Fang, S., Fonseca, A.F., Ovalle, R., Lima, M.D., Haque, M.H., Gartstein, Y.N., Zhang, M., Zakhidov, A.A., and Baughman, R.H., *Giant-stroke, superelastic carbon nanotube aerogel muscles.* Science, 2009. **323**(5921): p. 1575-1578.

26. Bar-Cohen, Y., Xue, T., Joffe, B., Lih, S.S., Shahinpoor, M., Simpson, J., Smith, J., and Willis, P. *Electroactive Polymers (EAP) Low Mass Muscle Actuators*. in *Smart Structures and Integrated Systems*. 1997. San Diego: SPIE.

27. Bar-Cohen, Y. *EAP as artificial muscles: progress and challenges*. in *Smart Struct. Mater. : Electroact. Polym. Actuators Devices*. 2004. San Diego: SPIE.

28. Bar-Cohen, Y. and Zhang, Q., *Electroactive polymer actuators and sensors.* MRS Bulletin-Materials Research Society, 2008. **33**(3): p. 173-181.

29. CNN. *Meet the artificial muscle man*. [cited 19/8/2005]; Available from: http://www.cnn.com/2003/TECH/ptech/10/09/popsci.muscle.man/index.html.

30. Ramanujan, R.V. and Lao, L.L., *The mechanical behavior of smart magnet-hydrogel composites.* Smart Materials and Structures, 2006. **15**(4): p. 952-956.

31. Barsi, L., Buki, A., Szabo, D., and Zrinyi, M., *Gels with magnetic properties.* Progress in Colloid and Polymer Science, 1996. **102**: p. 57-63.

32. Zrinyi, M., *Magnetic-field-sensitive Polymer Gels.* Trends in Polymer Science, 1997. **5**(9): p. 280-285.

33. Zrinyi, M., Barsi, L., and Buki, A., *Ferrogel: A new magneto-controlled elastic medium.* Polymer Gels and Networks, 1997. **5**(5): p. 415-427.

34. Zrinyi, M., Barsi, L., and Buki, A., *Deformation of ferrogels induced by nonuniform magnetic fields.* Journal of Chemical Physics, 1996. **104**(21): p. 8750-8756.

35. Zrinyi, M., Barsi, L., Szabo, D., and Kilian, H.G., *Direct observation of abrupt shape transition in ferrogels induced by nonuniform magnetic field.* Journal of Chemical Physics, 1996. **106**(13): p. 5685-5692.

36. Torok, G., Lebedev, V.T., Cser, L., and Zrinyi, M., *NSE-study of magnetic phase dynamics in poly(vinylalcohol) ferrogel.* Physica B: Condensed Matter, 2000. **276**: p. 396-397.

37. Torok, G., Lebedev, V.T., Cser, L., Kali, G., and Zrinyi, M., *Dynamics of PVA-gel with magnetic macrojunctions.* Physica B: Condensed Matter, 2001. **297**(1-4): p. 40-44.

38. Narita, T., Knaebel, A., Munch, J.P., Candau, S.J., and Zrinyi, M., *Diffusing-wave spectroscopy study of the motion of magnetic particles in chemically cross-linked gels under external magnetic fields.* Macromolecules, 2003. **36**(8): p. 2985-2989.

39. Hernández, R., Sarafian, A., López, D., and Mijangos, C., *Viscoelastic properties of poly (vinyl alcohol) hydrogels and ferrogels obtained through freezing–thawing cycles.* Polymer, 2004. **45**(16): p. 5543-5549.

40. Chatterjee, J., Haik, Y., and Jen Chen, C., *Biodegradable magnetic gel: synthesis and characterization.* Colloid and Polymer Science, 2003. **281**(9): p. 892-896.

41. Collin, D., Auernhammer, G.K., Gavat, O., Martinoty, P., and Brand, H.R., *Frozen-in magnetic order in uniaxial magnetic gels: preparation and physical properties.* Macromolecular Rapid Communications, 2003. **24**(12): p. 737-741.

42. Szabo, D., Szeghy, G., and Zrinyi, M., *Shape transition of magnetic field sensitive polymer gels.* Macromolecules, 1998. **31**(19): p. 6541-6548.

43. Zrinyi, M., Szabo, D., and Kilian, H.G., *Kinetics of the shape change of magnetic field sensitive polymer gels.* Polymer Gels and Networks, 1998. **6**(6): p. 441-454.

44. Zrinyi, M., Szabo, D., and Barsi, L., *Magnetic field sensitive polymeric actuators.* Journal of Intelligent Material Systems and Structures, 1999. **9**(8): p. 667-671.

45. Zrinyi, M., Szabo, D., and Feher, J. *Comparative studies of electric- and magnetic field sensitive polymer gels*. in *Smart Struct. Mater. : Electroact. Polym. Actuators Devices*. 1999. Newport Beach: SPIE.

46. Varga, Z., Filipcsei, G., and Zrinyi, M., *Magnetic field sensitive functional elastomers with tuneable elastic modulus.* Polymer, 2006. **47**(1): p. 227-233.

47. Yalcintas, M. and Dai, H., *Magnetorheological and electrorheological materials in adaptive structures and their performance comparison.* Smart Materials and Structures, 1999. **8**(5): p. 560-573.

48. Zhou, G.Y. and Jiang, Z.Y., *Deformation in magnetorheological elastomer and elastomer-ferromagnet composite driven by a magnetic field.* Smart Materials and Structures, 2004. **13**(2): p. 309-316.

49. Farshad, M. and Benine, A., *Magnetoactive elastomer composites.* Polymer testing, 2004. **23**(3): p. 347-353.

50. Schexnailder, P. and Schmidt, G., *Nanocomposite polymer hydrogels.* Colloid & Polymer Science, 2009. **287**(1): p. 1-11.

51. Fuhrer, R., Athanassiou, E.K., Luechinger, N.A., and Stark, W.J., *Crosslinking Metal Nanoparticles into the Polymer Backbone of Hydrogels Enables Preparation of Soft, Magnetic Field-Driven Actuators with Muscle-Like Flexibility.* Small, 2009. **5**(3): p. 383-388.

52. Czaun, M., Hevesi, L., Takafuji, M., and Ihara, H., *A novel approach to magneto-responsive polymeric gels assisted by iron nanoparticles as nano cross-linkers.* Chemical Communications, 2008. **2008**(18): p. 2124-2126.

53. Daniel-da-Silva, A.L., Lóio, R., Lopes-da-Silva, J.A., Trindade, T., Goodfellow, B.J., and Gil, A.M., *Effects of magnetite nanoparticles on the thermorheological properties of carrageenan hydrogels.* Journal of Colloid and Interface Science, 2008. **324**(1-2): p. 205-211.

54. Mitsumata, T., Horikoshi, Y., and Negami, K., *High-Power Actuators Made of Two-Phase Magnetic Gels.* Japanese Journal of Applied Physics, 2008. **47**(9): p. 7257-7261.

55. Satarkar, N.S. and Zach Hilt, J., *Hydrogel nanocomposites as remote-controlled biomaterials.* Acta Biomaterialia, 2008. **4**(1): p. 11-16.

56. Wang, Y., Hu, Y., Chen, L., Gong, X., Jiang, W., Zhang, P., and Chen, Z., *Effects of rubber/magnetic particle interactions on the performance of magnetorheological elastomers.* Polymer Testing, 2006. **25**(2): p. 262-267.

57. Raikher, Y.L., Stolbov, O.V., and Stepanov, G.V., *Shape instability of a magnetic elastomer membrane.* Journal of Physics D: Applied Physics, 2008. **41**(15).

58. Nagel, J.J., Mikhail, G., Noh, H.M., and Koo, J. *Magnetically Actuated Micropumps Using an Fe-PDMS Composite Membrane*. in *Smart Structures and Materials 2006*. 2006. San Diego: SPIE.

59. Mitsumata, T. and Okazaki, T., *Magnetization-induced reduction in dynamic modulus of polyurethane elastomers loaded with ferrite.* Japanese Journal of Applied Physics Part 1, 2007. **46**(7 A): p. 4220-4224.

60. Razzaq, M.Y., Anhalt, M., Frormann, L., and Weidenfeller, B., *Mechanical spectroscopy of magnetite filled polyurethane shape memory polymers.* Materials Science and Engineering A, 2007. **471**(1-2): p. 57-62.

61. Nikitin, L.V., Korolev, D.G., Stepanov, G.V., and Mironova, L.S., *Experimental study of magnetoelastics.* Journal of Magnetism and Magnetic Materials, 2006. **300**(1): p. 234-238.

62. Varga, Z., Filipcsei, G., and Zrinyi, M., *Smart composites with controlled anisotropy.* Polymer, 2005. **46**(18): p. 7779-7787.

63. Iannotti, V., Hison, C., Lanotte, L., Luponio, C., Ausanio, G., D'Agostino, A., and Germano, R., *Novel elastic magnets as actuators core.* International Journal of Applied Electromagnetics and Mechanics, 2004. **19**(1): p. 395-398.

64. Bednarek, S., *Changes of thickness and self-excited oscillations of the conducting porous magnetoelast nearby percolation threshold caused by current flow.* Materials Science and Engineering B, 2002. **94**(1): p. 89-94.

65. Zrinyi, M. and Szabo, D., *Muscular contraction mimiced by magnetic gels.* International Journal of Modern Physics B, 2001. **15**(6-7): p. 557-563.

66. Zrinyi, M., Szabó, D., and Kilian, H.G., *Kinetics of shape change of magnetic gels.* Polymer Gels & Networks, 1999. **6**: p. 441-454.

67. Rosenweig Ronald, E., *Ferro hydrodynamics*. 1985: Cambridge University Press.

68. Zrinyi, M., *Electrical and Magnetic Field-Sensitive Smart Polymer Gels*, in *Polymer Gels and Networks*, Osada, Y. and Khokhlov, A.R., Editors. 2002, Marcel Dekker: New York. p. 381.

69. Bednarek, S., *The giant magnetostriction in ferromagnetic composites within an elastomer matrix.* Applied Physics A, 1999. **68**(1): p. 63-67.

70. Faidley, L.E. and McLaurin, E.J. *Lumped parameter modeling of the actuator behavior of ferrogels*. in *Behav. Mech. Multifunc. Mater. Compos.* 2009. San Diego: SPIE.

71. Bednarek, S., *The giant linear magnetostriction in elastic ferromagnetic composites within a porous matrix.* Journal of Magnetism and Magnetic Materials, 2006. **301**(1): p. 200-207.

72. Guan, X., Dong, X., and Ou, J., *Magnetostrictive effect of magnetorheological elastomer.* Journal of Magnetism and Magnetic Materials, 2008. **320**(3-4): p. 158-163.

73. Cebers, A. and Javaitis, I., *Bending of flexible magnetic rods.* Physical Review E: Statistical, Nonlinear, and Soft Matter Physics, 2004. **70**(2): p. 21404.

74. Hison, C., Ausanio, G., Iannotti, V., Lanotte, L., Breglio, G., Cusano, A., and Giordano, M., *Experimental verification of the direct elastomagnetic effect.* International Journal of Applied Electromagnetics and Mechanics, 2007. **25**(1): p. 37-41.

75. Chen, J., Zhang, G., and Jin, J. *Preparation and deflection characterization of intelligent polymer gels controlled by magnetic fields*. in *IEEE Int. Conf. Rob. Biomimetics*. 2007. Sanya, China: IEEE.

76. Nikitin, L.V., Stepanov, G.V., Mironova, L.S., and Samus, A.N., *Properties of magnetoelastics synthesized in external magnetic field.* Journal of Magnetism and Magnetic Materials, 2003. **258**: p. 468-470.

77. An, Y. and Shaw, M.T., *Actuating properties of soft gels with ordered iron particles: basis for a shear actuator.* Smart Materials and Structures, 2003. **12**(2): p. 157-163.

78. Monz, S., Tschöpe, A., and Birringer, R., *Magnetic properties of isotropic and anisotropic $CoFe_2O_4$-based ferrogels and their application as torsional and rotational actuators.* Physical Review E: Statistical, Nonlinear, and Soft Matter Physics, 2008. **78**(2): p. 214041-214047.

79. Mitsumata, T., Horikoshi, Y., and Takimoto, J.I., *Flexible fluid pump using magnetic composite gels.* e-Polymers, 2007. **147**: p. 1–10.

80. Gollwitzer, C., Turanov, A., Krekhova, M., Lattermann, G., Rehberg, I., and Richter, R., *Measuring the deformation of a ferrogel sphere in a homogeneous magnetic field.* Journal of Chemical Physics, 2008. **128**(16): p. 164709.1-164709.5.

81. Zimmermann, K., Naletova, V.A., Zeidis, I., Böhm, V., and Kolev, E., *Modelling of locomotion systems using deformable magnetizable media.* Journal of Physics: Condensed Matter, 2006. **18**(38): p. S2973-S2983.

82. Schlemmer, C., Betz, W., Berchtold, B., Rühe, J., and Santer, S., *The design of thin polymer membranes filled with magnetic particles on a microstructured silicon surface.* Nanotechnology, 2009. **20**(25): p. 255301.1-255301.9.

83. Nagel, J.J., Mikhail, G., Noh, H., and Koo, J. *Magnetically actuated micropumps using an Fe-PDMS composite membrane*. in *Smart Struct. Mater.: Smart Electron., MEMS, BioMEMS, Nanatechnol.* 2006. San Diego: SPIE.

84. Abramchuk, S., Kramarenko, E., Grishin, D., Stepanov, G., Nikitin, L.V., Filipcsei, G., Khokhlov, A.R., and Zrinyi, M., *Novel highly elastic magnetic materials for dampers and seals: part II. Material behavior in a magnetic field.* Polymers for Advanced Technologies, 2007. **18**(7): p. 513 - 518.

85. Gangopadhyay, R. and De, A., *Conducting polymer nanocomposites: a brief overview.* Chemistry of Materials, 2000. **12**(3): p. 608-622.

86. Genetti, W., Yuan, W., Grady, B., O'rear, E., Lai, C., and Glatzhofer, D., *Polymer matrix composites: Conductivity enhancement through polypyrrole coating of nickel flake.* Journal of Materials Science, 1998. **33**(12): p. 3085-3093.

87. Jagur-Grodzinski, J., *Electronically conductive polymers.* Polymers for Advanced Technologies, 2002. **13**(9): p. 615-625.

88. Ausanio, G., Barone, A.C., Campana, C., Iannotti, V., Luponio, C., Pepe, G.P., and Lanotte, L., *Giant resistivity change induced by strain in a composite of conducting particles in an elastomer matrix.* Sensors and Actuators, A, 2006. **127**(1): p. 56-62.

89. Bednarek, S., *The coupling of magnetostriction and magnetoresistance in elastic ferromagnetic composites with conducting matrix.* Materials Science and Engineering B, 1999. **63**(3): p. 228-233.

90. Nguyen, V.Q. and Ramanujan, R.V., *Novel coiling behavior in Magnet-Polymer composites.* Macromolecular Chemistry and Physics, 2010. **211**(6): p. 618-626.

91. Josephson, R.K., *Mechanical power output from striated muscle during cyclic contraction.* Journal of Experimental Biology, 1985. **114**(1): p. 493.

92. Fernandez, D., Moreno, L., and Baselga, J. *Toward standardization of EAP actuators test procedures*. in *Smart Struct. Mater. : Electroact. Polym. Actuators Devices*. 2005. San Diego: SPIE.

93. Varga, Z., Filipcsei, G., Szilagyi, A., and Zrinyi, M., *Electric and magnetic field-structured smart composites.* Macromolecular Symposia, 2005. **227**: p. 123-133.

94. Gerlach, G. and Arndt, K., *Hydrogel Sensors and Actuators: Engineering and Technology*. 2009, New York: Springer Verlag. 272.

95. Adaptamat. *Actuator Applications*. [cited 12/1/2006]; Available from: http://www.adaptamat.com/technology/applications.php.

96. Zupan, M., Ashby, M.F., and Fleck, N.A., *Actuator classification and selection: The development of a database.* Advanced engineering materials, 2002. **4**(12).

97. Bell, D.J., Lu, T.J., Fleck, N.A., and Spearing, S.M., *MEMS actuators and sensors: observations on their performance and selection for purpose.* Journal of Micromechanics and Microengineering, 2005. **15**(3).

98. Shieh, J., Huber, J.E., Fleck, N.A., and Ashby, M.F., *The selection of sensors.* Progress in Materials Science, 2001. **46**: p. 461-504.

99. Qian, J. and Zhao, Y.P., *Materials selection in mechanical design for microsensors and microactuators.* Materials and Design, 2002. **23**(7): p. 619-625.

100. Srikar, V.T. and Spearing, S.M., *Materials selection for microfabricated electrostatic actuators.* Sensors and Actuators A: Physical, 2003. **102**(3): p. 279-285.

101. Ashby, M.F., Bréchet, Y.J.M., Cebon, D., and Salvo, L., *Selection strategies for materials and processes.* Materials and Design, 2004. **25**(1): p. 51-67.

102. Huber, J.E., *The selection of mechanical actuators based on performance indices.* Proceedings of the Royal Society of London Series A, 1997. **453**(1965): p. 2185-2205.

103. Liu, C. and Bar-Cohen, Y., *Scaling Laws of Microactuators and Potential Applications of Electroactive Polymers in MEMS.* Proceedings of SPIE's 6 thAnnual International Symposium on Smart Structures and Materials, Mar, 1999: p. 1-5.

104. Carpi, F., Smela, E., and MyiLibrary, *Biomedical applications of electroactive polymer actuators*. 2009, Wiltshire: Wiley Online Library. 496.

105. Otake, M., *Electroactive Polymer Gel Robots: Modelling and Control of Artifical Muscles*. 2010: Springer Verlag. 250.

106. Meijer, K., Rosenthal, M., and Full, R.J. *Muscle-like Actuators? A Comparison Between Three Electroactive Polymers*. in *Smart Structures and Materials 2001: Electroactive Polymer Actuators and Devices*. 2001.

107. Biomechanics-NTUPT. *Measurement of Muscle Strength*. [cited 2008 30/10]; Available from: http://www.pt.ntu.edu.tw/hmchai/Biomechanics/BMmeasure/MuscleStrengthMeasure.htm#strength.

108. Smolensky, A. and Ford, L., *The extensive length-force relationship of porcine airway smooth muscle.* Journal of Applied Physiology, 2007. **102**(5): p. 1906-1911.

109. Chai, H.-M. *Biomechanics of Skeletal Muscle*. [cited 10/10/2010]; Available from: http://www.pt.ntu.edu.tw/hmchai/bm03/bmmaterial/Muscle.htm.

110. Josephson, R.K., *Mechanical power output from striated muscle during cyclic contraction.* Journal of Experimental Biology, 1985. **114**: p. 493-512.

111. Colligan, L.H., *Muscles (The Amazing Human Body)*. 2009, New York: Benchmark Books. 78.

112. James, R.S., Cox, V.M., Young, I.S., and Altringham, J.D., *Mechanical properties of rabbit latissimus dorsi muscle after stretch and/or electrical stimulation.* Journal of Applied Physiology, 1997. **83**(2): p. 398-406.

113. Fernandez, D., Moreno, L., and Baselga, J. *Towards standardization of EAP actuators test procedures*. in *Smart Structures and Materials 2005: Electroactive Polymer Actuators and Devices*. 2005.

114. James, R.S., Wilson, R.S., and Askew, G.N., *Effects of caffeine on mouse skeletal muscle power output during recovery from fatigue.* Journal of Applied Physiology, 2004. **96**: p. 545-552.

115. Robert, J. and Meijer, K., *Metrics of Natural Muscle Function.* Electroactive Polymer (EAP) Actuators As Artificial Muscles: Reality, Potential, and Challenges, 2004.

116. Meijer, K. and Rosenthal, M. *Muscle-like actuators? A comparison between three electroactive polymers*. in *Smart Structures and Materials 2001: Electroactive Polymer Actuators and Devices* 2001. Newport Beach: SPIE.

117. Wood, D.S. and Camp, P.J., *Modeling the properties of ferrogels in uniform magnetic fields.* Physical Review E - Statistical, Nonlinear, and Soft Matter Physics, 2011. **83**(1): p. 01140211-01140219.

118. Stolbov, O.V. and Raikher, Y.L., *Deformation of a ferrovesicle in a uniform magnetic field.* Journal of Magnetism and Magnetic Materials, 2006. **300**(1): p. 199-202.

119. Morozov, K., Shliomis, M., and Yamaguchi, H., *Magnetic deformation of ferrogel bodies: Procrustes effect.* Physical Review E, 2009. **79**(4): p. 0408011-0408014.

120. Brauer, J.R., *Magnetic Actuators and Sensors*. 2006, Hoboken: Wiley-IEEE Press. 328.

121. Zrinyi, M., Szabo, D., and Barsi, L., *Magnetic Field Sensitive Polymeric Actuators*, in *Polymer sensors and actuators*, De Rossi, D. and Osada, Y., Editors. 1999, Springer: Berlin.

122. Diguet, G., Beaugnon, E., and Cavaillé, J.Y., *Shape effect in the magnetostriction of ferromagnetic composite.* Journal of Magnetism and Magnetic Materials, 2010. **322**(21): p. 3337-3341.

123. Rao, N.S. and O'Brien, K.T., *Design data for plastics engineers*. 1998, Cicinnati: Hanser Gardner. 207.

124. Snyder, R.L., Nguyen, V.Q., and Ramanujan, R.V., *The Mechanical Behavior of Magneto-Elastic Soft Actuators is Analogous to a Phase Transformation.* Acta Materialia, 2010. **58**(17): p. 5620-5630.

125. Thompson, J.M.T., *Instabilities and catastrophes in science and engineering*. 1982, Chichester: John Wiley and Sons. 226.

126. Snyder, R.L., Nguyen, V.Q., and Ramanujan, R.V., *Design of Magneto-elastic Soft Actuators.* Smart Materials and Structures, 2010. **19**(5): p. 055017-8.

127. Zrínyi, M., Szabó, D., and Kilian, H.-G., *Kinetics of the shape change of magnetic field sensitive polymer gels.* Polymer Gels and Networks, 1998. **6**(6): p. 441-454.

128. Medler, S. and Hulme, K., *Frequency-dependent power output and skeletal muscle design.* Comparative Biochemistry and Physiology, Part A, 2009. **152**(2009): p. 407-417.

129. Faidley, L., Han, Y., Tucker, K., Timmons, S., and Hong, W., *Axial strain of ferrogels under cyclic magnetic fields.* Smart Materials and Structures, 2010. **19**: p. 0750011-0750017.

130. Male, S.E., *Magnetic susceptibility and separation of inorganic material from UK coals.* Journal of Physics D: Applied Physics, 1984. **17**(1): p. 155-161.

131. Pankhurst, Q.A., Connolly, J., Jones, S.K., and Dobson, J., *Applications of magnetic nanoparticles in biomedicine.* Journal of Physics D: Applied Physics, 2003. **36**(13): p. 167-181.

132. Ngomsik, A.F., Bee, A., Draye, M., Cote, G., and Cabuil, V., *Magnetic nano- and microparticles for metal removal and environmental applications: a review: Thiochimie aux polyoxanions.* Comptes rendus. Chimie, 2005. **8**(6-7): p. 963-970.

133. Ohara, T., Kumakura, H., and Wada, H., *Magnetic separation using superconducting magnets.* Physica C, 2001. **357**(2002): p. 1272-1280.

134. Lide, D.R., *CRC handbook of chemistry and physics*. 85th ed. 2004, Florida: CRC Press Boca Raton.

135. O'Handley, R.C., *Modern Magnetic Materials: Principles and Applications*. 1999, New York: Wiley-interscience. 768.

136. Davis, J.R., *ASM handbook. Vol. 2, Properties and selection: nonferrous alloys and special-purpose materials*: ASM International.

137. McCurrie, R.A., *Ferromagnetic Materials: Structure and Properties*. 1994, San Diego: Academic Press.

138. Chicazumi, S., *Physics of Magnetism*. 1964, New York: John Wiley and Sons.

139. Brailsford, F., *Physical principles of magnetism*. 1966, London: Van Nostrand.

140. Gray, D.E., *American Institute of Physics handbook*. 1972, New York: McGraw-Hill.

141. Reddy, J.N., *An Introduction to the Finite Element Method. McGraw-Hill*. 2nd ed. 2006, New York: MaGraw-Hill.

142. Ansoft. *Maxwell SV Product*. [cited 20/8/2006]; Available from: http://www.ansoft.com/maxwellsv/.

143. Boyd Iv, J.G., Lagoudas, D.C., and Seo, C.S., *Arrays of micro-electrodes and electromagnets for processing of electro-magneto-elastic multifunctional composite materials.* Proceedings of SPIE, 2003. **5055**: p. 268.

144. Holmes, A.S., Hong, G., and Pullen, K.R., *Axial-flux permanent magnet machines for micropower generation.* Microelectromechanical Systems, Journal of, 2005. **14**(1): p. 54-62.

145. Pan, C.T., *Polymeric magnetic microactuator with efficient permalloy loop design.* Microsystem Technologies, 2005. **11**(1): p. 1-10.

146. Yamada, R., Kim, S.W., Lee, A., Wands, R., Rey, J.M., and Wake, M., *Quenches and resulting thermal and mechanical effects on epoxyimpregnated Nb 3 Sn high field magnets.* Particle Accelerator Conference, 2001. PAC 2001. Proceedings of the 2001, 2001. **5**.

147. Tang, W.C., Nguyen, T.C.H., and Howe, R.T., *Laterally driven polysilicon resonant microstructures.* Micro Electro Mechanical Systems, 1989, Proceedings,'An Investigation of Micro Structures, Sensors, Actuators, Machines and Robots'. IEEE, 1989: p. 53-59.

148. Ansys. *Multiphysics Product Overview*. [cited 23/11/2006]; Available from: http://www.ansys.com/products/multiphysics.asp.

149. Avdeev, I., Gyimesi, M., Lovell, M., and Ostergaard, D., *Strongly coupled three-dimensional finite element transducer.* Journal of Micromechanics and Microengineering, 2004. **14**(11): p. 1491-1502.

150. Gyimesi, M., Avdeev, I., and Ostergaard, D., *Finite-Element Simulation of Micro-Electromechanical Systems (MEMS) by Strongly Coupled Electromechanical Transducers.* Magnetics, IEEE Transactions on, 2004. **40**(2): p. 557-560.

151. Ansys, I., *Coupled-Field Analysis Guide*, in *ANSYS Release 10.0 Documentation*. 2006, Canonsburg: Pennsylvania, USA.

152. Shapoorabadi, R.J. and Kirk, A.G., *Comparison of three finite element models for analysis of MEMS micromirrors.* Proceedings of SPIE, 2004. **5577**: p. 849.

153. Chanda, M. and Roy, S., *Plastics Fundamentals, Properties, and Testing*. 2008, Boca Raton: CRC. 280.

154. Mark, J.E., *Physical properties of polymers handbook*. 2nd ed. 2007, New York: Springer Verlag. 1076.

155. Fried, J., *Polymer science and technology*. 2nd ed. 2003, Upper Saddle River: Prentice Hall. 608.

156. Progelhof, R. and Throne, J., *Polymer Engineering Principles. Properties, Processes, and Tests for Design*. 1992, Munich: Hanser Publishers. 936.

157. Eftekhari, A., *Nanostructured conductive polymers*. 2010, New York: John Wiley & Sons. 800.

158. Wong, C., Li, Y., and Lu, D., *Electrical Conductive Adhesives with Nanotechnologies*. 2009, New York: Springer Verlag. 437.

159. Inzelt, G., *Conducting Polymers: A New Era in Electrochemistry*, ed. Scholz, F. 2009, Berlin: Springer. 282.

160. Lux, F., *Models proposed to explain the electrical conductivity of mixtures made of conductive and insulating materials.* Journal of Materials Science, 1993. **28**(2): p. 285-301.

161. Lei, H., Pitt, W.G., McGrath, L.K., and Ho, C.K., *Modeling carbon black/polymer composite sensors.* Sensors and Actuators B: Chemical, 2007. **125**(2): p. 396-407.

162. Sun, D. and Wei, Y., *Study of the conductive paths of carbon black filled polyethylene composites by the alternating current impedance method.* Journal of Applied Polymer Science, 2008. **108**(6): p. 3748-3752.

163. Wu, Y., Zhou, W., Wang, B., and Yang, F., *Modeling and characterization of two-phase composites by Voronoi diagram in the Laguerre geometry based on random close packing of spheres.* Computational Materials Science, 2010. **47**(4): p. 951-961.

164. Ambroži , M., *The percolation threshold in systems of permeable ellipses.* The European Physical Journal Applied Physics, 2008. **41**(2): p. 121-127.

165. Keith, J.M., King, J.A., and Barton, R.L., *Electrical conductivity modeling of carbon filled liquid crystalline polymer composites.* Journal of Applied Polymer Science, 2006. **102**(4): p. 3293-3300.

166. Ambrozic, M. and Dakskobler, A., *Some aspects of numerical analysis of conductivity percolation threshold.* Journal of the European Ceramic Society, 2007. **27**(2-3): p. 541-544.

167. Dweiri, R. and Sahari, J., *Computer simulation of electrical conductivity of graphite-based polypropylene composites based on digital image analysis.* Journal of Materials Science, 2007. **42**(24): p. 10098-10102.

168. Mamunya, Y.P., Muzychenko, Y.V., Pissis, P., Lebedev, E.V., and Shut, M.I., *Percolation phenomena in polymers containing dispersed iron.* Polymer Engineering & Science, 2002. **42**(1): p. 90 - 100.

169. Clingerman, M.L., Weber, E.H., King, J.A., and Schulz, K.H., *Development of an additive equation for predicting the electrical conductivity of carbon filled composites.* Journal of Applied Polymer Science, 2003. **88**(9): p. 2280-2299.

170. Nakamura, S., Tommura, T., and Sawa, G. *Electrical conduction mechanism of polymer-carbon black composites below and above the percolation threshold*. 2002: IEEE.

171. Zhang, W., Dehghani-Sanij, A.A., and Blackburn, R.S., *Carbon based conductive polymer composites.* Journal of Materials Science, 2007. **42**(10): p. 3408-3418.

172. Vionnet-Menot, S., Grimaldi, C., Maeder, T., Strässler, S., and Ryser, P., *Tunneling-percolation origin of nonuniversality: Theory and experiments.* Physical Review B, 2005. **71**(6): p. 64201.

173. Novák, I. and Florián, Š., *Pressure-sensitive adhesives for electronic applications.* Journal of Materials Science Letters, 2003. **22**(18): p. 1237-1239.

174. Huang, J.C., *Carbon Black Filled Conducting Polymers and Polymer Blends.* Advances in Polymer Technology(USA), 2002. **21**(4): p. 299-313.

175. Chen, G., Lu, J., Lu, W., Wu, D., and Wu, C., *Time-dependence of piezo-resistive behavior for polyethylene/foliated graphite nanocomposites.* Polymer International, 2005. **54**(12): p. 1689-1693.

176. Ambroži , M., Dakskobler, A., and Valant, M., *Influence of the geometrical parameters on the conductivity percolation threshold.* The European Physical Journal Applied Physics, 2006. **35**(2): p. 85-92.

177. Lebovka, N., Lisunova, M., Mamunya, Y.P., and Vygornitskii, N., *Scaling in percolation behaviour in conductive–insulating composites with particles of different size.* Journal of Physics D: Applied Physics, 2006. **39**: p. 2264.

178. Xue, Q., *The influence of particle shape and size on electric conductivity of metal-polymer composites.* European Polymer Journal, 2004. **40**(2): p. 323-327.

179. Clingerman, M.L., King, J.A., Schulz, K.H., and Meyers, J.D., *Evaluation of electrical conductivity models for conductive polymer composites.* Journal of Applied Polymer Science, 2002. **83**(6): p. 1341-1356.

180. Mamunya, Y. *Polymer blends filled with carbon black: Structure and electrical properties*. in *Die Makromolekulare Chemie. Macromolecular symposia*. 2001: WILEY-VCH Verlag GmbH Weinheim.

181. Chung, D.D.L., *Self-monitoring structural materials.* Materials Science and Engineering: R: Reports, 1998. **22**(2): p. 57-78.

182. Machado, W.S., Athayde, P.L., Mamo, M.A., van Otterlo, W.A.L., Coville, N.J., and Hümmelgen, I.A., *Hydrostatic pressure sensor based on carbon sphere-Polyvinyl alcohol composites.* Organic Electronics, 2010.

183. Lacasse, M.A., Duchaine, V., and Gosselin, C. *Characterization of the electrical resistance of carbon-black-filled silicone: Application to a flexible and stretchable robot skin*. 2010: IEEE.

184. Gau, C., Ko, H., and Chen, H., *Piezoresistive characteristics of MWNT nanocomposites and fabrication as a polymer pressure sensor.* Nanotechnology, 2009. **20**: p. 185503.

185. Athanassiou, E., Krumeich, F., Grass, R., and Stark, W., *Advanced Piezoresistance of Extended Metal-Insulator Core-Shell Nanoparticle Assemblies.* Physical Review Letters, 2008. **101**(16): p. 166804.

186. Cochrane, C., Lewandowski, M., and Koncar, V., *A Flexible Strain Sensor Based on a Conductive Polymer Composite for in situ Measurement of Parachute Canopy Deformation.* Sensors, 2010. **10**(9): p. 8291-8303.

187. Wichmann, M.H.G., Buschhorn, S.T., Gehrmann, J., and Schulte, K., *Piezoresistive response of epoxy composites with carbon nanoparticles under tensile load.* Physical Review B, 2009. **80**(24): p. 245437.

188. Zavickis, J., Knite, M., Ozols, K., and Malefan, G., *Development of percolative electroconductive structure in piezoresistive polyisoprene-nanostructured carbon composite during vulcanization.* Materials Science and Engineering: C, 2010.

189. Nanni, F., Ruscito, G., Puglia, D., Terenzi, A., Kenny, J., and Gusmano, G., *Effect of carbon black nanoparticle intrinsic properties on the self-monitoring performance of glass fibre reinforced composite rods.* Composites Science and Technology, 2010.

190. Aneli, J.N., Zaikov, G.E., and Khananashvili, L.M., *Effects of mechanical deformations on the structurization and electric conductivity of electric conducting polymer composites.* Journal of Applied Polymer Science, 1999. **74**(3): p. 601-621.

191. Feng, J. and Chan, C., *Effects of strain and temperature on the electrical properties of carbon black-filled alternating copolymer of ethylene-tetrafluoroethylene composites.* Polymer Engineering & Science, 2003. **43**(5): p. 1064-1070.

192. Lanotte, L., Ausanio, G., Hison, C., Iannotti, V., Luponio, C., and Luponio Jr, C., *State of the art and development trends of novel nanostructured elastomagnetic composites.* Journal of Optoelectronics and Advanced Materials, 2004. **6**(2): p. 523-532.

193. Kost, J., Narkis, M., and Foux, A., *Effects of axial stretching on the resistivity of carbon black filled silicone rubber.* Polymer Engineering and Science, 1983. **23**(10): p. 567-571.

194. Flandin, L., Chang, A., Nazarenko, S., Hiltner, A., and Baer, E., *Effect of strain on the properties of an ethylene-octene elastomer with conductive carbon fillers.* Journal of Applied Polymer Science, 2000. **76**(6): p. 894-905.

195. Pramanik, P.K., Khastagir, D., and Saha, T.N., *Effect of extensional strain on the resistivity of electrically conductive nitrile-rubber composites filled with carbon filler.* Journal of Materials Science, 1993. **28**(13): p. 3539-3546.

196. Luheng, W., Tianhuai, D., and Peng, W., *Influence of carbon black concentration on piezoresistivity for carbon-black-filled silicone rubber composite.* Carbon, 2009. **47**(14): p. 3151-3157.

197. González-Correa, C., Screaton, G., Hose, D., Brown, B., Avis, N., and Kleinermann, F., *Resistivity changes in conductive silicone sheets under stretching.* Physiological Measurement, 2002. **23**: p. 183.

198. Zhang, R., Baxendale, M., and Peijs, T., *Universal resistivity–strain dependence of carbon nanotube/polymer composites.* Physical Review B, 2007. **76**(19): p. 195433.

199. Wang, L., Ding, T., and Wang, P., *Effects of compression cycles and precompression pressure on the repeatability of piezoresistivity for carbon black-filled silicone rubber composite.* Journal of Polymer Science Part B: Polymer Physics, 2008. **46**(11): p. 1050-1061.

200. Voet, A., Cook, F., and Sircar, A., *Relaxation of stress and electrical resistivity in carbon-filled vulcanizates at minute shear strains.* Rubber Chemistry and Technology, 1971. **44**: p. 175–84.

201. Kost, J., Foux, A., and Narkis, M., *Quantitative model relating electrical resistance, strain, and time for carbon black loaded silicone rubber.* Polymer Engineering and Science, 1994. **34**(21): p. 1628-1634.

202. Ding, T., Wang, L., and Wang, P., *Changes in electrical resistance of carbon-black-filled silicone rubber composite during compression.* Journal of Polymer Science Part B: Polymer Physics, 2007. **45**(19): p. 2700-2706.

203. Min, W., Ying, H., Yunjian, G., Xiulan, F., and Panfeng, H. *A Study of Resistance Relaxation Phenomenon Based on Carbon Black/Silicone Rubber System Flexible Tactile Sensor*. in *International Conference on Information Acquisiton*. 2007. Jeju City: IEEE.

204. Wang, L., Ding, T., and Wang, P., *Research on stress and electrical resistance of skin-sensing silicone rubber/carbon black nanocomposite during decompressive stress relaxation.* Smart Materials and Structures, 2009. **18**: p. 065002.

205. Wang, P. and Ding, T., *Creep of electrical resistance under uniaxial pressures for carbon black–silicone rubber composite.* Journal of Materials Science, 2010. **45**(13): p. 3595-3601.

206. Granta. *CES Material & Process Selectors*. [cited 3/9/2006]; Available from: http://www.grantadesign.com/products/ces/index.htm.

207. Budinski, K.G., *Engineering materials: properties and selection*. 7th ed. 2002: Prentice Hall.

208. Brydson, J.A., *Rubbery materials and their compounds*. 1988: Elsevier.

209. Rubber, T. *The elastomers*. [cited 17/7/2006]; Available from: http://www.timcorubber.com/definitions/index.asp.

210. Ciullo, P.A. and Hewitt, N., *The Rubber Formulary*. 1999: Plastics Design Library.

211. Corporation, Q.C.G.R. *Materials*. [cited 26/7/2006]; Available from: http://www.quickcutgasket.com/materials.html.

212. Harper, C.A., *Handbook of Plastics, Elastomers & Composites*. 2002: McGraw-Hill Professional.

213. Randall, D. and Lee, S., *The Polyurethanes Book*. 2002: Huntsman Polyurethanes; Distributed by John Wiley and Sons.

214. Salamone, J.C., *Polymeric Materials Encyclopedia.* CRC Press, Inc, 2000 Corporate Blvd, NW, Boca Raton, FL 33431, USA, 1996., 1996.

215. Bhowmick, A.K., Stephens, H.L., and Bhowmick, B.K., *Handbook of Elastomers*. 2001: CRC Press.

216. Mark, J.E., Lal, J., and Meeting, A.C.S.D.o.P.C.A.C.S., *Elastomers and rubber elasticity : based on a symposium*. 1982, Washington, D.C: The Society.

217. Treloar, L.R.G., *The Physics of Rubber Elasticity, Clarendon*. 3rd ed. 1975: Oxford.

218. Cha, W.I., Hyon, S.H., Graiver, D., and Ikada, Y., *Sticky poly (vinyl alcohol) hydrogels.* Journal of Applied Polymer Science, 1993. **47**(2): p. 339-343.

219. Company, S.-O. *Liquid Rubber and Mold Rubber from Smooth-On*. [cited 27/7/2006]; Available from: http://www.smooth-on.com/liqrubr.htm.

220. Silicones, G. *Product Category - Elastomers + Silicone Rubber*. [cited 27/7/2006]; Available from: http://www.gesilicones.com/gesilicones/am1/en/category/prod_category_landing.jsp?categoryId=7.

221. Jamani, K.D., Harrington, E., and Wilson, H.J., *Rigidity of elastomeric impression materials.* J Oral Rehabil, 1989. **16**(3): p. 241-8.

222. Coltène/Whaledent. *Product Information - C-silicone*. [cited 27/7/2006]; Available from: http://www.coltenewhaledent.biz/index.php?TPL=10034&x1200_article_id=117&x1200_node=29.

223. Smooth-On. *Ecoflex Series*. [cited 12/6/2006]; Available from: http://tb.smodev.com/tb/uploads/Ecoflex_Series.pdf.

224. Caruntu, D., Caruntu, G., Chen, Y., O'Connor, C.J., Goloverda, G., and Kolesnichenko, V.L., *Synthesis of variable-sized nanocrystals of $Fe_3O_4$ with high surface reactivity.* Chemistry of Materials, 2004. **16**(25): p. 5527-5534.

225. Solutions, M.E. *Electroless Nickel/Immersion Gold*. [cited 5/11/2006]; Available from: http://www.macdermid.com/electronics/finalfini_electroless.html.

226. Health, N.I.o. *ImageJ Homepage*. [cited 24/1/2006]; Available from: http://rsb.info.nih.gov/ij/.

227. James, R.S., Young, I.S., Cox, V.M., Goldspink, D.F., and Altringham, J.D., *Isometric and isotonic muscle properties as determinants of work loop power output.* Pflügers Archiv European Journal of Physiology, 1996. **432**(5): p. 767-774.

228. Worledge, D.C., *Reduction of positional errors in a four-point probe resistance measurement.* Applied Physics Letters, 2004. **84**(10): p. 1695-1697.

229. Polyakov, V.V. and Egorov, A.V., *Dependence of the magnetic permeability of ferromagnetic powder materials on particle size.* Powder Metallurgy and Metal Ceramics, 1995. **33**(1): p. 9-10.

230. Nowosielski, R., *Soft magnetic polymer-metal composites consisting of nanostructural Fe-basic powders.* Journal of Achievements in Materials and Manufacturing Engineering, 2007. **24**(1): p. 68-77.

231. Ngomsik, A.F., Bee, A., Draye, M., Cote, G., and Cabuil, V., *Magnetic nano-and microparticles for metal removal and environmental applications: a review.* Comptes rendus-Chimie, 2005. **8**(6-7): p. 963-970.

232. Gong, W., Li, H., Zhao, Z., and Chen, J., *Ultrafine particles of Fe, Co, and Ni ferromagnetic metals.* Journal of Applied Physics, 1991. **69**(8): p. 5119-5121.

233. Leslie-Pelecky, D.L. and Rieke, R.D., *Magnetic properties of nanostructured materials.* Chem. Mater, 1996. **8**(8): p. 1770–1783.

234. Farhoud, M.S., *Fabrication and Characterization of Nanostructured Magnetic Particles for Applications in Data Storage*. 2001, Massachusetts Institute of Technology. p. 148.

235. Gea, S., Bilotti, E., Reynolds, C., Soykeabkeaw, N., and Peijs, T., *Bacterial cellulose-poly (vinyl alcohol) nanocomposites prepared by an in-situ process.* Materials Letters, 2010. **64**(8): p. 901-904.

236. Bichara, D.A., Zhao, X., Bodugoz-Senturk, H., Ballyns, F.P., Oral, E., Randolph, M.A., Bonassar, L.J., Gill, T., and Muratoglu, O.K., *Porous Poly (vinyl Alcohol)-Hydrogel Matrix-Engineered Bio-Synthetic Cartilage*. Tissue Engineering, 2010(ja).

237. Nath, D.C.D., Bandyopadhyay, S., Yu, A., Blackburn, D., and White, C., *High strength bio-composite films of poly (vinyl alcohol) reinforced with chemically modified-fly ash.* Journal of Materials Science, 2010. **45**(5): p. 1354-1360.

238. Bodugoz-Senturk, H., Macias, C.E., Kung, J.H., and Muratoglu, O.K., *Poly (vinyl alcohol)-acrylamide hydrogels as load-bearing cartilage substitute.* Biomaterials, 2009. **30**(4): p. 589-596.

239. Pan, Y. and Xiong, D., *Study on compressive mechanical properties of nanohydroxyapatite reinforced poly (vinyl alcohol) gel composites as biomaterial.* Journal of Materials Science: Materials in Medicine, 2009. **20**(6): p. 1291-1297.

240. Peppas, N.A. and Merrill, E.W., *Poly (vinyl alcohol) hydrogels: Reinforcement of radiation-crosslinked networks by crystallization.* Journal of Polymer Science Polymer Chemistry Edition, 1976. **14**(2): p. 441-457.

241. Watase, M., Nishinari, K., and Nambu, M., *Rheological properties of an anomalous poly (vinyl alcohol) gel.* Polymer Communications (Guildford, England), 1983. **24**(2): p. 52-54.

242. Nambu, M., *Rubber-like poly (vinyl alcohol) gel.* Kobunshi Ronbunshu, 1990. **47**: p. 695–703.

243. Hyon, S., Cha, W., and Ikada, Y., *Preparation of poly(vinyl alcohol) hydrogels by low-temperature crystallization of the aqueous poly(vinyl alcohol) solution.* Kobunshi ronbunshu(Tokyo), 1989. **46**(11): p. 673-680.

244. Nagura, M., Hamano, T., and Ishikawa, H., *Structure of poly(vinyl alcohol) hydrogel prepared by repeated freezing and melting.* Polymer, 1989. **30**(4): p. 762-765.

245. Darwis, D., Yoshii, F., Makuuchi, K., and Razzak, M.T., *Improvement of hot water resistance of poly (vinyl alcohol) hydrogel by acetalization and irradiation techniques.* Journal of Applied Polymer Science, 1995. **55**(12): p. 1619-1625.

246. Cha, W.I., Hyon, S.H., and Ikada, Y., *Transparent poly (vinyl alcohol) hydrogel with high water content and high strength.* Macromolecular chemistry and physics(Print), 1992. **193**(8): p. 1913-1925.

247. Trieu, H. and Qutubuddin, S., *Poly (vinyl alcohol) hydrogels: 2. Effects of processing parameters on structure and properties.* Polymer, 1995. **36**(13): p. 2531-2539.

248. Guenet, J.M., *Thermoreversible gelation of polymers and biopolymers*. 1992: Academic Press London.

249. Farshad, M. and Le Roux, M., *Compression properties of magnetostrictive polymer composite gels.* Polymer testing, 2005. **24**(2): p. 163-168.

250. Carlson, J.D. and Jolly, M.R., *MR fluid, foam and elastomer devices.* Mechatronics, 2000. **10**(4): p. 555-569.

251. Ginder, J.M., Schlotter, W.F., and Nichols, M.E. *Magnetorheological elastomers in tunable vibration absorbers*. in *Smart Struct. Mater. : Damping and Isolation*. 2001. Newport Beach: SPIE.

252. Brown, W.F., *Magnetostatic Principles in Ferromagnetism*. 1962: North-Holland.

253. Pao, Y.H., *Electromagnetic forces in deformable continua*, in *Mechanics Today*, Nevat-Nasser, Editor. 1978, Pergamon Press: New York. p. A78-35706.

254. Moon, F.C., *Magneto-Solid Mechanics*. 1984, New York: John Wiley and Sons. 448.

255. Liu, M., Liu, X., Wang, J., Wei, Z., and Jiang, L., *Electromagnetic synergetic actuators based on polypyrrole/$Fe_3O_4$ hybrid nanotube arrays.* Nano Research, 2010. **3**(9): p. 670-675.

256. Hunter, I.W. and Lafontaine, S., *A comparison of muscle with artificial actuators*, in *Solid-State Sensor and Actuator Workshop, 1992. 5th Technical Digest., IEEE*. 1992, IEEE: Hilton Head Island p. 178-185.

257. Filipcsei, G., Csetneki, I., and Szilágyi, A., *Magnetic field-responsive smart polymer composites.* Advances in Polymer Science, 2007. **206**: p. 137-190.

258. Floyd, R.T. and Thompson, C.W., *Manual of structural kinesiology*. 2001, Boston: McGraw-Hill. 384.

259. Sorenson, K.G., *Post buckling behavior of a circular rod constrained within a circular cylinder*. 1984, Rice University. p. 157.

260. Hibbeler, R.C., *Mechanics of Materials*. 6th ed. 2005, Upper Saddle, NJ, USA: Prentice Hall. 873.

261. Moon, F.C., *Problems in magneto-solid mechanics.* Mechanics today, 1978. **4**: p. 307-390.

262. Woodson, H.H. and Melcher, J.R., *Electromechanical Dynamics, Part 11: Fields, Forces, and Motion*. 1968: John Wiley and Sons.

263. Valverde, J. and Van Der Heijden, G. *Instability of a whirling conducting rod in the presence of a magnetic field. Application to the problem of space tethers*. in *ASME Int. Des. Eng. Tech. Conf. & Comput. Inf. Eng. Conf.* 2005. Long Beach: ASME.

264. DeBlois, R.W., *Ferromagnetic Properties of Single Crystal Nickel Platelets and Submicron Whiskers.* Journal of Applied Physics, 1967. **38**: p. 1291.

265. Popelar, C.H. and Bast, C.O., *An experimental study of the magnetoelastic postbuckling behavior of a beam.* Experimental Mechanics, 1972. **12**(12): p. 537-542.

266. Naciri, J., Srinivasan, A., Jeon, H., Nikolov, N., Keller, P., and Ratna, B.R., *Nematic elastomer fiber actuator.* Macromolecules, 2003. **36**(22): p. 8499-8505.

267. Medler, S. and Hulme, K., *Frequency-dependent power output and skeletal muscle design.* Comparative Biochemistry and Physiology A: Physiology, 2009. **152**(3): p. 407-417.

268. Bhattacharya, S.K., *Metal-Filled Polymers: Properties and Applications*. 1986, New York: Marcel Dekker Ltd. 360.

269. Beruto, D., Capurro, M., and Marro, G., *Piezoresistance behavior of silicone-graphite composites in the proximity of the electric percolation threshold.* Sensors and Actuators A: Physical, 2005. **117**(2): p. 301-308.

270. Das, N., Chaki, T., and Khastgir, D., *Effect of axial stretching on electrical resistivity of short carbon fibre and carbon black filled conductive rubber composites.* Polymer International, 2002. **51**(2): p. 156-163.

271. Yamaguchi, K., Busfield, J., and Thomas, A., *Electrical and mechanical behavior of filled elastomers. I. The effect of strain.* Journal of Polymer Science Part B: Polymer Physics, 2003. **41**(17): p. 2079-2089.

272. Knite, M., Teteris, V., Polyakov, B., and Erts, D., *Electric and elastic properties of conductive polymeric nanocomposites on macro-and nanoscales.* Materials Science and Engineering: C, 2002. **19**(1-2): p. 15-19.

273. Ausanio, G., Barone, A., Hison, C., Iannotti, V., and Luponio, C., *Mechanical vibration sensor based on elastomagnetic composite.* Sensors and Actuators A: Physical, 2006. **129**(1-2): p. 25-28.

274. Goubault, C., Jop, P., Fermigier, M., Baudry, J., Bertrand, E., and Bibette, J., *Flexible magnetic filaments as micromechanical sensors.* Physical Review Letters, 2003. **91**(26): p. 260802-260805.

275. Electronics, B. *Bicron Tubular, Frame and Rotary Solenoids*. [cited 20/4/2006]; Available from: http://www.bcrn.com/solenoids.html.

276. Ullakko, K., Huang, J.K., Kantner, C., O'Handley, R.C., and Kokorin, V.V., *Large magnetic-field-induced strains in $Ni_2MnGa$ single crystals.* Applied Physics Letters, 1996. **69**(13): p. 1966-1968.

277. Joshi, C.H. *Compact magnetostrictive actuators and linear motors*. in *Actuator 2000*. 2000. Bremen.

278. Etrema. *Actuator products*. [cited 20/1/2006]; Available from: http://www.etrema-usa.com/products/actuators/.

279. Karaca, H.E., Karaman, I., Basaran, B., Ren, Y., Chumlyakov, Y.I., and Maier, H.J., *Magnetic Field-Induced Phase Transformation in NiMnCoIn Magnetic Shape-Memory Alloys-A New Actuation Mechanism with Large Work Output.* Advanced Functional Materials, 2009. **19**(7).

280. Karaca, H.E., Karaman, I., Basaran, B., Lagoudas, D.C., Chumlyakov, Y.I., and Maier, H.J., *On the stress-assisted magnetic-field-induced phase transformation in $Ni_2MnGa$ ferromagnetic shape memory alloys.* Acta Materialia, 2007. **55**(13): p. 4253-4269.

281. Nikitin, L.V. and Samus, A.N., *Magnetoelastics and Their Properties.* International Journal of Modern Physics B, 2005. **19**(07-09): p. 1360-1366.

282. Zimmermann, K., Naletova, V.A., Zeidis, I., Turkov, V.A., Kolev, E., Lukashevich, M.V., and Stepanov, G.V., *A deformable magnetizable worm in a magnetic field—A prototype of a mobile crawling robot.* Journal of Magnetism and Magnetic Materials, 2007. **311**(1): p. 450-453.

283. Forshaw, J.M. and Kirshner, D., *Encyclopedia of birds*. 2nd ed. Natural world. 1998, San Diego, CA: Academic Press. 240 p.

284. Zheng, Y., Cheng, Y., Bao, F., and Wang, Y., *Synthesis and magnetic properties of $Fe_3O_4$ nanoparticles.* Materials Research Bulletin, 2006. **41**(3): p. 525-529.

285. Madden, J., Rinderknecht, D., Anquetil, P., and Hunter, I., *Creep and cycle life in polypyrrole actuators.* Sensors and Actuators A: Physical, 2007. **133**(1): p. 210-217.

286. Webster, B., *A pair of skilled hands to guide and artificial heart: Robert Kiffler Jarvik*, in *The New York Times*. 1982: New York.

287. Abiomed. *Heart Replacement*. [cited 12/2/2007]; Available from: http://www.abiomed.com/products/heart_replacement.cfm.

288. Klein, D., *Current trends in cardiac transplantation.* Critical Care Nursing Clinics of North America, 2007. **19**(4): p. 445-460.

289. Fraden, J., *Handbook of modern sensors: Physics, Designs, and Applications*. 3rd ed. 2004, New York: Springer Verlag. 589.

290. Fleck, N., *Some aspects of clip gauge design.* Strain, 1983. **19**(1): p. 17-22.

291. Knite, M., Teteris, V., Kiploka, A., and Kaupuzs, J., *Polyisoprene-carbon black nanocomposites as tensile strain and pressure sensor materials.* Sensors and Actuators A: Physical, 2004. **110**(1-3): p. 142-149.

292. Hinkley, J.A., Savitzky, A.H., Rivera, G., and Gehrke, S.H., *Tensile Properties of Hydrogels and of Snake Skin*, in *First World Congr. Biomimetics Artif. Muscles*. 2002: Albuquerque, New Mexico.

293. Hassan, C.M. and Peppas, N.A., *Structure and applications of poly (vinyl alcohol) hydrogels produced by conventional crosslinking or by freezing/thawing methods.* Adv. Polym. Sci, 2000. **153**: p. 37–65.

# PUBLICATIONS AND CONFERENCES

**Journal Publications**

1. Nguyen, V.Q. and Ramanujan, R.V., *Novel coiling behavior in Magnet-Polymer composites.* Macromolecular Chemistry and Physics, 2010. **211**(6): p. 618-626. (featured in cover page)
2. Snyder, R.L., Nguyen, V.Q., and Ramanujan, R.V., *The Mechanical Behavior of Magneto-Elastic Soft Actuators is Analogous to a Phase Transformation.* Acta Materialia, 2010. **58**(17): p. 5620-5630.
3. Snyder, R.L., Nguyen, V.Q., and Ramanujan, R.V., *Design of Magneto-elastic Soft Actuators.* Smart Materials and Structures, 2010. **19**(5): p. 055017-8.
4. Ang, D., Nguyen, Q., Kayal, S., Preiser, P., Rawat, R., and Ramanujan, R., *Insights into the Mechanism of Magnetic Particle Assisted Gene Delivery.* Acta Biomaterialia, 2010. **7**(3): p. 1319-1326
5. Nguyen, V.Q., Rawat, R., and Ramanujan, R., *Dynamic Properties of Manget-Polymer Composites.* Composites Science and Technology, 2011. **submitted, in review**.
6. Nguyen, V. and Ramanujan, R., *Magnet-Polymer Artificial Muscles.* 2011. **in preparation**.
7. Nguyen, V. and Ramanujan, R., *Magnet-Polymer Composites as Soft Transducers.* 2011. **in preparation**.

**Conference Presentations**

1. Ramanujan, R. and Nguyen, Q. *Magnet-Polymer Soft Transducers*. in *MRS Spring Meeting*, USA. 2010.
2. Ramanujan, R. and Nguyen, Q. *Magnet-Polymer Nanocomposites for Shape Changing Structures* ***(invited talk)***. in *TMS Annual Meeting*, USA. 2009.
3. Nguyen, Q. and Ramanujan, R. *Mechanical Behavior of Novel Transducers Based on Magnetic-Polymer Composites* ***(invited talk)***. in *International Conference on Materials for Advanced Technologies*, Singapore. 2009.
4. Nguyen, Q. and Ramanujan, R. *Magnet-Polymer composite material for intelligent shape changing structures*. in *International Conference on Materials Processing for Properties and Performance*, Singapore. 2008.
5. Nguyen, Q. and Ramanujan, R. *Magnet-Polymer (MAGPOL) composite transducers for biomedical applications*. in *International Conference on Cellular and Molecular Bioengineering*, Singapore. 2007.

# APPENDIX A: PERFORMANCE BENCHMARK OF ARTIFICIAL MUSCLES

Table A summarizes the properties of typical candidate materials for artificial muscle applications.

**Table A:** Some performance benchmarks of artificial muscle materials (N/A is not available/applicable) ([12, 24])

| | **Mammalian Skeletal Muscle** | **Dielectric Elastomers** | **Relaxor Ferroelectric Polymers** |
|---|---|---|---|
| Strain (%) | 20 typical<br>40 maximum | 120 - 380 | 3.5 typical<br>7 maximum |
| Strain Rate (%s-1) | >50 maximum | 450 - 34000 | Typical N/A<br>> 2000 max |
| Stress (MPa) | 0.1 (sustainable)<br>0.35 maximum | 0.3 - 1.6 typical<br>3.2 - 7.7 maximum | 20 typical<br>40 maximum |
| Modulus (MPa) | 10 - 60 typical | 0.1 - 1 typical<br>1 - 3 maximum | 400 typical<br>1200 maximum |
| Work Density (kJ.m-3) | 8 typical<br>40 maximum | 10 - 150 typical<br>750 - 3400 max | 320 typical<br>>1000 max |
| Density (kg.m-3) | 1037 typical | 960 - 1100 | 1870 typical<br>2000 maximum |
| Specific Power (W.kg-1) | 50 typical<br>284 maximum | 3600 - 5000 | N/A |
| Efficiency (%) | 40 maximum | 25 - 30 typical<br>80 - 90 max | N/A |
| Coupling | NIL<br>NIL | 15 - 25 typical<br>80 - 90 maximum | 0.1 - 0.4 typical |
| Voltage (V) (Geometry dependent) | NIL<br>NIL | >1000 | Typical N/A<br>>1000 max |
| Max. Field ( MV/m) | NIL<br>NIL | 110 - 440 | 10 typical<br>150 maximum |
| Lifetime (cycles) | Unlimited | $10^7$ at 5%<br>$10^6$ at 10% | N/A |
| Advantages | -Large strain<br>-Moderate stress<br>-Variable stiffness<br>-High efficiency<br>-Superior cycle life (due to regeneration) | -Large strain, moderate stress<br>-Large work density<br>-Low cost<br>-Require low current<br>-Good efficiency and coupling | -Moderate strain<br>-High stress<br>-Excellent work density<br>-High stiffness<br>-Strong coupling<br>-Low operation current |
| Disadvantages | -Limited range of operating temperature<br>-No catch state (energy needed to sustain a force) | -High voltage<br>-Requires AC-DC converter<br>-Compliant<br>-Pre-stretching required. | -High voltage and field<br>- AC-DC conversion needed<br>-Low cycle life due to fatigue<br>-Limited temperature range |
| Comments | -A very refined mechanism which is difficult to mimic | -The operating electric fields can be lowered using high dielectric materials. | -The operating electric fields can be lowered using high dielectric materials. |

**Table A (cont.):** Some performance benchmarks of artificial muscle materials (N/A is not available/applicable) ([12, 24])

| | **Field driven Liquid Crystal Elastomers** | **Conducting Polymers** | **Molecular Actuators** |
|---|---|---|---|
| Strain (%) | 2 - 4 typical | 2 typical<br>12 maximum | 20% chemical activated<br>7% photoinduced |
| Strain Rate (%s-1) | 1000 | 1 typical<br>12 maximum | N/A |
| Stress (MPa) | N/A | 5 typical<br>34 maximum | 1 maximum |
| Modulus (MPa) | 100 | 200 typical<br>800 maximum | N/A |
| Work Density (kJ.m-3) | 20 | 100 | >100 kJ/$m^3$ |
| Specific Power (W.kg-1) | N/A | 150 maximum | N/A |
| Efficiency (%) | 75 | <1 typical<br>18 maximum | 10 |
| Coupling | N/A | < 0.1 | N/A |
| Voltage (V) (Geometry dependent) | 0.11 V applied to a 75nm thick film | 1.2 typical<br>10 maximum | ~ 2 V |
| Max. Field ( MV/m) | 25 | N/A | N/A |
| Lifetime (cycles) | N/A | 28,000 typical<br>800,000 max | N/A |
| Advantages | -Moderate to large strains<br>-High coupling | -Moderate strain<br>-High stress<br>-Low voltage<br>-High work density<br>-High stiffness | -Moderate to high stress<br>-Large strains<br>-Low voltage<br>-High work density |
| Disadvantages | -Creep<br>-Slow response<br>-High field<br>-Low efficiency | -Low electromechanical coupling<br>-Low frequency<br>-Encapsulation required | -Slow response<br>-Needs encapsulation |
| Comments | -New promising material with lots of characterization needed | -Promising for low voltage application.<br>-Strain rate improves considerably at small scales | -Potentially address many drawbacks of conducting polymer actuators, but still in early stages of development |

**Table A (cont.):** Some performance benchmarks of artificial muscle materials (N/A is not available/applicable) ([12, 24])

| | **Carbon Nanotubes** | **Ionic Polymer Metal Composites** | **Thermally Activated SMA** |
|---|---|---|---|
| Strain (%) | 0.2 typical<br>1 maximum | 0.5 typical<br>3.3 maximum | 5 typical<br>8 maximum |
| Strain Rate (%s-1) | 0.6 typical<br>19 maximum | 3.3 maximum | 300 typical |
| Stress (MPa) | 27 maximum | 15 maximum | 200 maximum |
| Modulus (MPa) | 1 paper<br>10 fiber | 0.1 typical | 83 maximum |
| Work Density (kJ.m-3) | 2 typical<br>40 maximum | 5.5 maximum | 1000 typical<br>10000 maximum |
| Density (kg.m-3) | 230 typical<br>1000 maximum | 1500 typical | 6450 typical |
| Specific Power (W.kg-1) | 10 typical<br>270 maximum | 2.56 maximum | 1000 typical<br>>50000 maximum |
| Efficiency (%) | 0.1 typical | 1.5 typical<br>2.9 maximum | < 5 maximum |
| Coupling | 0.001 typical | typical N/A<br>3 maximum | N/A |
| Voltage (V) (Geometry dependent) | 1 | 1 - 4 typical<br>7 maximum | 4 typical |
| Lifetime (cycles) | 33 reduction in strain over 140 cycles | N/A | 300 at 5%<br>$10^7$ at 0.5% |
| Advantages | -Low voltage<br>-High stress<br>-Very wide operating temperature range | -Low voltage<br>-Large displacement | -Very high stress<br>-Unsurpassed specific power<br>-Moderate to large strain<br>-Low voltage |
| Disadvantages | -Small strain<br>-Low coupling<br>-Expensive material | -Low efficiency and coupling<br>-No catch state<br>-Encapsulation needed | -Difficult to control<br>-Large currents and low efficiencies<br>-Cycle life is very limited, especially at large strain values |
| Comments | -Well-studied material with reported properties approaching individual nanotubes | -IPMC driven toys and demonstration kits are available | -Commercially available<br>-Response time in the range of millisecond can be achieved using current pulses |

**Table A (cont.):** Some performance benchmarks of artificial muscle materials (N/A is not available/applicable) ([12, 24])

| | **Ferromagnetic Shape Memory Alloys** | **Magnet-Polymer Composite** |
|---|---|---|
| Strain (%) | 6 typical<br>10 maximum | 40 maximum (from [32]) |
| Strain Rate (%s-1) | 10000 typical | 1500 (calculated from [38]) |
| Stress (MPa) | 1 typical<br>9 maximum | 0.06 maximum ( from [281]) |
| Modulus (MPa) | 2 typical<br>90 maximum | 0.07 (from [292]) |
| Work Density (kJ.m-3) | 100 typical | 3 (calculated from [65]) |
| Density (kg.m-3) | 8000 typical | > 1300 (from [293] ) |
| Coupling | 75 typical | N/A |
| Max. Field ( MV/m) | N/A | Maximum magnetic field ~ 40 kA/m (from [281]) |
| Advantages | -High stress<br>-High frequency<br>-Moderate strain<br>-High strain rate<br>-High coupling | -Different modes of shape change<br>-Highly flexible<br>-Fast response<br>-Large displacement<br>-Can be biocompatible |
| Disadvantages | -Single crystal is required and thus costly | -Small work density<br>-Low stress |
| Comments | -A restoring force is needed.<br>-No intermediate states<br>-Commercially available. | - More prototypes and systems need to be built based on these materials |

# APPENDIX B: LIST OF MAGNETIC PARAMETERS

Table B lists the magnetic parameters used in this thesis

**Table B:** List of magnetic parameters used

| Symbol | Name and description |
|---|---|
| $f_m$ | Magnetic force density, i.e., magnetic force per unit volume |
| $\mu_0$ | Magnetic permeability of vacuum |
| M | Sample magnetization |
| $\nabla H$ | The magnetic field gradient along the direction of deformation of the ferrogel |
| $\chi$ | The initial susceptibility of a Magpol sample |
| $H_{top}$ | Magnetic field strength at the top of a Magpol sample |
| $H_{bottom}$ | Magnetic field strength at the bottom of a Magpol sample |
| $H_{max}$ | Magnetic field strength at the electromagnet pole center. |
| $\alpha$ | The characteristic constant of magnetic field distribution |
| $k$ | $k = \gamma / \left(2\delta + \gamma\delta^2\right)$ is the decay constant of the electromagnetic field, $\delta$ is the electromagnet pole radius and $\gamma$ is a characteristic constant of each electromagnet. |
| $w_{mag}$ | The magnetic energy density of a magnetizable material |
| $w_{co}$ | The co-energy density, i.e., the area under a B-H curve |